UNIVERSITY OF READING

Department of Meteorology

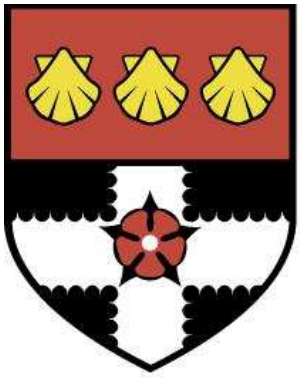

Simulations of interacting regions of tropical deep convection coupled by a weak-temperature gradient parameterization of the large-scale circulation

Chimene Laure Daleu

A thesis submitted for the degree of Doctor of Philosophy

April 19, 2013

Declaration

I confirm that this is my own work and the use of all material from other sources has been properly and fully acknowledged.

Chimene Laure Daleu

Abstract

In the Tropics, the large-scale circulation acts to redistribute density anomalies towards uniform density on isobaric surfaces. This is the weak-temperature gradient (WTG) approximation. In this thesis, a cloud-resolving model (CRM) is used to simulate the interactions between convection and the large-scale circulation which is parameterized using the WTG approximation.

As in other WTG studies, the large-scale circulation is derived under the requirement that the instantaneous domain-mean temperature remains close to a reference profile. Over uniform surface conditions, a large-scale descent develops within the simulated column no matter the relaxation profile and the initial conditions. This is similar to the results found in some other WTG studies but not all.

A new approach is developed to link two CRMs through the WTG derived large-scale circulation which constrains the domain-mean temperature profiles in the two CRMs to remain close to each other. This extension of the former approach enables the option of closing the heat and moisture budgets. In contrast to the reference column approach, no mean large-scale circulation develops under uniform surface conditions, regardless of the relative size of the columns. The sensitivity to non-uniform surface conditions is similar to that obtained in the simulations that used the reference column if the columns have large difference in areas, but is remarkably weaker for columns of equal areas.

The transient evolution of convection is investigated under the new approach. The simulation of the transition is forced by changing the surface forcing. The change in surface forcing drives changes in the strength of the large-scale forcing, which strongly influences the transition. The contributions from the large-scale forcing are equally divided between the heating and moistening effects. The timescale for the transition is examined for different forcing methods. The transition time is much longer when the transition is forced remotely compared to when it is forced locally.

Acknowledgements

I would like to thank my supervisors Dr Robert Plant and Dr Steve Woolnough for their guidance and support. I would also like to thank them for the fact that they have turned out to be very good counsellors. As a result, my study in Reading has been very enjoyable, and without their continuous encouragement and optimism I would never have made all this work through the three years. I must also thank Dr Maarten Ambaum, who has given me useful information concerning the possible ways of extending this work.

I would like to thank the University of Reading for the financial support, without which many of the International PhD's in Reading, including mine, would never have happened. I would also like to thank the UK Meteorological Office for the availability of the cloud resolving model used for this project.

I am very grateful to Dr Marc Stringer, who helped me to overcome the frustrations of running large numerical codes by answering numerous questions about the cloud resolving model. I relied on Mr Andrew Heaps for computing support and advice.

I would like to thank my monitoring committee members, Dr Mike Blackburn and Dr Len Shaffrey for their meticulous attention to details. In Reading, my inspiration has benefited from conversations with other members of the department. To everyone who has contributed to this project, both within and outside the department, I would like you to know that your help is really appreciated. Special mention should go to Dr Christospher Holloway and Dr Thomas Toniazzo for their helpful suggestions.

Finally, I would like to thank the guys in 2U06. A big thank to my family for giving me the opportunity to receive a good education. Special mention goes to my mother Mrs Jeanne Noupouatie, my grand-mother Mrs Odile Daleu and my lovely aunts Mrs Therese Celarie Wamou-Jost and Mrs Evone Ntchengeh.

This thesis is dedicated to my grand-mother Mrs Odile Daleu.

Contents

1 Introduction **1**

1.1 Tropical Convection and large-scale circulation 1

1.2 Simulation of the large-scale circulation 5

1.3 Simulation of tropical convection 7

1.4 Interactions between convection and the large-scale 9

1.5 Parameterization of the large-scale in limited-area models 11

1.5.1 Weak-temperature gradient approach 11

1.5.2 Weak-pressure gradient approach 14

1.5.3 Hydrostatic approach 16

1.5.4 Time-lagged approach 18

1.6 Thesis Aims 19

1.7 Thesis Plan 22

2 Single Column Model simulations with two-way coupling via the weak temperature-gradient approximation **25**

2.1 Introduction 25

2.2 Model description 26

2.2.1 Convection Scheme 26

2.2.2 Surface fluxes and Radiation 33

2.2.3 Moisture and energy conservations 34

2.2.4 Other details 35

2.3 Equilibrium behavior of the SCM 36

2.4 Coupling methodology 39

2.4.1 The weak-temperature gradient approximation 40

2.4.2 WTG adjustment profiles 45

2.4.3 Heat and moisture budgets 46

2.5 Equilibrium of the coupled SCMs over non-uniform surface conditions . . 47

2.5.1 Sensitivity to the WTG timescale 50

2.5.2 Sensitivity to the surface conditions 52

2.6 Equilibrium of the coupled SCMs over uniform surface conditions 55
2.7 Chapter Summary 58

3 Radiative-Convective Equilibrium Simulation 60
3.1 Introduction 60
3.2 Dynamics and Thermodynamics 61
3.2.1 Basic Equation Set 61
3.2.2 Reference state and Buoyancy 63
3.3 Subgrid Model 64
3.4 Boundary Conditions 65
3.5 Moist Processes and Microphysics 67
3.6 Radiation 67
3.7 Numerical Methods and Stability Criteria 69
3.8 Model dimensionality, size and resolution 70
3.9 Other details 72
3.10 Approach to Radiative Convective Equilibrium 73
3.10.1 Profiles at radiative-convective equilibrium 77
3.10.2 Statistical description of convection 82
3.10.3 Sensitivity to the SST 86
3.11 Conclusions 87

4 WTG calculations over uniform surface conditions 89
4.1 Introduction 89
4.2 Implementation of the WTG approximation 89
4.3 Reference column approach 90
4.3.1 Sensitivity to WTG adjustment timescale 94
4.3.2 Sensitivity to the initial conditions 99
4.4 Coupled-column approach 106
4.5 Conclusions 112

5 WTG calculations over non-uniform surface conditions 115
5.1 Introduction 115
5.2 Reference column approach 116
5.2.1 Time evolution and mean statistics at equilibrium 116
5.2.2 The large-scale circulation 120

5.2.3 Thermodynamic and convection structures . . . 121
5.2.4 Reference column versus RCE simulations . . . 126
5.3 Coupled-column approach . . . 127
5.3.1 Temporal evolution . . . 128
5.3.2 The WTG-derived large-scale circulation . . . 133
5.3.3 Thermodynamic and convective structures . . . 135
5.3.4 Sensitivity to the column sizes . . . 142
5.3.5 Coupled-column simulations versus RCE simulations . . . 143
5.4 Conclusions . . . 146

6 Transition from suppressed to active convection 148
6.1 Introduction . . . 148
6.2 Mean states of the columns prior to the simulation of the transition . . . 150
6.2.1 Parameterized large-scale circulation . . . 151
6.2.2 Thermodynamic profiles . . . 152
6.3 Simulations of the transition . . . 155
6.3.1 Time evolution of some column-integrated fields . . . 156
6.3.2 Time evolution of some vertical fields . . . 158
6.4 Sensitivity experiments . . . 162
6.4.1 Sensitivity to the method of forcing the transition . . . 162
6.4.2 Sensitivity to the troposphere moisture . . . 167
6.5 The transition time . . . 169
6.6 The roles of surface forcing and large-scale forcing . . . 173
6.7 Conclusions . . . 177

7 Conclusions 179
7.1 Summary and discussion . . . 182
7.2 Limitations . . . 189
7.3 Future work . . . 190

A Notation Conventions 194

B Interactive radiation 196
B.1 Introduction . . . 196
B.2 Radiative convective equilibrium simulations . . . 196
B.3 Reference column approach . . . 197

B.4 Coupled-column approach 200
B.5 Summary 200

C Computation of the large-scale vertical motion and the tendency terms 202
C.1 Introduction 202
C.2 Large-scale vertical velocity 202
C.3 Tendency terms due to the WTG-derived large-scale circulation 203

Bibliography 204

Chapter 1:
Introduction

This thesis aims to simulate the interactions between convection and the large-scale dynamic in the tropics. However, convection and the large scale dynamics are processes evolving at very different temporal and spatial scales. The life-cycle of convection is defined in terms of hours and the resulting clouds can have horizontal extent between $1-2$ km (or smaller) for a single cloud and up to 10 km for a spectrum of clouds. In contrast, the large-scale atmospheric dynamics are generally of order of 1000 km wide and evolve over several days. In practice, this separation of scales makes it difficult to simulate both processes in the same atmospheric model. This thesis explores these interactions by using and extending a commonly used approach to parameterize the large-scale dynamics in a high resolution model of convection.

1.1 Tropical Convection and large-scale circulation

Convection is an adjustment process which results from vertical instability in a fluid. Atmospheric convection usually occurs when the surface is heated until a surface parcel becomes warmer than the surrounding air. However, atmospheric convection can be triggered as a result of other processes like convergence of surface air, uplift along weather fronts and topography.

In the absence of moisture, a parcel of warm air lifted into an unstable environment rises as a result of being lighter than the surrounding air. During its ascent, it adiabatically expands and cools but does so at a rate less than the environment. Typically in the atmosphere, dry convection rarely occurs except within the boundary layer. Dry con-

vection transports heat and moisture from the near surface and redistributes through the boundary layer following the dry adiabatic lapse rate (Γ_d, theoretical temperature lapse rate of an unsaturated air parcel which moves adiabatically in the vertical).

In the presence of moisture condensation can occur and the parcel can continue to accelerate if the net latent heat released due to phase changes warms it sufficiently to maintain its positive buoyancy relative to the surrounding air. The temperature of such a parcel will follow the moist adiabatic lapse rate (Γ_m, theoretical temperature lapse rate of a saturated air parcel which moves adiabatically in the vertical). The vertical extent of the resulting cloud is determined by the stability of the environment. In a situation of absolute stability, the environmental lapse rate (Γ_e, the decrease of temperature with height) is smaller than Γ_m and hence, is smaller than Γ_d. In such a condition, if an air parcel is forced to rise (i.e. in response to low level convergence of air) its motion will be rapidly damped out. No cloud will likely form and if it does, it will be shallow, layered cloud like stratus. In a situation of conditional instability ($\Gamma_m < \Gamma_e < \Gamma_d$), deep cloud like cumulonimbus can form. However, shallow cumulus and stratocumulus can form if the unstable layer is limited in height.

An air parcel lifted from the surface rises following the dry adiabatic lapse rate (conserving its values of potential temperature and mixing ratio) until it reaches the saturation line; that is the lifted condensation level (LCL). From the LCL onwards, the parcel rises following the moist adiabatic lapse rate. Typically in the atmosphere, there is a region near the surface which is stable; and a certain amount of energy is required to overcome the negative energy barrier which causes the air parcel to accelerate downward. This negative energy barrier is called convective inhibition (CIN). In circumstances when the air parcel has enough energy to overcome the CIN, it will continue to rise following the moist adiabatic lapse rate until its temperature reaches the environmental temperature. If on further lifting the air parcel becomes positively buoyant relative to the surrounding air, one has found the level of free convection (LFC). The parcel will continue to rise through the free troposphere until its temperature reaches the environmental temperature.

If on further lifting from this level the parcel becomes stable, one has reached the level of neutral buoyancy (LNB). The parcel can continue to rise above the LNB because it has kinetic energy, but the parcel will overshoot while buoyancy forcing acts to decelerate its motion. In the atmosphere, an indicator of instability is the convective available potential energy (CAPE, or height-integrated buoyancy of an undiluted parcel lifted from the LFC to the LNB). The CAPE is proportional to the area between the temperature profile of the environment and the trajectory of a parcel taken from the LFC and lifted pseudo-adiabatically to the LNB without entrainment of the surrounding air.

A convective plume interacts in a complex way with the surrounding environment;
1- the detrainment of clouds at high levels reduces the amount of incoming shortwave radiation reaching the surface and at low levels reduces the cooling of the atmosphere due to loss of terrestrial radiation.
2- It is accompanied by a spatially extended pattern of divergent gravity waves which quickly redistribute the heating produced by condensation toward the surrounding environment (with a phase speed of about 50 m/s corresponding to deep convection) and which produce subsidence motions to compensate for the relatively narrow ascending motions. The compensating subsidence motions warm and dry the surrounding atmosphere.
3- The downdrafts produced from the drag of falling precipitation and cooling by evaporation may trigger secondary convection at the surface.
4- Finally, the convective system itself is modified in a highly non-linear way by fast subcloud scale processes like turbulence, entrainment of cold and dry environmental air and microphysics.

Convection is the primary global mechanism through which solar heating of the ocean and land is vertically redistributed through the free troposphere. The heat input can be either emitted back to space through longwave radiation or transported polewards by the global-scale circulation. Convection is also the mechanism through which the upper troposphere is enriched with water vapor and the upper-tropospheric humidity plays a

key role in preserving the natural greenhouse effect in the atmosphere.

Deep convective cloud systems are the main generator of tropical precipitation. They are also the great engines which drive the large-scale atmospheric flows and it is the large-scale flows which in turn are responsible for much of the variability of tropical convection. The interactions between convection and the large-scale determine the structure of temperature, moisture and cloud in the free troposphere in the tropics and is an important aspect in determining the Earth's climate. Hence, it is important to better understand the full complexity of the interactions of convection with the large-scale.

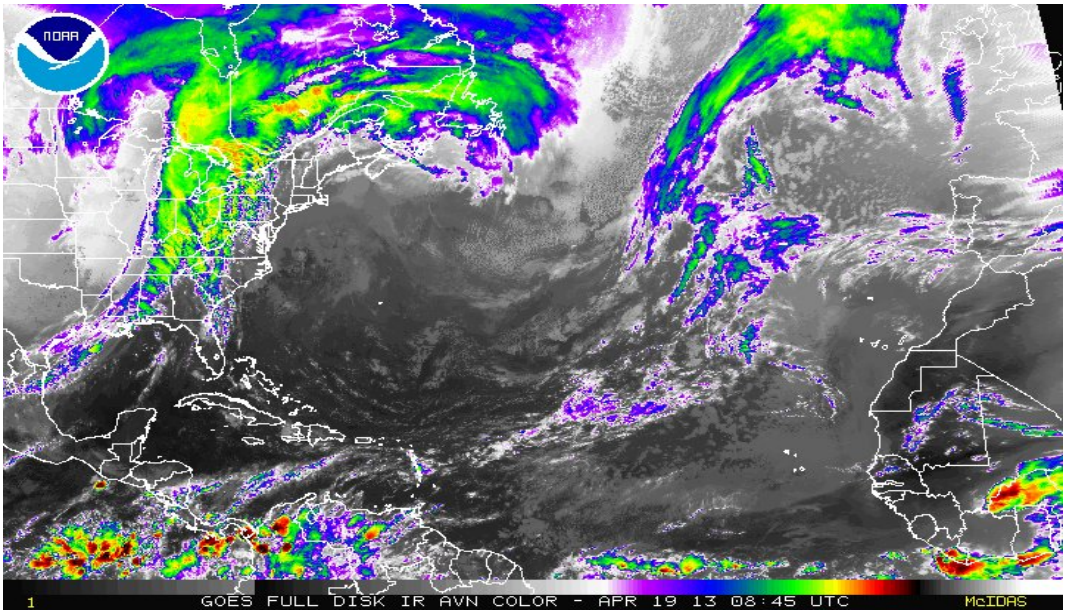

Figure 1.1 *Snapshot of clouds over North Atlantic Ocean, Caribbean sea, Gulf of Mexico and part of East Pacific Ocean. Snapshot taken on April 19 2013 at 08:45 UTC. Image from http://www.ssd.noaa.gov/PS/TROP/Basin$_A$tlantic.html*

Figure 1.1 shows a snapshot illustrating the distribution of clouds over North Atlantic Ocean, Caribbean sea, Gulf of Mexico and part of East Pacific Ocean. This snapshot was taken on April 19 2013 at 08:45 UTC. There is a wide range of spatial scales involved in this distribution. Over North Atlantic Ocean, clouds are mostly organized into clusters by mid–latitude weather systems. The clusters can extend horizontally over thousands of kilometers, leaving the surrounding area free from clouds or with clouds which appear

as isolated cells. Over the Caribbean Sea, Gulf of Mexico and East Pacific Ocean clouds are also organized into clusters but with scales smaller than those observed over North Atlantic Ocean. The organization of clouds into clusters is in response to (and feed back on) the global-scale atmospheric dynamics. For examples, the Madden Julian Oscillations (MJO,Sui and Lau (1992)), the El Nino Southern Oscillation (ENSO), Equatorial waves and African Easterly waves (AEWS). However, the large range of scales between individual convective clouds and the large-scale dynamics makes the simulation of their interactions a difficult task because of computational limitations. Currently there are only few studies which have explicitly simulated moist convection and the large-scale in the same atmospheric models (e.g. Grabowski et al., 2000; Shutts and Palmer, 2007; Liu et al., 2009; Holloway et al., 2012).

1.2 Simulation of the large-scale circulation

General Circulation Models (GCMs) are powerful tools to study various aspects of the large-scale tropical circulation. However, GCMs suffer from a range of problems associated with the need for parameterizing processes that occur at a scale smaller than the model horizontal resolution. One example is the parameterization of convection or cumulus parameterization scheme which makes assumptions about the level of convection present at any given place and time in order to determine its mean effect and its feedback on the large scale environment (e.g. Lin et al., 2006; Dai, 2006; Lin et al., 2008b; Randall et al., 2007). The improved parameterization of small scale processes may improve the ability of GCMs to simulate accurately the observed climate and it has been shown that failure to do so may account for some biases in the representation of the large-scale flows (e.g. Palmer et al., 1986). Unfortunately, the results of GCM simulations are sensitive to the details of cumulus parameterization used to represent the cumulative effects of convective processes happening at scales smaller than the model grid cell (e.g. Yano et al., 1998). As a consequence, a set of GCMs can display a wide range of skill in simulating

the large-scale flows (e.g. Lin et al., 2008a).

Despite the improvement in the parameterization of small-scale processes, current state-of-art GCMs still have difficulties and display a wide range of skill in simulating the large-scale circulation and associated variability. Hence, the ability of current state-of-art GCMs to respond realistically to climate perturbations are still affected. An example of study is the one conducted by Lin et al. (2008a), which evaluates the ability of 14 coupled GCMs (participating in the Intergovernmental Panel on Climate Change (IPCC) Fourth Assessment Report (AR4)) to represent the subseasonal variability associated with the Indian Summer Monsoon. To quantitatively evaluate the model simulations, the authors used the meridional profile of total subseasonal (2-128 day) variance in precipitation in the three major regions of the Indian summer monsoon: the Indian summer monsoon (ISM, 5°–25°N and 60°– 100°E), the East Asian summer monsoon (EASM, 25°–40°N and 100°-160°E) and the Western North Pacific summer monsoon (WNPSM, 5°–25°N and 110°-170°E). The meridional profile of total subseasonal variance in precipitation obtained in each of the 14 coupled GCMs are compared with that obtained from the daily data of the Global Precipitation Climatology Project (GPCP) Version 2 Precipitation (Huffman et al., 2001) for the ISM region in Figure 1.2 (a) and for the WNPSM and EASM regions in Figure 1.2 (b).

The results from the 14 coupled GCMs display a wide range of skill in the representation of the total subseasonal variance in precipitation in these three monsoon regions. Among the 14 models, three can simulate a variance that approaches the observed value in the ISM region and only one model can simulate a variance that is close to the observed value in the WNPSM region. In the EASM region the total subseasonal variance in the 14 models is weaker than the observed variance. Overall, most of the models underestimate the total subseasonal variance in precipitation. Only a couple of models can produce realistic variance in one or two monsoon regions. However, no model can simulate variance that approaches the observed values in the three monsoon regions.

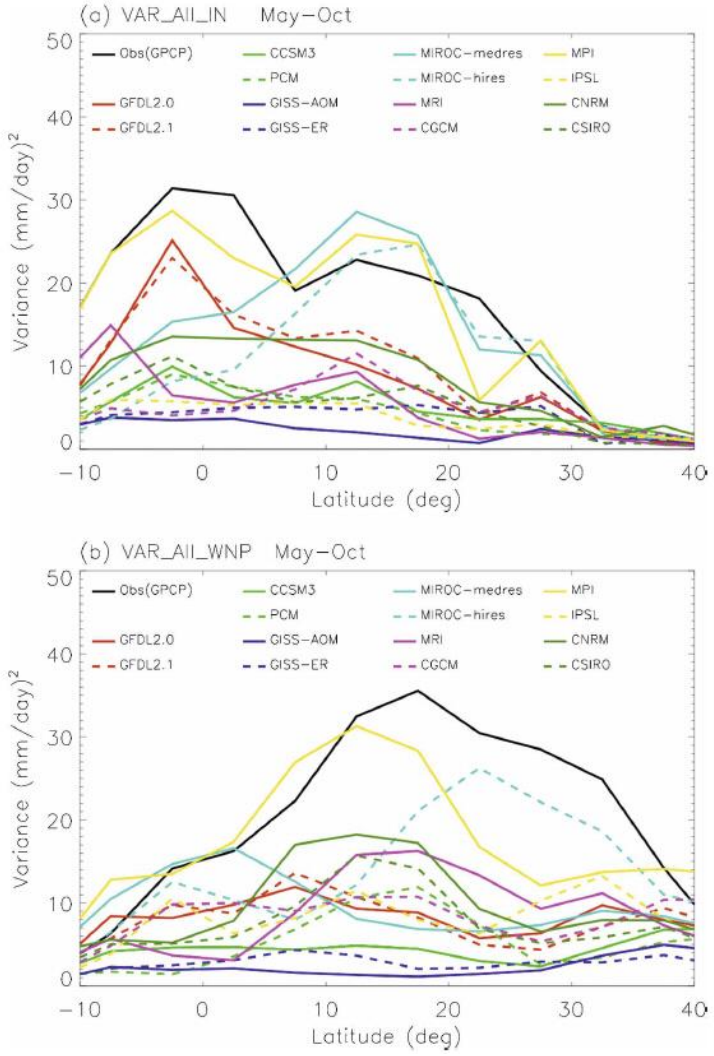

Figure 1.2 *Meridional profile of the total subseasonal (2-128 day) variance of precipitation anomaly averaged between* 60° *and* 100°E *(a), and between* 120° *and* 160°E *(b). The results are those obtained in the 14 coupled GCMs and observations (Huffman et al., 2001). This Figure is taken from Lin et al. (2008a).*

1.3 Simulation of tropical convection

The resolution in numerical models determines the method of representing convection. Current digital computers cannot simulate global-scale processes with resolution down to

the scale of individual clouds. As a result, various types of atmospheric model are developed to simulate some subset of processes with a limited range of spatial and temporal scales. In low-resolution numerical models such as the GCM, the important sub-grid scale processes are parameterized. On the other hand, state-of-art GCMs are very sensitive to the choice of cumulus parameterization scheme (e.g. Yano et al., 1998) and most of them misrepresent the climate variability (e.g. Lin et al., 2008a,c). An alternative is the use high resolution models such as the Large Eddy Model (LEM) which remove the need of using cumulus parameterization. LEM explicitly resolves the small scale processes responsible for most of the energy transport and leaves only cloud microphysics, radiation, small scale processes and turbulence to be parameterized. However, with this level of complexity the LEM can not be integrated in a large enough area to capture the large-scale systems which often act as a forcing for convection.

Until recently, LEM studies have ignored the full interactions between convection with the large-scale flow; thus, advection by the large-scale circulation is either neglected or prescribed. LEM studies that neglect the large-scale flows assume that convection is entirely disconnected from any evolution of the large scale atmospheric circulation. Simulations that apply this assumption are integrated over a sufficiently long time (over a life cycle of many clouds) until an approximate balance between the energy loss due to radiative processes and energy gain due to phase changes is obtained; that is the radiative convective equilibrium (RCE) (e.g. Robe and Emanuel, 1996; Tompkins and Craig, 1998a; Cohen and Craig, 2006). On the other hand, there are LEM studies that use a predefined large-scale forcing of convection, possibly based on idealization or experimental campaigns (e.g. Vincent, 1994; Tompkins, 2001; Xu et al., 2002; Petch et al., 2002). Such studies simulate only the one-way interaction which is the response of convection to the prescribed large-scale forcing, under the assumption that small scale processes including convection occur on a time scale which is short compared to the timescale characterizing changes in the large-scale. A disadvantage of such simulations is that the amount of precipitation produced is not entirely determined from the model physics. In contrast, it is too much constrained due to the predefined large-scale horizontal advection of moisture

(Mapes, 1997; Sobel and Bretherton, 2000). Hence, such simulations can not be used to understand what factors control the occurrence and intensity of tropical deep convection (Sobel et al., 2004).

Despite the fact that the former type of LEM study does not allow any interaction between convection and the large scale flows and the latter does not allow convection to alter the advective large-scale forcing, it must be recognized that these two types of LEM studies have been successful for understanding many aspects of the mechanisms of the formation of tropical convection. In practice, however, there are close links between tropical convection and the large-scale flows such that ignoring the interactions between the two or treating one as the forcing for the other is not necessarily appropriate, particularly in non-equilibrium conditions (Mapes, 1997; Holloway and Neelin, 2010; Masunaga, 2012) and especially in the tropics where the large-scale vertical advection is important.

1.4 Interactions between convection and the large-scale

In order to understand how convection influences the evolution of the large-scale flows and how the large-scale flows in turn influence the evolution of convection, there is a need for approaches in which the large scale flows and convection are both simulated. LEMs run in the Cloud-Resolving Mode (CRM) (high horizontal resolution on the order of ≈ 1 km) over a domain on the order of the large-scale circulation (≈ 10000 km) or GCMs run with very high horizontal resolution are currently the most realistic models available for simulating the coupling of small scale processes such as moist convection to the evolution of the large-scale flows. However, such level of realism comes with high computational cost. As a result, the domain for CRMs is usually limited to a size that does not allow for the explicit simulation of the large-scale dynamics while the grid spacing for GCMs is usually increased to a size that does not allow for explicit simulation of convection.

Recent advances in computer power have allowed the development of new approaches allowing simulation of the large-scale tropical dynamics while explicitly simulating convective processes. These include the super-parameterization approach of Randall et al. (2003) in which the subgrid flow within each grid square of a GCM is determined from an embedded CRM. However, despite the use of super-parameterization in order to explicitly simulate convection and other subgrid scale processes, these GCM simulations still suffer from many of the weakness seen in the traditional GCMs. On the other hand Grabowski et al. (2000) simulated the large-scale circulation driven by a prescribed sea surface temperature (SST) gradient using a global two-dimensional CRM. The large-scale flow showed two distinct circulations in the upper and lower troposphere with structure which was somehow more complex compared to the first baroclinic mode structure associated with the classic Walker-like circulations.

An alternative approach was proposed by Kuang et al. (2005), in which the scale difference between convection and large-scale circulation was reduced using a Diabatic Acceleration and REscaling approach in order to be able to resolve both scales within a three-dimensional CRM. However, for too large a rescaling, the troposphere becomes deeper and the length of convective life-cycle is increased relative to synoptic phenomena (Garner et al., 2007).

Recently, it has became feasible to simulate the interactions between convection and large-scale circulation in large-domain, high-resolution experiments such as those conducted at the Earth simulator center[1] (e.g. Liu et al., 2009) and in projects such as Cascade (e.g. Holloway et al., 2012). However, these large-domain, high-resolution simulations still make many parameterizations of the unresolved processes and the simulated patterns present many differences when compared with observations over the tropics.

Each of these new approaches have strengths and weaknesses, but a common disadvantage of all of them is that integrations remain computationally expensive, so that it is not practical to study large sets of multiple experiments in order to test mechanisms and

[1] http://www.es.jamstec.go.jp/index.en.html

assess sensitivities.

1.5 Parameterization of the large-scale in limited-area models

From the previous studies mentioned above, it is seen that simulations of convection with a predefined large-scale forcing are over-constrained and that simulations of both convection and the large scale flow remain difficult because of computational limitations. One possible solution is to parameterize the large-scale forcing in limited area model such as the CRM or the Single Column Model (SCM). In particular, the idea is to extend the traditional CRM or SCM to a model which allows the evolution of convection within the model to feedback on the large-scale forcing. Previous formulations have differed in how the large-scale circulation is parameterized. In some applications, the vertical motion was related to the domain-mean temperature, or to the domain-mean heating or else both the heating and vertical motion were decomposed into vertical modes with different length and time scales. Some of those formulations are discussed below.

1.5.1 Weak-temperature gradient approach

In deep Tropics (near the equator) where the action of the Coriolis force is almost zero, gravity waves act to rapidly redistribute buoyancy anomalies, thus maintaining a nearly uniform density on isobaric surfaces. Hence, the large-scale horizontal gradients, and time tendencies of potential temperature can be assumed to be negligible ($\nabla_h \cdot \theta \approx 0$ and $\frac{\partial \theta}{\partial t} \approx 0$).

In many studies, the parameterization of the large-scale circulation in limited area models has relied on these two assumptions. For instance, Sobel and Bretherton (2000)

used those assumptions to simplify the prognostic equation of potential temperature

$$\frac{\partial \theta}{\partial t} + \nabla_h \cdot (\mathbf{v}\theta) + \rho^{-1} \frac{\partial \rho w \theta}{\partial z} = S_\theta \tag{1.1}$$

to the diagnostic equation for the large-scale vertical motion

$$\overline{w} \frac{\partial \overline{\theta}}{\partial z} = \overline{S}_\theta \tag{1.2}$$

where S_θ is the diabatic source of potential temperature. By using Equation 1.2, the authors diagnosed the large-scale vertical motion necessary to hold the domain-mean potential temperature fixed in the presence of diabatic heating. Hence, the column-mean potential temperature differences are zero. Following their study, this formulation has become known as the Weak Temperature Gradient (WTG) approximation. On the other hand, Raymond and Zeng (2005) applied a weaker constraint that the large-scale vertical motion acts to reduce the column-mean potential temperature differences over a fixed timescale. That is

$$\overline{w} \frac{\partial \overline{\theta}}{\partial z} = \frac{\overline{\theta} - \overline{\theta}_{ref}}{\tau} \tag{1.3}$$

where τ is timescale related to the propagation speed of gravity waves across the system. The parameterization of the large-scale circulation using Equation 1.2 as in Sobel and Bretherton (2000) is a strict application of the WTG approximation. The strict application of the WTG approximation can also be achieved using Equation 1.3 in the limit of $\tau = 0$.

The WTG approximation is not valid in the planetary boundary layer. This is due to strong vertical mixing which counteracts the dynamical adjustment process that homogenizes temperature in the free troposphere and hence, ties the temperature there to the underlying surface temperature. Previous studies applying the WTG approximation (e.g. Sobel and Bretherton, 2000; Raymond and Zeng, 2005, and many others) specify the large-scale vertical flow in the planetary boundary layer by interpolating linearly in pressure or height between its value at the first model level above the planetary boundary layer to the value of zero at the surface.

Previous WTG studies have coupled the traditional CRM or SCM to a reference reservoir column (e.g. Sobel and Bretherton, 2000; Raymond and Zeng, 2005; Sobel et al.,

2007; Sessions et al., 2010; Wang and Sobel, 2011). The coupling to a reservoir column may be justified by assuming that the region to be simulated is very small in comparison with its surroundings. A typical situation would be to consider that surface conditions are uniform almost everywhere, except for a localized region with a different surface condition (e.g., high SST). It is expected that a descending (or ascending) branch arises over the local region, with compensating motion within the surroundings that is negligibly weak because of the large difference in areas. The WTG-derived large-scale flow will redistribute the heating associated with convection and hence, will maintain the local temperature profile close to large-scale mean temperature profile of the surroundings. A typical objective is to study the effects of coupling to the large-scale area on the precipitation within the explicitly-simulated local area. Conceptually, the coupling to a reservoir column could be viewed as a limit of the two-column models (e.g. Pierrehumbert, 1995; Nilsson and Emanuel, 1999; Raymond and Zeng, 2000), in which one of the columns is much larger than the other representing the local area.

Sobel and Bretherton (2000) implemented the WTG approximation to a SCM version of the first quasi-equilibrium tropical model (QTCM1) of Neelin and Zeng (2000). In their case, the large-scale vertical flow was derived from the requirement that the temperature profile above the planetary boundary layer remains equal to a specified equatorial mean temperature profile. For unchanged surface conditions, the climatological mean rain rate obtained was not significantly different to that in the corresponding SCM version of the QTCM1 without the WTG parameterization of a large-scale circulation.

In contrast to Sobel and Bretherton (2000), Sobel et al. (2007) obtained a stronger precipitation rate in the SCM version of the GEOS-5 GCM when modified to implement the WTG approximation, in comparison with the rate obtained in an RCE simulation of the same SCM with the same surface conditions. For the case of WTG studies over inhomogeneous surface conditions, Sobel et al. (2007) and Bellon and Sobel (2010) used respectively the SCM version of the GEOS-5 GCM and the second version of the QTCM (Sobel and Neelin, 2006, QTCM2) to explain the existence of two distinct quasi-steady

states of the model under the WTG approximation.

Raymond and Zeng (2005) used the WTG approximation to diagnose a large-scale circulation for use with the CRM simulations. In their case, the large-scale vertical flow was derived from the requirement that the instantaneous domain-mean potential temperature profile be maintained close to a reference profile, the reference state itself having previously been determined from the RCE configuration of the same model at a given SST. In a homogeneous environment (i.e., with the same surface conditions as for the RCE configuration) a large-scale circulation develops with descent in the simulated region. In contrast, Wang and Sobel (2011) obtained no mean large-scale circulation in two and three dimensional simulations with the Weather Research and Forecasting Model (WRF) modified to implement the WTG approximation over uniform surface conditions. Analogous simulations for inhomogeneous surface conditions performed by Sessions et al. (2010) showed that two distinct equilibrium states could arise in a CRM when coupled to a fixed reference state through the WTG parameterization of large-scale circulation.

The WTG approximation has been used widely, differentiated by the WTG adjustment profile and by the treatment of the horizontal moisture advection by the WTG-derived large-scale circulation. However, other studies have used different formulations for parameterizing large-scale dynamics. Some of those formulations are briefly described below.

1.5.2 Weak-pressure gradient approach

In another formulation, the two-dimensional anelastic linearized perturbation equations of momentum, continuity and hydrostatic balance which are written respectively as

$$\overline{\rho}\frac{\partial u'}{\partial t} = -\frac{\partial P'}{\partial x} - \varepsilon\overline{\rho}u', \tag{1.4}$$

$$\frac{\partial \overline{\rho}u'}{\partial x} + \frac{\partial \overline{\rho}w'}{\partial z} = 0, \tag{1.5}$$

$$\frac{\partial P^{'}}{\partial z} = \overline{\rho} g \frac{\theta^{'}}{\overline{\theta}} \tag{1.6}$$

are resolved by considering a single horizontal wavenumber k at a time. Hence, this formulation assumes that Equations 1.4 to 1.6 have solutions of the form the

$$[u^{'}, w^{'}, \theta^{'}, P^{'}](x,z,t) = Re[\hat{\mathbf{V}}, \hat{w}, \hat{\theta}, \hat{P}](z,t) exp(-ikx) \tag{1.7}$$

where the prime denotes the fluctuations from the background mean state represented with the overbar. ε is the mechanical damping coefficient.

From Equations 1.4, 1.5, 1.6 and applying a solution of the type in Equation 1.7, the vertical motion is diagnosed from the domain-mean temperature as:

$$\left[\left(\frac{\partial}{\partial t} + \varepsilon\right) \frac{\partial \overline{\rho} \hat{w}}{\partial z}\right] = -k^2 \frac{\overline{\rho} g}{\overline{\theta}} \hat{\theta} \tag{1.8}$$

Hence, the large-scale dynamics is simplified to a linear wave of single horizontal wavenumber. A full description of this formulation is given in Kuang (2008) and the results from its application are presented in Kuang (2008), Kuang (2011) and Romps (2012). The details of the implementation of this formulation differ from one study to another but in all studies the common feature is a parameterization of the momentum equation. The direct effect of this parameterized momentum equation is to produce weak gradients of pressure between the column and its surroundings and following Romps (2012), this formulation has been referred to as the "weak pressure gradient (WPG) approximation". The WPG approximation has been a useful and relatively cheap framework for studying wave-convection interaction. However, unlike the simulations that applied the WTG approximation, the horizontal potential temperature differences in the simulations that applied the WPG approximation may remain very large.

Kuang (2008) implemented the WPG approximation in a limited domain cloud-system-resolving model (CSRM). Simulated convectively coupled waves are able to develop without feedback from radiation, surface fluxes, or wave radiation into the stratosphere. However, they are not able to persist when moisture advection by the large-scale waves is switched off. In addition, the simulated convective heating pattern is similar for

all wavelengths and is consistent with observations. This study was followed by that of Kuang (2011) which examined the wavelength dependence of the Gross moist stability (GMS) in the CSRM modified to implement the WPG approximation. In their study, the temperature anomalies are found to increase with wavelength. As a result, the GMS which is often considered as a constant in theoretical model of the tropical circulation, is found to be smaller at longer wavelengths. As a consequence of this result, to maintain the balance of momentum, heat, and moisture and to maintain a consistency in the behavior of cumulus convection, the shape of the divergent flow is constrained to be less top-heavy for the case of longer wavelengths.

Romps (2012) is the first study that compares the accuracy of the WTG and WPG approximations. This comparative study is done in the context of the three-dimensional (3D), linearized Boussinesq equations. Despite the fact that the two approximations failed to capture the two different time scales present in the full 3D equations, the author showed some disadvantages of the WTG approximation over the WPG approximation. For example: the WTG underestimates the buoyancy anomalies generated by an applied heating because of its nature of reducing temperature anomalies over a fixed time scale; the WTG failed to capture the adiabatic lifting of air below an initial buoyancy perturbation and finally, the WPG shows that a large-scale ascent can develop in a domain with zero column-integrated buoyancy, in contrast with the WTG which derives the vertical velocity from the buoyancy.

1.5.3 Hydrostatic approach

Another formulation examines the interaction between the large-scale flows and a radiative-convective environment by extending the SCM for radiative-convective equilibrium (described by Rennó et al., 1994) to a side-by-side two-column radiative convective model.

In this formulation, the system is assumed to be linear, hydrostatic and non rotating.

The governing dynamical equation is

$$\frac{\partial u}{\partial t} = -\frac{\partial \Phi}{\partial x} + \frac{\partial}{\partial P}\mu\frac{\partial u}{\partial P} \tag{1.9}$$

where μ is the viscosity, Φ is the geopotential height.

The continuity equation

$$\frac{\partial u}{\partial x} + \frac{\partial \omega}{\partial P} = 0 \tag{1.10}$$

allows the velocity field to be related to a stream function, Ψ:

$$(u, \omega) = (-g\frac{\partial \Psi}{\partial P}, g\frac{\partial \Psi}{\partial x}) \tag{1.11}$$

For the case of two columns of equal lengths, L, the vertical velocity in the updraught column, ω_U, is calculated as

$$\omega_U = g\frac{\Psi(P,t)}{L} \tag{1.12}$$

and the vertical velocity in the downdraught column, ω_D, is derived from the requirement that

$$\omega_U + \omega_D = 0 \tag{1.13}$$

The derived flow field is then used to advect heat and moisture between the columns. However, unlike the simulations that applied the WTG approximation, the horizontal potential temperature differences in the simulations that applied this formulation can remain very large. A full description of this formulation is given in Nilsson and Emanuel (1999) to which the reader is referred for more details. In their study, a positive feedback between advective drying by the large-scale circulation, clear sky water vapor and infrared cooling is able to destabilize the local RCE. As a result, the system attains a circulating equilibrium characterized by a moist updraught column and a dry downdraught column. Two distinct equilibria with circulations which are distinguished by the features of the descending branch are attained in the limit of an inviscid atmosphere: one branch with deep convection but where the heating produced by convection vanishes due to surface evaporation and radiation, and one branch with shallow or no convection where the free troposphere is disconnected to the boundary layer.

1.5.4 Time-lagged approach

To parameterize the large-scale effects in limited area models, another formulation assumes that the development of anomalous ascent is the delayed response to domain-mean heating anomalies. An examples of the application of this formulation in the CRM is described in Mapes (2004). Mapes (2004) divided large-scale vertical advection into three parts. That are:

1. large-scale vertical advection by a background forcing which sets up the strength and depth of the convective cloud ensemble;

2. large-scale vertical advection by a stimulus forcing which introduces some idealized examples of remotely driven changes to the region containing the convective cloud ensemble; and

3. advection by a parameterized anomalous large-scale motion, $w_p(z,t)$, driven by the domain-mean convective heating anomalies, $Q(z,t)$, produced by the CRM.

$w_p(z,t)$ is computed as a time-lagged function of $Q(z,t)$ and its effects are applied as advection-like source terms constructed like:

$$\overline{w}\frac{\partial\overline{\theta(t)}}{\partial z} = \overline{S}_\theta(t-\tau) \tag{1.14}$$

$$\overline{w}\frac{\partial\overline{q(t)}}{\partial z} = \overline{S}_q(t-\tau) \tag{1.15}$$

The time lag, τ, is considered to be the time for a gravity wave to travel half the width of the domain.

w_p and $Q(z,t)$ are decomposed spectrally into modes of a vertical structure equation (Fulton and Schubert, 1985) and w_p is constructed by superposing the simpler Fourier modes, each of which is characterized by a different time lag corresponding to its gravity wave speed. For simplification purposes, the author uses the same fixed vertical structure of the source terms S_θ and S_q, for both background forcing and advection by w_p. It was found that the rain rate increases (or decreases) are the direct response to the stimulus forcing corresponding to an upward (or downward) displacement by the large-scale wave of first baroclinic mode structure. In addition, the changes in rainfall are equally

divided between the dependence on temperature and free tropospheric humidity. For the case of stimulus forcing corresponding to the second baroclinic mode (vertical dipole) perturbations, the convective response is dominated by the sign of the lower-tropospheric displacement. For instance, upper-level subsidence does not prevent an increase in precipitation due to low-level ascent.

1.6 Thesis Aims

This study will investigate the interactions between convection and the large-scale circulation using the WTG approximation to parameterize the large-scale circulation. Previous studies have largely used the reference column approach in which one column of the tropical atmosphere is coupled to a reference reservoir column via the WTG approximation. However, WTG studies that use a reference column, the heat and moisture budgets of the full system consisting of the reference and the simulated column are, by construction, not closed. For example, suppose that large-scale descent is diagnosed within the simulated region. By mass continuity that should be accompanied by ascent in a neighboring region. The ascent will act to cool and moisten the neighboring region. Such feedback effects are omitted in the reference column approach, since they can be assumed to be weak if distributed over a very large area. The main aim of this thesis is to implement a WTG-derived large-scale circulation in a configuration that explicitly incorporates such feedbacks and thereby allows one to remove the assumption of infinite size of one of the columns. To do this a new approach in which two columns of the tropical atmosphere are coupled together via the WTG approximation will be developed. The profiles in the columns will not be specified a priori but rather they will be computed during the simulation, which will allow a full range of interactions between them. This new configuration (henceforth referred to as the coupled-column configuration) is a valuable extension of the reference column configuration (i.e., a configuration that uses a reference reservoir column). It will provide a new tool for investigating a wider range of important problems

in tropical meteorology, in which the interactions between convection and the large-scale flows are known to play a key role.

Although some previous studies have coupled together two columns of an SCM (e.g. Nilsson and Emanuel, 1999; Raymond and Zeng, 2000; Shaevitz and Sobel, 2004), this will be the first time to couple two columns of a CRM via the WTG parameterization of the large-scale circulation. An intriguing result using two SCMs is the inhomogeneous response of the system to homogeneous surface conditions, as found by Raymond and Zeng (2000). From their results, two SCMs with the same SST can produce different rates of precipitation in each; an equilibrium state maintained by a large-scale circulation which is established between the columns.

In this study, simulations will be performed under the coupled-column configuration, and direct comparison with their equivalents under the reference column configuration will help in identifying how the energetically closed system differs from the open system. The study will start by examining convection within a homogeneous environment before considering spatially-varying and time-varying boundary conditions. Results from these experiments will contribute to an improved understanding of processes such as convective organization driven by SST variations and large-scale flows. The fundamental questions addressed in this study are the following:

Q1. *Can (and if so how, and under what conditions, does) a large-scale circulation driven by convection develop in a homogeneous environment?*

Q2. *How does convection develop in response to spatially inhomogeneous boundary conditions (SST variations)?*

The answers to these questions will be obtained by performing a series of simulations over homogeneous and inhomogeneous surface conditions. In both cases, the equilibrium response of the system will be examined as well as the sensitivity of the equilibrium response to the WTG parameters. Raymond and Zeng (2005) found reduced precipitation in a CRM modified to implement the WTG approximation, compared to the same CRM run without the effect of the large-scale circulation and with the same SST. This study will

aim to investigate whether such a response is an artifact of the reference column configuration. The large-scale circulation that develops in the reference column configuration with homogeneous boundary conditions (Raymond and Zeng, 2005) may indicate the possibility for inhomogeneous responses or oscillatory responses of the coupled-column system to homogeneous boundary conditions.

By specifying the relative area of the columns, the coupled-column configuration permits a wider range of studies and direct comparison with the reference column configuration will be made for the situation with large difference in column areas. For the situation of equal areas, one would expect to find the largest differences from the reference column configuration. An important question to ask, therefore, will be whether those differences are actually substantial, or whether a reference column configuration might be sufficient. For the situation with very different areas, one might expect to find similar behavior using either a reference column or the coupled-column configurations.

The study will also analyze the transient behavior of convection with a spatially-varying and time-varying boundary conditions. Results from these experiments will contribute to an improved understanding of processes such as the transition from shallow to deep convection. The specific questions to be answered here are the following:
Q3. *How does convection evolve in response to time-varying boundary conditions (with prescribed variations)?*
Q4. *How do two-way interactions between convection and the large-scale influence the transition from a suppressed to more active phase of convection?*
Through the analysis of the simulations performed under the coupled-column configuration with inhomogeneous surface conditions a column with suppressed convection will be identified. A series of experiments will be performed in which the column with suppressed convection will be forced to undergo the transition to a more active phase of convection. The transition from a suppressed to a more active phase of convection will be forced by either increasing the local SST (i.e. a transition to active convection driven by surface forcing) or decreasing the remote SST (i.e. a transition to active convection

driven by changes in the large-scale circulation that are caused by a remote change in convection).

This study will involve the use of two numerical models of different complexities. One of the models will be a very simple and computationally cheap SCM and the other will be a CRM. The simple model will be constructed from simplified parameterization schemes. It will be very cheap to run but its economy will be achieved at the expense of ignoring many of the complexities of the real convective atmosphere. The CRM will be based on the UK Meteorological Office LEM at version 2.4. The domain will be two-dimensional and the model setup will be simplified to a fixed SST and a fixed radiative cooling in order to eliminate cloud-radiation feedbacks. The aim of this study is to have a clear understanding of a simple setup and laying the groundwork for more complex setups including additional processes such as, (a) the third dimension, (b) cloud-radiation feedbacks and, (c) coupled to surface models. However, direct comparison of the CRM simulations to the simple SCM simulations is not the aim of this study. Rather, the simple SCM will be used to test the WTG approach and to do some exploratory work that will help to identify key sensitivities and simulations that will be more fully explored using the CRM.

1.7 Thesis Plan

This thesis is organized as follows: Chapter 2 presents the parameterization schemes used to build a simple SCM and discusses its approach to RCE as well as its sensitivity to physical parameters. The same chapter details the coupling methodology; that is the WTG approximation, followed by its application in the simple SCM. The SCM modified to implement the WTG approximation is used to perform a number of simulations and the results obtained are used to identify the experiments that will need further investigations in a model that better simulates convection.

Chapter 3 introduces the CRM based on the LEM at version 2.4 of the UK Meteorological Office. The setup of the model is detailed and choices which may be different from other CRM studies of tropical deep convection are highlighted. The CRM is run to RCE with different values of SST and the mean state and statistics at RCE are discussed.

In Chapter 4, the CRM described in Chapter 3 is modified to implement the WTG approximation. The modifications are done using both the reference column and the coupled-column approaches. A number of experiments are performed over homogeneous boundary conditions. The sensitivities to the initial conditions are investigated along with the sensitivities to some coupling parameters, for example, the WTG coupling time scale and the WTG adjustment rate profiles. At each stage, the main results of the simulations performed under the reference column system are compared to those of the simulations performed under the coupled-column system for the case of columns of equal areas and the case of large difference in column areas.

In Chapter 5, the response to anomalies in the surface conditions are investigated. As done in Chapter 4, the behavior of the reference column system is compared to that of the coupled-column system for the case of columns of equal areas and the case of large difference in column areas.

Chapter 6 compares the states of the columns and the strength of the large-scale circulation that develops in a series of simulations performed under the coupled-column approach with the same initial SST difference. Instantaneous states obtained at quasi-equilibrium of those simulations are used to initialize a new series of simulations in which the coldest column is forced to undergo the transition from a suppressed to a more active phase of convection. The transition is forced by changing the local convection and/or by changing the remote convection. In each case, the transient evolution of convection is examined within a time-varying surface forcing and large-scale forcing. The transition time is defined and its sensitivity to free tropospheric moisture and to the methods applied to force the transition are investigated.

Finally, the conclusions of this study are presented and discussed in Chapter 7. In the same chapter there is also some discussion of extensions of this study and further investigations are suggested.

Chapter 2:
Single Column Model simulations with two-way coupling via the weak temperature-gradient approximation

2.1 Introduction

Chapter 1 discussed the different techniques used to simulate the interactions between convection and large-scale dynamics. It was highlighted that numerical model simulations using a prescribed large-scale forcing fail to explain what controls the occurrence of deep convection. The aim of this thesis is not to impose the large-scale forcing but to parameterize it using the WTG approximation and simulate its interactions with the simulated convection.

This chapter will introduce a new framework, in which two CRMs are coupled together via the WTG parameterization of the large-scale circulation. It is an extension of the reference column approach in which a CRM or SCM is coupled to a reference reservoir column via the WTG parameterization of the large-scale circulation. The reference column approach was designed to simulate convection and large-scale circulation in a small column coupled to a fixed one while the new approach will allow the interactions between convection and large-scale circulation to be simulated in a fully coupled two-column configuration. In this chapter, the two columns configuration will consist of two columns of a simple and relatively cheap version of a Single Column Model (SCM) that is built using simple parameterization schemes. Investigation will focus on the equilibrium

state of the coupled SCMs over non-uniform surface conditions although the equilibrium state from perturbed initial conditions over uniform surface conditions will be also analyzed. The simulations performed in the coupled SCMs and presented in this chapter will form the basis of further investigations in a more sophisticated model in chapters 4, 5 and 6.

Firstly, the parameterization schemes used to build the SCM will be presented and the approach to radiative-convective equilibrium (RCE) will be discussed, including the sensitivity to some physical parameters. Then, the details of the coupling methodology will be detailed. Finally, an analysis will be presented of the equilibrium response of the coupled SCMs over non-uniform surface conditions and over uniform surface conditions.

2.2 Model description

In attempt to reduce the complex atmospheric system, a simple and computationally cheap numerical model is constructed through simplified equations that illustrate the key physical mechanism. This numerical model has one dimension. It is constructed with the purpose of testing the concept of two-way coupling via the weak temperature gradient (WTG) approximation in order to study the interactions between convection and the large-scale. The simple parameterization schemes used are presented in the next subsections.

2.2.1 Convection Scheme

Convection is the result of vertical instability. It is associated with turbulent mixing and complex microphysical processes which modify the dynamic and thermodynamic properties of the plume and its surroundings. A convective plume transports heat and moisture from the surface to redistribute into the boundary layer and the free troposphere. It en-

trains relatively dry and cold environmental air and it detrains relatively warm and cloudy air into its surroundings. The heating induced by condensation drives compensating subsidence motion and excites gravity waves which propagate away from the convective area in order to redistribute density anomalies on isobaric surfaces. Finally, the resulting clouds interact with radiation. For a model formulated in pressure coordinates, the governing equations for an ensemble of convective plumes are simplified following Gregory and Rowntree (1990) as

$$-\frac{\partial M_p}{\partial P} = E - D_{mix} - D_{final} \tag{2.1}$$

$$-\frac{\partial \theta_p M_p}{\partial P} = E\theta - D_{mix}\theta_p + \frac{LQ}{C_p} \tag{2.2}$$

$$-\frac{\partial q_p M_p}{\partial P} = Eq - D_{mix}q_p - Q \tag{2.3}$$

The entrainment rate E of environmental air is given by:

$$E = \xi M_p \tag{2.4}$$

while the detrainment rate D_{mix} of cloudy air through turbulent mixing processes at the edge of the plume is given by:

$$D_{mix} = \delta M_p \tag{2.5}$$

θ is the potential temperature and q is the specific humidity of water vapor of the environment. The subscript p is used to refer to dynamic and thermodynamic properties of the plume and C_p is the heat capacity at constant pressure. M is the mass flux, Q is the rate of conversion of water vapor to liquid water, L is the latent heat of condensation and P is the pressure. ξ and δ are the fractional mass entrainment and detrainment coefficients respectively. D_{final} is the forced detrainment. It occurs when the plume reaches the level of neutral buoyancy (LNB) and it is zero until such a level is reached.

Laboratory water tank experiments undertaken by Morton et al. (1956) and Turner (1963) describing a dilution of a thermal plume by entrainment of the surrounding air

gave a quantitative description of fractional mass entrainment coefficient with height

$$\Xi \approx \frac{0.2}{R_p} \tag{2.6}$$

where R_p is the plume radius. A similar relation was suggested by Simpson and Wiggert (1969). Ξ is the fractional mass entrainment coefficient in height coordinates. Ξ transformed to pressure coordinates gives,

$$\xi \approx \frac{1}{\rho g}\frac{0.2}{R_p} \tag{2.7}$$

where $g \approx 10$ m s^{-2} is the acceleration due to gravity and $\rho(z) = 1$ kg m^{-3} is the density. For simplification purposes, this study assumed a fixed mass entrainment coefficient with height or equivalently a fixed cloud radius with height (Equation 2.7). Assuming a plume radius R of $= 1000$ m, $\xi = 2 \times 10^{-3}$ hPa^{-1}. For a first guess of the mass flux at the base of the plume that is $M_p^1 = 10^{-2}$ hPa s^{-1}, the entrainment rate $E = 1.7$ d^{-1}, a value which is in the same order of magnitude as the value diagnosed by Yanai et al. (1972).

From Equation 2.1, the change of mass flux with height is evaluated from $\xi - \delta$ as

$$M_p^{-1}\frac{\partial M_p}{\partial P} = \xi - \delta \tag{2.8}$$

Since ξ and δ are positive values, δ must be less than ξ to cause the mass flux of a buoyant plume to increase with height as described in the laboratory experiments undertaken by Morton et al. (1956) and Turner (1963) or as found in the observational studies of cumulus clouds by Warner (2010). This study set δ as one third of ξ. That is $\delta \approx 0.67 \times 10^{-3}$.

D_{final} and Q are first ignored. In the finite difference formulation needed here, entrainment and detrainment are assumed to occur at the same level k and the pressure derivative is performed using an upwind scheme. For an adiabatic ascent from level k to $k+1$ (k increasing upward) the following set of discrete equations are obtained

$$M_p^{k+1} = M_p^k[1 + (\delta - \xi)\Delta P], \tag{2.9}$$

$$\theta_p^{k+1} = \frac{\theta_p^k(1 + \delta\Delta P) - \xi\theta^k\Delta P}{1 + \Delta P(\delta - \xi)}, \tag{2.10}$$

$$q_p^{k+1} = \frac{q_p^k(1+\delta\Delta P) - \xi q^k \Delta P}{1+\Delta P(\delta-\xi)}, \tag{2.11}$$

with

$$\Delta P = P^{k+1} - P^k \tag{2.12}$$

being the pressure difference between two consecutive levels. There are 75 levels in the vertical, on a stretched grid with resolution moving from 6 hPa near the surface to 18 hPa in the mid-troposphere.

The black curves in Figure 2.1 are the mean seasonal temperature, T and specific humidity, q, profiles for West indies area that were measured during the "hurricane season" lasting from July to October (Jordan, 1958). These profiles are used as input for the set of discrete equations 2.9 to 2.11. To start the integrations, the values of q_p, θ_p and M_p are specified at the base of the plume (first model level, $k = 1$). These are; $q_p^1 = q^1$, $\theta_p^1 = \theta^1$ and the first guess of the mass flux at the base of the plume is $M_p^1 = 0.01$ hPa s^{-1}.

The specific humidity and the virtual temperature profiles of an air parcel launched into that environment (the environment with the mean thermodynamic profiles shown by the black curves in Figure 2.1) are shown in Figure 2.1 and its mass flux is shown in Figure 2.2. The plume rises continuously when D_{final} is not considered in the integrations. In the absence of any phase changes, the plume rises following almost the dry adiabatic lapse rate and its specific humidity decreases more slowly so that its virtual temperature decreases more rapidly than the environmental values. Under these circumstances, convection could not continue because the air parcel is denser than the environmental air.

The next stage is to allow water vapor to be converted into liquid water. In this model, all other forms of hydrometeors are not allowed to occur. The conversion is done using a simple moisture saturation scheme where the amount of condensation occurring in the plume is computed as

$$\Delta_\phi q_c^k = max\left[q_p^k - q^{*k}\left(T_p^k + \frac{q_p^k - q^{*k}(T_p^k, P^k)}{\frac{C_p}{L_v} + \frac{\partial q^{*k}(T_p^k, P^k)}{\partial T}}, P^k\right), 0\right] \tag{2.13}$$

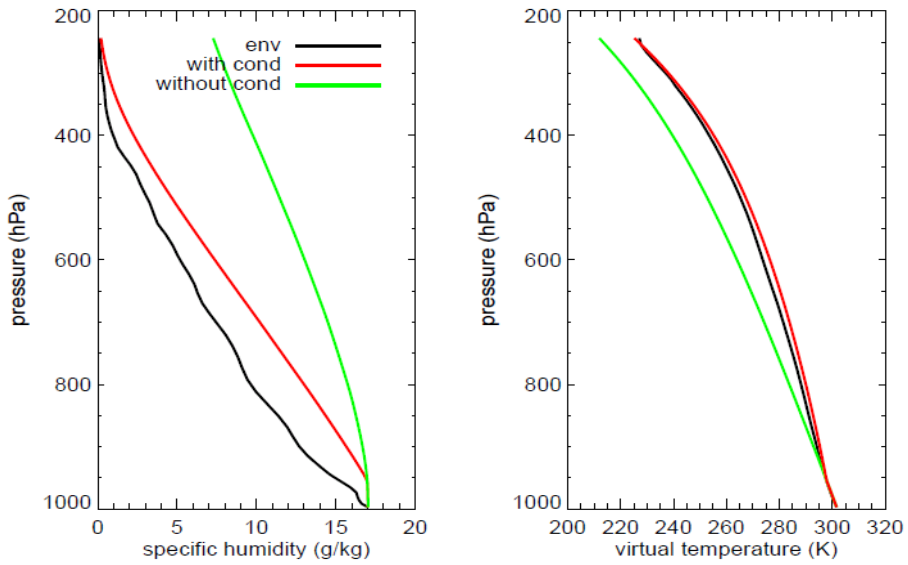

Figure 2.1 *Specific humidity (left-hand panel) and virtual temperature (right-hand panel) profiles of the environment (black curves) and the plume when Q is not considered (green curves) and when Q is considered (red curves) in the integrations.*

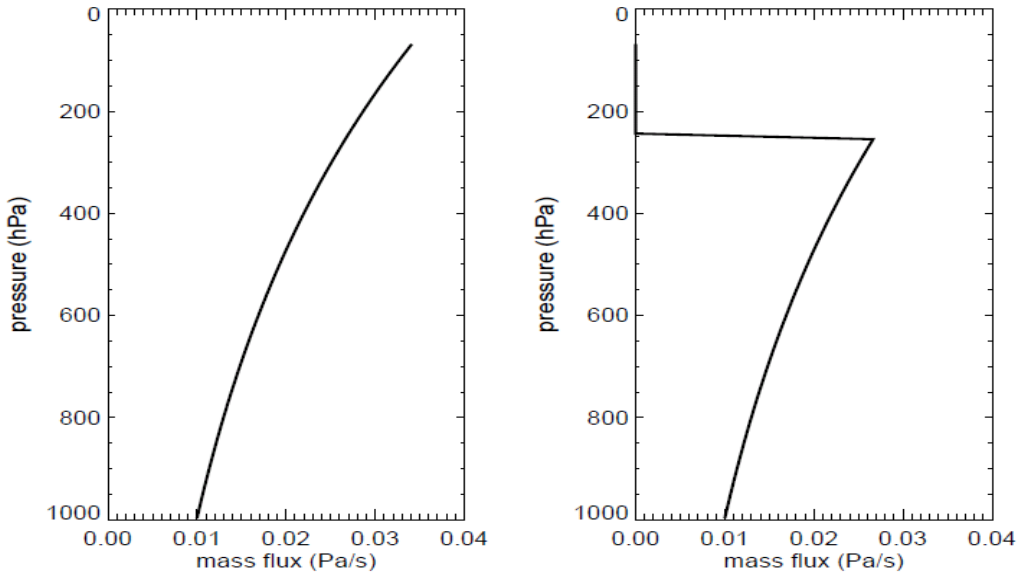

Figure 2.2 *Mass flux of a single convective plume when D_{final} is not considered (left-hand panel) and when D_{final} is considered (right-hand panel) in the integrations.*

Δ_ϕ is used to denote the increment due to phase changes only and $q^{*k}(T_p^k, P^k)$ is the saturation specific humidity with respect to T_p^k.

Condensation starts at about 900 hPa and the heating produced by condensation warms the plume so that it becomes positively buoyant. The plume moves upward following the moist adiabatic lapse rate and stops at LNB located at about 255 hPa. Knowing at which level the plume stops, an expression for D_{final} is derived as

$$D_{final} = -\frac{1}{\Delta P} M_p^k [1 + \Delta P(\delta - \xi)] \tag{2.14}$$

where k corresponds to the model level located immediately below the LNB.

Finally, D_{final} is implemented in the integrations and the final profile of mass flux is shown on the right-hand panel of Figure 2.2.

The tendencies of T and q are

$$\left(\frac{\partial T}{\partial t}\right)_{conv} = \mathbf{det}(T_p - T) - M_p \frac{\partial T}{\partial P} \tag{2.15}$$

and

$$\left(\frac{\partial q}{\partial t}\right)_{conv} = \mathbf{det}(q_p - q) - M_p \frac{\partial q}{\partial P} \tag{2.16}$$

respectively, with

$$\mathbf{det} = \begin{cases} D_{mix} & \text{for } k < k_{LNB} \\ D_{mix} + D_{final} & \text{for } k = k_{LNB} \\ 0 & \text{for } k > k_{LNB} \end{cases} \tag{2.17}$$

and where t is the time and k_{LNB} is the model level located at the LNB. The changes in environmental temperature are due to diabatic warming by the detrainment of heat from the plume and adiabatic warming by the compensating subsidence motion while the changes in environmental specific humidity consist of a moistening due to detrainment of moisture from the plume and a drying from subsidence.

Closure

To complete the convective scheme the magnitude of the energy produced by convection must be determined in terms of known large-scale variables (the closure problem). For a mass flux closure scheme, this is achieved by rescaling the mass flux of the plume in the initial convective layer. The intensity of convective activity is often predicted using the convective available potential energy (CAPE, definition given in Section 1.1 of Chapter 1) (e.g. Emanuel, 1994). Here, the CAPE is assumed to be consumed by cumulus convection over a timescale τ_{CAPE} (known as the CAPE timescale). The rate of change in CAPE between two consecutive time levels t and $t+\Delta t$ is calculated as

$$\Lambda \frac{CAPE(t) - CAPE(t+\Delta t)}{\Delta t} = \frac{CAPE(t)}{\tau_{CAPE}} \tag{2.18}$$

The value of τ_{CAPE} can be specified. Knowing the rate of change in the magnitude of the $CAPE$, the aim becomes to determine which value of the mass flux the air parcel should have in the initial convective layer in order to consume the CAPE at the rate given in Equation 2.18. This is achieved by rescaling the mass flux at the base of the plume by the factor Λ. That is

$$M_p^1 = \Lambda M_p^1 \tag{2.19}$$

In this study, the time step Δt is equal to 5 min to satisfy the CFL criterion[1]. With this formulation of the closure, there is no contribution from the large-scale and the CAPE is the only criterion that determines the development of convection. This closure follows the work of Fritsch and Maddox (1981) which assumed that the time required for the large-scale processes to generate the CAPE is longer than the time required for cumulus convection to consume it.

The value of τ_{CAPE} determines the rate at which the CAPE is consumed. Hence, the larger the value of τ_{CAPE} the more weaker convective cells are generated for a given atmospheric stability.

[1] Criterion to be met in order to guarantee stability of the upwind scheme in numerical modeling

2.2.2 Surface fluxes and Radiation

The lower boundary should represent the stresses and fluxes associated with flow across the surface. A simple representation of the distribution of surface fluxes through a boundary layer which has the depth of 83.5 hPa (the first ten model levels) is introduced. No explicit diffusion of heat and moisture is represented in this model.

A bulk formula is used to calculate the upward fluxes of heat and moisture across the surface:

$$F_S = C_p \beta (T^s - T^n) \tag{2.20}$$

and

$$F_L = L_v \beta [q^*(T^s) - q^n] \tag{2.21}$$

respectively.

The superscripts s and n are used to refer to properties of the surface and near surface air[2] respectively. C_p is the heat capacity at constant pressure and L_v the latent heat of vaporisation. $q^*(T^s)$ is the saturation specific humidity calculated from the underlying surface temperature T^s. In this study, β is set to a constant but in reality it would be a function of the exchange coefficient, the near surface wind speed and density (Nilsson and Emanuel, 1999).

The tendencies of T and q due to sensible heat and latent heat fluxes across the surface are

$$\left(\frac{\partial T}{\partial t}\right)_{BL} = \frac{g}{\Delta P_{BL}} \beta (T^s - T^n) \tag{2.22}$$

and

$$\left(\frac{\partial q}{\partial t}\right)_{BL} = \frac{g}{\Delta P_{BL}} \beta [q^*(T^s) - q^n] \tag{2.23}$$

respectively. These tendency terms are zero above the boundary layer. ΔP_{BL} is the depth of the boundary layer.

[2] which corresponds to the first model level ($k = 1$) located at about 1000 hPa

Convection is forced in the domain using a non-interactive cooling through the troposphere. This forcing will be henceforth referred to as a radiative cooling. It is set to a value of 1.5 K d^{-1} up to 290 hPa and then decreases linearly to 0 K d^{-1} at the tropopause located at about 244 hPa. This radiative cooling profile correspond to a typical cooling rate in the tropics (e.g. Raval et al., 1994).

2.2.3 Moisture and energy conservations

The heat and moisture budgets are written as

$$\int_{P_S}^{P_{Top}} \frac{d}{dt}(C_pT + gz)\frac{dP}{g} = \int_{P_S}^{P_{BL}} \left(\frac{\partial T}{\partial t}\right)_{BL} \frac{C_p dP}{g} + \frac{L_v}{g} \sum_{k(\Delta_\phi q_c^k > 0)} \Delta_\phi q_c^k M^k + \int_{P_S}^{P_{Top}} \left(\frac{\partial T}{\partial t}\right)_{Rad} \frac{C_p dP}{g} \tag{2.24}$$

and

$$\int_{P_S}^{P_{Top}} \frac{dq}{dt}\frac{dP}{g} = \int_{P_S}^{P_{BL}} \left(\frac{\partial q}{\partial t}\right)_{BL} \frac{dP}{g} - \sum_{k(\Delta_\phi q_c^k > 0)} \Delta_\phi q_c^k \frac{M^k}{g} \tag{2.25}$$

respectively. P_S, P_{Top} and P_{BL} refer to the pressure at the surface, at the top of the model and at the top of the boundary layer respectively.

The three terms on the right-hand side of Equation 2.24 represent sensible heat flux (first), the heating from phase changes (second) and the heating from radiation (third) and their sum must balance the changes in the dry static energy (term on the left-hand side of Equation 2.24) defined as the sum of the enthalpy (C_pT) and potential energy (gz). The terms on the right-hand side of Equation 2.25 represent evaporation (first) and precipitation (second) and their difference must balance the change in column water vapor (term on the left-hand side of Equation 2.25). However, the changes in column water vapor and and dry static energy must be equal to zero at equilibrium.

2.2.4 Other details

The model top is at 69 hPa. There are 75 levels in the vertical, on a stretched grid with more levels near the surface. The lower boundary is a time-independent sea surface temperature (SST) of 299.5 K. The top and bottom of the model are rigid lids. Parameter choices are listed in Table 2.1.

Sea surface temperature (SST)	299.5 K
Entrainment rate (ξ)	0.002 hPa^{-1}
Detrainment rate (δ)	$\xi/3$
Cape Timescale (τ_{CAPE})	1 h
β	0.01 $\text{kg/m}^2 s$

Table 2.1 *Values of the parameters used to perform a control single column model simulation.*

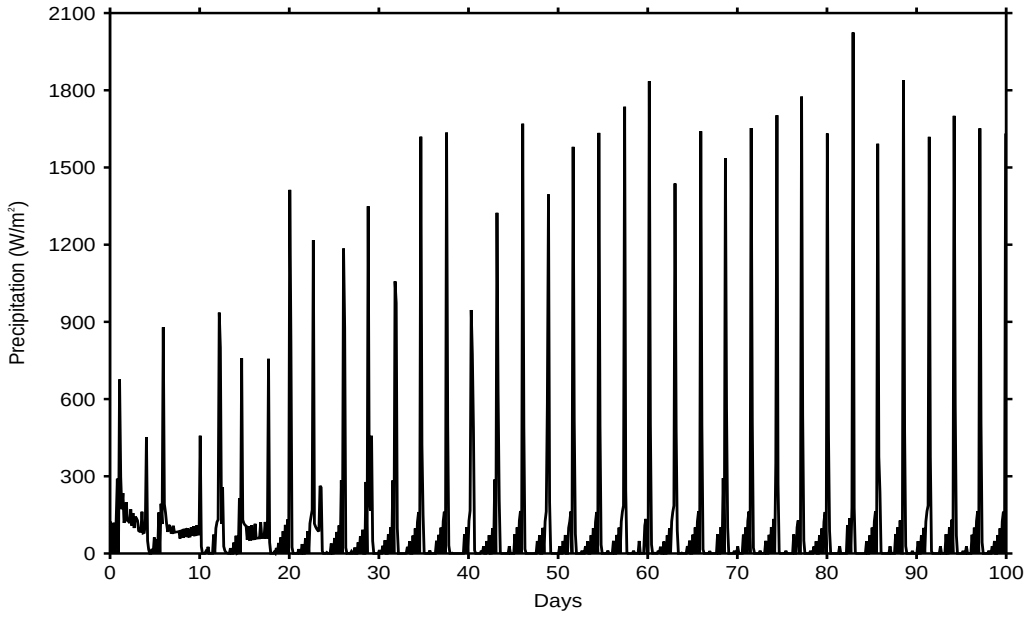

Figure 2.3 *Three hour average precipitation time series.*

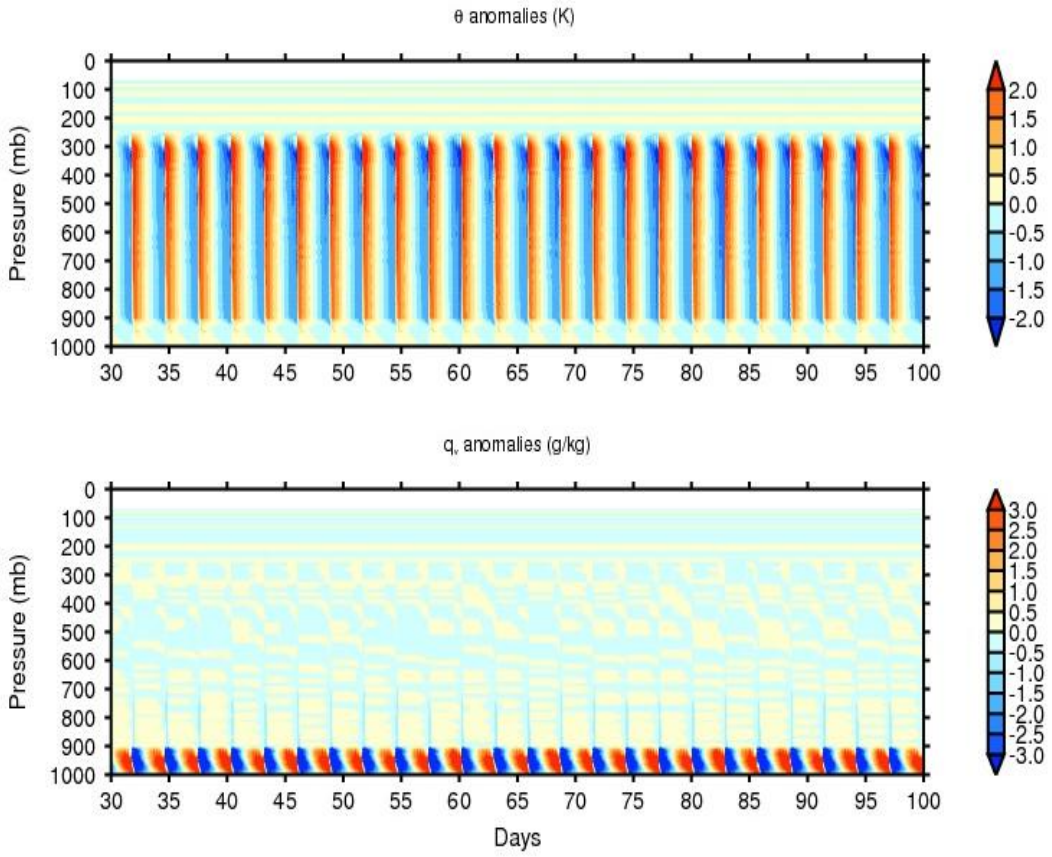

Figure 2.4 *Contour plots of the environmental potential temperature and specific humidity anomalies which respect to the last 70 days mean profiles.*

2.3 Equilibrium behavior of the SCM

The model is initialized with mean seasonal temperature and specific humidity profiles measured during the "hurricane season" from the West indies area (black curves on the left and right hand sides of Figure 2.1) and is run for 100 days. Figure 2.3 shows the three hour average precipitation time series and Figure 2.4 shows contour plots of the environmental potential temperature and specific humidity plotted as anomalies with respect to

the last 70 days mean profiles. The net heating (cooling or warming) is the sum of the heating produced by condensation and the prescribed radiative cooling. When convection does not occur, the column cools down. When convection occurs, the column may continue to cool down or may start to warm up depending on how large is the convective heating compared to the prescribed radiative cooling. Deep convection produces a large amount of precipitation and the corresponding heating from condensation exceeds the prescribed radiative cooling. Hence, the column warms up, dries and becomes stable. It is then inhibited from further deep convection. In the absence of further deep convection, the column starts to cool down and moisture is recharged through surface evaporation and shallow convection until new deep convection is triggered. This cycle is repeated with a period of almost three days over the last 70 days of integration. The averages over days 30 to 100 are used to define the state and the statistics of the sounding at equilibrium. The mean rain rate at equilibrium is 4.19 mm d^{-1}. It corresponds to a warming of ≈ 1.44 K d^{-1}, as compared to the prescribed radiative cooling of 1.5 K d^{-1}; that is the RCE. Note that the small difference in convective heating rate and radiative cooling rate points to the minor role for sensible heat fluxes in this situation. However, this very regular behavior of convection is likely due to the simplicity of the schemes used and the choice of some controlling parameters (e.g. the CAPE timescale).

Figure 2.5 shows the mean profiles at equilibrium of potential temperature and mass fluxes for precipitating and non precipitating convective plumes. The boundary layer is well mixed and the free troposphere is absolutely stable with a strong inversion at the tropopause located at about 250 hPa. Most of the precipitating convective plumes reach the tropopause while all the non precipitating convective plumes are simply the result of shallow convective overturning in the boundary layer.

The sensitivity to the SST, the CAPE timescale and the radiative cooling rate is investigated. Additional series of simulations are performed with: (a) the values of SST ranging from 297.5 K to 304.5 K, (b) the CAPE timescale τ_{CAPE} equal to 40 min, 2 and 3 h, and (c) the imposed radiative cooling rate having the values of 0.5, 1 and 2 K d^{-1}.

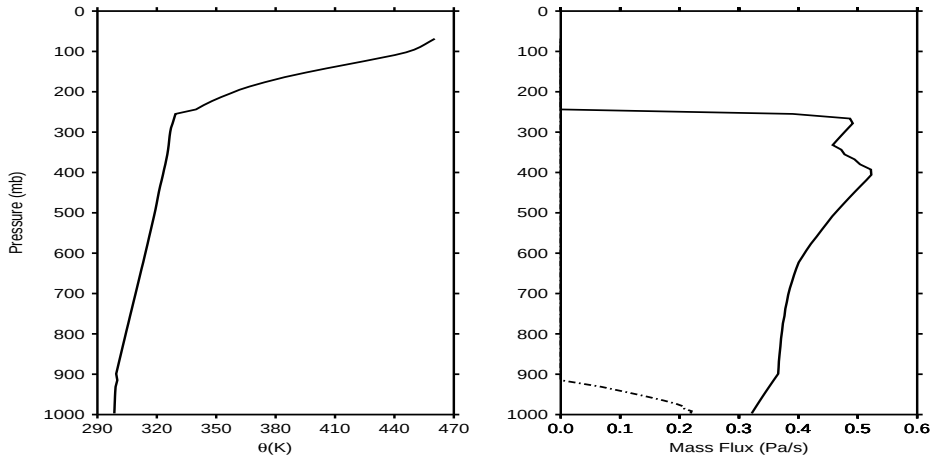

Figure 2.5 *Mean potential temperature profile (left-hand panel) and mass flux profiles (right-hand panel) of precipitating convection (solid curve) and non precipitating convection (dash-dotted curve). The profiles are obtained by averaging over days 30 to 100.*

The latent heat flux increases slightly with SST whilst the sensible heat flux decreases in order to keep the total flux (sum of sensible and latent heat fluxes) in balance with the prescribed radiative cooling rate. As a result, the mean rain rate at equilibrium increases slightly with the SST.

Figure 2.6 shows the three hour average precipitation time series obtained in the simulation performed with $\tau_{CAPE} = 3$ hr. It is compared to the three hour average precipitation time series in the simulation performed with $\tau_{CAPE} = 1$ h (results shown in Figure 2.3). There is no significant change in the equilibrium mean rain rate with τ_{CAPE}. However, the frequency of occurrence of precipitating convection increases with the CAPE timescale. For shorter τ_{CAPE}, precipitating convection is less frequent but there is a periodic occurrence of deep convection producing large amounts of precipitation in order to maintain the long time average rain rate close to the value achieved in the simulations performed with a longer τ_{CAPE}. Simulations with a shorter τ_{CAPE} do not support continuous deep convection. Its periodic pattern is realistic of how a single convective cloud operate locally whereas the continuous precipitation pattern observed in simulations with a longer

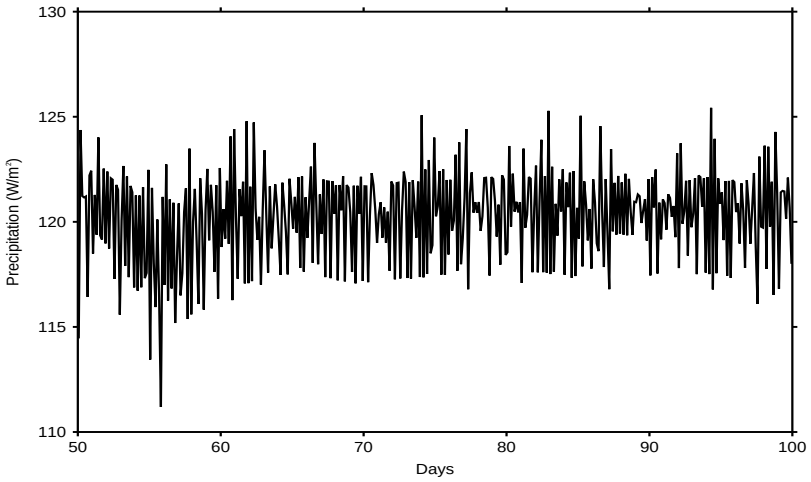

Figure 2.6 *Three hour average precipitation time series in the RCE simulation with* $\tau_{CAPE} = 3$ *hr.*

τ_{CAPE} is realistic for a large domain where there is always precipitating convection happening somewhere.

For the simulations performed with different values of radiative cooling rate, the changes in sensible heat flux are relatively small compared to the changes in surface evaporation (results not shown). The frequency of occurrence of precipitating convection increases with increasing radiative cooling rate (result not shown) and in each case, the column adjusts to a new quasi-equilibrium state in which the heating produced by condensation nearly balances the prescribed radiative cooling.

2.4 Coupling methodology

In the simulations described in section 2.3 convection is simulated as the response to radiative cooling and surface fluxes only. Convection does not interact with the large-scale circulation.

In this section, the SCM is modified such as to allow the full interactions between convection and the large-scale forcing. This is achieved by coupling two columns of the SCM via the weak-temperature gradient (WTG) approximation. The definition of the WTG approximation and the details of its implementation are described in the following section.

2.4.1 The weak-temperature gradient approximation

In flux form the equation for the evolution of potential temperature is

$$\frac{\partial \theta}{\partial t} + \nabla_h \cdot (\mathbf{v}\theta) + \frac{\partial(\omega\theta)}{\partial P} = S_\theta \tag{2.26}$$

with

$$S_\theta = -Q_R + Q_C \tag{2.27}$$

and the continuity equation is

$$\nabla_h . \mathbf{v} + \frac{\partial \omega}{\partial P} = 0, \tag{2.28}$$

where P is the pressure, ρ is a horizontally–uniform reference density, $\mathbf{v}$ is the horizontal velocity vector, ω is the vertical velocity and ∇_h is the horizontal gradient operator. S_θ is the diabatic source term. Q_R and Q_C are the radiative cooling and condensation heating rates respectively.

In the tropical free troposphere, large-scale horizontal gradients and time tendencies of temperature are small because buoyancy anomalies are rapidly redistributed by gravity waves. Thus substituting Equation 2.28 into Equation 2.26, the prognostic equation of potential temperature can be simplified to a diagnostic equation for vertical velocity by assuming a first order balance in Equation 2.26 that is; the vertical advection of potential temperature acts to (nearly) balance the diabatic heating; i.e.

$$\overline{\omega}\frac{\partial \overline{\theta}}{\partial P} \approx \overline{S}_\theta \tag{2.29}$$

where the overbar represents a suitably-filtered large-scale flow.

The weak temperature gradient (WTG) approximation (Equation 2.29) is implemented in a numerical model using a two-column configuration as illustrated in Figure 2.7. The subscripts 1 and 2 are used to label the horizontal-mean properties in each column. H is the height of the domain, L is the length of the full system (e.g., of the two columns), with individual column lengths $L_1 = (1-\varepsilon)L$ and $L_2 = \varepsilon L$, so that $\varepsilon = L_2/(L_1+L_2)$.

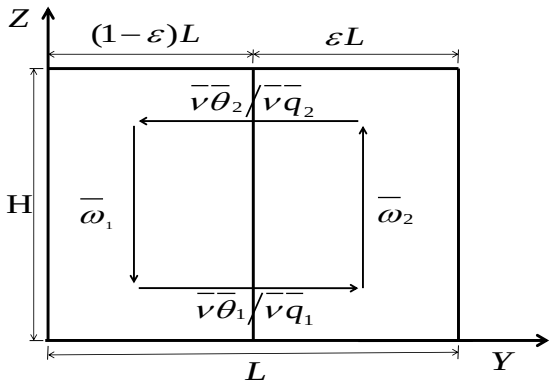

Figure 2.7 *Schematic of the two-column model.*

Sobel and Bretherton (2000) applied Equation 2.29 in order to diagnose the large-scale vertical velocity $\overline{\omega}$ necessary to hold the potential temperature fixed in the free troposphere. This study applies a weaker constraint that the large-scale circulation acts to reduce the difference in the column-mean potential temperature profiles between the two columns over a specified timescale. Thus,

$$\overline{\omega}_2 \frac{\partial \overline{\theta}_2}{\partial P} - \overline{\omega}_1 \frac{\partial \overline{\theta}_1}{\partial P} = \lambda(P)(\overline{\theta}_2 - \overline{\theta}_1) \tag{2.30}$$

with

$$\lambda(P) = \frac{f(P)}{\tau} \tag{2.31}$$

The dimensionless function $f(P)$ is introduced to allow the WTG adjustment rate $\lambda(P)$ to be a function of pressure. Choices of the vertical functions used in this study are presented and motivated in Section 2.4.2. The parameter τ is the timescale over which the large-scale circulation acts to balance the heating associated with the simulated convection, thus reducing the horizontal temperature and pressure gradients: it can be thought

of as being related to the time for gravity waves to propagate across the system and so is related to the system size.

Although the relative size of the columns, ε does enter in the diagnosis of the large-scale circulation below, the total system size L plays no role except in the sense just described: e.g., that the system size one has in mind will influence the choice of a suitable value for τ. An important implication is that the size of the simulation domains can be chosen for practical convenience and need not correspond with the implicit size of the physical system.

Equation 2.30 contains two unknowns, $\overline{\omega}_1$ and $\overline{\omega}_2$. By applying the two-column form of the mass continuity equation,

$$(1-\varepsilon)\overline{\omega}_1 + \varepsilon\overline{\omega}_2 = 0 \tag{2.32}$$

By eliminating $\overline{\omega}_2$ from Equation 2.30 and Equation 2.32, the WTG-derived vertical velocity $\overline{\omega}_1$ can be calculated as

$$\overline{\omega}_1 = \frac{f(P)}{\tau}\frac{\overline{\theta}_1 - \overline{\theta}_2}{\frac{\partial\overline{\theta}_1}{\partial P} + \frac{1-\varepsilon}{\varepsilon}\frac{\partial\overline{\theta}_2}{\partial P}} \tag{2.33}$$

and substituting Equation 2.33 into Equation 2.32, $\overline{\omega}_2$ can be calculated as

$$\overline{\omega}_2 = -\frac{f(P)}{\tau}\frac{\overline{\theta}_1 - \overline{\theta}_2}{\frac{\partial\overline{\theta}_2}{\partial P} + \frac{\varepsilon}{1-\varepsilon}\frac{\partial\overline{\theta}_1}{\partial P}} \tag{2.34}$$

In the WTG study of Sobel and Bretherton (2000), the horizontal potential temperature gradient is zero. Thus, $\tau = 0$. That is a strict implementation of the WTG approximation. This is a limit impossible to reach in our numerical experiments because of computational limitations. In the limit of $\tau \to \infty$, $\omega_1 \approx \omega_2 \approx 0$ so that the two columns become totally decoupled and will reach their own RCE state. However, for finite values of τ, the temperature profiles in the two columns are allowed to vary but are forced to remain close to each other.

This configuration allows the two columns to vary in response to the diagnosed large-scale circulation. It is proposed as a useful framework for studying the influence on local

convection of changes in remote convection. It is an extension of the reference column configuration applied by Sobel and Bretherton (2000); Raymond and Zeng (2005); Sessions et al. (2010); Bellon and Sobel (2010); Wang and Sobel (2011). The reference column configuration was designed to simulate the effects of a large-scale circulation on convection isolated within a small area coupled to an infinitely large environment. It can be recovered from the coupled-column configuration described above in the strict limit of $\varepsilon = 0$ (or $\varepsilon = 1$) in which case the WTG-derived vertical velocity vanishes in the infinitely large reference column, and agrees with that used by other studies (e.g. Raymond and Zeng, 2005; Wang and Sobel, 2011) for the negligibly small column, specifically

$$\overline{\omega} = -\frac{f(P)}{\tau}\frac{\overline{\theta} - \overline{\theta}_{ref}}{\frac{\partial\overline{\theta}}{\partial P}} \tag{2.35}$$

Assuming that the stratification remains similar in both columns for $0 < \varepsilon < 1$, the two columns are relaxed towards each other with a WTG effective relaxation timescales τ_{eff_1} and τ_{eff_2} for column 1 and column 2 respectively. τ_{eff_1} and τ_{eff_2} are different and longer than in the corresponding reference column limit, being rescaled by factors of $\approx 1/\varepsilon$ and $\approx 1/(1-\varepsilon)$ respectively.

$$\tau_{eff_1} \approx \tau/\varepsilon \tag{2.36}$$

and

$$\tau_{eff_2} \approx \tau/(1-\varepsilon) \tag{2.37}$$

The adjustment is slower in column 2 (relative to the adjustment in the simulated column of the reference column configuration) because column 1 is being adjusted as well which reduces w_2 compared to the reference column approach.

The WTG approximation only holds if the horizontal gradient in potential temperature is much smaller than the vertical gradient. In this two-column configuration, the requirement is that $\frac{|\overline{\theta}_1 - \overline{\theta}_2|}{L} \ll \left|\frac{\partial\overline{\theta}_1}{\partial P} + \frac{\partial\overline{\theta}_2}{\partial P}\right|$. However, in the model simulations, the prescribed radiative cooling profile may sometimes result in a very weak static stability in the upper troposphere which would in turn cause the WTG calculation to produce very large and unphysical large-scale vertical velocities. To prevent such large vertical velocities developing in the simulations a lower bound of 1 K km^{-1} is imposed on the

static stability when using Equations 2.33 and 2.34 to calculate the WTG velocity in the columns. A similar condition was imposed in Raymond and Zeng (2005). The impact of the limiter is to reduce the strength of the diagnosed WTG circulation at upper levels and hence the induced temperature and moisture tendencies.

Velocities derived from Equations 2.33 and 2.34 are named the WTG vertical velocities and are denoted as $\overline{\omega}_1^{\mathrm{WTG}}$ and $\overline{\omega}_2^{\mathrm{WTG}}$. They are used to compute large-scale advective tendencies of heat and moisture in the two columns. The change in the intensive, horizontal column mean quantity $\overline{\chi}$ due to the WTG-derived large-scale circulation is written in flux form as:

$$\frac{\partial \overline{\chi}}{\partial t} + \nabla_h.(\mathbf{v}^{\mathrm{WTG}}\overline{\chi}) + \frac{1}{\overline{\rho}}\frac{\partial}{\partial P}(\overline{\rho\omega}^{\mathrm{WTG}}\overline{\chi}) = 0 \tag{2.38}$$

The large-scale convergence term, $\nabla_h.(\mathbf{v}^{\mathrm{WTG}}\overline{\chi})$ acts between columns 1 and 2. It is assumed to be all into or all out of one of the columns. A localized heating is redistributed by the WTG derived large-scale circulation over the timescale τ. To ensure that the derived large-scale motion is conservative, the heat and moisture advected by the large-scale circulation are calculated in a flux form using an upwind advection scheme. The tendency of $\overline{\chi}_1$ due to the WTG derived circulation is written as

$$\left(\frac{\partial \overline{\chi}_1}{\partial t}\right)_{\mathrm{WTG}} = \frac{\chi_*}{\overline{\rho}}\frac{\partial}{\partial P}(\overline{\rho\omega}_1^{\mathrm{WTG}}) - \frac{1}{\overline{\rho}}\frac{\partial}{\partial P}(\overline{\rho\omega}_1^{\mathrm{WTG}}\overline{\chi}_1) \tag{2.39}$$

and similarly for $\overline{\chi}_2$. Here χ_* is the appropriate upwind value of $\overline{\chi}$ in the horizontal. Equation 4.5 of Chapter 4 is a version of Equation 2.39 written in a z-coordinate and the details of its numerical implementation in the LEM are shown in Appendix C. Equation 2.39 is used to calculate the WTG advective tendencies of potential temperature and water vapor only. The WTG circulation does not advect any form of hydrometeor. On the right hand side of Equation 2.39, the first term represents the horizontal transport between the columns while the second term represent the vertical transport by the diagnosed large-scale circulation. Theses terms are calculated at each time step and they represent additional source or sink for heat and moisture.

This study includes the horizontal advection of moisture by the large-scale circulation. Raymond and Zeng (2005) parameterized the horizontal advection by the large-

scale circulation anytime that the domain-mean humidity profile was different from the reference profile. In contrast, Wang and Sobel (2011) assumed horizontally uniform humidity field on large-scales in order to prevent the simulated convection from being altered by the intrusion of reference profiles humidity.

The WTG calculations are performed on a coupling timestep, dt_{wtg}, of 5 minutes. The choice of dt_{wtg} is essentially arbitrary and might be thought of as equivalent to the time step of a General Circulation Model. A sensitivity study of the results to dt_{wtg} was done for values ranging between 0.5 and 60 minutes. In most respects, the nature of the results was unchanged and in particular no significant variations in the equilibrium mean rain rates were found.

2.4.2 WTG adjustment profiles

Most of the experiments performed in this study use a WTG timescale which is constant with height in the free troposphere, i.e.

$$f(P) = f_1(P) = 1 \quad \text{for } P_{\mathrm{BL}} \geqslant P \geqslant P_{\mathrm{top}} \tag{2.40}$$

where P_{top} is the pressure at the top of the domain. As noted by Sobel and Bretherton (2000), the WTG scaling approximation of Equation 2.29 does not hold in the boundary layer because of strong vertical overturning motions which counteract the dynamical processes acting to equally redistribute buoyancy in the free troposphere. The approach adopted in here is to not use the WTG approximation to calculate the large-scale vertical velocity in the boundary layer but rather to linearly interpolate in pressure from the diagnosed WTG vertical velocity at a level P_{BL} a little above the boundary layer to a prescribed value of zero at the surface. Here P_{BL} is chosen to be a model level at about 900 hPa. Hence, the horizontal temperature gradient between the two columns may be significantly greater within the boundary layer even if it is forced to remain close to zero above the boundary layer.

Some sensitivity experiments used a WTG adjustment rate profile given by

$$f(P) = f_2(P) = \begin{cases} \sin\left(\pi \frac{P_s - P}{P_s - P_t}\right) & \text{for } P_{\mathrm{BL}} \geqslant P \geqslant P_t \\ 0 & \text{for } P < P_t \end{cases} \tag{2.41}$$

where P_s andP_t are the pressure at the surface and at the level near the tropopause respectively. Here, $P_t = 200$ hPa; a level where the specified radiative cooling vanishes. The half sine wave profile gives a maximum adjustment rate in the mid-troposphere and might be considered to be appropriate to a first internal mode structure. Although the function f_2 tends smoothly to zero as z approaches the surface, nonetheless the WTG vertical velocity below z_{BL} is calculated by interpolation, as described above. This special treatment in the boundary layer makes the definition of f_1 similar to that used by Sobel and Bretherton (2000) to implement the WTG approximation in a single column model and the definition of f_2 similar to that used by Raymond and Zeng (2005) to implement the WTG approximation in a cumulus ensemble model.

2.4.3 Heat and moisture budgets

The heat and moisture budgets for the two-column system can be written as:

$$\sum_{i=1,2} \left\{ \frac{C_p}{g} \int_{P_S}^{P_{BL}} \left(\frac{\partial T_i}{\partial t}\right)_{BL} dP + \frac{L_v}{g} \sum_{k(\Delta_\phi q_{ci}^k > 0)} \Delta_\phi q_{ci}^k M_i^k + \frac{C_p}{g} \int_{P_S}^{P_{\mathrm{Top}}} \left[\left(\frac{\partial T_i}{\partial t}\right)_{\mathrm{Rad}} + \left(\frac{\partial T_i}{\partial t}\right)_{\mathrm{WTG}} \right] dP \right\} = 0 \tag{2.42}$$

and

$$\sum_{i=1,2} \left\{ \int_{P_S}^{P_{BL}} \left(\frac{\partial q_i}{\partial t}\right)_{BL} \frac{dP}{g} - \sum_{k(\Delta_\phi q_{ci}^k > 0)} \Delta_\phi q_{ci}^k \frac{M_i^k}{g} + \int_{P_S}^{P_{\mathrm{top}}} \left(\frac{\partial q_i}{\partial t}\right)_{\mathrm{WTG}} \frac{dP}{g} \right\} = 0 \tag{2.43}$$

respectively. P_{Top}, P_{BL} and P_S refer to the pressure at the top of the model, at the top of the boundary layer and at the surface respectively. Equations 2.42 and 2.43 are the extension of Equations 2.24 and 2.25 respectively and the additional terms represent the heat and moistening from the WTG-diagnosed large-scale circulation. The WTG terms

are conservative but the energy and moisture content of the system can change. As a result, Equations 2.24 and 2.25 apply only in equilibrium.

In RCE, there are no WTG contributions and Equations 2.24 and 2.25 are recovered by removing the summation sign from Equations 2.42 and 2.43: i.e., the heat and moisture budgets are balanced within each column separately. In the reference column approach, the summation signs should also be removed since only the budget of the freely evolving column is under consideration. The WTG contributions therefore act as external source terms in that case. A two-column system could also have been formulated with similar source terms arising from assumed interactions with an external reservoir, in which case $(\partial T_1/\partial t)_{WTG} \neq (\partial T_2/\partial t)_{WTG}$ and/or $(\partial q_1/\partial t)_{WTG} \neq (\partial q_2/\partial t)_{WTG}$. However, a two-column system may also be considered as an isolated system without external source terms, as it is done here. In that case, in contrast to the reference column approach, the WTG circulation is conservative. As a result, the heat and moisture budgets at equilibrium are satisfied for the full, closed system.

The WTG contributions are equivalent to the integral of the horizontal transport of temperature and moisture between the columns, as the integral of the vertical advection within each column is equal to zero when expressed in flux form. The use of a flux form to calculate the large-scale advective tendencies is therefore convenient in ensuring conservation of heat and moisture in the system as a whole.

2.5 Equilibrium of the coupled SCMs over non-uniform surface conditions

Two columns of the simple version of the SCM are coupled using the WTG calculations described in Section 2.4. The parameter choices are listed in Tables 2.1. Convective ensembles in the two columns are subjected to same conditions (same values of ξ, δ, τ_{CAPE}, radiative cooling, ...). The columns have equal area ($\varepsilon = \frac{1}{2}$ thus, $\omega_2 = -\omega_1$) and are ini-

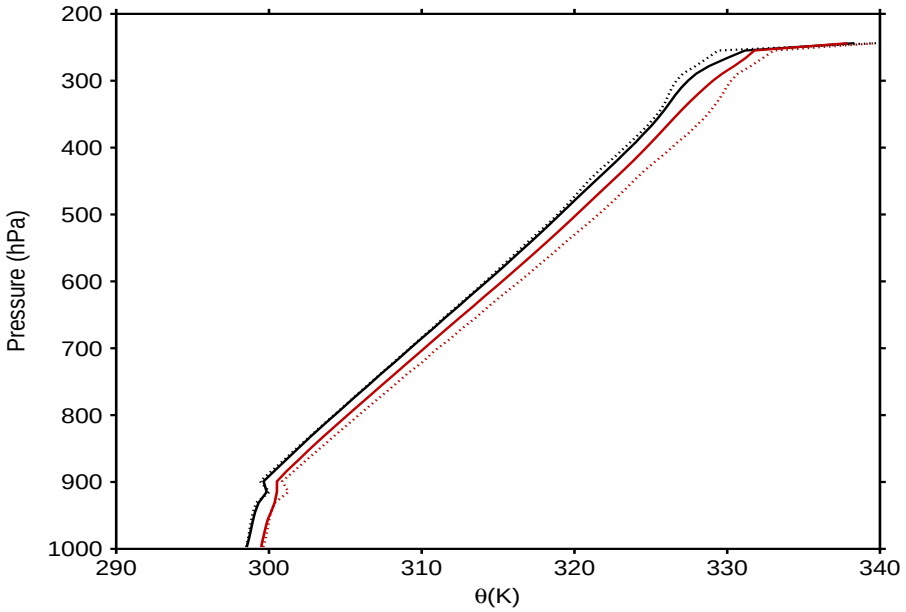

Figure 2.8 *Mean potential temperature profiles at equilibrium for column 1 (black curves) and column 2 (red curves) in the simulation performed with* $\tau = \infty$ *(dotted curves) and in the simulation performed with* $\tau = 24$ *h (solid curves).*

tialized with the same temperature and specific humidity profiles. These initial profiles are those obtained at RCE from the simulation of the simple SCM with an SST of 299.5 K. The SST in column 1 is equal to 299.5 K and that in column 2 is equal to 300.5 K. The quality of the results obtained from the simulations performed in this coupled SCM system is insensitive to the type of the WTG adjustment profile used. The results presented here are those obtained from the simulations performed with the uniform adjustment profile f_1.

A simulation with the WTG calculations off is performed. In such a simulation, the two columns evolve independently and each of them reaches an equilibrium state in which the heating from condensation balances the prescribed radiative cooling. The mean rain rates at equilibrium are 4.17 and 4.30 mm d^{-1} for column 1 and 2 respectively. The dotted black and red curves in Figures 2.8 and 2.9 show the corresponding mean

potential temperature profiles at equilibrium for columns 1 and 2. RCE simulations with different values of SST lead to different potential temperature profiles at equilibrium. The horizontal potential temperature gradients increase with height from the value of almost 1 K in the boundary layer to the maximal value of 3.5 K at about 255 hPa.

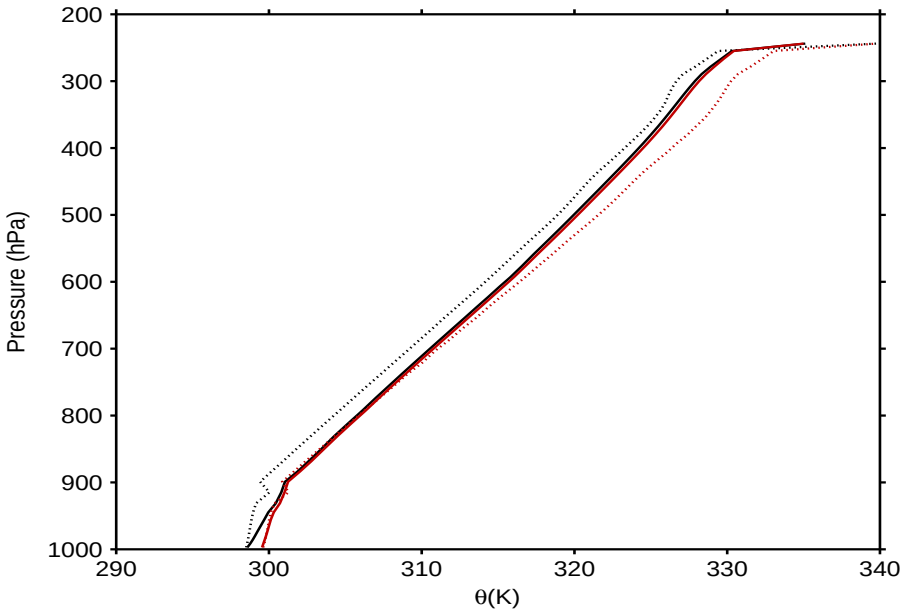

Figure 2.9 *Mean potential temperature profiles at equilibrium for column 1 (black curves) and column 2 (red curves) in the simulation performed with* $\tau = \infty$ *(dotted curves) and in the simulation performed with* $\tau = 2$ *h (solid curves).*

Another simulation with $\tau = 24$ h is performed. For a finite value of τ, the SST gradient between the columns drives a large-scale circulation which reduces the horizontal potential temperature gradients between the two columns making column 2 less stable and column 1 more stable to convection. In column 2, the mean rain rate at equilibrium increased by 22% (now 5.25 mm d^{-1}). The increase in mean rain rate in column 2 is compensated by a reduction in mean rain rate in column 1 by 32% (now 2.84 mm d^{-1}). The heating associated with precipitation in each column does not balance the prescribed radiative cooling. Rather, the excess of heating in column 2 and the excess of cooling

in column 1 are respectively balanced by the heat sink and heat source due to the WTG-diagnosed large-scale circulation which corresponds to ascent in column 2 and descent in column 1. The solid black and red curves in Figure 2.8 are the potential temperature profiles obtained at equilibrium for column 1 and column 2 respectively in the simulation performed with $\tau = 24$ h. The horizontal potential temperature gradients have reduced when compared to the values obtained at RCE (dotted black and red curves for columns 1 and 2 respectively).

2.5.1 Sensitivity to the WTG timescale

The sensitivity to the value of τ is investigated by performing a series of additional simulations with $\tau = 2$, 6, 12 , 24 and 240 h. The solid black and red curves in Figure 2.9 are the mean potential temperature profiles obtained at equilibrium for column 1 and column 2 respectively in the simulation performed with $\tau = 2$ h. By increasing the strength of the large-scale circulation, the resulting horizontal potential temperature gradients between the columns are considerably reduced when compared to the values obtained in the simulation performed with $\tau = 24$ h (Figure 2.8).

Figure 2.10 shows the mean rain rates at equilibrium for column 1 and 2 as a function of τ. For a shorter τ, the increase in precipitation in column 2 is balanced by the reduction in precipitation in column 1 in response to the diagnosed large-scale circulation which has its descending branch in column 1. For τ much longer than 24 h, for example $\tau = 240$ h, the strength of the large-scale circulation is very weak and the equilibrium state reached in each of the columns is similar to their RCE state. The mean state of the system at equilibrium under the WTG calculations is now compared to the mean state of the system at equilibrium without the WTG parameterization of the large-scale circulation. Figure 2.11 shows the deviation from the system-mean specific humidity profile at RCE of the system-mean profiles at equilibrium under the WTG approach. The system-mean profiles at equilibrium under the WTG approach are the mean of the pro-

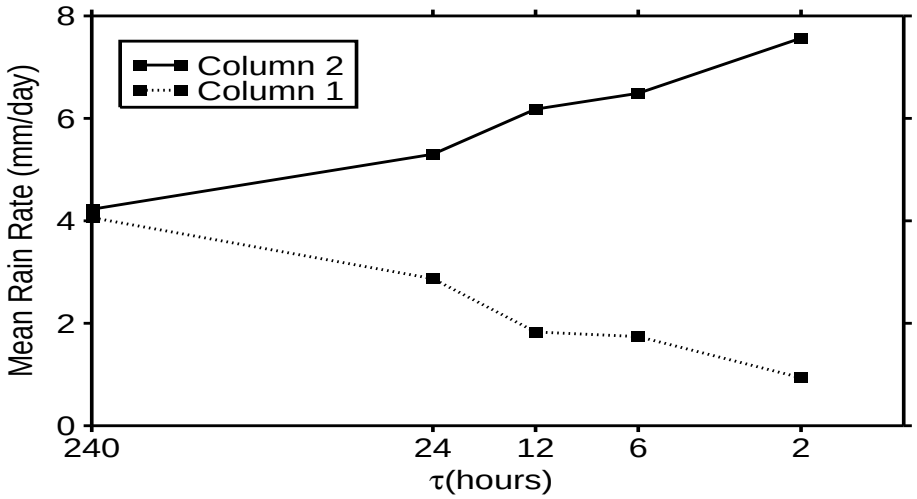

Figure 2.10 *Mean rain rate at equilibrium for column 1 (dotted line with squares) and column 2 (solid line with squares) as a function of the WTG adjustment timescale* τ*. The SST in column 2 is* 1 *K warmer than the value in column 1.*

files obtained for columns 1 and 2 in each of the simulations described in Figure 2.10 while the system-mean profile at RCE is the mean of the profiles for columns 1 and 2 in their own RCE. In the simulations performed with $\tau > 24$ h, the system-mean moisture profile agrees well with that from the RCE state with moisture profiles difference of less than 0.2 g kg^{-1} throughout the whole of the boundary layer and free troposphere. However, in the simulations performed with $\tau \leqslant 24$ h, there is a large-scale circulation which develops in the system. Relative to the RCE state, the reduction in humidity within the subsiding column is greater than the increase in humidity within the ascending column. As a result, system-mean state remains relatively drier than the RCE state. Similarly, the system-mean column-integrated water vapor (CWV) at equilibrium under the WTG approximation is not conserved. It remains relatively small compared to the value obtained at RCE but increases with increasing τ. For example, the values of CWV are 42.55, 42.84, 47.13, 50.34 and 50.82 mm for the simulations performed with $\tau = 2$, 6, 12 ,24

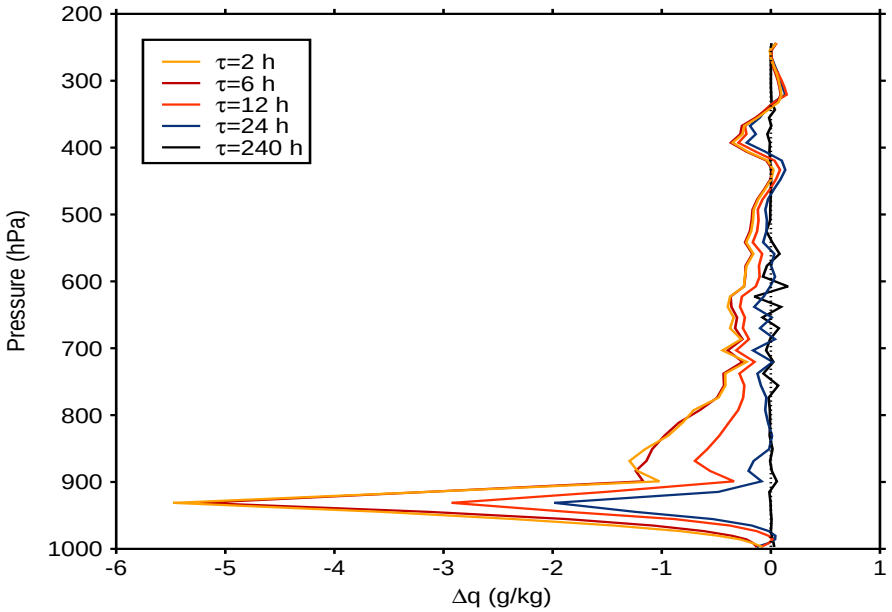

Figure 2.11 *Deviation from the system-mean specific humidity profile at RCE of the system-mean profiles at equilibrium of the same set of simulations as those described in Figure 2.10. The system-mean profile at RCE is the mean of the profiles obtained in the RCE simulations with the SSTs of* 299.5 *and* 300.5 *K.*

and 240 h respectively as compared to the system-mean value of 51.90 obtained in the simulation performed without the implementation of the WTG approximation.

The drying of the system-mean by virtue of the large-scale circulation that developed in the system has been found in the numerical experiments of Bretherton et al. (2005) and Tompkins (2001) and this will be investigated further in the coupled Cloud Resolving Model experiments described in Chapter 5.

2.5.2 Sensitivity to the surface conditions

In this section, columns 1 and 2 are identical and they are initialized with the same profiles which are those obtained in the RCE simulation of the uncoupled SCM with an SST of 299.5 K. The sensitivity to surface conditions is then investigated by changing

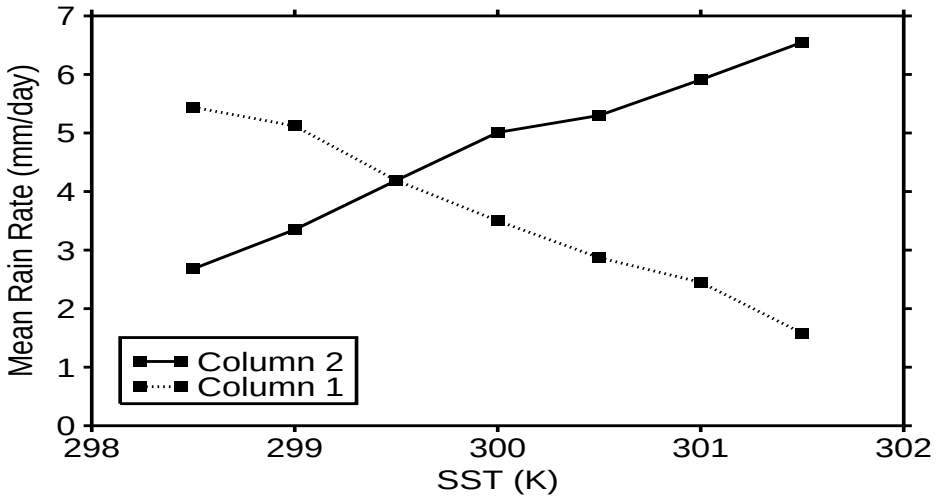

Figure 2.12 *Mean rain rate at equilibrium for column 1 (dotted line with squares) and column 2 (solid line with squares) as a function of the SST in column 2.* $\tau = 24$ *h.*

either the SST, or else by changing the near surface wind speed in one of the columns. The near surface wind speed is changed by changing the value of β. The results from changing either the SST or the value of β are qualitatively similar and only the results from changing the SST will be discussed here.

Figure 2.12 shows the mean rain rates at equilibrium for columns 1 and 2 as a function of the SST in column 2 and Figure 2.13 shows the absolute differences in horizontal potential temperature between columns 1 and 2 in the layer above 900 hPa, representing the free troposphere. For all these simulations, column 1 has an SST of 299.5 K and the value of τ is chosen to be equal to 24 h. Over uniform surface and initial conditions, a symmetric response of the two columns is obtained. Further below, a sensitivity study will be conducted in order to determine if and under which conditions a large-scale circulation can develop under uniform surface conditions. Over non-uniform surface conditions, the column that is warmer at the surface precipitates more strongly to balance the extra cool-

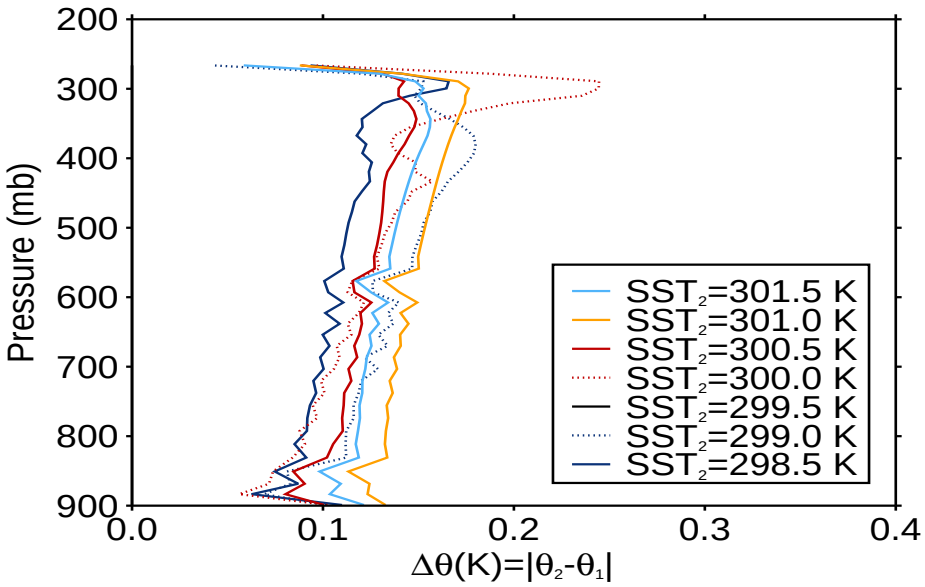

Figure 2.13 *Horizontal potential temperature differences between columns 1 and 2 in the simulations performed over non-uniform surface conditions with* $\tau = 24$ *h. The results are the absolute values and they are presented for the layer above* 900 *hPa, representing the free troposphere.*

ing caused by the diagnosed large-scale ascent within that column. On the other hand the other column precipitates less in response to the warming and the drying effects caused by the descending branch of the large-scale circulation.

For all these simulations, the horizontal differences in potential temperature are small and do not seem to scale directly with the SST difference. Their values are within 0.2 K in the free troposphere; a range of values which is small compared to that obtained in the simulations without the WTG parameterization of the large-scale forcing. In addition, the horizontal potential temperature gradients are not an increasing function of the difference in surface forcing. Hence, the precipitation difference between columns 1 and 2 is driven by the absolute difference in surface forcing only and the absolute temperature seems to be of little importance.

2.6 Equilibrium of the coupled SCMs over uniform surface conditions

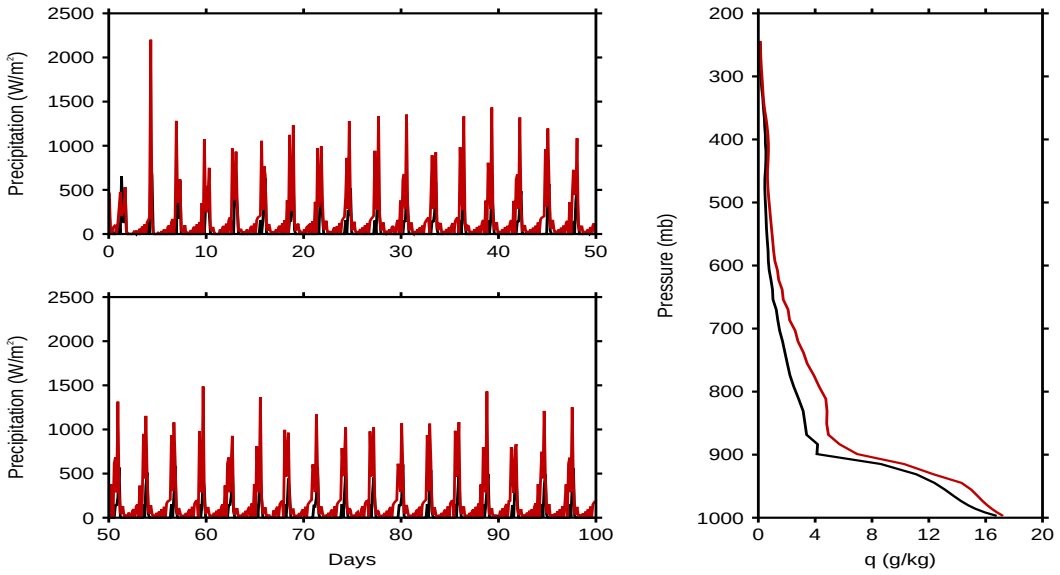

Figure 2.14 *Three hour average precipitation time series (left-hand panel) and mean specific humidity profiles at equilibrium (right-hand panel) for columns 1 (black curve) and 2 (red curve) in the simulation in which P1 is applied. The mean profiles at equilibrium are obtained by averaging over days 70 to 100.* $\tau = 2$ *h.*

As presented in Section 2.5.2, the coupled-column simulations over uniform surface and initial conditions do not develop a large-scale circulation and the columns produce the same mean states and statistics. To determine if and under which conditions a large-scale circulation can develop under uniform surface conditions, a sensitivity to the initial conditions is investigated. This is achieved by performing additional simulations in which one of the columns is perturbed from its initial RCE state. For all these simulations, the columns are initialized with RCE profiles with SST$=$ 299.5 K and the perturbation to the initial profiles of one of the columns is introduced in a completely arbitrary way. It is introduced either to the specific humidity or to the potential temperature, either in the

BL or in the free troposphere. A list of the perturbations tested is as follow:

- P1: the boundary layer in column 2 is 1 g kg^{-1} moister than at RCE.
- P2: the free troposphere in column 1 is 1 g kg^{-1} moister than at RCE.
- P3: the free troposphere in column 1 is 1 K colder than at RCE.

For each type of these perturbations, the temporal evolution of the system is examined for simulations performed with $\tau = 24$ and 2 h. For $\tau = 24$ h, a very weak large-scale circulation develops and is maintained throughout the integrations (results not shown). Hence, the perturbation introduced in the system does not fall off to zero. For the case of simulations performed with $\tau = 2$ h, the direction of the large-scale circulation is preserved whereas its strength is increased.

Figure 2.14 shows the three hour average precipitation time series and the specific humidity profiles at equilibrium for columns 1 and 2 for the simulation in which P1

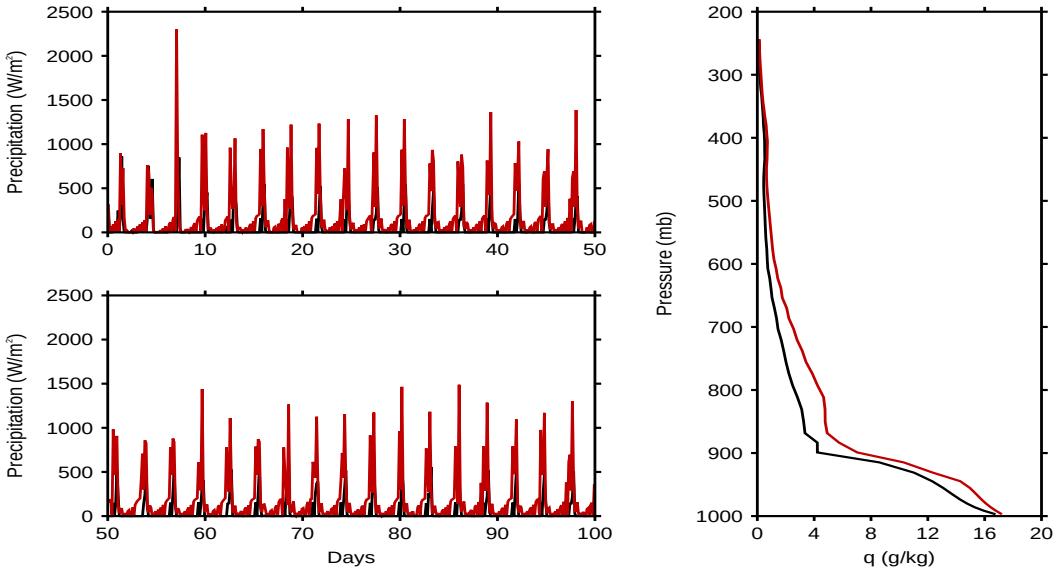

Figure 2.15 *As in Figure 2.14 but for the simulation in which P3 is applied.* $\tau = 2$ *h.*

is applied. The symmetry between the two columns is broken when the perturbation is introduced and the system reaches a new quasi-equilibrium state characterized by a large-scale circulation with ascent in column 2. The mean rain rates at equilibrium are 1.69 and 6.51 mm d^{-1} for columns 1 and 2 respectively. The rainfall difference which is 4.82 mm d^{-1} in this simulation decreases as τ increases. It is reduced to 0.9 mm d^{-1} in the simulation performed with $\tau = 12$ h and it is close to zero in the simulations performed with $\tau \geqslant 24$ h. An equilibrium state characterized by a large-scale circulation with its ascending branch being in column 1 is obtained in the simulation in which P2 is applied (results not shown). For both P1 and P2, precipitation increases in the column with larger initial specific humidity and the difference in the heating associated with precipitation drives a large-scale circulation which keeps the rainier column warmer and moister and the drier column. However, despite the fact that the large-scale circulations that develop have opposite directions, their strength are similar.

The simulation in which P3 is applied immediately develops a large-scale circulation with descent in column 1, as would be expected from the potential temperature difference between the two columns. The corresponding three hour average precipitation time series and mean specific humidity profiles at equilibrium are shown in Figure 2.15. The strength of the circulation that develops is similar to that in the simulation in which P1 is applied and hence is similar to that of the simulation in which P2 is applied. As a result, the mean rain rates at equilibrium for the dry and wet columns in the simulations in which P1 or else P2 or else P3 is applied are similar. In addition, the mean profiles at equilibrium for the dry and wet columns are very close between the experiments (compare the right-hand panels of Figures 2.14 and 2.15). No matter when the perturbation is applied, or the way in which the perturbation is applied, the coupled SCM system is always found to adjust to a final equilibrium state characterized by a large-scale circulation of similar strength.

The sensitivity to the entrainment and detrainment rates and the sensitivity to the CAPE timescale is investigated by changing the values of the fractional mass entrainment and detrainment coefficients and the values of the CAPE timescale. The strength of the

large-scale circulation is indeed found to be sensitive to these parameters. For instance, the simulation which applied P1 with $\xi = 0.001$ hPa^{-1} and $\delta = 0.001/3$ hPa^{-1} develops a large-scale circulation with descent in column 1 and with a rainfall difference of 3.2 mm d^{-1} while the simulation which applied P1 with $\xi = 0.001$ hPa^{-1} and $\delta = 0.002/3$ hPa^{-1} develops a large-scale circulation with descent in column 1 and with a rainfall difference of 1.28 mm d^{-1}. In both cases, the direction of the large-scale circulation is maintained. However, the rainfall difference differs from that obtained in the simulation which applied one of the perturbations with $\xi = 0.002$ hPa^{-1} and $\delta = 0.002/3$ hPa^{-1}. In few cases, a quasi-steady state with no mean large-scale circulation is obtained. This is the case in the simulation performed with $\xi = 0.001$ hPa^{-1}, $\delta = 0.002/3$ hPa^{-1} and $\tau_{CAPE} = 2$ h.

2.7 Chapter Summary

Simple parameterization schemes were used to build a cheap and simple SCM to examine some of the sensitivities to the WTG approach. It was designed to represent convective processes and their interactions with the surrounding environment. The SCM was integrated for 100 days and reached a quasi-steady equilibrium state in which the heating induced by precipitation nearly balances the prescribed radiative cooling by day 30. The frequency of occurrence of precipitating convection increases with the increasing CAPE timescale, and increasing radiative cooling rate. The mean rain rate at equilibrium is insensitive to the CAPE timescale but increases with the prescribed radiative cooling.

Two columns of the SCM have been coupled via the WTG derived large-scale circulation. The coupled SCM simulations over uniform surface with uniform initial conditions produced an equilibrium state with no large-scale circulation. The coupled SCM simulations over uniform surface conditions and perturbed initial conditions produced an equilibrium state with a large-scale circulation, although some sensitivity studies reveal cases of an equilibrium state with no mean large-scale circulation. The coupled SCM

simulations over non-uniform surface conditions produced an equilibrium state characterized by a large-scale circulation with ascent within the column which is more strongly forced at the surface. The large-scale circulation was driven by the absolute difference in surface conditions rather than the tropospheric potential temperature. i.e. the strength of the circulation was related to the absolute difference in surface forcing but not to related to the horizontal potential temperature difference. In all cases of simulations performed with a finite value of WTG coupling timescale, the horizontal potential temperature differences between the columns were reduced compared to the values obtained in the radiative-convective equilibrium simulation. These results were qualitatively insensitive to the choice of the WTG adjustment rate profiles and the strength of the circulation established was found to vary inversely with the WTG coupling timescale.

This version of the SCM has been useful to test the WTG calculations. A number of WTG simulations were performed and an overview of the results have been obtained. For instance, a large-scale circulation can develop over uniform surface conditions. However, it may be recognized that this version of the SCM is very simple and nature of the large-scale circulation depends on the representation of convection. This motivates the need to perform similar WTG simulations using a more powerful model that explicitly resolves convection; that model will be the Large-Eddy Model at version 2.4 of the Met Office.

Chapter 3:
Radiative-Convective Equilibrium Simulation

3.1 Introduction

Chapter 2 described the simple parameterization schemes which are used to build a simple version of the single column model (SCM). It also details the WTG approximation that is used to modify the simple SCM in order to simulate the two-way interactions between convection and the large-scale circulation. However, this simple SCM described does not include all the important features in the convective processes. Here, the concern is the explicit nature and the development of convective clouds and the suggested model that fulfils these aims is the Large-Eddy Model (LEM) run in Cloud Resolving Mode (CRM) (Shutts and Gray, 1994; Petch and Gray, 2001). In such a model a grid length is used to filter the flow into large and subgrid scale components. The large scale components responsible for most of the turbulent energy and transport of the flow are explicitly resolved leaving only cloud microphysics, radiation and subgrid scale turbulence responsible for the dissipation of kinetic energy to be parameterized. This model has been used for a wide range of case study simulations including shallow convection, deep convection and the transitions between them (e.g. Abel and Shipway, 2007; Petch and Gray, 2001; Woolnough et al., 2010).

This chapter will first detail the model equations, and highlight the choices which may be different from other CRM studies of tropical deep convection. Finally, the approach to radiative-convective equilibrium will be discussed and the sensitivity to some parameters

will be investigated.

3.2 Dynamics and Thermodynamics

3.2.1 Basic Equation Set

The LEM code solves the Boussinesq-type equation set which consists of:
the momentum equation

$$\frac{Du_i}{Dt} = -\frac{\partial}{\partial x_i}\left(\frac{P^{'}}{\overline{\rho}}\right) + \delta_{i3}\mathbf{B}^{'} + \frac{1}{\overline{\rho}}\frac{\partial \tau_{ij}}{\partial x_j} - 2\varepsilon_{ijk}\Omega_j u_k \tag{3.1}$$

the continuity equation

$$\frac{\partial \overline{\rho} u_i}{\partial x_i} = 0 \tag{3.2}$$

the prognostic equation for potential temperature

$$\frac{D\theta}{Dt} = \frac{1}{\overline{\rho}}\frac{\partial h_i^{\theta}}{\partial x_i} + \left(\frac{\partial \theta}{\partial t}\right)_{mphys} + \left(\frac{\partial \theta}{\partial t}\right)_{rad} \tag{3.3}$$

and the prognostic equation for all other scalar variables

$$\frac{Dq_n}{Dt} = \frac{1}{\overline{\rho}}\frac{\partial h_i^{q_n}}{\partial x_i} - \left(\frac{\partial q_n}{\partial t}\right)_{mphys} \tag{3.4}$$

where the rate of change following the parcel of air is defined by

$$\frac{D}{Dt} = \frac{\partial}{\partial t} + u_i\frac{\partial}{\partial x_i} \tag{3.5}$$

In these equations

$\overline{\chi}$	denotes the basic state of χ
χ'	denotes a perturbation from the basic state of χ
u	is the vector flow velocity field (u, v, w)
θ	is the potential temperature
q_n	represents all other scalar variables
P	is the pressure

ρ	is the density
B	is the buoyancy
τ	is the subgrid stress
Ω	is the Earth's angular velocity (f-plan approximation)
h^{θ}	is the subgrid scale flux of θ
h^{q_n}	is the subgrid scale flux of q_n
δ_{i3}	is the kroneker delta function
ε_{ijk}	is the alternating pseudo-tensor
$\left(\frac{\partial\theta}{\partial t}\right)_{mphys}$	is the source term of θ due to microphysics
$\left(\frac{\partial q_n}{\partial t}\right)_{mphys}$	is the loss term of q_n due to microphysics
$\left(\frac{\partial\theta}{\partial t}\right)_{rad}$	is the source term of θ due to radiation

The above set of equations (Equations 3.1 to 3.4) are a Boussinesq-type equation set written using tensor notation. A full derivation is shown in Appendix B of Derbyshire et al. (1994).

The vector field, **u**, and the scalar fields, θ and q_n describe the resolved flow and the subgrid contribution to the flow is determined entirely through the subgrid parameterization schemes described in section 3.3. The mean reference state is defined by $\overline{\rho}$, $\overline{\theta}$ and $\overline{P}$ and the departures from this mean reference state ($\rho^{'}$, $\theta^{'}$ and $P^{'}$ respectively) are assumed to be small.

LEM simulations have been used successfully to study the boundary layer (e.g. Deardorff, 1970a,b). In the boundary layer the vertical derivatives of ρ, θ and P may be considered to be negligible and LEM studies which apply to the boundary layer often use a reference state which is constant with height (incompressible Boussinesq system). However, the vertical derivatives of ρ, θ and P are not small in the free troposphere and hence, for LEM studies which apply also to the free troposphere, the Boussinesq approximation is extended to the quasi-Boussinesq or anelastic approximation, in which the

reference state is a function of height only.

3.2.2 Reference state and Buoyancy

In the LEM, the user specifies the mean reference potential temperature profile, $\overline{\theta}$, and the mean reference profiles of density, $\overline{\rho}$, and pressure, $\overline{P}$, are calculated using the universal gas law and hydrostatic approximation with appropriate boundary conditions. Hence

$$\overline{P} = \overline{\rho} R \overline{\theta} \left(\frac{\overline{p}}{p_{ref}} \right)^{\frac{R}{C_p}} \tag{3.6}$$

and

$$\frac{d\overline{P}}{dz} = -g\overline{\rho} \tag{3.7}$$

where R is the gas constant, C_p is the heat capacity at constant pressure, g is the acceleration due to gravity and $P_{ref} = 1000\ hPa$ is the standard reference pressure used to convert temperature to potential temperature and vice versa. Given the profile of $\overline{\theta}$, the profile of $\overline{P}$ is calculated by eliminating $\overline{\rho}$ from Equations 3.6 and 3.7. That leaves

$$\frac{1}{\overline{P}} \frac{d\overline{P}}{dz} \left(\frac{\overline{P}}{P_{ref}} \right)^{R/C_p} = -\frac{g}{R\overline{\theta}} \tag{3.8}$$

The profile of $\overline{P}$ is obtained from Equation 3.8 with the boundary condition being the specification of the pressure at the surface. Given the profile of $\overline{P}$, the profile of $\overline{\rho}$ is calculated from Equation 3.7.

The thermodynamic variable of the LEM is the departure of potential temperature from the mean reference state, θ'. The prognostic equation of θ' can be derived from the prognostic equation of θ (Equation 3.3) as:

$$\frac{D\theta'}{Dt} + w\frac{d\overline{\theta}}{dz} = \frac{1}{\overline{\rho}} \frac{\partial h_i^{\theta'}}{\partial x_i} + \frac{1}{\overline{\rho}} \frac{\partial h_3^{\overline{\theta}}}{\partial z} + \left(\frac{\partial \theta'}{\partial t} \right)_{mphys} + \left(\frac{\partial \theta'}{\partial t} \right)_{rad} \tag{3.9}$$

The virtual potential temperature term, θ'_v is defined in terms of θ' as

$$\theta'_v = \theta' + \overline{\theta} c_{n,i} q_{n,i} \tag{3.10}$$

where c_n is the coefficient representing the impact of q_n on the density of the parcel of air. $\theta_v^{'}$ is used purely as a measure of buoyancy, $B^{'}$. That is:

$$B' = g\frac{\theta_v'}{\overline{\theta}} \tag{3.11}$$

3.3 Subgrid Model

The largest eddies in the flow are the primary generator of energy. The subgrid contribution to the flow through which energy is dissipated are parameterized based on a first order Smagorinsky-Lilly approach along with some improvements by Mason (1989). Details regarding the subgrid model are fully described in Derbyshire et al. (1994) and Brown et al. (1994).

The subgrid shear stress, τ_{ij}, and scalar flux, $h_{n,i}$ are specified by

$$\tau_{ij} = \overline{\rho}\nu S_{ij} \tag{3.12}$$

and

$$h_{n,i} = -\overline{\rho}\nu_h \frac{\partial q_n}{\partial x_i} \tag{3.13}$$

respectively. Here ν is the subgrid eddy-viscosity and ν_h is the corresponding diffusivity for scalars. S_{ij} is the rate of strain tensor calculated as:

$$S_{ij} = \frac{\partial u_i}{\partial x_j} + \frac{\partial u_j}{\partial x_i} \tag{3.14}$$

In the classical Smagorinsky-Lilly approach, ν is prescribed through

$$\nu = \lambda_0^2 S \tag{3.15}$$

and

$$\nu = \nu_h \tag{3.16}$$

where λ_0 is the basic mixing length and S is the modulus of S_{ij} calculated as:

$$S = \left(\frac{1}{2}\sum_{i,j=1,3} S_{ij}^2\right)^{\frac{1}{2}} \tag{3.17}$$

The approach used for non-neutral conditions by the LEM is an extension of the classical Smagorinsky-Lilly approach. ν and ν_h are functions of a local Richardson number, Ri_p, and the mixing length scale, λ, characterizing the size of the eddies. . Those are:

$$\nu = \lambda^2 S f_m(Ri_p) \tag{3.18}$$

and

$$\nu_h = \lambda^2 S f_h(Ri_p) \tag{3.19}$$

where f_m and f_h are Richardson number dependent functions which are given in Gray et al. (2001). Ri_p, is defined through

$$Ri_p = \frac{\partial B/\partial z}{S^2} \tag{3.20}$$

As noted above, the LEM approach differs from the classical Smagorinsky-Lilly approach by the presence of the local Richardson number dependent function. In addition, the LEM approach allows a smoother transition between λ in the interior of the flow, where $\lambda = \lambda_0$, and that near the ground, where λ is a function of distance from the surface. λ is estimated through

$$\frac{1}{\lambda^2} = \frac{1}{\lambda_0^2} + \frac{1}{[\kappa(z+z_0)]^2} \tag{3.21}$$

where κ is the von Karman constant and z_0 the roughness length. λ_0 is proportional to the grid spacing. That is $\lambda_0 = C_s\Delta$. Here, $\Delta = \Delta y$ and the appropriate value for C_s is 0.23 (see Section 3.2 of Gray et al. (2001)).

3.4 Boundary Conditions

In the LEM, the lateral boundary conditions are periodic for all prognostic variables. The treatment of the upper boundary is different to that of the lower boundary. Both boundaries are rigid lids, such that $w = 0$. However, lower boundary conditions should

represent the effects of flux across a surface while the upper boundary should represent the effects of the remainder atmosphere.

Bulk aerodynamic formulae are used to compute the sensible heat and latent heat fluxes from the surface

$$F_s = C_p \rho^n C_E V^n (T^s - T^n) \tag{3.22}$$

$$F_L = L_v \rho^n C_E V^n (q^*(T^s) - q^n) \tag{3.23}$$

The subscripts s and n are used to refer to properties of the surface and near-surface respectively. C_p is the heat capacity at constant pressure, L_v is the latent heat of vaporization, ρ is the density and C_E is the exchange coefficient. $q^*(T^s)$ is the saturation specific humidity value at the surface temperature T^s and V^n is the near-surface wind speed.

Here, the Monin-Obukhov similarity theory is used and the full expression for C_E is given in the LEM manual Bull and Derbyshire (1990).

A Newtonian damping layer is implemented in the upper part of the LEM domain in order to prevent vertically propagating gravity waves from being reflected back into the main part of the domain. The rate of damping of all prognostic variables is

$$\frac{\partial \chi}{\partial t} = \frac{1}{\tau_D} \left[exp\left(\frac{z - z_D}{H_D} \right) - 1 \right] (\chi - \overline{\chi}) \tag{3.24}$$

where τ_D is the damping timescale, H_D is the damping depth and z_D is the height above which the damping layer is implemented. χ is the prognostic variable being damped and $\overline{\chi}$ is the horizontal domain-mean of χ. z_D is chosen so as not to interfere with the radiative cooling profile (see Figure 3.1) and in addition, H_D must be greater than the vertical wavelength of typical waves which may develop in the lower stratosphere in order to prevent undesirable wave reflections.

3.5 Moist Processes and Microphysics

This version of the LEM uses a three-phase microphysics parameterization which is a bulk-water scheme. The bulk-water scheme is based on the parameterizations described in Lin et al. (1983) and Rutledge and Hobbs (1984) with some improvements to the representation of cloud ice by Flatau et al. (1989). In this scheme, all types of water particles are divided into five discrete categories which are, liquid water, rain (liquid water drops), cloud ice (small ice crystals), snow (low density ice aggregates) and graupel (heavily rimed ice particles). Six model variables are used to represent the mass mixing ratios of the five water categories and the mass mixing ratio of water vapor. In addition to these six variables, a further variable is used to represent the number concentration of ice. Hence, the bulk-water scheme used in this study is described as ”double-moment” for ice and ”single moment” for all other water categories.

3.6 Radiation

Some LEM studies have used an interactive radiation scheme (e.g. Tompkins and Craig, 1998a) to allow the tropospheric cooling due to the loss of terrestrial radiation to vary in response to the temperature and humidity in the column. The radiation scheme distributed in the LEM code is the same as that used in the Met Office Unified Model (Cullen, 1993). It is described in Edwards and Slingo (1996). More detail is given in Ingram et al. (1997) and the details of the features not included in the Unified Model (e.g. the treatment of precipitating hydrometeors) are given in Gray et al. (2001).

Held et al. (1993); Tompkins and Craig (1998a) demonstrated that radiative-convective feedbacks encourage convective organization. In this study the energy budget will be controlled in order to help with the analysis and moreover, the organization of convection might not be very realistic in two-dimensions (e.g. Tompkins, 2000; Bretherton and Smolarkiewcz, 1989). Therefore, unless otherwise stated, this form of convective

organization is avoided here by applying a fixed horizontally homogeneous and non-interactive cooling due to radiation. This radiative forcing will be henceforth referred to as a radiative cooling. It consists of a vertically uniform value of 1.5 K d^{-1} from the surface to 220 hPa and then decreases linearly in pressure to reach zero at 120 hPa as shown in Figure 3.1. This profile of radiative forcing agrees well with the numerical results of experiments of Shutts and Gray (1994) and Tompkins and Craig (1998a) and observations of Raval et al. (1994). A radiative forcing profile similar to this has been used in previous studies (e.g. Nakajima and Matsuno, 1988; Islam et al., 1993; Robe and Emanuel, 1996) and has been found to produce a realistic equilibrium state.

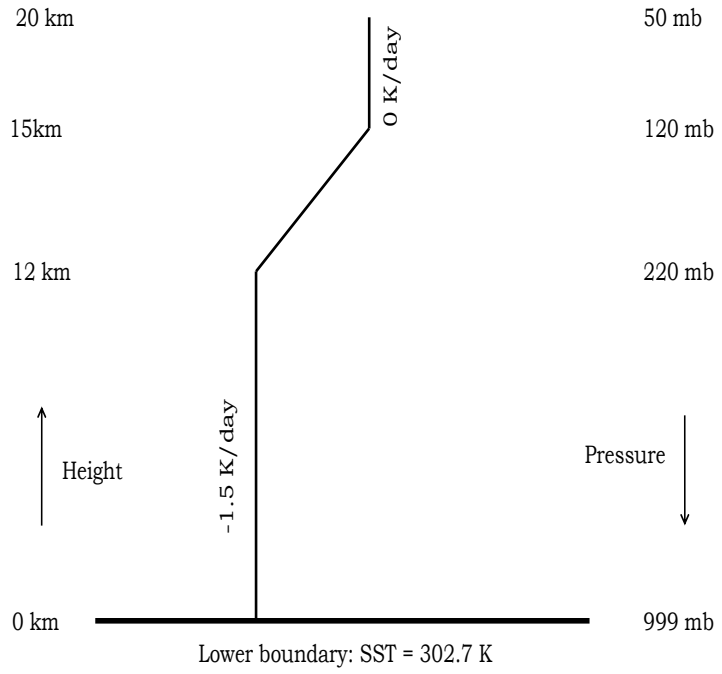

Figure 3.1 *Profile of the tropospheric cooling ($\frac{\partial T}{\partial t}$) due to loss of terrestrial radiation.*

3.7 Numerical Methods and Stability Criteria

The LEM uses a Lorenz grid in the vertical and an Arakawa C-grid (Arakawa and Lamb, 1977) in the horizontal. It supports two advection schemes. These are, the centred difference scheme of Piacsek and Williams (1970) and total variance diminishing (TVD) scheme of Leonard et al. (1993) also known as ULTIMATE. The Piacsek-Williams scheme is used for advection of momentum. It is linearly and quadratically preserving but not positive definite. On the other hand, in one dimensional flow ULTIMATE is referred to as "monotonicity preserving" because it advects sharp gradients without overshooting. In multi-dimensional flow, the "monotonicity preserving" is relaxed to "positivity preserving" as any advected field which is initially positive will remain so. It is used for advection on scalars.

Both advection and viscous terms independently place stability constraints on the model timestep. These constraints are expressed in terms of limitations on the advective Courant number or CFL (Courant, Friedrichs and Levy) number. In one dimensional flow, the CFL number is given by

$$CFL = \frac{u\Delta t}{\Delta x} \tag{3.25}$$

In the LEM code, the timestep can be variable during the run. The constraints on the timestep are applied using the two extreme values of the CFL number, which are the largest advective Courant number and the "worst case" viscous stability parameter. In generalizing to three dimensions, the largest advective Courant number is given by

$$CVEL = \Delta t \left(\left(\frac{u}{\Delta x} \right)_{max} + \left(\frac{v}{\Delta y} \right)_{max} + \left(\frac{w}{\Delta z} \right)_{max} \right) \tag{3.26}$$

and the "worst case" viscous stability parameter is given by

$$CVIS = max \left[4\Delta t \nu_h \left(\frac{1}{\Delta x^2} + \frac{1}{\Delta y^2} + \frac{1}{\Delta z^2} \right) \right] \tag{3.27}$$

The overall CFL number is defined in terms of CVEL and CVIS as

$$CFL = \frac{CVEL}{CVEL_{max}} + \frac{CVIS}{CVIS_{max}} \tag{3.28}$$

where $CVEL_{max}$ and $CVIS_{max}$ represent the maximum permitted values of $CVEL$ and $CVIS$. Their values are pre-specified and the timestep is set so that the CFL equals one to ensure stability in the model. However, this criteria is subjected to a specified tolerance which allows the model to run with the maximum timestep that does not cause numerical instability.

3.8 Model dimensionality, size and resolution

According to the studies of Tao et al. (1987) and Grabowski et al. (1998), the use of either a two dimensional or a three dimensional configuration has limited effect on the statistical properties of cloud ensembles. In contrast, some previous studies have underlined many differences between the two dimensional and the three dimensional simulations. For example, Tompkins (2000) suggested that two dimensional simulations may artificially enhance cool pools. He demonstrated that two dimensional simulations lead to a warmer and moister boundary layer and a warmer mean tropospheric state compared to the equivalent three dimensional simulations; which is a consequence of the two dimensional geometry to artificially maintaining the strong surface wind speed caused by deep convective downdrafts and so transporting more heat and moisture from the surface to the boundary layer. In addition, Tompkins (2000) demonstrated that large-domain two dimensional simulations encourage mesoscale self aggregation of convective cells and that areas free from convection around the clouds are inhibited from further convection by becoming very dry and leading to a relatively dry atmosphere compared to the equivalent three dimensional simulations. This result is similar to that found in the study of Bretherton and Smolarkiewcz (1989) who demonstrated that a spontaneous organization of convection is increased in two dimensional simulations because of the enhancement of subsidence motions in the regions surrounding the clouds. In the same study, they also demonstrated that two dimensional simulations artificially spread the compensating subsidence motion associated with the simulated convection. Petch et al. (2008)

demonstrated that convective cells do not sufficiently entrain dry air in two dimensional simulations compared to three dimensional simulations while Zeng et al. (2007) showed that two dimensional simulations produce excessive buoyancy oscillations which cause high frequency fluctuations in the time-mean and the domain-mean thermodynamic and microphysical properties.

On the other hand, Tompkins (2000) also pointed out the fact that the equilibrium properties of convective ensembles in smaller two dimensional simulations are comparable to those of three dimensional simulations. This is because small two dimensional simulations artificially reduce surface wind speed, and also restrict self aggregation of convective cells. Unless otherwise stated, this study uses a small two- dimensional CRM with a simple fixed radiative forcing and no imposed wind shear. Hence, convective organization is not expected.

The model has a length of 128 km and a height of 20 km. The domain is large enough to accommodate an ensemble of convective clouds together with the compensating subsidence motions. At the same time, it is not so large as to allow spontaneous mesoscale organization of convection (Tompkins, 2000; Bretherton and Smolarkiewcz, 1989). From previous studies, the tropospheric resolution should be no coarser than 25 hPa for a good resolution of the processes that determine the water vapor profile (Tompkins and Emanuel, 2000). Hence there are 60 levels in the vertical, on a stretched grid with resolution moving from 80 m in the boundary layer where turbulence processes are stronger to 330 m in the mid-troposphere. This study uses a horizontal grid spacing of 500 m. Such a grid spacing is smaller than typical values used in many RCE simulations. For example, Tompkins and Craig (1998b), Cohen and Craig (2006), Pauluis and Held (2002) and many others used 2 km. Although an horizontal grid spacing of 2 km has been used in many CRM experiments, Bryan et al. (2003) demonstrated that for the large-scale energy containing eddies of scale of about 10 km (a typical vertical and horizontal scales of a thunderstorm), a horizontal grid spacing greater or equal to 1 km is not sufficient to simulate a fully turbulent flow. From their study, a grid spacing on the order of 100 m

was the appropriate value for a good resolution of individual deep moist convective cells. However, the results from their numerical experiments showed that the 500 m simulation was able to reproduce the overall structure observed in the simulations using a finer grid spacing of 125 m.

3.9 Other details

The lower boundary is an ocean surface, with roughness length of 2×10^{-4} m and a prescribed spatially–uniform and time–independent SST. The control run has an SST of 302.7 K corresponding to the mean value of SST measured during the Tropical Ocean Global Atmosphere - Coupled Ocean Atmosphere Response Experiment (TOGA-COARE) from the western Pacific warm pool (Webster and Lukas, 1992).

In the along-domain direction, the mean wind is relaxed to a vertically uniform value of 0 m s^{-1} with a relaxation timescale of 2 hr. This is done to avoid the propagation of convective cells and to avoid the development of artificial along-domain wind shear which may otherwise occur in two-dimensional simulations (Tompkins, 2000; Mapes and Wu, 2001) and which would encourage the formation of squall lines (e.g. Rotunno et al., 1988; Robe and Emanuel, 2001; Tao et al., 1999). In the across-domain direction, a vertically uniform wind speed of 5 m s^{-1} is imposed. This wind speed is strong enough so that surface wind fluctuations within the domain do not much matter for the surface fluxes of heat and moisture. This choice affects the simulations via the bulk aerodynamic formulae which are used to compute surface fluxes as described in section 3.4. The wind in the across-domain direction does not affect the dynamics of convection. It is simply used to increase the value of surface evaporation compared to its no wind value.

Domain size ($y \times z$)	128×20 km
Number of horizontal grid points	256
Number of vertical levels	60
Horizontal resolution	500 m
Vertical resolution	Function of height: more levels near the surface and in the boundary layer
Lateral boundary conditions	Periodic
Top and bottom boundary conditions	Rigid lids
Sea surface temperature	302.7 K
Newtonian damping layer	$z_D = 15$ km $H_D = 2.5$ km $\tau_D = 1000$ seconds
Roughness length	$z_0 = 0.2$ m
Wind profile	x direction speed: 5 m s^{-1} y direction speed: 0 m s^{-1} Broclinic wind shear: none Relaxation timescale: $\tau = 2$ hr
Coriolis parameter	zero

Table 3.1 *Parameters used in the model.*

3.10 Approach to Radiative Convective Equilibrium

This section examines the evolution of some fields in response to the prescribed radiative forcing. Figure 3.2 shows the potential temperature and humidity profiles used to initialize the model. These profiles are taken from measurements during the TOGA-COARE field campaign. The model is run for 40 days using the parameters summarized in Table 3.1. This period of integration is long enough for the simulation to reach a quasi-steady state in which the heating induced by precipitation and surface sensible heat

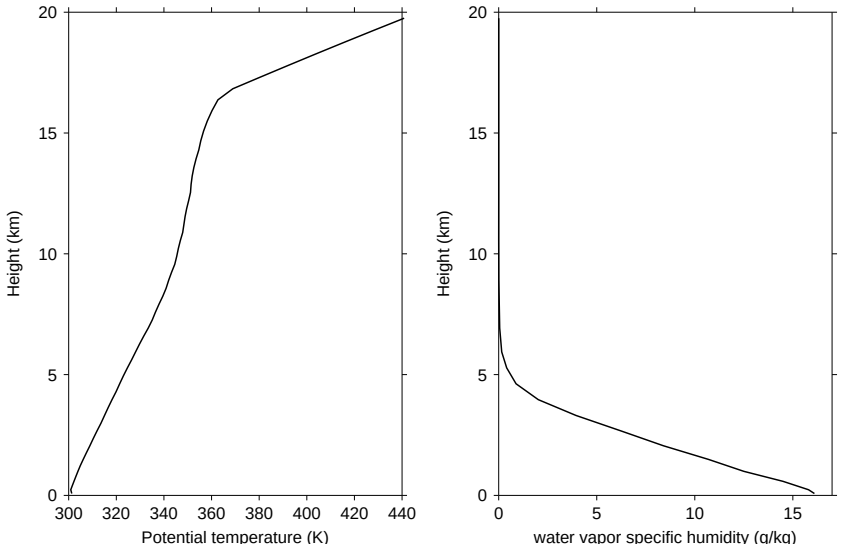

Figure 3.2 *Potential temperature and specific humidity profiles used to initialize the control run. They are taken from measurements during the TOGA-COARE field campaign.*

flux balance the prescribed radiative forcing; that is the RCE state (Tompkins and Craig, 1998a).

Figures 3.3 and 3.4 shows the time series of adjustment of key fields to the prescribed radiative forcing. The adjustment timescale is defined by the rate at which the model adjusts its thermodynamic profiles due to the mixing of water vapor in the subsidence region surrounding the cloud (Emanuel, 1994). The time series are those of column integrated water vapor (CWV), precipitation, maximum vertical velocity and heat budget. The wind speed applied in the across-domain direction helped the simulation to come into an RCE state. The simulation is initialized from consistent data for the SST. As a result, the fields take about 10 days to reach a quasi-steady state with shorter timescale oscillations about their mean values. However, the adjustment timescale would have been much longer if the simulation was initialized from less suitable profiles. This adjustment timescale is very close to the 12 days found by Cohen and Craig (2004). However, it is shorter than the 30 days found by Tompkins and Craig (1998b) and even shorter than the adjustment timescale of fields from previous two dimensional simulations of Held et al.

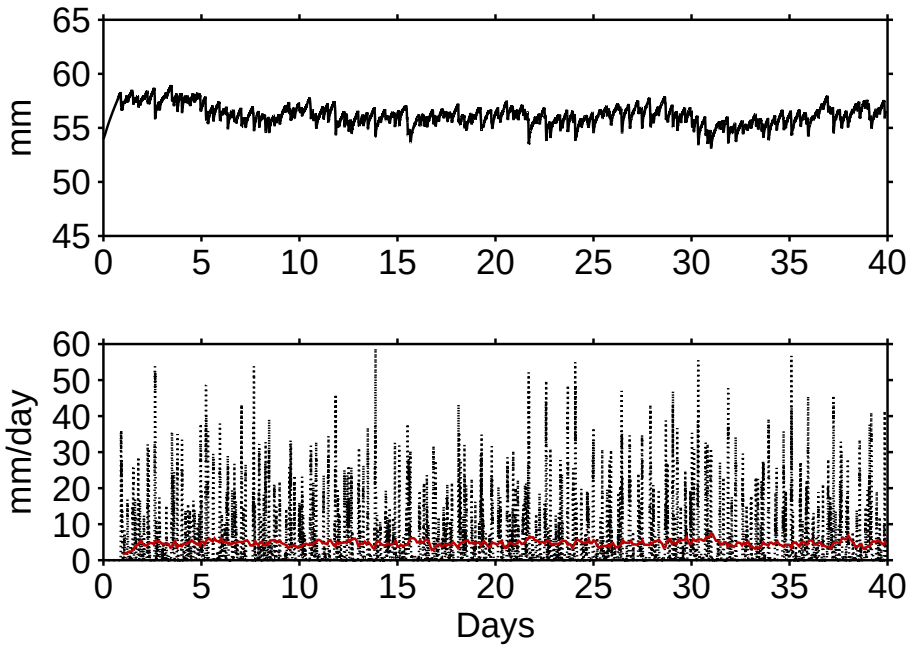

Figure 3.3 *Time series of column integrated water vapor (CWV[mm])(top panel) and the rain rate (bottom panel in mm d^{-1}) for the entire integration. The solid red curve on the bottom panel represents the daily running mean rain rate.*

(1993), Sui et al. (1994) and Grabowski et al. (1996). The daily-mean maximal vertical velocity remains above 1 m s^{-1}. This is an indication of the presence of continuous convective activity (e.g. LeMone and Zipser, 1980).

The heat budget in the column can be written as:

$$F_S + C_p \int_0^{z_{\text{top}}} \left[\left(\frac{\partial T}{\partial t} \right)_\mu + \left(\frac{\partial T}{\partial t} \right)_{\text{rad}} \right] \rho dz = 0 \tag{3.29}$$

where C_p is the heat capacity at constant pressure. F_S is the sensible heat flux, and the two temperature tendency terms in square brackets represent the heating from condensation and the heating from radiation. The heating from radiation is a constant calculated from the time-independent radiative cooling profile shown in Figure 3.1. The F_S is very weak and hence, the important point is that at equilibrium the heating induced by condensation supports the prescribed radiative cooling.

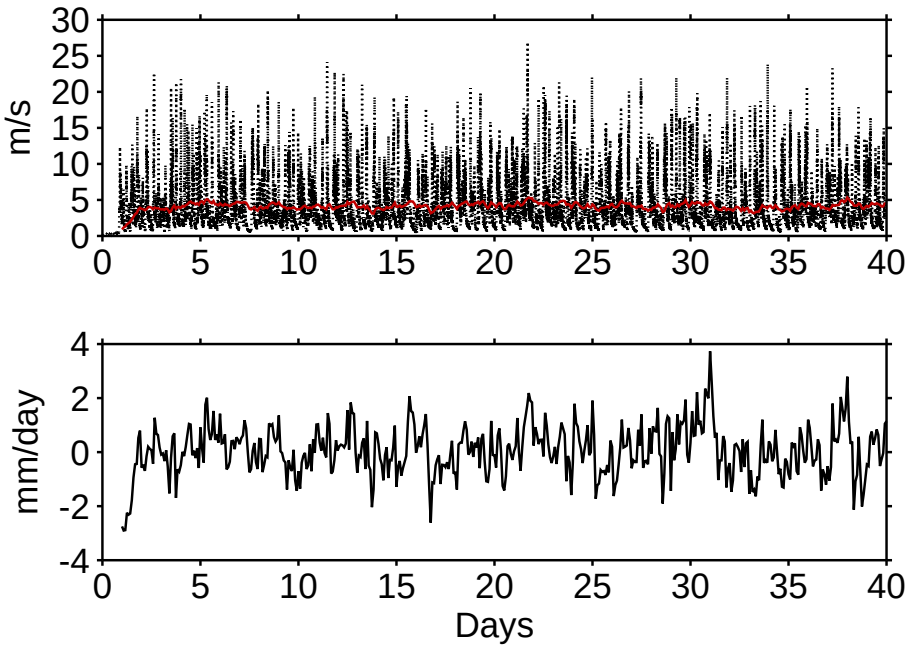

Figure 3.4 *Time series of maximal vertical velocity (top panel in m s^{-1}) and daily running mean heat budget (bottom panel in mm d^{-1}). The solid red curve represents the daily running mean maximal vertical velocity. The heat budget is the sum of sensible heat flux, heating from condensation and radiation and it should be zero at equilibrium.*

The time series of column-integrated quantities do not provide information about the vertical structures obtained. Figure 3.5 shows contour plots of the time variation (daily running mean) in the vertical of the potential temperature and specific humidity anomalies with respect to their mean profile over the 40 days of integration. The height has been limited to 15 km because processes occurring in the damping layer are artificial. An equilibrium state is reached at all model levels before day 20. From day 35, there is a drift in potential temperature at upper levels. This may indicate that the simulation is not run quite long enough to reach a true RCE state. An average over days 20 to 40 is used to define the model state and statistics at equilibrium. The mean rain rate at equilibrium is 4.77 mm d^{-1}, as compared to 4.80 mm d^{-1} of the surface evaporation rate.

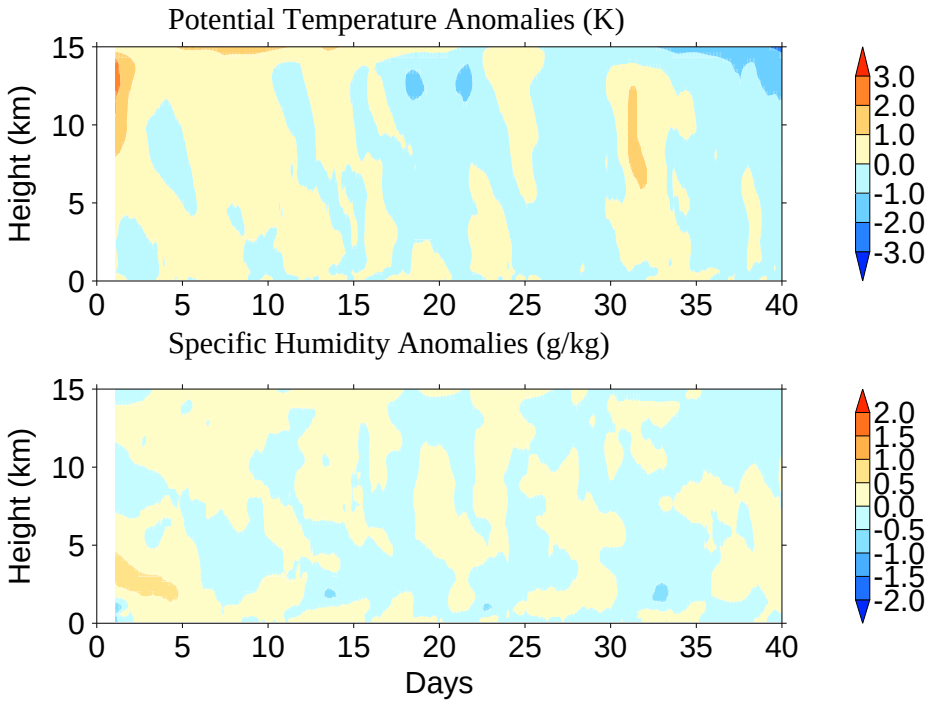

Figure 3.5 *Contour plots of the daily running mean potential temperature (K) and specific humidity (g* kg^{-1}*) anomalies which respect to the* 40 *days mean profiles.*

3.10.1 Profiles at radiative-convective equilibrium

Figure 3.6 shows the profiles of temperature and specific humidity plotted in a tephigram. These profiles are used as reference profiles , as well as providing initial conditions for the WTG experiments described in the next chapters. The wind speed applied in the across-domain direction increased the near surface humidity relative to the initial state and helped the simulation to reach a quasi-steady state. There is a reduction of moisture from the top of the boundary layer to 800 hPa and there is a bulge in humidity between 800 hPa and 240 hPa corresponding to the layer at which most intermediate and deep convective towers undergo their final detrainment.

The lowest 20 hPa is well mixed and represents the model's boundary layer. The temperature profile is conditionally unstable between 900 and 600 hPa. From 600 to

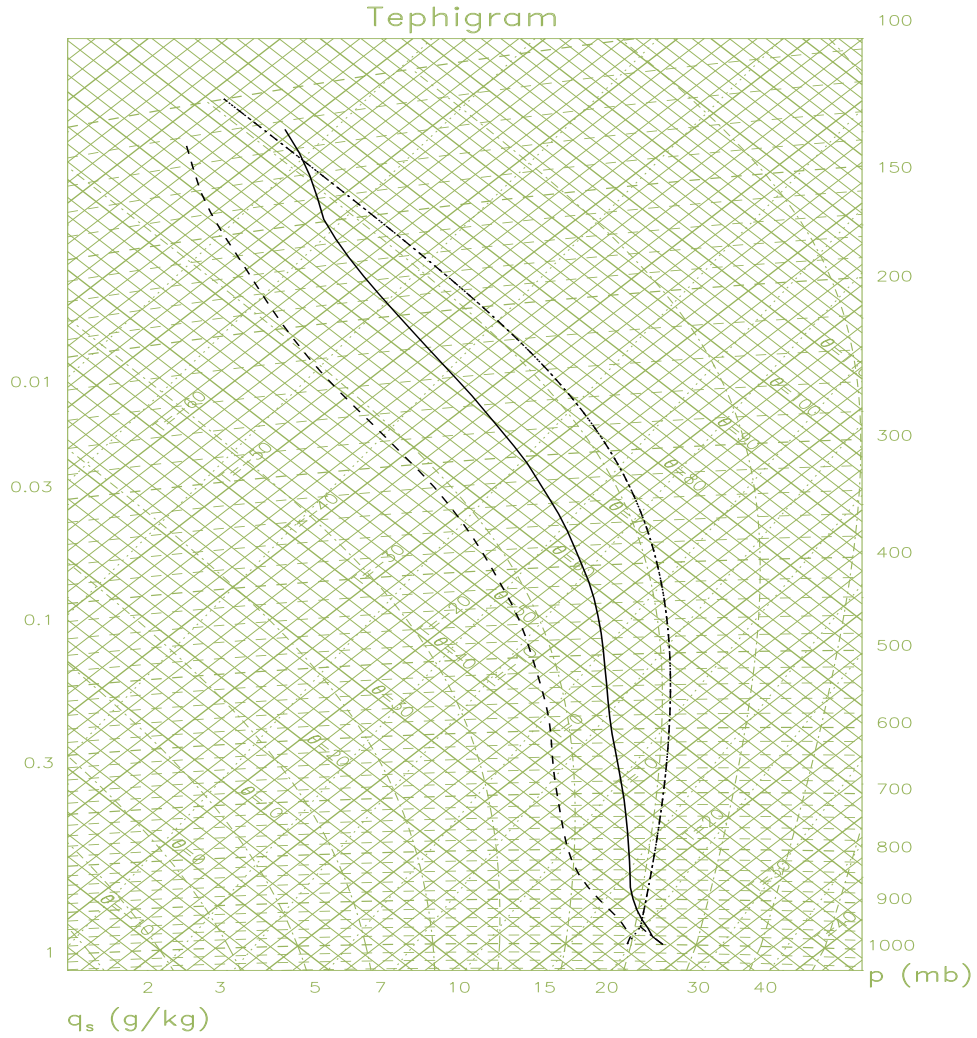

Figure 3.6 *Domain-mean temperature (solid curve) and specific humidity (dashed curve) profiles obtained at equilibrium. The profiles are plotted on a tephigram and the dash-dotted curve represents parcel ascent from the surface ignoring entrainment.*

260 hPa, the temperature profile closely follows the moist adiabatic lapse rate and the freezing level is located at about 570 hPa. The temperature profile becomes absolutely stable from 260 hPa and there is a strong inversion at about 140 hPa which indicates the level of thermal tropopause.

The convective inhibition (CIN) is about 11.6 J kg^{-1} while the convective available

potential energy (CAPE) for an undiluted parcel is about 1981 J kg^{-1}. The values of CIN and CAPE are comparable to the typical values calculated using soundings collected by the National Oceanic and Atmospheric (NOAA) Gulfstream-IV (G-IV) aircraft within 1000 km of the center of tropical cyclones (Molinari et al., 2012). This value of CAPE is close to the value calculated using soundings from the Deep-Broad convection but it is higher than the values calculated using soundings from the Deep-Narrow and shallow convection collected during the TOGA-COARE (Kingsmill and Houze, 1999).

A parcel ascent (dashed dotted curve) from the surface, conserving its potential temperature and specific humidity reaches the lifting condensation level at about 960 hPa. It reaches the level of free convection at about 940 hPa. By ignoring the dilution of the parcel due to entrainment of the relatively dry and cool environmental air, the parcel continues to ascend following the moist adiabatic lapse rate and stops once it becomes colder than the environment at about 115 hPa. The level at 115 hPa is called the level of neutral buoyancy (LNB) and it corresponds to the level of final detrainment of an undiluted convective parcel.

In reality, turbulence mixing processes occurring at the edges of convective clouds promote their dilution through the penetration of dry and cool environmental air. This dilution process encourages the convective towers to undergo their final detrainment well below or at the level of thermal tropopause (strong inversion at about 140 hPa. See Figure 3.6) which in this study is located at 25 hPa below the LNB.

The total changes in the potential temperature and specific humidity are written as:

$$\frac{d\theta}{dt} = \left(\frac{\partial\theta}{\partial t}\right)_{adv} + \left(\frac{\partial\theta}{\partial t}\right)_{\mu} + \left(\frac{\partial\theta}{\partial t}\right)_{rad} \tag{3.30}$$

and

$$\frac{dq}{dt} = \left(\frac{\partial q}{\partial t}\right)_{adv} + \left(\frac{\partial q}{\partial t}\right)_{\mu} \tag{3.31}$$

respectively. The terms on the right-hand side represent the tendencies due to advection and microphysics in addition to the tendency due to radiation in the potential temperature tendency equation (Equation 3.30). The tendency of temperature due to advection

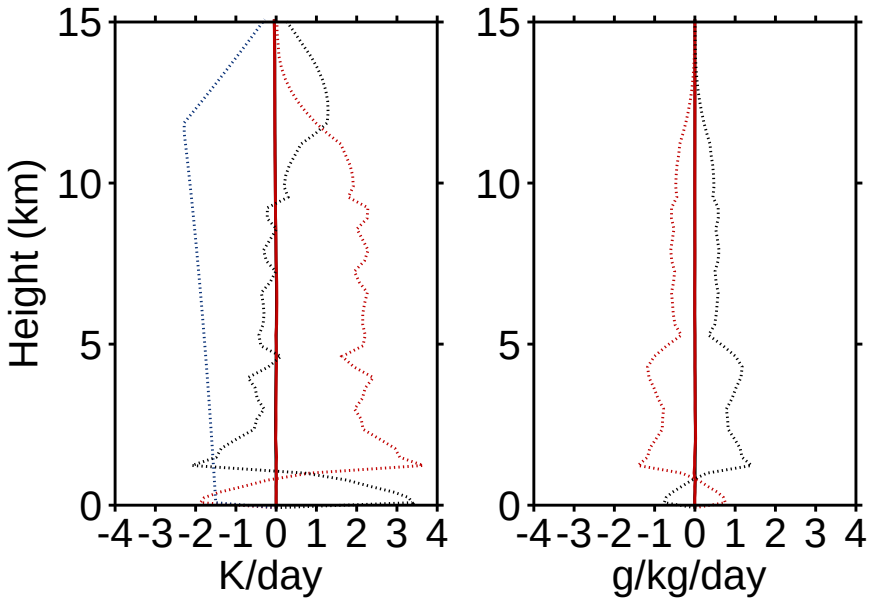

Figure 3.7 *Domain-mean temperature (left-hand panel) and moisture (right-hand panel) tendency profiles obtained at equilibrium. The changes in temperature ($\frac{d\theta}{dt}$) and specific humidity ($\frac{dq}{dt}$) (solid black curves) are almost indistinguishable from the sum (solid red curves) of contributions from microphysics (dotted red curves), advection (dotted black curves) and radiation (dotted blue curves).*

includes the tendency due to subgrid, which as diagnosed by the model includes the surface sensible heat flux. Similarly, the tendency of humidity due to advection includes the tendency due to subgrid, which as diagnosed by the model includes the surface latent heat flux. Figure 3.7 show the mean potential temperature and specific humidity tendency profiles at equilibrium. At each model level, the tendencies due to advection and microphysics nearly balance each other in the moisture budget (Equation 3.31) while their sum nearly balances the prescribed radiative cooling in the heat budget (Equation 3.30). The tendency profiles shows a free tropospheric heating and drying in response to precipitating convection and a low level cooling and moistening in response to surface evaporation and non-precipitating shallow convection.

Figure 3.8 shows the profiles at equilibrium of dry static energy, moist static energy and relative humidity which respect to liquid water. The dry and moist static energies are

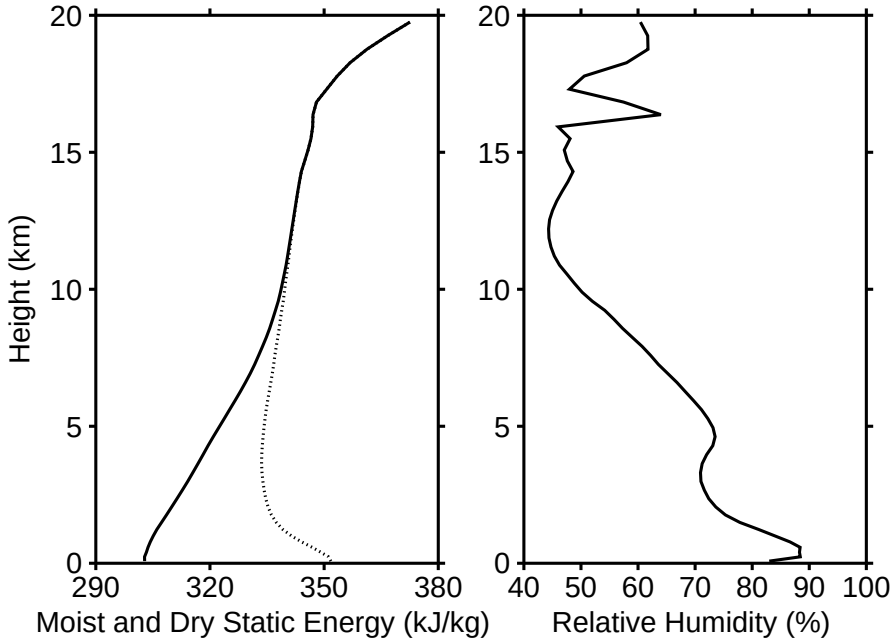

Figure 3.8 *Domain-mean mean profiles at equilibrium of dry static energy (solid curve on the left-hand side), moist static energy (dotted curve) and relative humidity (right-hand side).*

computed as:

$$\mathrm{s} = C_p T + gz \tag{3.32}$$

and

$$\mathrm{h} = \mathrm{s} + Lq_v \tag{3.33}$$

respectively. s is the sum of enthalpy (first term on the right-hand side of Equation 3.32) and potential energy (second term) and h is the sum of s and the latent energy (second term on the right-hand side of Equation 3.33). s is approximately conserved during dry adiabatic ascent while h is approximately conserved during both dry and moist adiabatic ascents. s increases with height. h decreases with height from the surface and reaches its minimum value at about 4 km. From 4 km, it starts to increase with height. h is greater than s in the lower and middle troposphere and it becomes indistinguishable from s above 12 km where humidity is close to zero.

The near surface layer is very moist with relative humidity close to 90%. This ratio

sharply decreases with height and reaches 70% at about 3 km and there is a secondary maximum at about 5 km; a level near the freezing level identified on the tephigram (see Figure 3.6). This relative humidity profile agrees fairly well with observations although the minimum value of relative humidity is at 12 km compared to 7 km in the observed soundings of Liu et al. (1991) and Sun and Lindzen (1993).

3.10.2 Statistical description of convection

In this section, attention is given to the structure of convection. This is done by examining the statistical distribution of convective cloud along with the convective mass flux and the fractional area covered by convection.

The vertical distribution of cloud is examined using the cloud fraction defined as the sum of grid points where the mixing ratio of cloud (water and ice) exceeds 10^{-6} kg kg^{-1} normalized by the total number of grid points. This cloud threshold is somewhat arbitrary and was applied by Wang and Sobel (2011) and many others. In contrast,Tompkins and

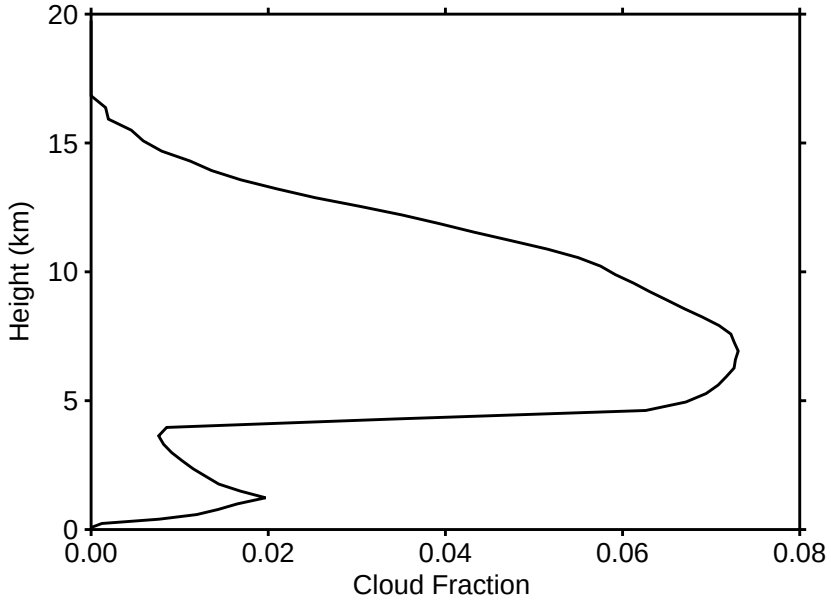

Figure 3.9 *Domain-mean cloud fraction profile at RCE.*

Craig (1998a) defined cloud as the sum of all the hydrometeors (cloud water, rain, snow, ice and graupel) and applied a threshold of 5×10^{-6} kg kg^{-1} (5 times greater than the threshold applied here) to identify cloudy grid points.

Cloud fraction is shown in Figure 3.9 and has a bimodal distribution. The first mode is centred at about 1.5 km and represents fair weather cumulus clouds resulting from shallow convective cells. The second and broadest mode extends from 4 to 15 km and it is centred at about 7 km. This mode represents both congestus and deep clouds resulting from intermediate and deep convective cells respectively. There is an evidence of a mode of intermediate cloud near the freezing level located at about 5 km. However, the mode of intermediate cloud is not clearly separated from the those of shallow and deep clouds as it is in the studies of Johnson et al. (1999). The mode of intermediate and deep clouds covers about 7% of the domain and it extends at levels which correspond to the levels of enhancement of humidity identified on the tephigram. These values of cloud fraction are consistent with those obtained by Tompkins and Craig (1998a) except below 3 km where cloud fraction here is relatively small and goes to zero as the height approaches zero. This is due to the definition of cloud which here does not include rain in the identification of cloudy grid points as is the case in the analysis of Tompkins and Craig (1998a).

The structure of convection is examined further using the fractional area covered by strong and cloudy updrafts, σ_u, and strong convective downdrafts, σ_d, along with the mass flux of strong and cloudy updrafts, M_u, and strong convective downdrafts M_d. The strong updrafts and downdrafts cores are defined using the vertical velocity criteria $w > 1$ m s^{-1}and $w < -1$ m s^{-1} respectively. These vertical velocity criteria are based on the aircraft observational study of Zipser and LeMone (1980). They are arbitrary and have been used as a standard definition in CRM studies. Similarly to Robe and Emanuel (1996), an additional criterion is applied to estimate M_u. That is a lower bound of 10^{-6} kg kg^{-1} on the mixing ratio of cloud (cloud water and ice) content in order to consider only the strong buoyant and cloudy updrafts.

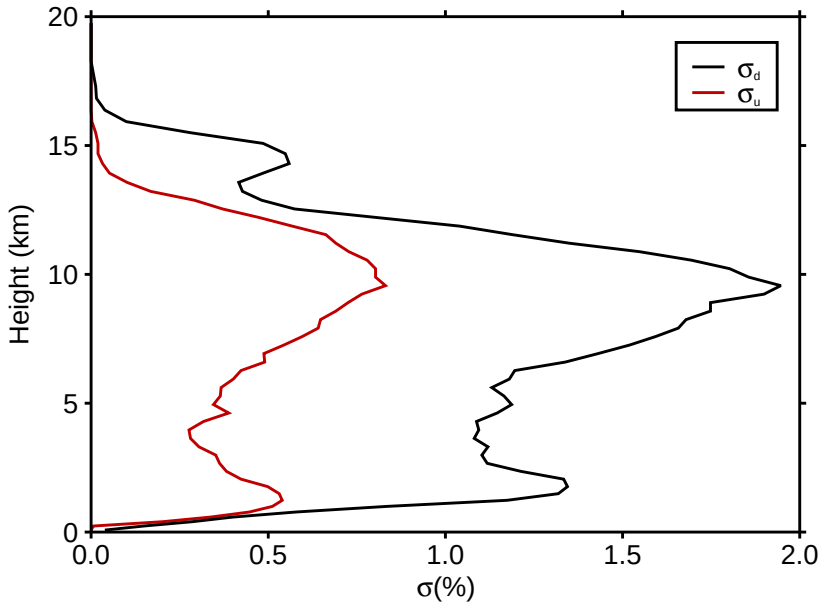

Figure 3.10 *Fractional area covered by strong and cloudy updrafts (red curve) an strong convective downdrafts (black curve) as a function of height.*

From the above criteria, σ_u and M_u are calculated as:

$$\sigma_u = \sum_{q_c > 10^{-6} kg/kg, w > 1 m/s} N_j / N \tag{3.34}$$

and

$$M_u = \sigma_u \sum_{q_c > 10^{-6} kg/kg, w > 1 m/s} \rho_j w_j \tag{3.35}$$

while σ_d and M_d are calculated as

$$\sigma_d = \sum_{w < -1 m/s} N_j / N \tag{3.36}$$

and

$$M_d = \sigma_d \sum_{w < -1 m/s} \rho_j w_j \tag{3.37}$$

with no lower bound applied on cloud content in order to count for both clear and cloudy grid points with strong descent. ρ is the density, N_j indicates the grid points and N is the total number of grid boxes.

Figure 3.10 shows σ_u and σ_d as a function of height. There are two convective modes within the free troposphere. The 2D CRM simulations can have strong gravity waves which could artificially increase the fractional areas of strong updrafts and downdrafts. In this study, σ_d lies between 1% and 2% for the whole of the free troposphere. In response to the cloud criteria applied to define cloudy buoyant updrafts, σ_u is considerably reduced compared to σ_d. It values lies between 0.5% and 1%. However, these range of values of σ_d and σ_u are distinctively larger than those obtained in the experiments that used the 3D numerical model (Robe and Emanuel, 1996; Tompkins and Craig, 1998a).

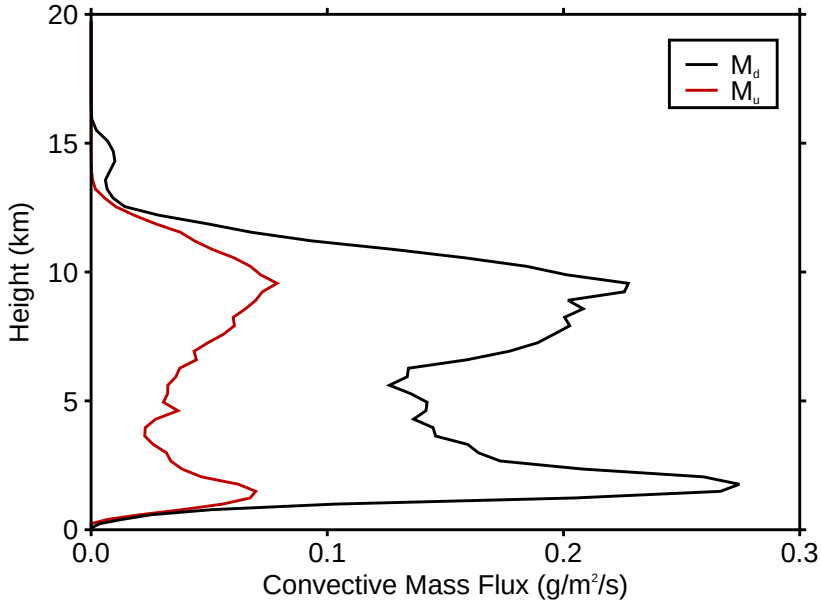

Figure 3.11 *Convective mass flux of strong and cloudy updrafts (red curve) and strong downdrafts (black curve) as a function of height. The mass flux of strong downdrafts is the absolute value.*

Figure 3.11 shows M_u and M_d as a function of height. The mass flux of strong downdrafts is the absolute value. There is a coexistence of shallow, intermediate and deep convective towers together with the descending clear environmental air. For the whole of the free troposphere, M_d is larger than M_u. However, further investigation revealed that M_u is larger than M_d if the former is estimated from both clear and cloudy grid points (results not shown). M_u peaks at about 1.5 km and at about 10 km. M_d and σ_d peak at heights near to those where M_u and σ_u do respectively. This feature clearly suggests the

importance of the outflow from convective cloud feeding downdrafts which develop as hydrometeor evaporates when falling through the underlying unsaturated air. Convection induces subsidence motions which dry the troposphere through downward advection of upper-tropospheric dry air. However, the re-evaporation of hydrometeors provided by deep convection also recharges moisture within the free troposphere (Sun and Lindzen, 1993).

3.10.3 Sensitivity to the SST

To investigate the sensitivity to the SST, a series of additional RCE simulations are performed with SSTs of 301.7, 303.7, 304.7 and 305.7 K. Each simulation is run for 40 days and is initialized from the potential temperature and humidity profiles shown in Figure 3.2. For all these simulations, the quasi-steady state in which the heating induced by precipitation balances the prescribed radiative cooling is achieved before day 20. An average over days 20 to 40 are used to define the model state and statistics at RCE. In each of these RCE simulations including the RCE simulations performed with SST of 302.7 K, the temperature profile obtained at equilibrium closely follow the moist adiabatic lapse rate in the middle and upper troposphere (see Figure 3.6 for the RCE simulation with SST of 302.7 K).

The RCE simulation performed with an SST of 302.7 K and described above will be henceforth be referred as the uncoupled control run. Its corresponding potential temperature and specific humidity profiles at equilibrium are used to define the reference column profiles in WTG experiments, as well as providing initial conditions for some of the WTG experiments in the next chapters.

Figure 3.12 shows the deviation from the uncoupled control profiles for the RCE experiments with SSTs of 301.7, 303.7, 304.7 and 305.7 K. The higher the SST, the warmer and moister is the column at RCE. The change in gradient which occurs below 5 km reflects the freezing level. However, the height of the freezing level increases with

the SST. It is located at about 590, 570,550,535 and 510 hPa for the RCE simulations performed with an SST of 301.7, 302.7, 303.7, 304.7 and 305.7 K respectively. As a result, the change in gradient occurs at a height which increases with the SST. The profiles at equilibrium obtained in these simulations are used to provide a set of additional initial profiles for the WTG experiments.

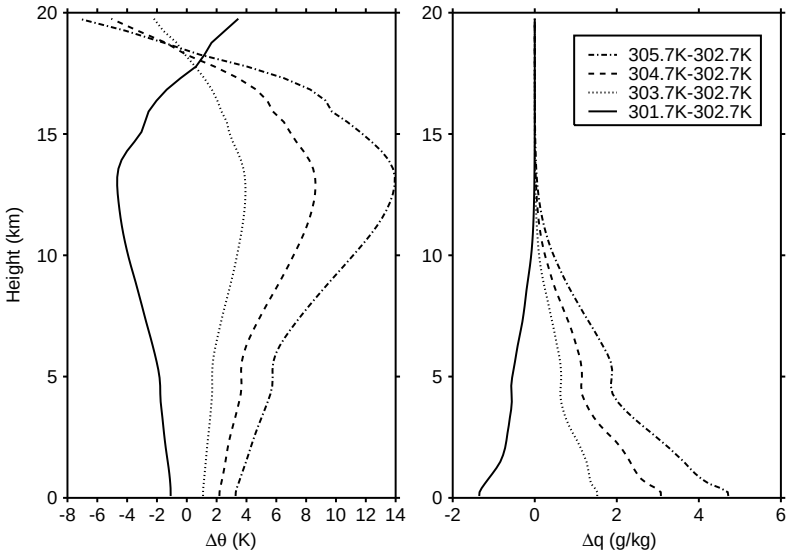

Figure 3.12 *Deviations from the control integration RCE profiles of potential temperature (left) and specific humidity (right) for the RCE simulations with SSTs of* 301.7*,* 303.7*,* 304.7 *and* 305.7 *K.*

3.11 Conclusions

This chapter describes the LEM at version 2.4 of the UK Meteorological Office and discusses its approach to the RCE state. This model is appropriate to simulate cloud scales while small scale processes which have less effect in the development of clouds are parameterized.

The model was run in CRM mode with a fixed radiative cooling profile. A two dimensional domain is used with size large enough to simulate an ensemble of convective cells

along with the compensating subsidence motions and small enough to prevent mesoscale organization of convection. A domain-mean wind speed is applied in the across-domain direction to increase surface evaporation. There is no wind shear in the along-domain direction to prevent the formation of squall lines. The domain-mean wind speed in the along-domain direction is relaxed towards zero. There are no large-scale forcing terms and convection is forced only by the prescribed radiative cooling of the column which is balanced by fluxes of heat and moisture from the surface.

The model is run for 40 days. The adjustment timescale to the prescribed radiative forcing is about ten days in terms of vertically averaged quantities and a quasi-steady state is reached at each model level before day 20. Average over days 20 to 40 is used to define the mean state profiles at RCE. The thermodynamic and dynamics profiles at equilibrium are comparable to the profiles obtained in previous RCE studies although the cloud profile at equilibrium does not show a separate mode of intermediate clouds in contrast with the result of Johnson et al. (1999). Finally, the sensitivity to the SST is investigated; the column is found to become warmer and moister as the SST is increased.

Chapter 4:
WTG calculations over uniform surface conditions

4.1 Introduction

Chapter 3 describes the Cloud-Resolving model (CRM) used in this study. It shows the simulations performed at radiative-convective equilibrium (RCE). In such simulations, convection is explicitly simulated but, is disconnected from any evolution of the large-scale environmental flow. In this chapter convective development is connected to the evolution of the large-scale environmental flow using the weak-temperature gradient (WTG) approximation detailed in chapter 2.

This chapter is organized as follows. Section 4.2 gives the details of the implementation of the WTG calculation in the CRM. Section 4.3 shows the results from simulations performed with a CRM coupled to a reference column via the WTG approximation while Section 4.4 shows the results from simulations performed on two CRMs coupled together via the same WTG approximation. Conclusions are presented in Section 4.5.

4.2 Implementation of the WTG approximation

The WTG approximation described in Section 2.4 of Chapter 2 is used to modify the CRM. CRM is a height model and its levels are staggered. The large-scale vertical ve-

locities are calculated at half levels. Their expressions are

$$\overline{w}_1 = \frac{f(z)}{\tau} \frac{\overline{\theta}_1 - \overline{\theta}_2}{\frac{\partial \overline{\theta}_1}{\partial z} + \frac{1-\varepsilon}{\varepsilon} \frac{\partial \overline{\theta}_2}{\partial z}} \tag{4.1}$$

and

$$\overline{w}_2 = -\frac{f(z)}{\tau} \frac{\overline{\theta}_1 - \overline{\theta}_2}{\frac{\partial \overline{\theta}_2}{\partial z} + \frac{\varepsilon}{1-\varepsilon} \frac{\partial \overline{\theta}_1}{\partial z}} \tag{4.2}$$

for columns 1 and 2 respectively. $f(z)$ can be either

$$f(z) = f_1(z) = 1 \quad \text{for } z_{\text{BL}} \leqslant z \leqslant z_{\text{top}} \tag{4.3}$$

or

$$f(z) = f_2(z) = \begin{cases} \sin(\frac{\pi z}{z_t}) & \text{for } z_{\text{BL}} \leqslant z \leqslant z_t \\ 0 & \text{for } z > z_t \end{cases} \tag{4.4}$$

where z_{top} is the top of the domain, z_{BL} is a level a little above the boundary layer and z_t is the level near the tropopause. Here, $z_{\text{top}} \approx 20$ km, $z_{\text{BL}} \approx 1.5$ km and $z_t \approx 15$ km. As described in Section 2.5 of Chapter 2, the WTG approximation is not valid in the boundary layer. There, the vertical velocities are calculated as the linear interpolation in height from the diagnosed WTG vertical velocity at a level z_{BL} to a prescribed value of zero at the surface.

The change in the horizontal domain-mean quantity $\overline{\chi}$ due to the WTG-derived large-scale circulation is calculated in the z-coordinate as:

$$\left(\frac{\partial \overline{\chi}_1}{\partial t}\right)_{\text{WTG}} = \frac{\chi_*}{\overline{\rho}} \frac{\partial}{\partial z}(\overline{\rho} \overline{w}_1^{\text{WTG}}) - \frac{1}{\overline{\rho}} \frac{\partial}{\partial z}(\overline{\rho} \overline{w}_1^{\text{WTG}} \overline{\chi}_1) \tag{4.5}$$

and similarly for $\overline{\chi}_2$.

A full description of the numerical computation of Equations 4.1, 4.2 and 4.5 in the CRM is presented in Appendix C.

4.3 Reference column approach

This section shows results from applying a reference column approach as in Raymond and Zeng (2005) for example. In this approach one of the columns (the reference column)

is held fixed and is assumed to be infinitely large. Its potential temperature and specific humidity profiles are those previously obtained at equilibrium in the RCE simulation of the uncoupled CRM with an SST of 302.7 K (see the profiles shown in Figure 3.6 of chapter 3). This RCE simulation of the uncoupled CRM with an SST of 302.7 K will be henceforth referred to as the control run. The other column (the test column) is allowed to evolve and is coupled to the infinitely large reference column via the WTG derived large-scale circulation. Thus, its domain-mean free tropospheric potential temperature profile is constrained to relax toward the target profile prescribed by the reference column state. Here the free troposphere is defined somewhat arbitrarily as levels between $z_{\rm BL}$ and $z_{\rm t}$.

The RCE reference profiles are also used to initialize the test column. The WTG adjustment timescale τ is chosen to be 2 h. An approximate indication of the associated spatial scale for the circulation is that a gravity wave moving at 50 m s^{-1} (the phase speed of a typical gravity wave front resulting from deep convection) would travel 360 km in this time. The simulation is run for 40 days with the SST and surface wind speed in the test column set equal to those of the RCE reference column; 302.7 K and 5 m s^{-1} respectively. The WTG calculations are performed on a coupling timestep, $dt_{\rm wtg}$, of 10 minutes. It is twice the value used in the WTG simulations that used the simple SCM in Chapter 2. However, as already mentioned in Chapter 2, the choice of $dt_{\rm wtg}$ is essentially arbitrary and the quality of the results are insensitive to the choice of $dt_{\rm wtg}$ with value ranging from 0.5 to 30 minutes. Experiments with both uniform and sinusoidal WTG adjustment rate profiles (Eqs. 4.3 and 4.4) have been used and lead to qualitatively similar results. The results presented here are those obtained from simulations performed with the uniform WTG adjustment rate profile.

Figure 4.1 shows the time series of column-integrated water vapor (CWV) (solid curve) and daily mean rain rate (dotted curve) obtained in the test column. CWV decreases from its initial value equal to the RCE reference value, and reaches a drier quasi-steady state at around day 20. The mean rain rate averaged over days 20 to 40 is 1.99 mm d^{-1} as compared to 4.46 mm d^{-1} of surface evaporation. This mean rain rate is

much lower than that during the first 20 days of the integration and much lower than the 4.77 mm d^{-1} obtained at RCE in the uncoupled control run. Despite the fact that the test column is initialized to have the same characteristics (thermodynamic profiles, surface forcing, radiative cooling etc.) as the reference column, the equilibrium state obtained by applying the WTG approximation using a reference column clearly differs from the RCE state.

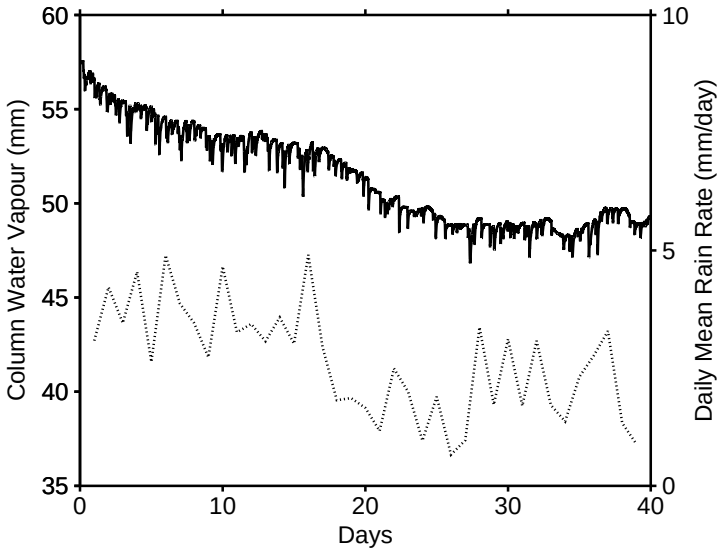

Figure 4.1 *Time series over* 40 *days of column-integrated water vapor (solid line, scale on left axis) and daily-mean rain rate (dotted line, scale on right axis) from the reference-column simulation performed with* $\tau = 2$ *h and the test column initialized with reference state profiles.*

The test column precipitates less than it evaporates. The net imbalance of precipitation minus evaporation must be balanced by a moisture sink due to the WTG-diagnosed large-scale circulation which corresponds to descent in the test column with convergence aloft and divergence of moist air below.

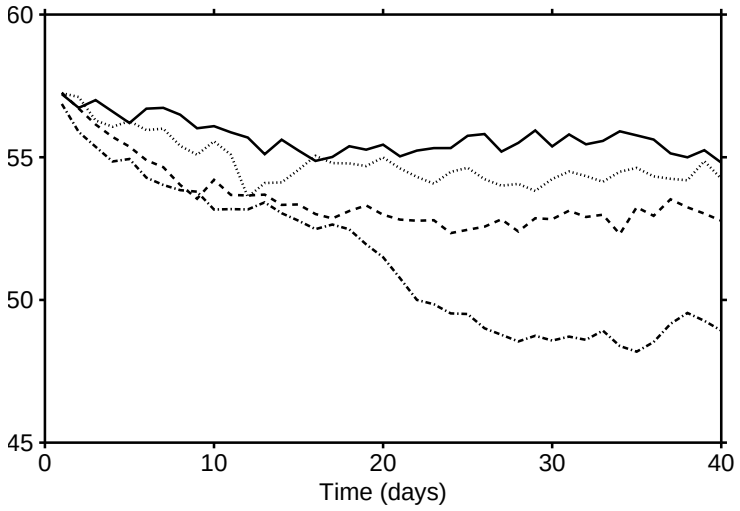

Figure 4.2 *Time series of the daily-mean column-integrated water vapor in the reference-column simulation performed with* $\tau = 2$ *h (dash-dotted),* $\tau = 6$ *h (dashed),* $\tau = 12$ *h (dotted),* $\tau = 24$ *h (solid) and the test column initialized with reference state profiles. The results are shown for the entire integration.*

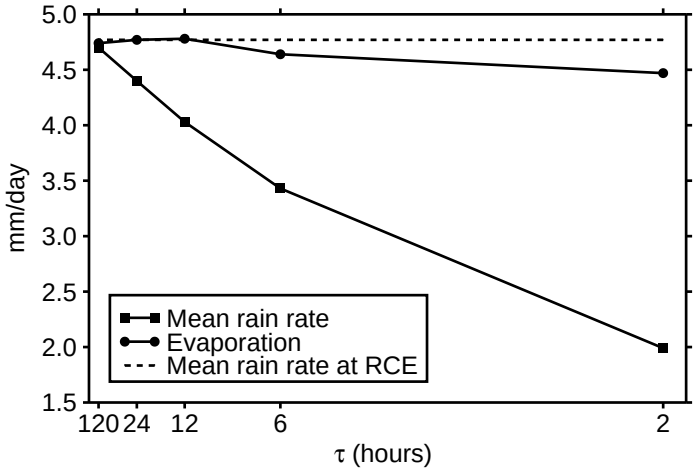

Figure 4.3 *Mean rain rate (squares) and mean surface evaporation (circles) at equilibrium for the simulations performed with* $\tau = 2,\ 6,\ 12,\ 24$ *and* 120 *h and the test column initialized with reference state profiles. The dashed horizontal line represents the mean rain rate obtained at RCE in the uncoupled control integration. Note that the horizontal axis is scaled as the reciprocal of* τ*.*

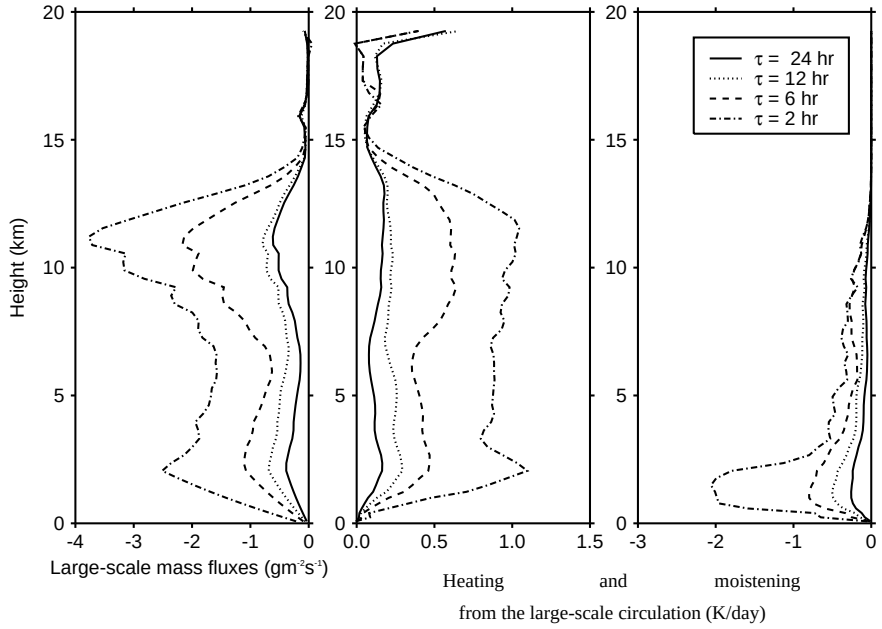

Figure 4.4 *Large-scale mass fluxes, $\overline{\rho}\overline{w}$ (left), heating (middle) and moistening rates (right) in the test column due to the large-scale circulation. The results are obtained by averaging the last* 20 *days of data from simulations performed with various values of* τ*:* 2 *h (dash–dotted),* 6 *h (dashed),* 12 *h (dotted) and* 24 *h (solid). The test column was initialized with reference state profiles in all cases. The large-scale mass flux is computed as the product of the density and the WTG-diagnosed large-scale vertical velocity.*

4.3.1 Sensitivity to WTG adjustment timescale

The sensitivity to the WTG adjustment timescale has been investigated with additional simulations using the WTG coupling timescales of $\tau = 6$, 12, 24 and 120 h. The spatial scales associated with these values of τ are: 1080, 2160, 4320 and 21600 km respectively. Figure 4.2 shows the time series of daily-mean CWV for the test column in the simulations performed with $\tau = 2$, 6, 12, 24 h. In each of these simulations, the CWV decreases from its initial RCE reference value and the test column reaches a new quasi-steady state which is drier compared to the RCE reference state. However, the CWV increases with increasing τ. The corresponding mean rain rates (squares) and surface evaporation (circles) at equilibrium in each of these simulations, and in the simulation performed with

$\tau = 120$ h, are plotted in Figure 4.3. As τ is increased, the mean rain rate increases towards the RCE reference value obtained in the uncoupled control run (indicated by the dashed horizontal line). For the simulation with $\tau = 120$ h, the mean rain rate and surface evaporation are not statistically different from the control run. For all other simulations, the test column adjusts to a new, distinct equilibrium with a significantly lower CWV and lower mean rain rate at equilibrium. The equilibrium state obtained in these simulations with the test column coupled to a reference column configuration shows a clear asymmetry between the test and the reference columns, a situation which is maintained by a large-scale circulation having its descending branch in the test column. For relatively weak WTG coupling the mean rain rate appears to reduce approximately linearly with the inverse of τ, i.e., with the WTG adjustment rate. For shorter coupling timescales this linear relationship appears to break down. Surface evaporation changes are much smaller than the precipitation changes with the only significant (compared to the variability of the daily mean at RCE) reductions in surface evaporation occurring for the simulations with $\tau = 2$ and 6 h.

The large-scale circulation mass fluxes and the heating and the moistening rates from the large-scale circulation are shown respectively on the left, middle and right panels of Figure 4.4. The large-scale mass flux is computed as the density times the large-scale vertical velocity. The profiles are those obtained at equilibrium in the simulations performed with $\tau = 2$, 6, 12 and 24 h. They correspond to subsidence drying and warming occurring within the test column, balancing the excess of evaporation over precipitation and the difference between the convective heating and the imposed radiative cooling. The large-scale mass flux profiles are large in the upper troposphere as a result of the low static stability there as shown by the domain-mean dry static energy profile obtained at equilibrium in the uncoupled control run (see Figure 3.8 of Chapter 3). Note that the relatively uniform heating profile through much of the free troposphere implies a relatively uniform potential temperature difference between the test and reference columns. The drying profiles show a peak in the lower troposphere where both the humidity and the horizontal divergence are large. The energy budget in the test column is closed by the

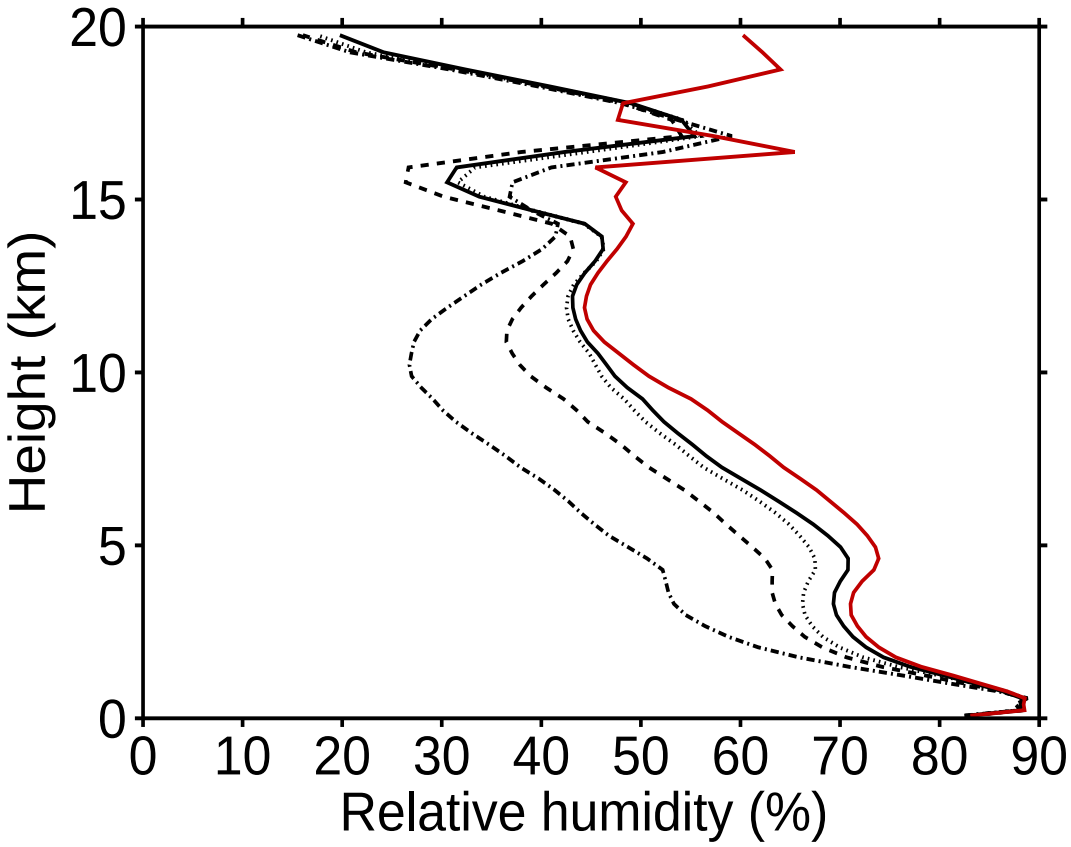

Figure 4.5 *Mean relative humidity profiles at equilibrium. These profiles are at equilibrium in the same set of simulations as in Figure 4.4 and they are compared to the mean relative humidity profile obtained at RCE of the control run (solid red curve).*

sources due to the large-scale circulation. However, energy and moisture transported out of the test column do not affect the reference column. The significance of this point for the large-scale circulation that develops in homogeneous conditions is discussed in Section 4.4. The presence of a large-scale circulation at equilibrium with descent in the test column is insensitive to the choice of the WTG adjustment rate profile. A similar circulation with the same sense has also been seen previously in similar experiments with other models (e.g. Raymond and Zeng, 2005; Raymond, 2007; Sessions et al., 2010), although other models do not produce a circulation under homogeneous conditions (e.g. Sobel and Bretherton, 2000; Wang and Sobel, 2011).

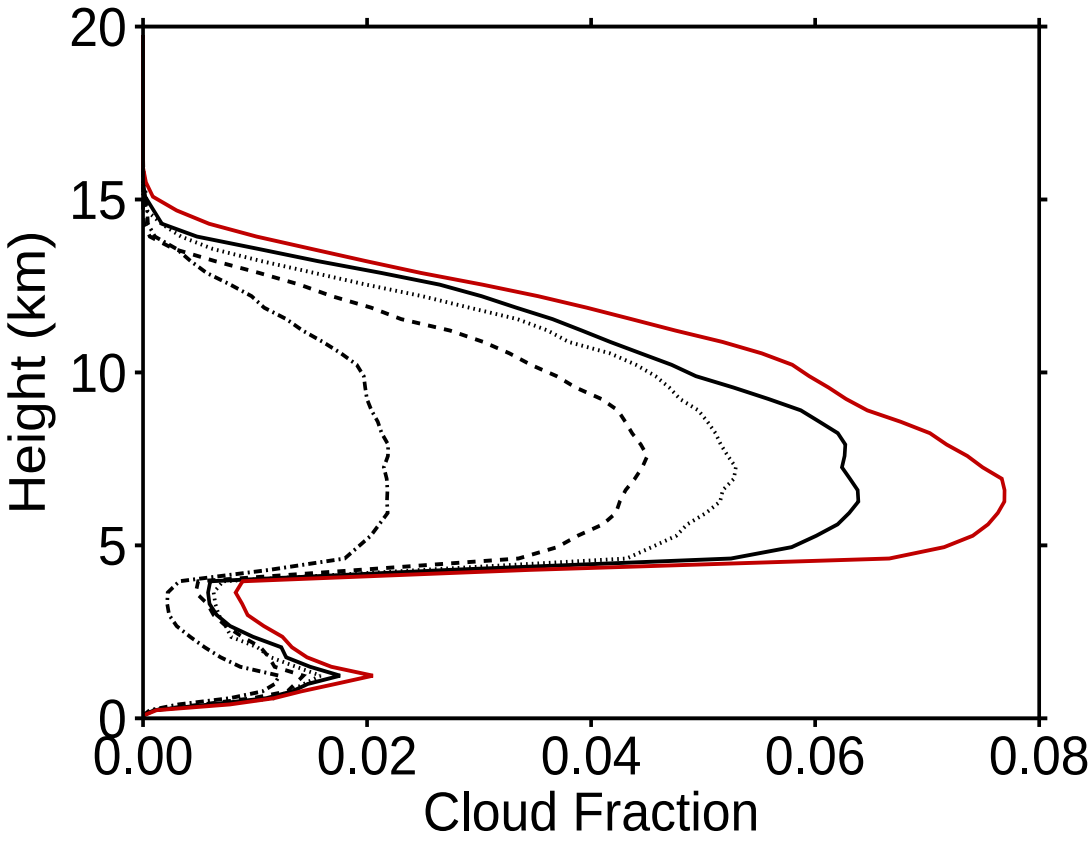

Figure 4.6 *Mean cloud fraction profiles at equilibrium in the same set of reference column simulations as in Figure 4.4. These cloud fraction profiles are compared to the mean cloud fraction profile obtained at RCE of the uncoupled control run (solid red curve).*

Figures 4.5 to 4.7 show the mean relative humidity, cloud fraction and vertical velocity variance profiles at equilibrium for the same reference column simulations as in Figure 4.4. The profiles are compared to the mean profiles obtained at RCE of the control integration (solid red curve). Here, the total cloud fraction is estimated using the same definition as in Chapter 3. The shape of the profiles at equilibrium are similar and are similar to the shape of the profiles obtained at RCE of the uncoupled control run. The relative humidity profiles show a secondary maximum at about 5 km. As described in section 3.8.1 of Chapter 3, this secondary maximum reflects the freezing level. The height of the freezing level decreases as τ is decreased. In addition, the cloud fraction,

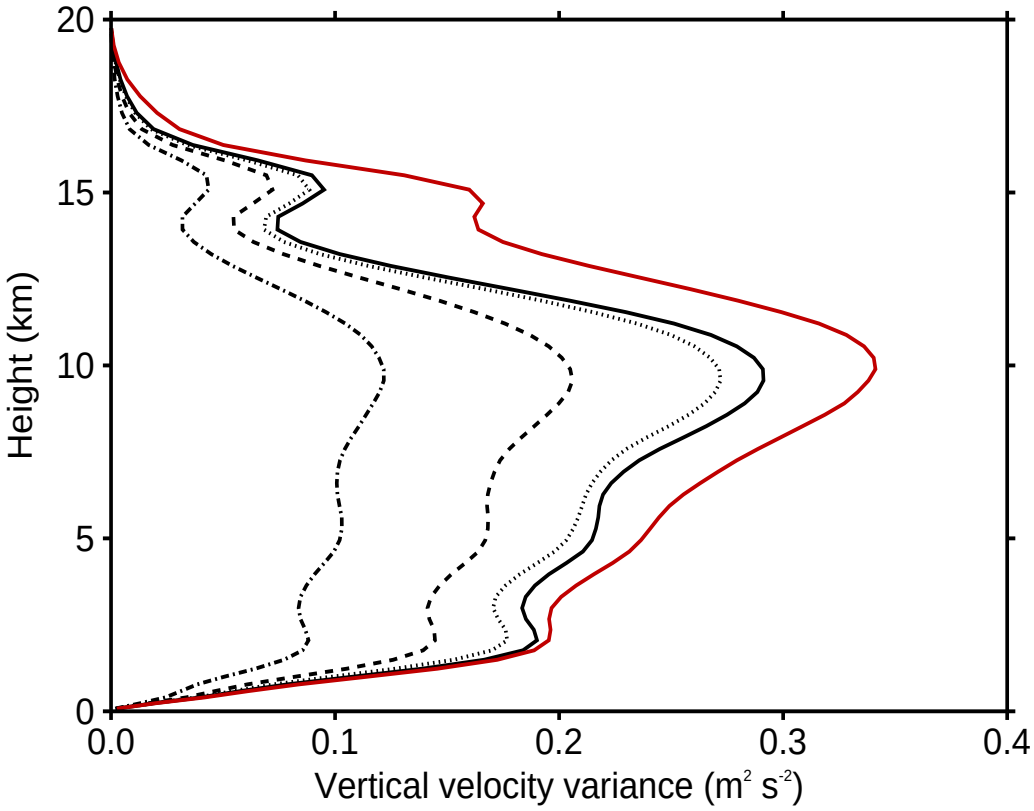

Figure 4.7 *Mean vertical velocity variance profiles at equilibrium in the same set of reference column simulations as in Figure 4.4. These profiles are compared with the mean vertical velocity variance profile obtained at RCE of the uncoupled control run (solid red curve).*

relative humidity and vertical velocity variance decrease as τ does but for all these simulations, the strength of the circulation that develops is not strong enough to entirely suppress deep convection over the test column and the system adjusts the test column to a new, distinct equilibrium state with a reduced relative humidity, convective activity and cloud fraction compared to the RCE reference state. As τ is increased, the relative humidity, the vertical velocity variance and total cloud mixing ratio increase toward the RCE reference values. Note that the reference column approach reaches an RCE state for a large value of the WTG adjustment time scale i.e., $\tau = 5$ days, so that the mean profiles at equilibrium are not statistically distinguishable from those obtained in the uncoupled

control integration (results not shown).

However, although there are significant variations in the mean CWV at equilibrium with τ, the near surface humidity remains relatively unchanged. Therefore the simulations maintain a well-mixed boundary layer close to the surface where the large-scale circulation is inactive. The use of a mean horizontal wind (normal to the model domain) in the surface flux calculations means that the surface fluxes are relatively insensitive to the reduction in near-surface perturbation winds associated with the reduction in convective activity.

4.3.2 Sensitivity to the initial conditions

To examine the sensitivity of the equilibrium state to the initial conditions, a series of simulations is performed in which the test column is initialized from RCE profiles previously obtained for other values of SST, ranging from 301.7 to 305.7 K. The WTG adjustment timescale of 2 h is used for all these simulations. The initial states include the complete two dimensional flow field and active spun-up convection from the uncoupled control run. The initial profiles are shown in Figure 3.12 of chapter 3. Figure 4.8 shows the time series of daily-mean rain rate from the simulations initialized with the RCE profiles previously obtained at 301.7 K, 302.7 K (i.e., the integration described in Section 4.3) and 304.7 K. Respectively, these results provide examples of the behavior found for a larger set of simulations with the test column initialized colder and drier than the reference profiles, equal to the reference profile, and warmer and moister than the reference profiles.

Simulations in which the test column is initialized with the RCE profiles for SSTs colder than the control integration immediately develop a large-scale circulation with descent in the test column, as would be expected from the difference between the initial and reference potential temperature profiles. The mean rain rate remains below that of the uncoupled control integration throughout the simulation and the final equilibrium state is

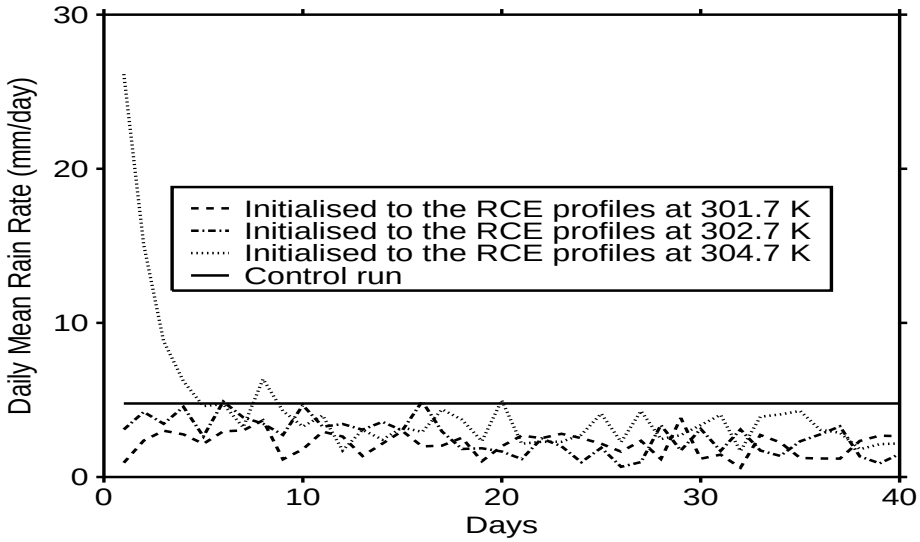

Figure 4.8 *Time series over* 40 *days of daily-mean rain rate from reference column simulations performed with* $\tau = 2$ *h. The test column was initialized with RCE profiles previously obtained for SSTs of* 301.7 *K (dashed),* 302.7 *K (dash–dotted) and* 304.7 *K (dotted). The solid horizontal line represents the mean rain rate obtained at RCE in the uncoupled control run, with SST of* 302.7 *K.*

very similar to that obtained when the integration is initialized with the reference profiles. Figure 4.9 shows the heating and moistening source due to the large-scale circulation averaged over days 0 to 4 and 30 to 40 for the same integrations as in Figure 4.8. The heating and moistening rates in the cold initialization case are very similar to those for the integration initialized with the reference profiles in both the early stages of the simulation and at equilibrium. This indicates that the integration initialized with the reference profiles develops a large-scale descent within the first four days.

Simulations in which the test column is initialized with the profiles warmer and moister than those of the RCE reference column initially develop a large-scale circulation with ascent in the test column as would be expected from the initial positive potential temperature difference between the columns. The time evolution of the daily-mean potential temperature and specific humidity horizontal differences between the columns are shown in Figure 4.10. The difference is computed as the difference between the daily-mean pro-

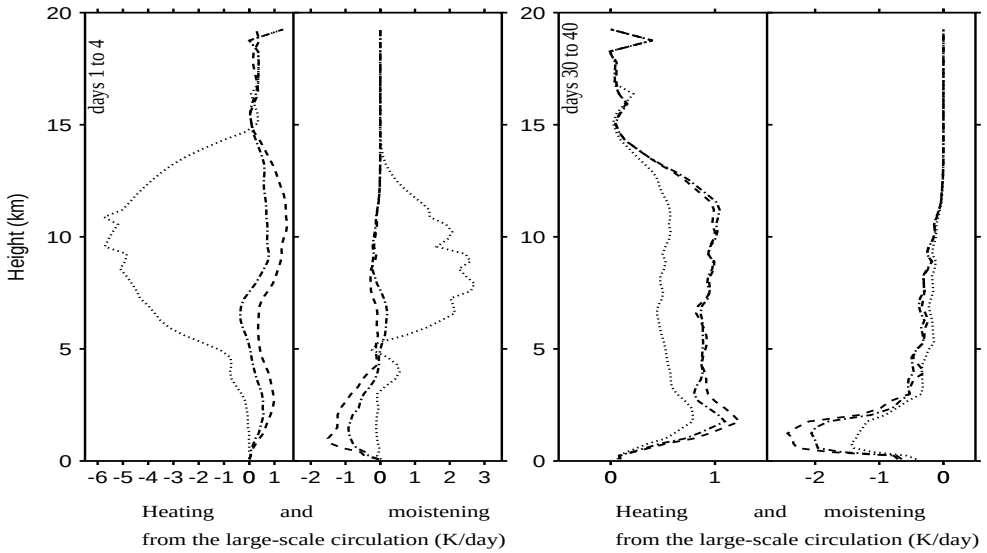

Figure 4.9 *Heating and moistening rates in the test column due to the large-scale circulation. The results are obtained by averaging from days* 1 *to* 4 *(left-hand panel) and from days* 30 *to* 40 *(right-hand panel). Line definitions are as in Figure 4.8.*

files in the test column and the RCE profiles of the uncoupled control run. These results are shown for the simulation in which the test column is initialized with the RCE profiles at 304.7 K. The potential temperature and specific humidity differences rapidly decrease but remain positive throughout most of the free troposphere until day 5. The initial rain rate exceeds that in the RCE reference column in response to the initial large-scale ascent diagnosed in the test column. The test column precipitation decreases rapidly as the potential temperature difference decreases, such that (by day 5 in the example shown in Figure 4.8) it quickly becomes similar to that in the control integration. However, the test column precipitation continues to drop until a large-scale descent is established in the test column by day 9 when the potential temperature difference becomes negative throughout the troposphere. This large-scale descent progressively dries the test column and by day 30 a new quasi-equilibrium state is established in which the precipitation and the tropospheric humidity in test column are significantly lower than that of the control integration and which resembles the integrations initialized with the reference column

profiles or colder.

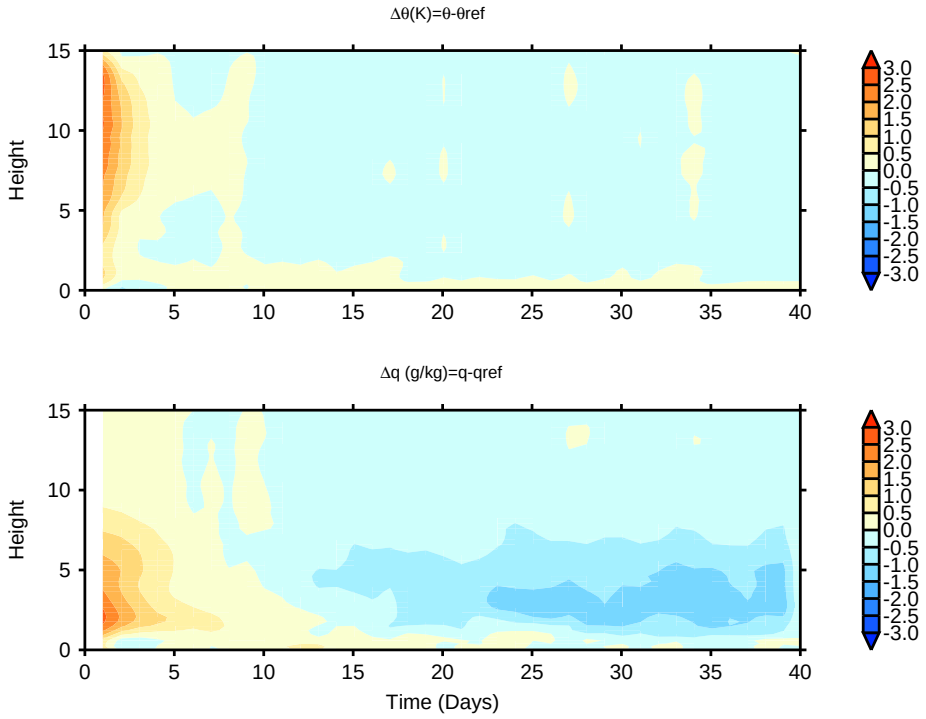

Figure 4.10 *Time series over* 40 *days of the potential temperature (upper panel in K) and specific humidity (lower panel in g/kg) horizontal differences. The horizontal differences are computed as the difference between the daily-mean profiles in the test column and the RCE reference profiles. The plots are obtained from a reference column simulation performed with* $\tau = 2$ *h and the test column initialized to the RCE profiles previously obtained for an SST of* 304.7 *K.*

Figure 4.9 shows that the large-scale ascent at early times has a top heavy profile, partly because of the profile of the initial temperature difference (see Figure 4.10) and partly because of feedback from the shape of the convective heating profile which develops in response to the imposed additional cooling. In the example shown, the large-scale ascent over the first 4 days leads to a cooling that corresponds to a sink of energy from the column of 177 W m^{-2}. In order to maintain ascent in the test column sufficient moisture would have to be transported into the column so as to produce enough precipi-

tation to balance the additional cooling. However the energy associated with the moisture source is only 91 W m^{-2} as the top-heavy circulation produces maximum convergence at mid-levels where the humidity is relatively small. Thus, the initial large-scale circulation extracts moist static energy from the column and the strength of the large-scale circulation reduces.

The moist static energy budget in the test column is considered in order to investigate further how the test column evolves from an initial state with large-scale ascent to a final equilibrium state with large-scale descent. Figure 4.11 shows a scatter plot of the daily-mean tendency of column-integrated moist static energy in the test column due to the large-scale circulation against the difference in column-integrated moist static energy between the test and the reference columns. The plot is for the integration initialized with the warm, moist RCE profiles at 304.7 K described above. Figure 4.12 shows the daily-mean tendency of column-integrated moist static energy in the test column due to the combined effects of both surface evaporation and radiation. Given that the radiative cooling is prescribed and held fixed in time this quantity is equivalent to the difference in surface evaporation between the test column and the RCE value for the reference column. Aside from the action of the large-scale circulation on the test column, this is the only other source of difference in the column-integrated moist static energy budget between the test and RCE state.

The initial large-scale ascent rapidly extracts moist static energy from the test column due to the excess of cooling over moistening for the reasons discussed above. The moist static energy in the test column remains greater than that of the reference column until day 10. From day 9, the large-scale circulation provides a source of moist static energy to the test column (Figure 4.11 inset). However, the surface evaporation in the test column at this time is lower than the RCE evaporation rate appropriate for the reference column (Figure 4.12). This difference is larger than the import of moist static energy into the test column and so the moist static energy continues to drop. The reduction in evaporation during this period is associated with higher boundary layer humidity in the test column

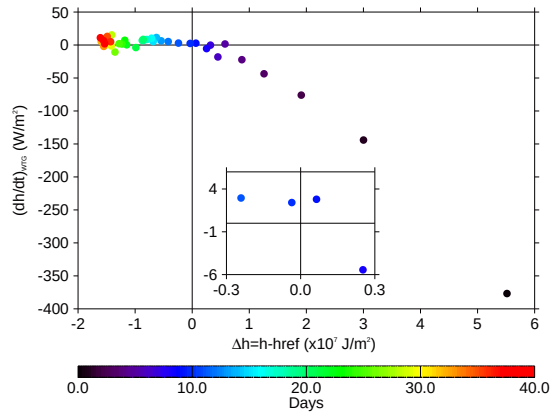

Figure 4.11 *Scatter plot of the difference in the column-integrated moist static energy (daily mean in the test column minus the value for the reference column) and the column-integrated moist static energy tendency due to the large-scale circulation. The results are obtained from the reference column simulation performed with* $\tau = 2$ *h and the test column initialized with RCE profiles previously obtained for an SST of* 304.7 *K. Each dot corresponds to a daily mean and the color bar indicates the time. The inset panel shows a zoom around the origin.*

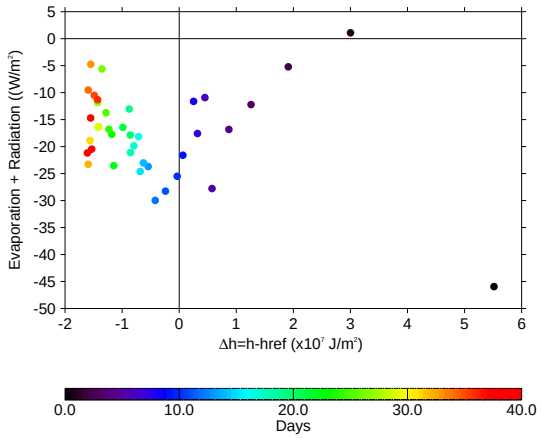

Figure 4.12 *As in Figure 4.11 but with the y-axis showing the column-integrated moist static energy tendency in the test column due to surface evaporation and radiation.*

compared to that in the RCE state of the reference column. At equilibrium there is a small net import of moist static energy into the test column by the large-scale circulation

and this is compensated by a small reduction in the surface evaporation rate compared to the uncoupled control RCE integration. Such an equilibrium is established by day 30 and is very similar to the state established in the corresponding integrations initialized with the reference profile or colder.

Additional sensitivity tests were conducted with initial conditions taken from instantaneous (rather than time-mean) states of RCE simulations at a range of SSTs. In all cases, the results obtained were similar, producing an equilibrium state of the coupled system with large-scale descent and reduced precipitation in the test column. Further experiments were also performed to test the sensitivity to the WTG adjustment rate profile $f(z)$, and again in all cases an equilibrium developed with descent in the test column.

In the configuration considered so far, with homogeneous surface and forcing conditions being used for the test and reference columns, an equilibrium state develops with descent in the test column. The large-scale circulation with descent is a robust result. However, the result must be interpreted with caution, and in particular, it cannot be assumed that a large-scale circulation would develop in analogous conditions for a two-column configuration. The apparent absence of any equilibrium solution with ascent in the test column is counter intuitive to the existence of a stable equilibrium with a large-scale circulation in a configuration where the implied feedback from the test column is taken into account. In a two-column configuration, mass conservation implies that descent in one column must be accompanied by ascent in the other, and one might expect at least some of the simulations to be able to capture this part of the presumed full two-column equilibrium solution. As discussed in Section 2.4.1 of chapter 2, in the reference column approach the WTG-derived circulation provides source terms to the heat and moisture budgets and in practice it is found that their evaluation produces source terms at equilibrium which always have the same sense and so are always associated with the descending branch of a large-scale circulation in the simulated column. The next step is to test whether the existence of an equilibrium with a large-scale circulation under homogeneous forcing can be maintained in the coupled two-column system described in

Section 4.4, for which a WTG-derived circulation does not provide any net sources to the heat and moisture budgets of the full system.

4.4 Coupled-column approach

This section describes results from experiments in which the WTG approximation is used to couple together two CRM simulations, with the large-scale circulation affecting both columns. Unless otherwise stated, $\varepsilon = 0.5$ thus, $w_2 = -w_1$. Key experiments performed under the reference-column approach are repeated under the coupled-column approach. As an example, Figure 4.13 shows the evolution of CWV and daily-mean precipitation for columns 1 and 2, in a simulation in which column 1 is initialized to the RCE profiles at 302.7 K, and column 2 is initialized to the RCE profiles at 304.7 K. The SST is 302.7 K in both columns and the WTG adjustment timescale τ is 2 h. The effective WTG adjustment time scale is 4 h in both columns (see section 2.4.1 of Chapter 2). As with the reference column approach, $dt_{wtg} = 10$ min.

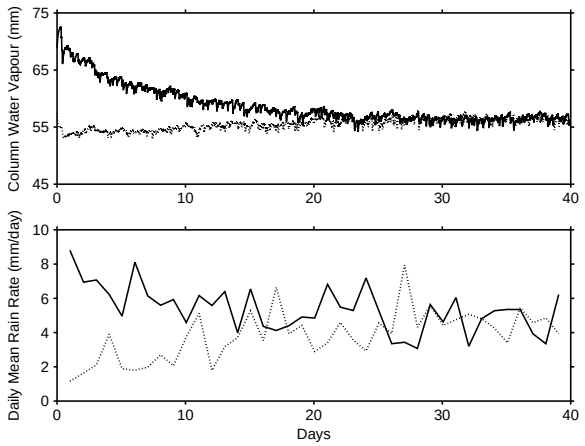

Figure 4.13 *Time series over* 40 *days of CWV (upper panel) and daily mean rain rates (lower panel) from a coupled-column simulation performed with* $\tau = 2$ *h. Columns 1 (dotted lines) and 2 (solid lines) are initialized to the RCE profiles previously obtained for SSTs of* 302.7 *K and* 304.7 *K respectively.*

The CWV in column 2 gradually decreases to the same value as that in column 1, such

that by day 30 the two curves are indistinguishable and within 1 mm of the RCE value for the uncoupled control integration. Initially the precipitation in column 2 exceeds that in column 1 with more than 80% of the precipitation on the first day falling in column 2. This fraction decreases with time. The mean rain rate and surface evaporation at equilibrium are obtained by averaging over days 30 to 40. Their values, and the values obtained at RCE of the uncoupled control integration are summarized in Table 4.1. The mean rain rate and surface evaporation rate are equal in the two columns and are equal to the RCE value for the uncoupled control integration to within 0.03 mm d^{-1}, and the imposed radiative cooling is separately balanced within each column..

	Rain	Evaporation
Control run	4.77	4.80
Column 1	4.81	4.81
Column 2	4.77	4.81

Table 4.1 *Mean rain rate and surface evaporation at equilibrium. The values are obtained from a coupled-column simulation performed with* $\tau = 2$ *h and columns 1 and 2 initialized to the RCE profiles at 302.7 K and 304.7 K respectively. Results are also shown for the uncoupled control run.*

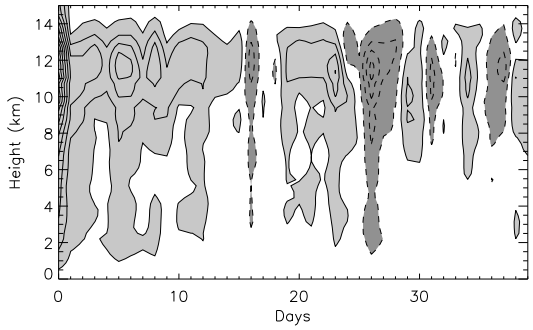

Figure 4.14 *Time series over* 40 *days of the daily-mean large-scale vertical velocity in column 2 from a coupled-column simulation performed with* $\tau = 2$ *h. Columns 1 and 2 are initialized to the RCE profiles previously obtained for SSTs of* 302.7 *K and* 304.7 *K respectively. The contour interval is* 0.5 *cm* s^{-1} *with the contours beginning at* ± 0.25 *cm* s^{-1}*. Light shading and solid contours show ascent, and dark shading and dashed contours show descent.*

Figure 4.14 shows the time evolution of the daily-mean vertical velocity in column

2 and Figure 4.15 shows the large-scale vertical velocity profiles averaged over days 0 to 14 and 30 to 40 for the same integration as in Figure 4.13. An initial large-scale ascent develops in column 2 as would be expected from the initial potential temperature difference between the two columns. By mass continuity this is accompanied by a large-scale descent in column 1 as shown by the large-scale vertical velocity profiles at the early stage of the integration (results shown on the left-hand panel of Figure 4.15.) The large-scale circulation decreases in strength as the temperature difference is reduced and from about day 16 an oscillation begins to develop in the vertical velocity with periods of ascent and descent. These oscillations continue throughout the integration but by day 30 there is no preferred column for ascent and the average WTG vertical velocity over days 30 to 40 (results shown on the right-hand panel of Figure 4.15) in each column is close to zero.

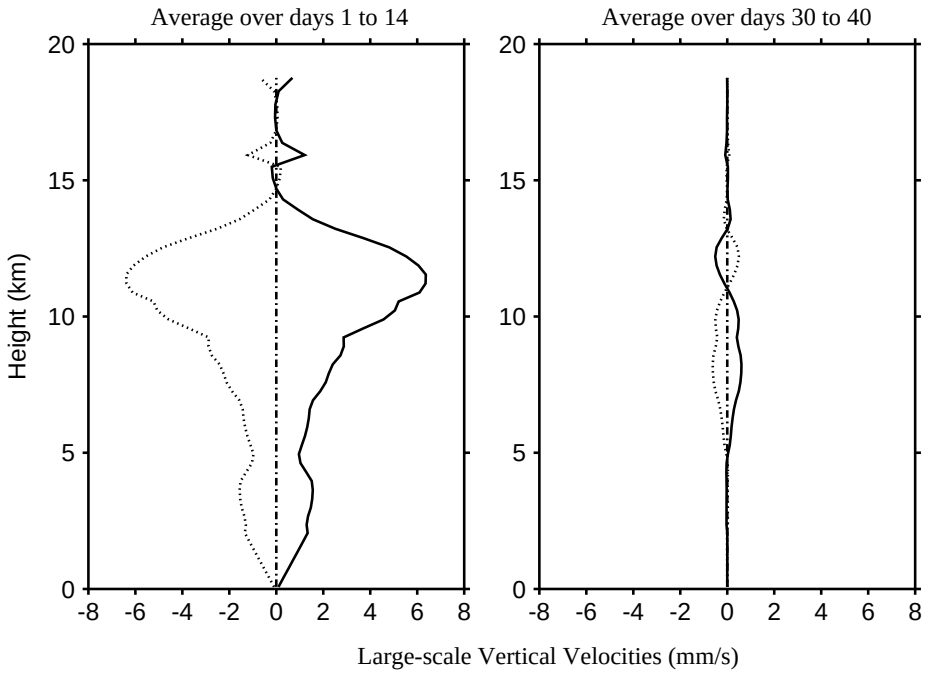

Figure 4.15 *Large-scale WTG vertical velocity profiles for columns 1 (dotted curves) and 2 (solid curves). The profiles are obtained by averaging over days* 1 *to* 14 *(left-hand panel) and* 30 *to* 40 *(right-hand panel).*

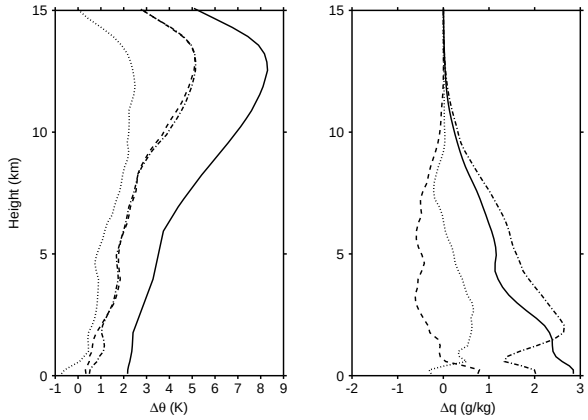

Figure 4.16 *Deviation from the reference profiles of potential temperature (left) and specific humidity (right) for the domain-mean profiles in the test column (dotted), in columns 1 (dashed) and 2 (dash-dotted) at the end of day one of the simulations performed with* $\tau = 2$ *h and either column 2 of the coupled-column model or else the test column of the reference column model initialized to the RCE profiles at* 304.7 *K. The solid curves represent the initial potential temperature difference and the initial specific humidity difference between the columns.*

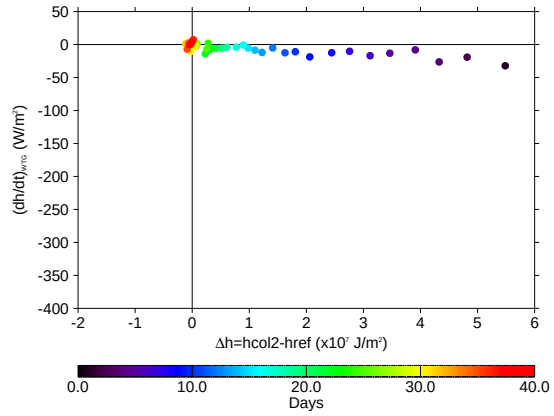

Figure 4.17 *As in Figure 4.11 but for the coupled-column simulation performed with* $\tau = 2$ *h and columns 1 and 2 initialized to the RCE profiles at* 302.7 *K and* 304.7 *K respectively. The x-axis shows the difference in column-integrated moist static energy between column 2 and the value obtained at equilibrium in the uncoupled control integration.*

The behavior of this simulation is compared to its equivalent in the reference column configuration. Figure 4.16 shows the deviation from the reference profiles for the domain-mean profiles at the end of day one of the simulations performed with $\tau = 2$ h and either column 2 of the coupled-column model or else the test column of the reference column model initialized to the RCE profiles at 304.7 K. Also considered is Figure 4.17 which shows a scatter plot of the daily-mean tendency of column-integrated moist static energy in column 2 due to the large-scale circulation against the difference in column-integrated moist static energy between column 2 and the RCE value obtained in the uncoupled integration. In the coupled-column model, the initial large-scale circulation cools and moistens the warm column. At the same time, because heat and moisture transported out of one of the columns are being allowed to affect the other column, the circulation also warms and dries the cold column. The temperature difference between the columns quickly reduces such that by the end of the first day the temperature difference above the boundary layer is small; of order of 0.1 K compared to 0.5 K to 2 K temperature difference between the test column and the reference column. As a result, a weak circulation between the columns is obtained very quickly and the timescale for adjustment back to the RCE profiles is governed by the internal moisture adjustment timescale within each column (e.g. Tompkins and Craig, 1998b). In the reference column approach, the initial large-scale circulation extracts more moist static energy from the test column than it does from column 2 of the coupled-column model. For example, averaged over day 1 380 Wm^{-2} of moist static energy is transported out of the test column by the large-scale circulation compared to only 30 Wm^{-2} that is transported out of column 2 of the coupled-column simulation. In addition, a much larger rate of precipitation can be achieved in the test column because, by construction, the cooling by the large-scale circulation in the test column is not offset by any warming of the other column. Hence, precipitation can be strong enough to dry the test column with the result that both temperature and moisture are adjusted toward RCE over the first day.

During the first 20 days, whilst the coupled-column system equilibrates, the mean precipitation in the columns is about 90% of that required to balance the imposed ra-

diative cooling and the system loses heat energy. Evaporation during the same period is about 87% of that required to balance the imposed cooling resulting in a net loss of moist static energy and a conversion of latent energy to heat energy.

In the same manner as for the reference-column approach, sensitivity experiments have been performed with different initial profiles and different values of the WTG timescale. No matter what the strength of initial temperature difference, or what the strength of the initial large-scale circulation, the coupled-column approach with homogeneous surface condition was always found to adjust the columns to produce a quasi-steady state with no mean large-scale circulation and the mean statistics of the corresponding uncoupled RCE simulation.

The coupled two-column approach with columns of equal area (i.e., $\varepsilon = 0.5$), is a configuration for which the reference column approach was certainly not designed. Rather the reference-column approach is intended to describe a small area embedded within a large-scale environment. As noted in Section 2.4.1 of chapter 2, a reference-column approach can be recovered from the coupled-column approach by setting $\varepsilon = 0$. An interesting question arising from the above results is whether the coupled-column approach exhibits similar behavior to the reference-column approach as $\varepsilon \to 0$.

Table 4.2 summarizes the values of mean rain rates and surface evaporation rates at equilibrium for columns 1 and 2 in the simulations performed with $\varepsilon = 0.1$ and $\varepsilon = 0.01$. As $\varepsilon \to 0$, equilibrium states with no mean large-scale circulation are again established. However, the timescale of adjustment of the columns to their final equilibrium state increases as ε decreases; that is 90 days in the simulation performed with $\varepsilon = 0.01$ and 50 days in the simulation performed with $\varepsilon = 0.1$ compared to 23 days in the simulation performed with $\varepsilon = 0.5$ (see Figure 4.13). The final equilibrium state established was insensitive to the WTG coupling timescale, the WTG adjustment rate profile and the initial conditions. This supports the interpretation that the character of the equilibrium state is dependent on whether the simulated system is closed, as in this section, or is open, with external source terms in the heat and moisture budgets. By construction, the

coupled-column system studied here is closed for any non-zero ε, however small.

	$\varepsilon = 0.1$		$\varepsilon = 0.01$	
	Rain	Evaporation	Rain	Evaporation
Column 1	4.79	4.81	4.82	4.83
Column 2	4.78	4.80	4.77	4.82

Table 4.2 *Mean rain rates and surface evaporation at equilibrium (mm d^{-1}). The results are shown for columns 1 and 2 in the simulation performed under the coupled-column approach with columns 1 and 2 initialized to the RCE profiles at* 302.7 *K and* 304.7 *K respectively and* $\tau = 2$ *h. The values are obtained by averaging over days* 50 *to* 100 *in the simulation performed with* $\varepsilon = 0.1$ *and over days* 90 *to* 200 *in the simulation performed with* $\varepsilon = 0.01$.

4.5 Conclusions

The WTG approximation has been used in various studies to derive a large-scale circulation in order to couple a single column model or cloud resolving model to a predefined reference column (e.g. Sobel and Bretherton, 2000; Raymond and Zeng, 2005; Sessions et al., 2010; Sobel et al., 2007). The reference column approach was designed to study the behavior of convection within a small area where conditions are different from the mean conditions within a much larger area to which it is coupled. Here, the modeling framework is extended in order to couple two cloud resolving model simulations. The coupled columns approach is theoretically equivalent to the reference column approach in the limit of an infinite ratio of the column areas, $\varepsilon = 0$, but also allows for studies of WTG couplings between columns of comparable area. Two SCMs have been coupled through the WTG or similar approaches in the past (e.g. Nilsson and Emanuel, 1999; Raymond and Zeng, 2000; Shaevitz and Sobel, 2004) but to the best of our knowledge this is the first time that the WTG approximation has been used to couple two CRMs.

When coupled to a reference column profile generated from a previously uncoupled

RCE simulation and when using the same surface forcing as in the RCE reference column, the coupled CRM produced an equilibrium state characterized by large-scale descent in the simulated column and mean precipitation less than the RCE simulation. A similar equilibrium state was produced in Raymond and Zeng (2005) for example, although other studies indicate that this is a model-dependent result (e.g. Sobel et al., 2007; Wang and Sobel, 2011). In the present study, the existence of the dry equilibrium state with suppressed convection was found to be insensitive to the choice of the WTG adjustment rate profile or to the initial conditions in the test column, although the strength of the circulation established is sensitive to the WTG timescale.

The final equilibrium state found here is associated with net transport of moist static energy into the test column by the WTG derived large-scale circulation which is accompanied by a small compensating reduction in the surface evaporation. The inability of the reference-column approach to produce an equilibrium state with ascent in the simulated column is related to the shape of the large-scale vertical velocity profile generated. For circulations with ascent in the test column the large-scale vertical velocity profile is top heavy with the maximum convergence above 5 km. The result is that, initially, the moisture convergence from the circulation is not sufficient to balance the cooling and so moist static energy is lost from the test column. As the simulation approaches the near radiative convective equilibrium conditions a weak import of moist static energy into the column by the large-scale circulation is observed. However this is not sufficient to balance a reduction in the surface fluxes associated with high boundary layer humidity. Thus, the moist static energy of the simulated column is reduced further until a new equilibrium is reached with descent in the test column.

The presence of an equilibrium with descent in the simulated column, and the absence of an equilibrium solution with ascent in the test column is not physically realistic. Despite the homogeneous forcing that is applied in these experiments, the test column and the reference column are not interchangeable. Moreover, the energy budget of the entire system is not closed in the reference- column approach.

To explore the role of the fixed reference column in producing this dry equilibrium state of the test column, an extension of the WTG approach to couple together two CRMs has been developed. In this fully-coupled configuration, the budgets of the total system are now closed.

The reference column and the coupled-column approaches used the same convective model. Hence, key experiments performed under the reference column approach were repeated under the coupled-column approach in order to compare the coupling techniques, which are the one-way and two-way couplings. The coupled-column system reaches an equilibrium which has no time-mean large-scale circulation between the two columns and which is very similar to the equilibrium state of a single uncoupled CRM. In particular, this equilibrium was insensitive to the magnitude of the initial temperature difference between the two columns, to the WTG adjustment timescale and profile, and to the relative areas of the two columns. As suggested by the contrasting results of previous studies, it is possible that the presence, or otherwise, of a dry equilibrium state in the reference-column approach may depend on the choice of the representation of convection or boundary layer mixing, or on some details of the implementation of the WTG framework. However, the key finding here is that even for small ε the fully-coupled approach produces a qualitatively different equilibrium state from the reference-column approach.

The differences in behavior of the coupled-column and reference-column approaches highlight the importance of a careful consideration of the appropriate energy and moisture budgets when interpreting results from studies of this nature. Most of the WTG studies to date have followed a reference-column approach and have focused on the sensitivity of the simulated precipitation in the test column to the surface forcing. The next chapter describes a similar set of experiments with both the reference-column configuration and the coupled-column configuration.

Chapter 5:
WTG calculations over non-uniform surface conditions

5.1 Introduction

Given the marked difference in behavior between the coupled-column and reference-column approaches for homogeneous surface conditions, some key WTG experiments that have been reported in the literature under inhomogeneous surface conditions are re-examined here. A typical objective is to investigate the effects of the difference in surface conditions on convection within the simulated column. Here, analogous experiments using the reference-column approach are repeated and are compared with their equivalents using the the coupled-column approach.

The sensitivity to non-uniform surface conditions has been investigated by changing either the SST in one of the columns (as in Sobel et al., 2007; Wang and Sobel, 2011) or the component of the wind perpendicular to the simulated domain (as in Raymond and Zeng, 2005; Sessions et al., 2010). However, results from changing the SST or the surface wind speed in one of the columns are broadly similar and mainly the results from changing the SST will be discussed here. Other experiments were also performed altering the WTG adjustment rate profile and showed that this has little effect on the results presented below.

This chapter is organized as follows. The WTG experiments for non-uniform surface forcing are compared in Sections 5.2 and 5.3 for the cases of simulations performed un-

der the reference column approach and under the coupled-column approach respectively. Sections 5.2.4 and 5.3.5 compare the state of the test column of the reference column approach and the column-mean state of the coupled-column approach to that of the equivalent uncoupled column run at radiative-convective equilibrium (RCE). Conclusions are presented in Section 5.4

5.2 Reference column approach

In this section the results from changing the surface forcing in the test column are shown. The reference reservoir column is defined with profiles obtained from the RCE simulation of the uncoupled CRM with an SST of 302.7 K and a surface wind speed of 5m s^{-1} (control run). For all the simulations performed under the reference column approach, the WTG adjustment timescale is 2 h and the test column is initialized with profiles from the reference column and hence is expected to develop deep convection except for surface forcing sufficiently lower than the RCE value. Each of these simulations are run for 40 days and an average over the last 15 days is used to describe the system at its quasi-steady state.

5.2.1 Time evolution and mean statistics at equilibrium

The temporal evolution of some fields towards equilibrium for a difference in surface forcing under the WTG framework is examined in this section, including the mean statistics that define the system at its quasi-equilibrium state.

Figure 5.1 shows the daily running mean column integrated water vapor (CWV) from the reference column simulations with different values of SST in the test column. In each case, the CWV starts from the RCE reference value and evolves toward a new quasi-steady state. The mean CWV at equilibrium is an increasing function of SST. For an SST

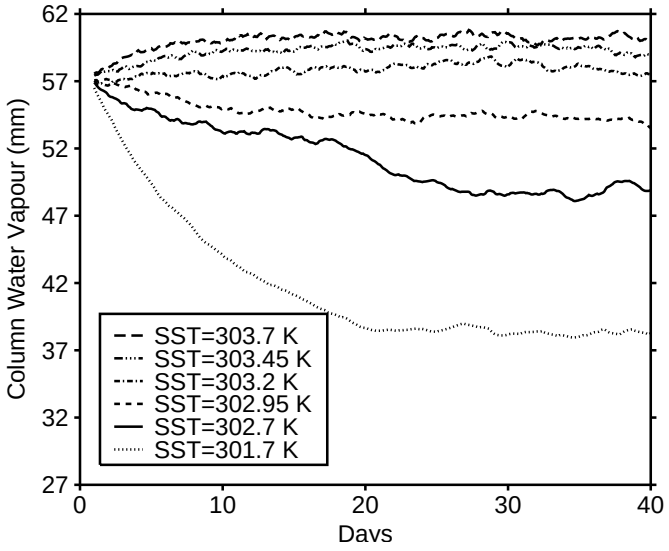

Figure 5.1 *Daily-running-mean column water vapor (CWV [mm]) for 40 days from six experiments performed under the reference column approach with different values of SST.*

lower than 302.95 K, the CWV takes about 20 days to reach the new quasi-equilibrium state. This adjustment timescale is much longer than the adjustment time scale obtained in the simulations performed with an SST greater than 302.95 K.

The moisture transported by the large-scale circulation, the mean rain rates and surface evaporation at equilibrium are summarized in Figures 5.2 and 5.3 as functions of SST ranging from 301.7 K to 303.7 K and as functions of surface wind speed ranging from 0 m s^{-1} to 15 m s^{-1}. As presented in Section 4.3 of chapter 4 the precipitation in the test column under homogeneous surface conditions is less than that in the corresponding uncoupled RCE simulation used to define the reference column state. A mean precipitation equivalent to that of the reference column is not achieved in the test column unless its surface wind speed is increased (similar to Raymond and Zeng, 2005) or its SST is increased.

The mean rain rates, surface evaporation and moistening from the large-scale circulation at equilibrium increase monotonically with surface forcing although the changes in surface evaporation are small compared to the changes in rainfall rate and moisture

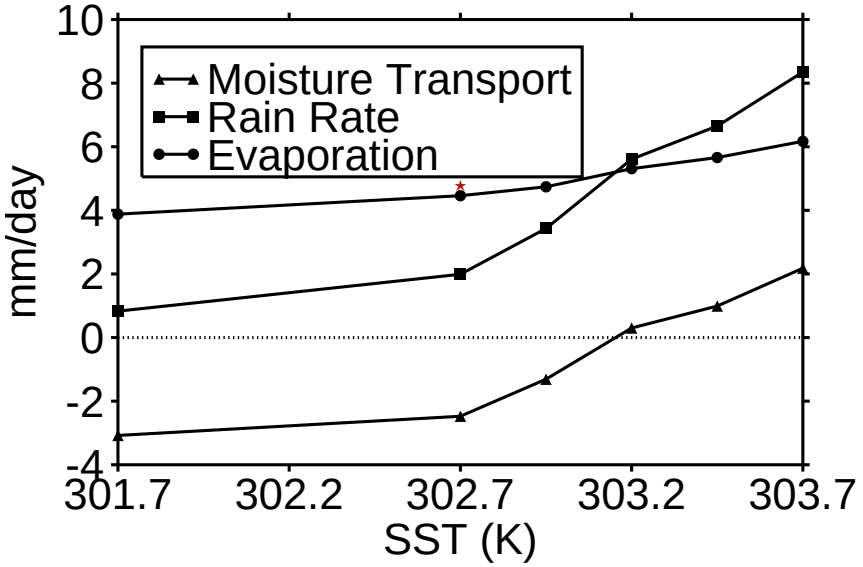

Figure 5.2 *Mean moisture transport into the column by the WTG circulation (solid line with triangles), rain rates (solid line with squares) and surface evaporation (solid line with circles) at equilibrium for the test column in the simulations performed with different values of SST. The red star represents the rain rate or evaporation rate obtained in the uncoupled RCE simulation. The SST in the test column is plotted on the horizontal axis.*

transported by the large-scale circulation. For both changes in SST and changes in surface wind speed, there is a slow increase of mean rain rate with surface forcing followed by a more rapid increase as the surface forcing increases past the value used to define the RCE reference column state. There are two distinct regimes in each of these set of simulations. The first regime (SST $\leqslant$ 302.95 K or else surface wind speed $\leqslant$ 6 m s^{-1}) consists of a moisture sink due to the diagnosed large-scale circulation balancing the excess of evaporation over precipitation while in the second regime (SST $\geqslant$ 303.2 K or else surface wind speed $\geqslant$ 7 m s^{-1}) there is a deficit of evaporation compared to precipitation balanced by an import of moisture into the test column by the the diagnosed large-scale circulation. The lines of mean rain rates and surface evaporation cross between 302.95 K and 303.2 K (in figure 5.2) and between 6 m s^{-1} and 7 m s^{-1} (in figure 5.3) confirming that the reference column configuration reaches a RCE state with no large-scale circulation at a value of surface forcing greater than the value used to define the uncoupled RCE

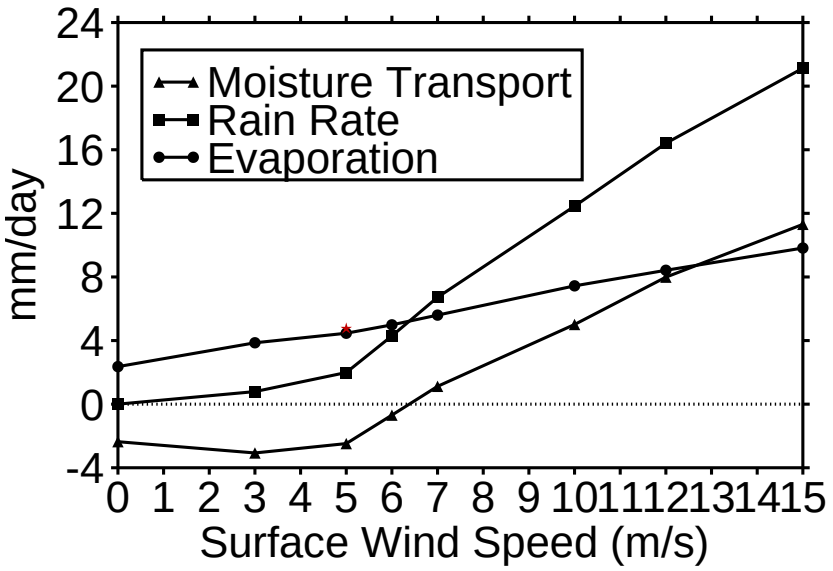

Figure 5.3 *Mean moisture transport into the column by the WTG circulation (solid line with triangles), rain rates (solid line with squares) and surface evaporation (solid line with circles) at equilibrium for the test column in the simulations performed with different values of surface wind speed. The red star represents the rain rate or evaporation rate obtained in the uncoupled RCE simulation. The surface wind speed in the test column is plotted on the horizontal axis.*

reference column. These two regimes are referred as "dry" and "wet" regimes.

The sensitivity of the precipitation in the test column to the difference in the surface forcing is similar in magnitude to that seen in previous studies using the reference-column approach. As an example, compare Figure 5.3 to the top panel of Figure 11 in Raymond and Zeng (2005).

Figure 5.4 shows the values of rain rate plotted versus column relative humidity (CRH). The CRH is calculated as the ratio between the column-integrated water vapor and its saturation value. The values are for the test column in the simulations with different surface wind speed. For the values of surface wind speed ranging from 0 to 15 m s^{-1}, the rain rate has increased by 20.73 mm d^{-1} for a total increase of 47% in the mean CRH. The changes in CRH are much greater in the dry regime compared to the

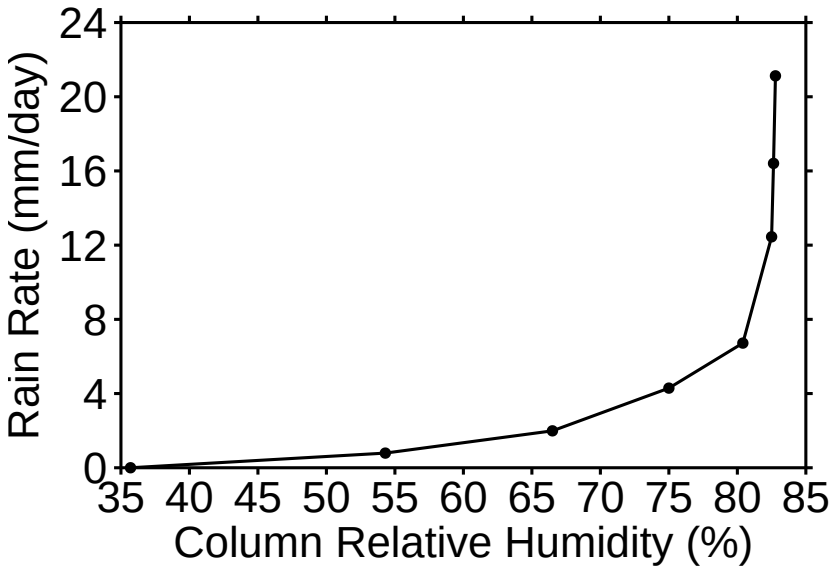

Figure 5.4 *Mean rain rate versus column relative humidity for the test column in the simulations performed under the reference column approach. The values of surface wind speed perpendicular to the test column are* 0, 3, 5, 6, 7, 10, 12 *and* 15 $m\ s^{-1}$.

wet regime and there is an upper limit of about 83 %. The changes in rain rate are relatively small for CRH less than 55 %. There is a significant increase in rain rate for CRH greater than 55%, followed by a sharp pickup of rain rate for CRH above 80%. The relationship between CRH and rain rate is qualitatively similar to that seen in observations (e.g. Bretherton et al., 2004; Holloway and Neelin, 2009) and to that obtained in other idealized models (e.g. Wang and Sobel, 2011; Raymond and Zeng, 2005).

5.2.2 The large-scale circulation

This section examines the structure of the derived large-scale circulation in the quasi-steady state of each of the simulations described in Figure 5.1. The derived large-scale circulation is analyzed through the large-scale mass flux, which is calculated as the product of the air density and the WTG-derived large-scale vertical velocity, w^{WTG}.

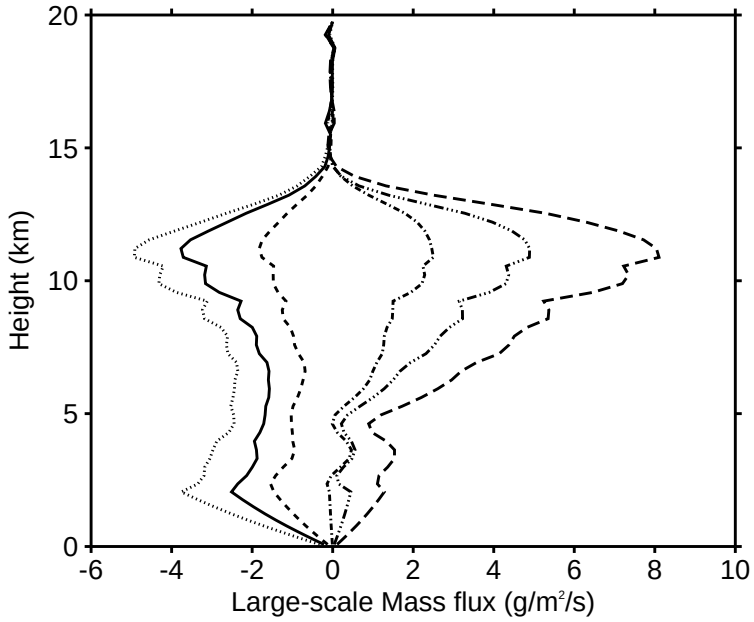

Figure 5.5 *Mean profiles of large-scale mass flux at equilibrium of each of the simulations shown in Figure 5.1. The large-scale mass flux is computed as a product of the air density and the WTG vertical velocity. Lines definition are as in Figure 5.1.*

Figure 5.5 shows the mean large-scale mass flux profiles at equilibrium. The shapes of the profiles are similar within each regime. As the SST increases, the large-scale mass flux increases, moving from negative to positive values. The large-scale mass flux is top heavy for all SST but the ascending side is more top-heavy than the descending side.

5.2.3 Thermodynamic and convection structures

This section will examine the structure of relative humidity and cloud distributions under the WTG calculations.

Figure 5.6 shows the mean relative humidity profiles at equilibrium for the same set of simulations as in Figure 5.1. Simulations performed under the reference column configuration exhibit a quite moist boundary layer with a relative humidity close to 90%. These

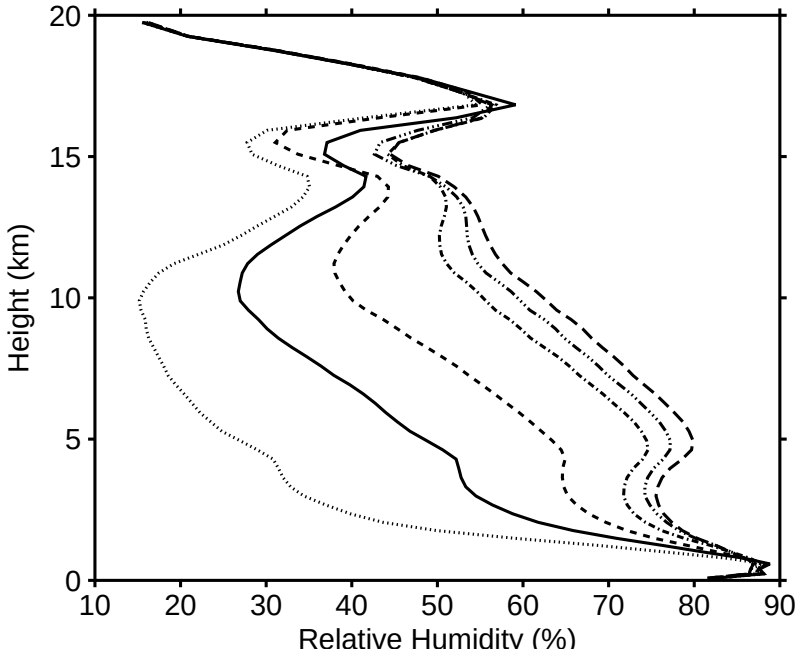

Figure 5.6 *Mean relative humidity profiles at equilibrium of each of the simulations shown in Figure 5.1. Lines definition are as in Figure 5.1.*

small changes in RH with SST in the boundary layer result in very small changes in surface evaporation as described above. In the simulation performed with an SST of 301.7 K, the mean relative humidity decreases rapidly with height in response to subsidence motions from the diagnosed large-scale circulation which inhibits the test column from developing deep convection. Similar results have been found in previous WTG experiments (e.g. Sobel and Bretherton, 2000; Raymond and Zeng, 2005; Sessions et al., 2010). Simulations performed with SSTs of 302.7 and 302.95 K also develop a large-scale descent in the test column resulting in a relative humidity lower than that of the reference column. The mean relative humidity in the simulations performed with an SST$\geqslant$ 303.2 K (wet regime) remains above 70% until 8 km. This is in response to the source of moisture from the diagnosed large-scale circulation which enhances the frequency of occurrence of deep convection within the test column and hence, keeps its relative humidity relatively large compared to that of the reference throughout the free troposphere. However, the larger mid-tropospheric relative humidity values will also make the deep convection

more efficient in producing rainfall.

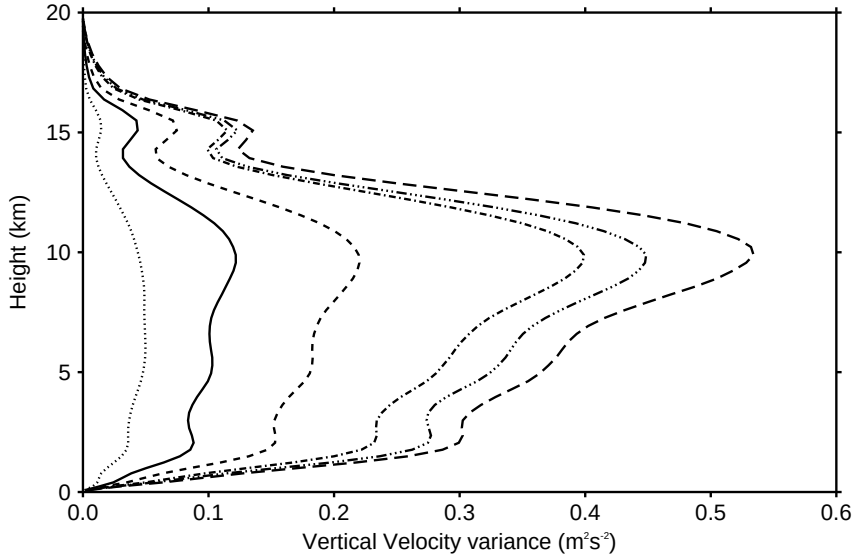

Figure 5.7 *Mean vertical velocity variance profiles at equilibrium of each of the simulations shown in Figure 5.1. Lines definition are as in Figure 5.1.*

The vertical velocity variance is one way to measure convective activity. Figure 5.7 shows the mean profiles obtained at equilibrium for the same set of simulations as in Figure 5.1. The vertical velocity variance increases as the SST does. Simulations that develop a large-scale descent in the test column have a mean vertical velocity variance smaller than the RCE reference value (see the red curve in Figure 4.7 of chapter 4). As the SST increases past 302.95 K, the mean vertical velocity variance becomes greater than the RCE reference value in response to the ascending large-scale circulations which favor convection within the test column. The vertical velocity variance profiles have similar shapes characterized by three peaks in the free troposphere. The peaks located near 2 and 10 km suggest high activity from shallow and deep convection respectively. They are connected by the activity from intermediate convection which has its peak at the freezing level located at about 5 km.

Other ways to examine convection within the test column are the mass fluxes of strong

and cloudy updrafts (M_u) and strong downdrafts (M_d) along with the fractional areas covered by each of them (σ_u and σ_d respectively). σ_u, σ_d, M_u and M_d are calculated as in Chapter 3.

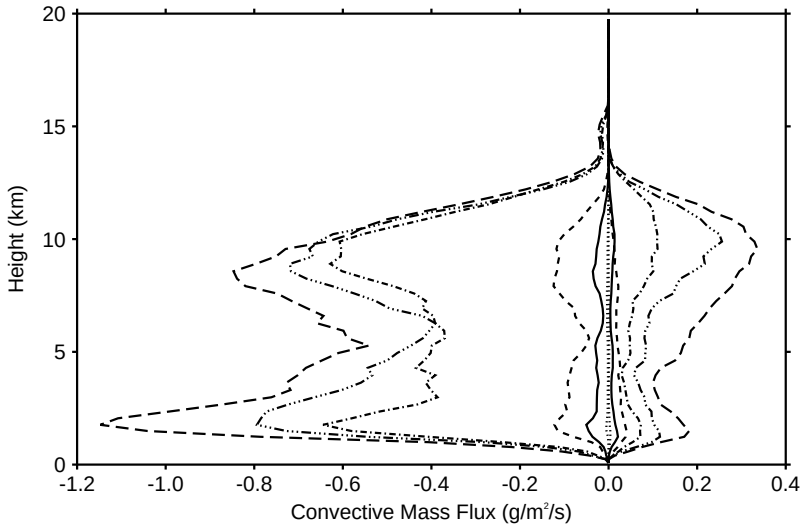

Figure 5.8 *Mean profiles of convective mass flux of strong and cloudy updrafts and strong downdrafts in each of the simulations shown in Figure 5.1. Lines definition are as in Figure 5.1.*

Figure 5.8 shows the mean profiles at equilibrium of M_u and M_d and Figure 5.9 shows the profiles at equilibrium of σ_u and σ_d. The results are for the same set of simulations as in Figure 5.1. For all of these simulations, M_d and σ_d are larger than M_u and σ_u respectively but, further investigations reveal that M_d and σ_d are respectively smaller than M_u and σ_u if the latter are estimated from both clear and cloudy grid points (results not shown).

In the driest simulation (SST= 301.7 K), the profiles of M_u and M_d are close to zero. M_u increases with SST and becomes more top heavy as the SST increases past 302.95 K. For the whole troposphere, M_u is lower than the RCE reference values in the dry regime and it is greater than the RCE reference values in the wet regime. However, M_u does not always have its largest value in the upper troposphere, as does the vertical velocity variance and σ_u. This is the case for simulations performed with an SST $\leqslant$

302.95 K where M_u peaks at about $\approx$ 1.5 km. Note that this result may be partly due to the suppression of deep convection or to the density weighted factor in the calculation of M_u. For the simulations performed with an SST $>$ 302.95 K, M_u has two maxima in the free troposphere with the largest value located at levels of high activity of convection as identified on the vertical velocity variance profiles.

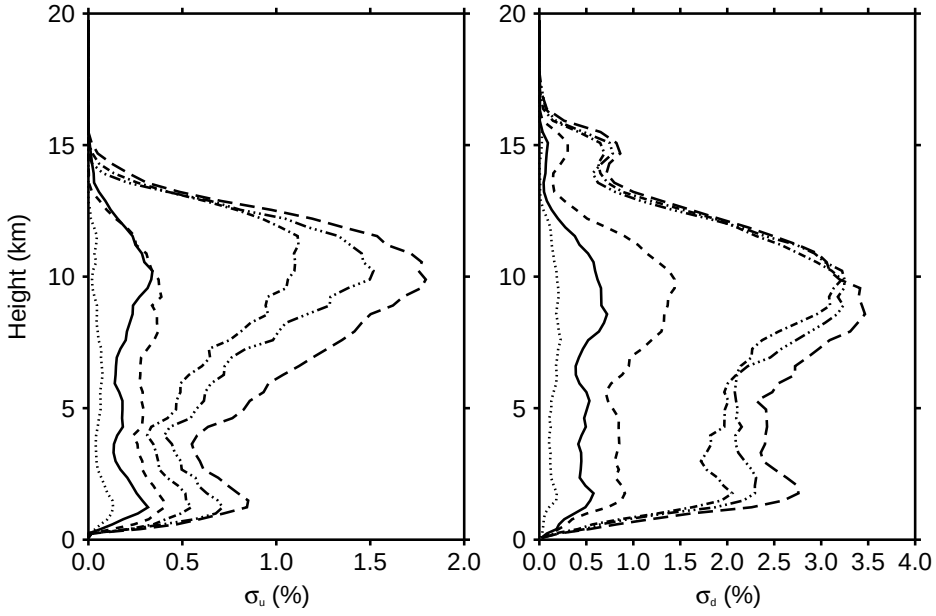

Figure 5.9 *Mean profiles of fractional area covered by strong and cloudy updrafts (left) and strong downdrafts (right) in each of the simulations shown in Figure 5.1. Lines definition are as in Figure 5.1.*

M_d also increases as the SST does and for all SST it shows two distinct modes located at the top of the boundary layer and at a level just below 10 km. M_d peaks at heights just below those where M_u does and similarly σ_d peaks at heights just below those where σ_u does. These seems consistent with the downdraft being initiated by detrainment from updraft clouds and re-evaporation of precipitating clouds when falling through the underlying unsaturated air. Similarly to convective mass flux, the values of σ_u and σ_d increase with SST and become greater than the RCE values as the SST increases past 302.95 K.

The corresponding cloud fraction is estimated using the same definition as in Chap-

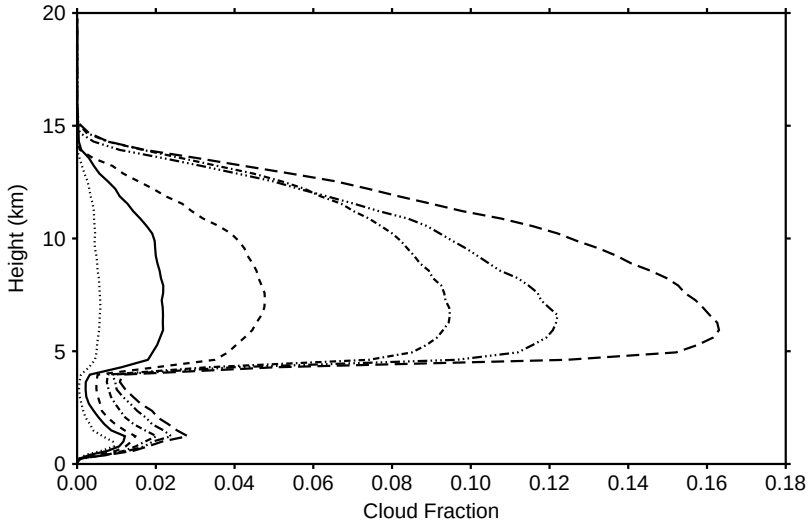

Figure 5.10 *Mean cloud fraction profiles at equilibrium in each of the simulations shown in Figure 5.1. Lines definition are as in Figure 5.1.*

ter 3. The mean profiles at equilibrium are shown in Figure 5.10. Cloud increases as the SST does. It covers about 1% in the simulation performed with an SST of 301.7 K and extends to up to 16% in the simulation performed with an SST of 303.7 K. For all SST, the profiles have similar shape which is characterized by two modes. The first mode is a shallow cumulus cloud from shallow convection. It is centred at about 1.5 km. The mode of cloud from intermediate and deep convection is centred in the middle troposphere in between the heights of high activities of convection identified from the vertical velocity variance profiles.

5.2.4 Reference column versus RCE simulations

This section compares the behavior of the test column of the reference column approach to that of the corresponding uncoupled RCE simulations.

A series of additional RCE simulations is performed with different values of SST ranging from 301.7 K to 303.7 K. The corresponding mean CWV at equilibrium is shown

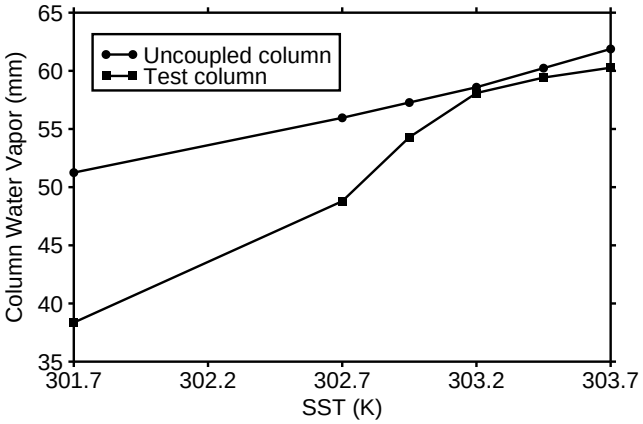

Figure 5.11 *Mean CWV at equilibrium as a function of SST. Results are shown for the simulated column in the same set of simulations as in Figure 5.1 (solid line with squares). The SST in the test column is plotted on the horizontal axis. Results are also shown for the uncoupled column run at RCE equilibrium (solid line with circles). The SSTs in RCE simulations are plotted on the horizontal axis.*

in Figure 5.11 along with the mean CWV at equilibrium for the test column in the same set of simulations as in Figure 5.1. For all these simulations, the mean CWV increases as the SST does. It increases nearly linearly with the SST in the RCE simulations while in the reference column simulations there is a rapid increase in the dry regime followed by a much slower increase in the wet regime. For each value of SST used, the mean CWV obtained at equilibrium in the reference column simulation is smaller than the mean value obtained at equilibrium in the corresponding RCE simulation. A mean CWV very close to that obtained in the corresponding RCE simulation is not achieved in the test column unless the reference column system is in an equilibrium state with no large-scale circulation.

5.3 Coupled-column approach

In this section results from an equivalent set of the coupled-column experiments are presented. The SST or the surface wind speed in column 2 have changed and the SST and

the surface wind speed in column 1 are kept to the fixed values of 302.7 K and 5m s^{-1} respectively. Unless otherwise stated, the simulations are performed with the WTG adjustment timescale of 2 h and the columns have equal size; that is $\varepsilon = 0.5$ and thus, $w_2 = -w_1$ (derived from Equation 2.32 of chapter 2). All the simulations are run for 50 days with the columns initialized from the profiles obtained from the RCE simulation of the uncoupled CRM with an SST of 302.7 K and a surface wind speed of 5m s^{-1} (control run). The last 20 days of each simulation are averaged to represent the mean state and statistics of the system at the quasi-equilibrium state.

5.3.1 Temporal evolution

The time evolution of vertical velocity variance anomalies with respect to the mean profile obtained at RCE of the control integration (see the red curve in Figure 4.7 of Chapter 4) is shown in Figure 5.12. The results are shown for columns 1 and 2 for a coupled-column simulation performed with an SST= 302.7 K in columns 1 and 2 and for a coupled-column simulation with an SST of 302.7 K in column 1 and an SST of 303.7 K in column 2. Over uniform surface forcing, the vertical velocity variance profiles in columns 1 and 2 oscillate around the mean profile obtained at RCE of the control run with a period of few days. However, there is not a preferred column of suppressed or enhanced convection and the day 30 to 50 average vertical velocity variance anomaly is close to zero in each column. In the simulation with non-uniform surface forcing, convection is enhanced in column 2 while it is suppressed in column 1 relative to the RCE state achieved in the control run. Examination of the convective activity in other simulations indicates that convection is always more active in the column that has a strong surface forcing compared to the other column.

Further information on the response of precipitation to the difference in surface forcing is provided by Figure 5.13, which shows the time series of the daily running mean and five days running mean rain rate. Over uniform surface forcing, precipitation in columns

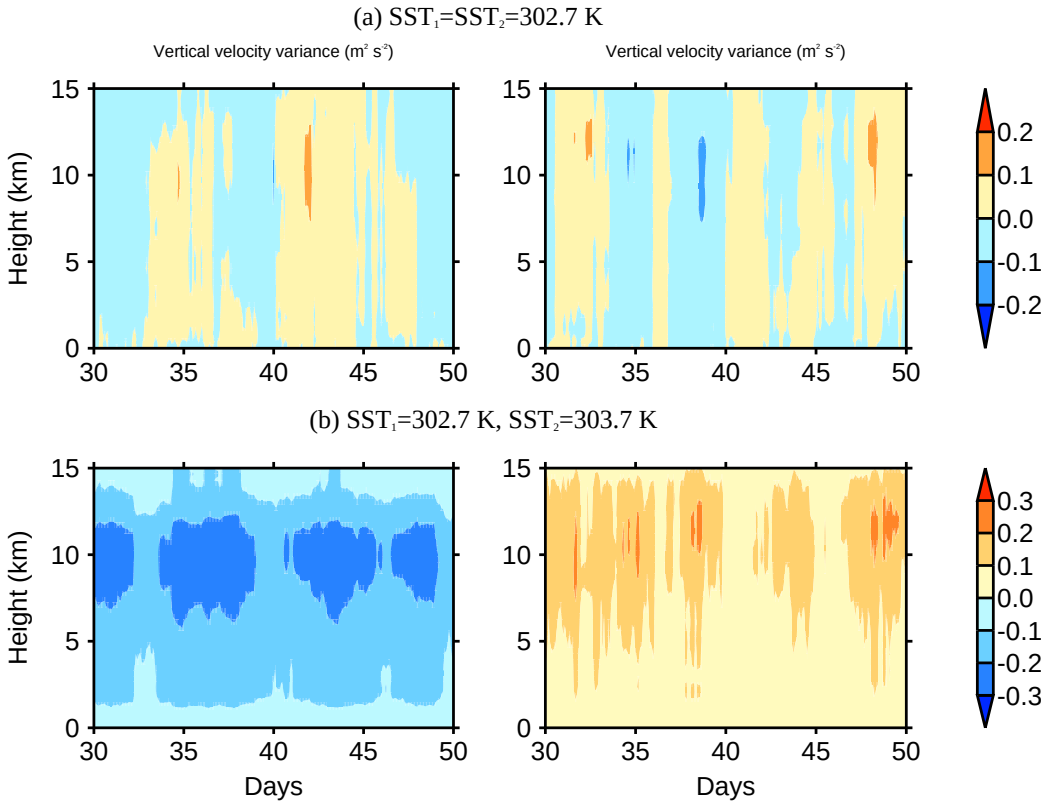

Figure 5.12 *Time evolution of daily mean vertical velocity variance anomalies for columns 1 (left) and 2 (right) in the coupled-column simulations performed over uniform surface forcing (top panel) and non-uniform surface forcing (with an SST of* 303.7 *K in column 2) (bottom panel). The anomalies are computed as the deviation of daily-mean vertical velocity variance profiles from the mean profile obtained in the control run. The results are shown for the last 20 days of each integration.*

1 and 2 is approximately the same with the mean value comparable to that found at RCE of the control integration. With an SST of 303.7 K in column 2, precipitation increases in column 2 while it decreases in column 1. As first pointed out by Grabowski et al. (1998), the time series of rain rate obtained in the two dimensional simulations presents higher-frequency variability than the time series obtained in the three dimensional simulations (e.g. Tompkins and Craig, 1998a; Wang and Sobel, 2011). However, the higher-frequency variability obtained here could be the simple consequence of a sampling over smaller number of grid points rather than a consequence of excessive buoyancy oscil-

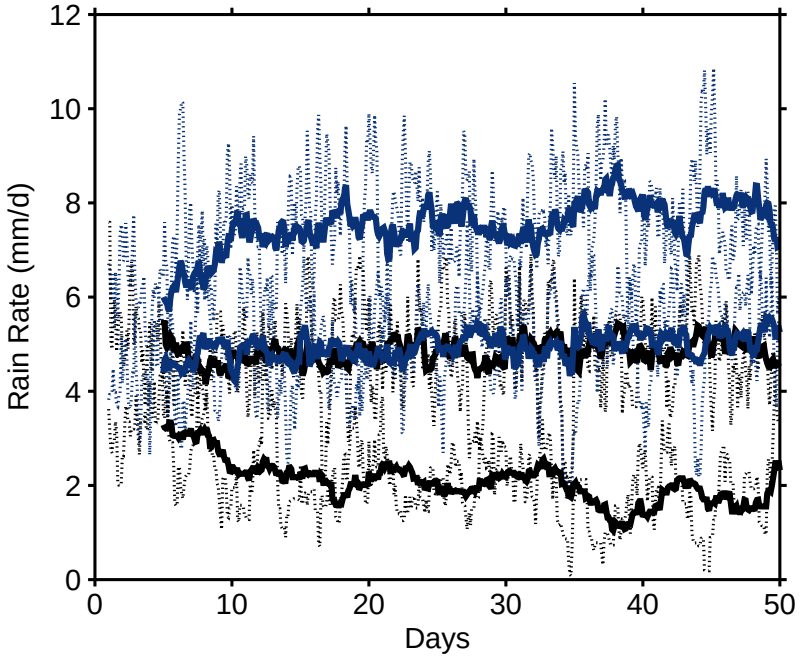

Figure 5.13 *Time series of daily (dotted curves) and five day average (solid curves) rain rate for columns 1 (black curves) and 2 (blue curves) in the coupled-column simulations performed over uniform surface forcing (middle curves) and over non-uniform surface forcing (with an SST of* 303.7 *K in column 2) (top and bottom curves). The results are shown for the entire integrations.*

lations produced in two dimensions as suggested by Zeng et al. (2007). It not easy to identify which effects are responsible for the higher-frequency variability observed in these simulations and this study does not attempt to do so.

The mean rain rates at equilibrium for columns 1 and 2 are shown as functions of SST in column 2 (see Figure 5.14) and as functions of surface wind speed in column 2 (see Figure 5.15). The mean values at equilibrium are compared with those obtained in the equivalent simulations performed under the reference-column approach.

As discussed in Section 4.4 of chapter 4, no mean large-scale circulation develops in the coupled-column system under homogeneous surface conditions no matter the type of the adjustment profiles used and the initial conditions. Hence, the CRM simulations

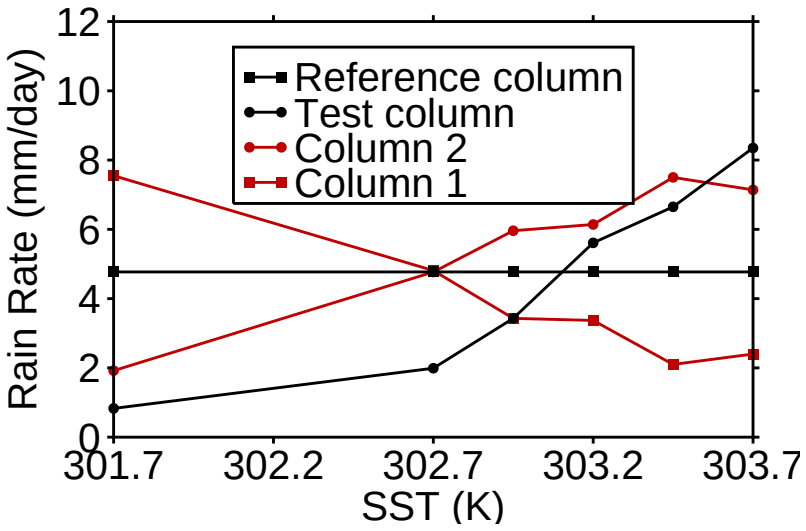

Figure 5.14 *Rain rates at equilibrium as a function of the SST. Results are shown for columns 1 (red line with squares) and 2 (red line with circles) in a set of simulations performed under the coupled-column approach. The SST of column 2 is plotted on the horizontal axis, and the SST of column 1 is* 302.7 *K. Results are also shown for the test column (black line with circles) and the RCE reference column (black line with squares) in a set of simulations performed under the reference-column approach. The SST of the test column is plotted on the horizontal axis, and the SST of the RCE reference column is* 302.7 *K.*

modified to implement the WTG calculations (two-way coupling) over uniform surface forcing do not differ from the RCE state obtained in the uncoupled control run.

With non uniform surface forcing, a large-scale circulation driven by the surface forcing difference develops with ascent in the column which has a stronger surface forcing. The column into which the ascending branch of the large-scale circulation is established warms through convective adjustment and its rain fall rate increases in response to the low level convergence of moisture by the large-scale circulation. This increase in precipitation is balanced by a reduction in precipitation in the other column, such that the energy balance of the whole system is maintained without an external source. In order to respect this constraint, for the case of columns of equal area, the simulated precipitation is required to be much less sensitive to differences in surface forcing than in the reference-column approach. In general, the mean rain rate in column 2 increases as its

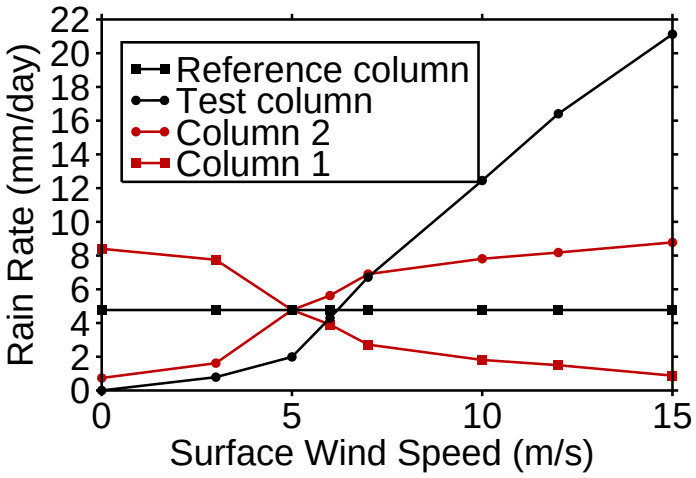

Figure 5.15 *Rain rates at equilibrium as a function of the surface wind speed perpendicular to the simulated domain. Results are shown for columns 1 (red line with squares) and 2 (red line with circles) in a set of simulations performed under the coupled-column approach. The surface wind speed in column 2 is plotted on the horizontal axis. Results are also shown for the test column (black line with circles) and the RCE reference column (black line with squares) in a set of simulations performed under the reference-column approach. The surface wind speed in the test column is plotted on the horizontal axis.*

surface forcing does. It is either less or greater than the mean value obtained at RCE of the control run as the diagnosed large-scale circulation has its descending or ascending branch in column 2.

As with the reference column approach, the relationship between CRH and rain rate is examined in the experiments performed under the coupled-column approach. The red curve in Figure 5.16 illustrates the mean rain rate versus CRH at equilibrium for column 2 in the coupled-column simulations with different surface wind speed in column 2. The total increase in CRH is much smaller in the ascending column compared to the descending column. When comparing with the results obtained in the equivalent simulations performed under the reference column approach (black curve in Figure 5.16), the column relative humidity is much less sensitive to the difference in surface forcing than in the reference column approach. In addition, the transition to rapidly increasing precipitation with CRH appears sharper in the reference column approach than in the

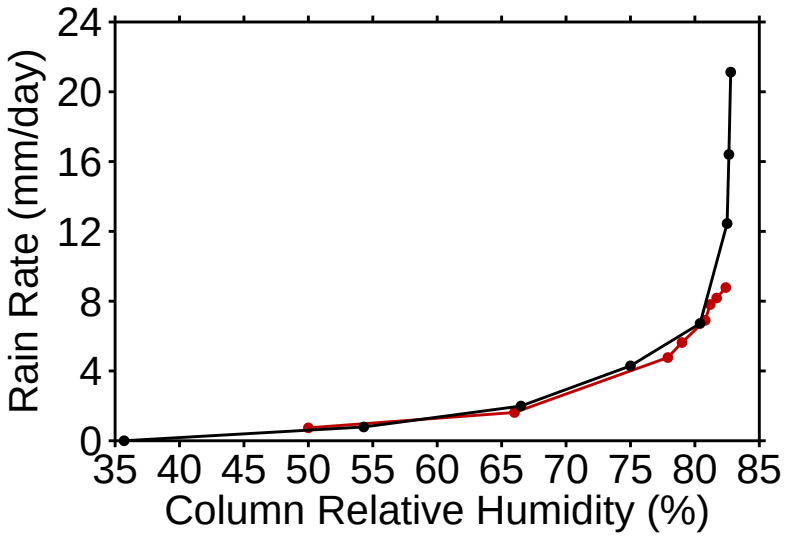

Figure 5.16 *Mean rain rate versus column relative humidity. Results are shown for the test column (black curve with circles) in the simulations performed under the reference column approach and for column 2 (red curve with circles) in the simulations performed under coupled-column approach with* $\varepsilon = 0.5$. *The values of surface wind speed perpendicular to the test column or else column 2 are* 0, 3,5,6,7,10,12 *and* 15 $m\ s^{-1}$.

coupled-column approach. For each value of surface wind speed, the values of mean rain rate and CRH obtained under the reference column approach do not correspond to those obtained under the coupled-column approach since the large-scale vertical motion is different. However, note that the relationship between the mean rain rate and CRH is qualitatively similar under both approaches, but the state achieved depends on the strength of the circulation.

5.3.2 The WTG-derived large-scale circulation

This section examines the structure of the diagnosed large-scale circulation at equilibrium state using the large-scale mass flux defined in section 5.2.2.

Figure 5.17 shows the large-scale mass flux profiles at equilibrium for column 2. For the case of simulations performed with $\varepsilon = 0.5$ thus $w_2 = -w_1$, the profiles of large-scale

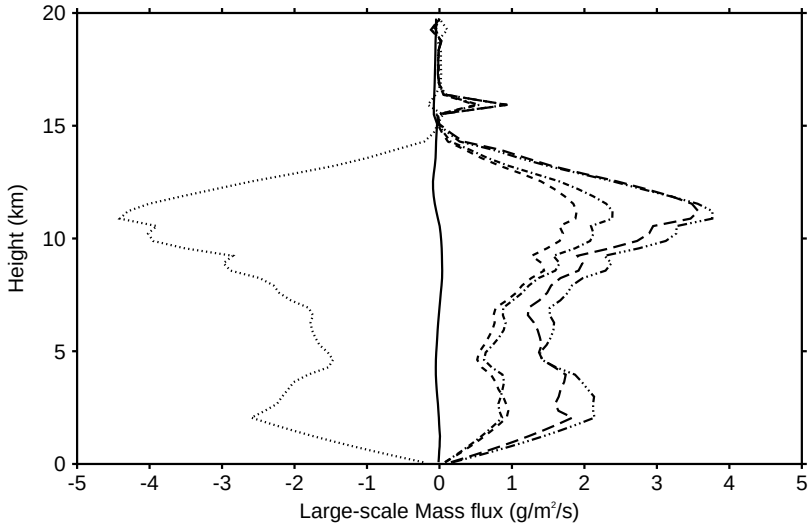

Figure 5.17 *Mean large-scale mass flux profiles for column 2. The profiles are shown for simulations performed with different SSTs in column 2. The line definitions for SSTs in column 2 are as in Figure 5.1.*

mass flux in column 1 are the opposite of those obtained in column 2. As expected, the large-scale mass flux profiles at equilibrium are nearly zero in the simulations performed over uniform surface forcing. In the simulation performed over non-uniform surface forcing, the large-scale mass flux is top heavy. The peak is centred at about 12 km and it increases as the surface forcing in column 2 increases. The top-heavy large-scale mass flux profile is typical of the western Pacific warm pool region (Back and Bretherton, 2006). However, the coupled-column configuration also produces a consistent peak in the large-scale mass flux profiles which is centered somewhere below the freezing level. The exact height at which the second maximum is centred cannot easily be identified from Figure 5.17 because of the special treatment of the large-scale vertical velocity w^{WTG} in the boundary layer (see section 2.4.2 of chapter 2). Comparison with the reference column figure (Figure 5.5) shows that a reference column can produce this double-peak structure. In the sensitivity experiments to the RCE reference potential temperature profile conducted by Raymond and Sessions (2007), this double-peak structure was found in the test column at equilibrium with a large-scale ascent. It is also observed in reanalysis data sets of the East Pacific (Back and Bretherton, 2006).

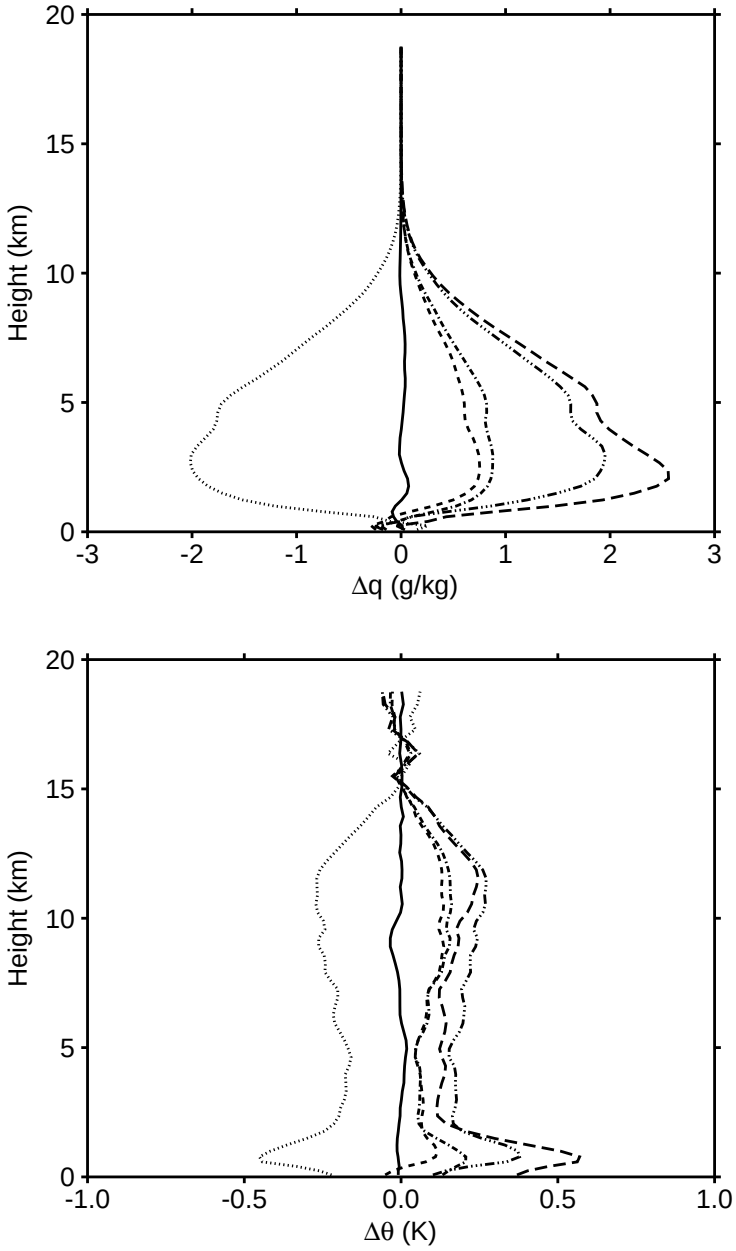

Figure 5.18 *Mean specific humidity (top panel) and potential temperature (bottom panel) difference profiles. The difference is between the mean profiles at equilibrium in column 2 and column 1. The profiles are shown for different SSTs in column 2. The line definitions for SSTs in column 2 are as in Figure 5.1.*

5.3.3 Thermodynamic and convective structures

This section examines the structure of the mean profiles at equilibrium of some thermodynamic variables, including the relative humidity, under the WTG calculations. The

convective properties and the bulk cloud properties are also examined.

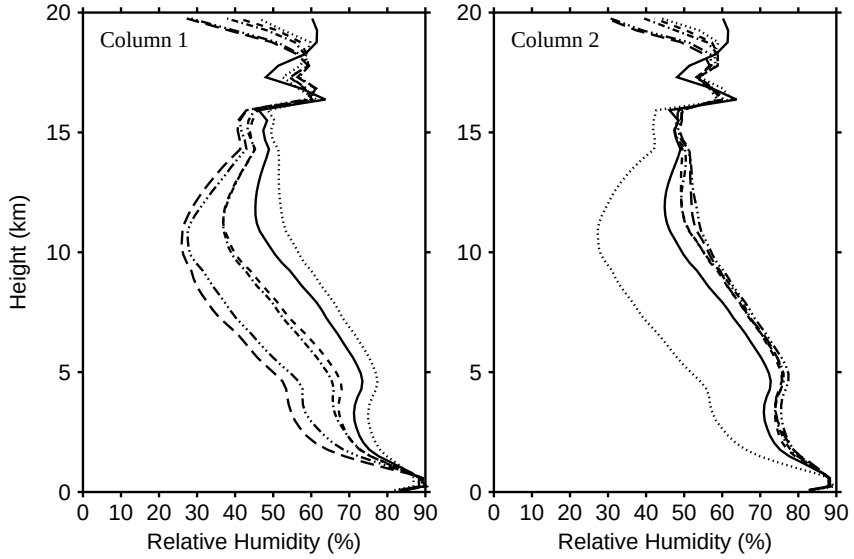

Figure 5.19 *Mean relative humidity profiles for columns 1 (left) and 2 (right). The profiles are shown for different SST simulations. The line definitions for SSTs in column 2 are as in Figure 5.1.*

Figure 5.18 shows the horizontal potential temperature and specific humidity differences under the WTG calculations. The horizontal difference is between the mean profiles obtained at equilibrium for column 2 and column 1. The horizontal differences are nearly zero at all model levels in the simulations performed over uniform surface forcing. The horizontal specific humidity difference increases as the surface forcing does, due to the transport of moisture from the cold column to the warm column by the large-scale circulation. The horizontal potential temperature difference increases with SST in the boundary layer but much less so in the free troposphere. As expected, the horizontal potential temperature difference in the free troposphere is less than the value obtained in the equivalent simulations without the WTG parameterization of the large-scale circulation. In these simulations, the horizontal potential temperature difference has a maximum value of about 0.3 K in the upper troposphere where latent heat release is also maximal. The horizontal potential temperature difference can be up to 3.5 K in the RCE simulations

with 1 K difference in SST (see the left hand panel of 3.12 of Chapter 3) as compared to the potential temperature difference of up to 3 K obtained by Ramsay and Sobel (2011) in the RCE simulations of an SCM with 1 K difference in SST. However, the temperature of the boundary layer remains closely tied to the underlying SST since the WTG calculations are not applied there. As a result, the horizontal potential temperature difference may be significantly greater within the boundary layer.

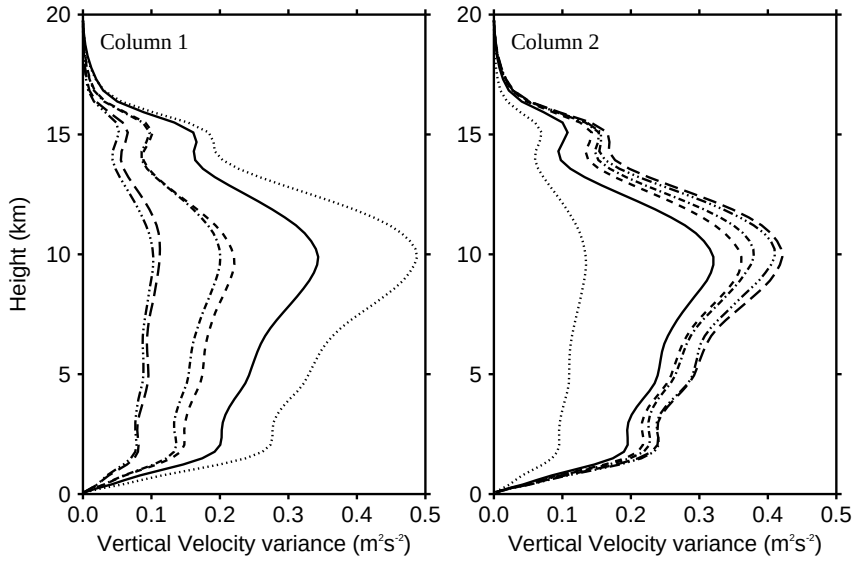

Figure 5.20 *Mean vertical velocity variance profiles for columns 1 (left) and 2 (right). The profiles are shown for different SST simulations and the line definitions are as in Figure 5.1.*

Figure 5.19 shows the mean relative humidity profiles at equilibrium for columns 1 and 2. The mean relative humidity profiles for columns 1 and 2 in the simulation performed over uniform surface forcing are very close and are very close to the mean profile obtained at RCE of the uncoupled control run (see the left hand panel of Figure 3.8 of Chapter 3) to within 1.5% difference. For 1 K difference in SST between columns 1 and 2, the column with the weaker surface forcing becomes relatively dry. This result is in response to the large-scale drying effect which suppresses convective moistening within that column relative to the other column. In column 1, the free tropospheric relative hu-

midity decreases as the SST in column 2 increases. In column 2, the free tropospheric relative humidity increases as its SST does. In the ascending column, the relative humidity has an upper limit. For that reason, the relative humidity profiles within the ascending column are very close and in addition, their values at each model level are not always an increasing function of surface forcing in column 2. In contrast to the ascending column, the relative humidity in the descending column is much more sensitive to the difference in surface forcing. As a result, the change in relative humidity with respect to the RCE profile is much greater in the descending column compared to the ascending column.

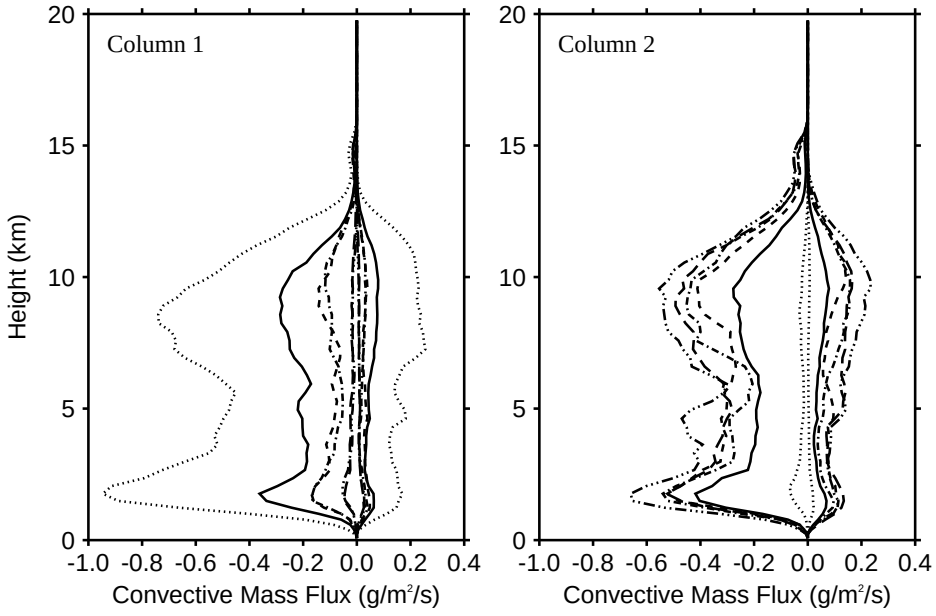

Figure 5.21 *Mean convective mass flux profiles of strong and cloudy updrafts and strong downdrafts for columns 1 (left) and 2 (right). The profiles are shown for different SST simulations and the line definitions are as in Figure 5.1.*

Further information on the response of relative humidity to the difference in surface forcing is provided by the plot of mean rain rate versus CRH for column 2 (see Figure 5.16). For an equilibrium state with a large-scale circulation, the ascending column results in much weaker sensitivity of CRH to the difference in surface forcing than the descending column. The profiles of relative humidity for each column show a bulge and

a trough near the freezing layer and near 12 km respectively. As the diagnosed large-scale circulation is strengthened, the bulge becomes flat and the trough becomes deeper within the descending column while the bulge becomes deeper and the trough becomes flat within the ascending column. These features are certainly related to the reduction of vertical transport associated with suppressed convective fluxes within the descending column and the increase of vertical transport associated with enhanced convective fluxes within the ascending column.

The mean vertical velocity variance profiles are shown in Figure 5.20. They are used to evaluate the convective activity within each of the columns. The shapes of the profiles are similar and are similar to those obtained in the reference column simulations (Figure 5.7). As expected, over uniform surface conditions the columns have similar convective activity as at RCE. Over non-uniform surface conditions, convective activity increases in the column with the stronger surface forcing while it decreases in the other column. The adjustment of convection within column 2 is due to the local increase or decrease in its surface evaporation through the changes in its surface forcing. The difference in temperature between the columns drives a large-scale circulation which in turn suppresses or enhances convection in column 1 depending on where its descending branch is established. In the coupled-column model, the energy budget must balance without any external source. To respect this constraint in the simulations with columns of equal sizes, column 2 must be less sensitive to the change in surface forcing than the test column of the reference column approach (compare Figure 5.7 with the right-hand side of Figure 5.20). In addition, convective activity within the ascending column is less sensitive to surface forcing. For instance, with 1 K difference in SST between columns 1 and 2, the total change (which respect to the RCE state) in convective activity within the ascending column is almost half the total change in convective activity within the descending column.

Convection within each of the columns is examined using M_u, M_d, σ_u and σ_d. Their mean profiles at equilibrium are shown in Figures 5.21 and 5.22.

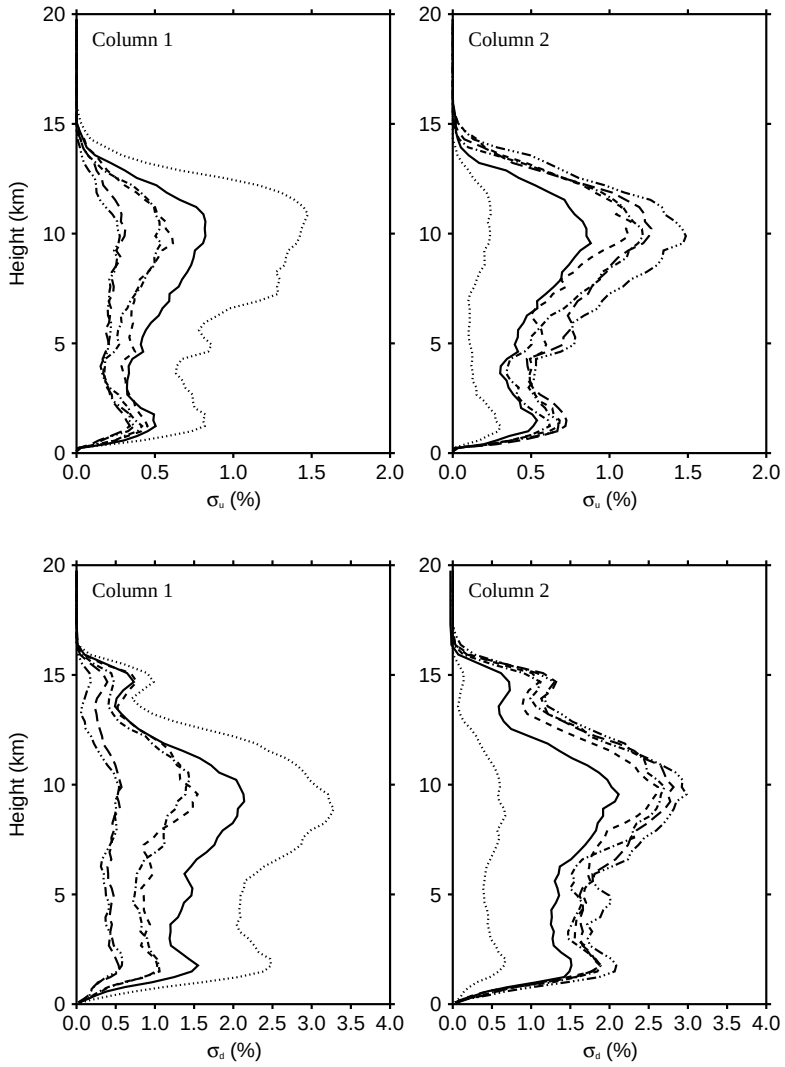

Figure 5.22 *Mean profiles of fractional area covered by strong and cloudy updrafts (top) and Strong downdrafts (bottom). The profiles are shown for columns 1 (left) and 2 (right) for the different SST simulations and the line definitions are as in Figure 5.1.*

The shapes of the profiles are similar and are similar to those obtained in the reference column simulations (see Figure 5.8). Over uniform surface conditions, columns 1 and 2 have nearly the same profiles of M_u, M_d, σ_u and σ_d. Over non-uniform surface conditions, M_u increases in the column within which the ascending branch of the large-scale circulation is established and decreases in the other column. Similarly to the convective mass flux, σ_u and σ_d increase in the column within which the ascending branch of the

large-scale circulation is established and decrease in the other column.

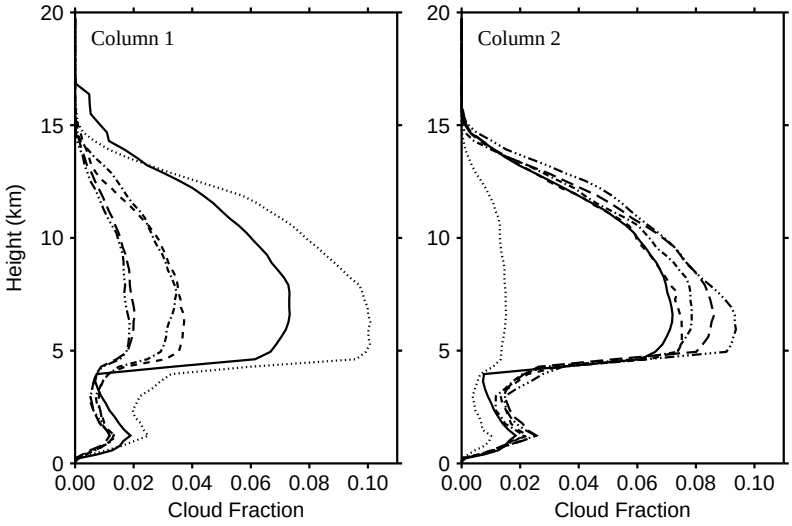

Figure 5.23 *Mean profiles of cloud fraction for columns 1 (left) and 2 (right).The profiles are shown for different SST simulations and the line definitions are as in Figure 5.1.*

The mean cloud fraction profiles are shown in Figure 5.23. The shape of the profiles are similar to those obtained in the equivalent experiments performed under the reference column approach (Figure 5.10). As expected, over uniform surface conditions, cloud fraction profiles for columns 1 and 2 are very close (covering about 7% of the domain) and are very close to the profile obtained in the uncoupled control RCE run. Over non-uniform surface conditions, the diagnosed large-scale circulation enhances convection within the column with strong surface forcing and suppresses convection within the other column. As a result, cloud fraction increases within the the column within which the ascending branch of the diagnosed large-scale circulation is established and decreases within the other column.

5.3.4 Sensitivity to the column sizes

All the coupled-column simulations described above were performed with columns of equal area, a configuration which certainly does not describe the reference column approach. As noted in section 2.4.1 of chapter 2, the reference column approach can be theoretically obtained from the coupled-column approach by setting $\varepsilon = 0$ (or $\varepsilon = 1$)

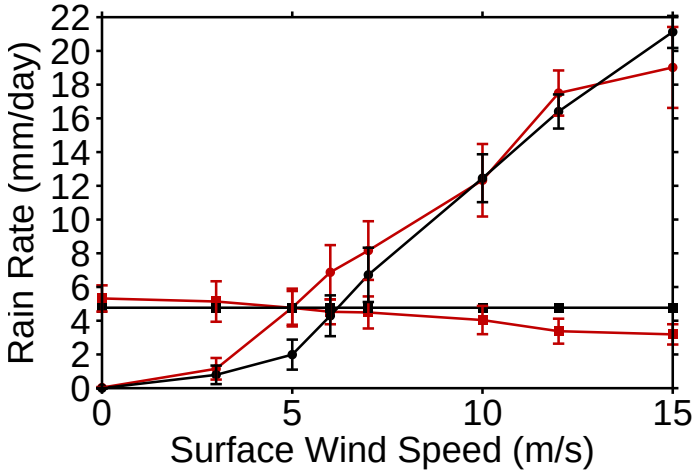

Figure 5.24 *Rain rates at equilibrium as a function of the surface wind speed perpendicular to the simulated domain. Results are shown for columns 1 (red line with circles) and 2 (red line with squares) in a set of simulations performed under the coupled-column approach with* $\varepsilon = 0.1$ *and* $\tau = 4$ *h. The surface wind speed perpendicular to column 2 is plotted on the horizontal axis. Results are also shown for the test column (black line with circles) and the RCE reference column (black line with squares) in a set of simulations performed under the reference-column approach. The surface wind speed perpendicular to the test column is plotted on the horizontal axis. The vertical bars represent* ± 1 *standard errors. The standard errors are calculated based on daily accumulated values.*

This section examines whether the coupled-column simulations exhibit similar behavior to the reference-column simulations if the former are performed with $\varepsilon \to 0$ (or $\varepsilon \to 1$). The coupled-column simulations described above are repeated for the cases of $\varepsilon = 0.1$ and $\varepsilon = 0.01$. In these simulations the WTG adjustment timescale, τ, is doubled

from 2 to 4 h in order to produce a very similar strength of the adjustment rate λ as in the reference column model (see Section 2.4.1 of Chapter 2).

For the case of simulations performed with a large difference in column areas, the smallest column is column 2 and the sensitivity to surface conditions has been investigated by changing either the SST or the surface wind speed in column 2. Some of the results from changing the surface wind speed in column 2 are shown in Figure 5.24 for the case of $\varepsilon = 0.1$. In Figure 5.24, the mean rain rates at equilibrium for columns 1 and 2 are compared to those obtained in the equivalent experiments performed under the reference column approach. The vertical bars represent ± 1 standard errors calculated based on daily accumulated values. As described in section 4.4 of chapter 4, for $\varepsilon = 0.1$, the coupled-column simulations over uniform surface forcing do not differ from the RCE state, whereas the reference column simulation do. Similar result is obtained even for the case of $\varepsilon = 0.01$. On the other hand, by choosing ε to be small, for example $\varepsilon = 0.1$ (results shown in Figure 5.24) and 0.01 (result not shown)) the coupled-column system recovers a very similar sensitivity to the difference in surface conditions as in the reference column system. Differences in sensitivity do however remain for small changes in surface conditions.

5.3.5 Coupled-column simulations versus RCE simulations

A simulation is performed under the coupled-column approach with columns 1 and 2 having SSTs of 301.7 and 303.7 K respectively, $\varepsilon = 0.5$ and $\tau = 2$ h. As described above, the difference in SST between the columns drives a large-scale circulation with ascent in column 2. Once the equilibrium is established in the system, the SSTs are flipped over the course of one day such that column 1 becomes the column with the higher SST. How the convection within each column adjusts in response to the change in SST is not investigated in this section and this will form the basis of the next chapter. Rather, the purpose of this section is to compare the system-mean state of the full two-column system

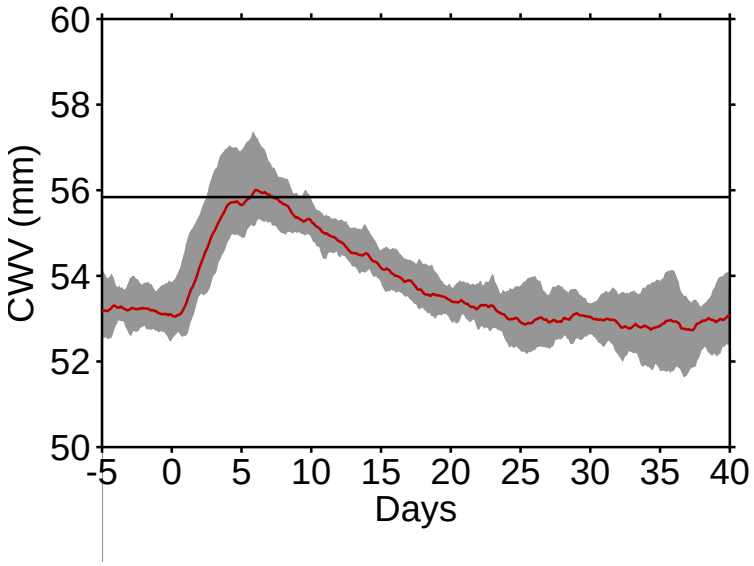

Figure 5.25 *Time evolution of daily running mean CWV in the coupled-column system. The mean CWV of the coupled-column system is computed as the sum of the fractional area times the CWV of each column. Results are shown from 5 days before the SSTs are flipped between the columns. The shaded area represents the maximal and minimal values of column-mean CWV of the 5 ensemble realizations. The solid horizontal line represents the mean CWV obtained at equilibrium in the RCE simulation of the uncoupled system with an SST of* 302.7 *K and an horizontal length of* 256 *km.*

under the WTG approach to the analogous state at RCE.

The state of the system is estimated from an ensemble average over the states obtained in 5 realizations. There is a two day difference in the timing of each realization but the averages are made by considering the start of the flip to be time zero. Figure 5.25 shows the time evolution (daily-running-mean) of the column-mean CWV in the coupled-column system starting from day 5 before the SST reversal. The column-mean CWV is computed as $(1-\varepsilon)CWV_1 + \varepsilon CWV_2$, where the subscripts 1 and 2 are used to refer to the CWV in column 1 and 2 respectively and ε is the fractional area of column 2. This column-mean CWV is compared to the mean CWV obtained in the RCE simulation of the uncoupled single CRM with an SST of 302.7 K and an horizontal domain of 256 km. These values are equal to the column-mean SST and the sum of the lengths of the two

columns.

After the SST reversal at day zero, the strength of the diagnosed large-scale circulation rapidly decreases to nearly zero within five days or so. A new large-scale circulation is established by day 7 with its ascending branch being in column 1. Column-integrated heat and moisture sources from the large-scale circulation show that days 5 to 7 correspond to the transition period over which there is a weak or no mean large-scale circulation in the coupled-column system. As with the test column of the reference column approach, the column-mean CWV in the coupled-column system at equilibrium with a diagnosed large-scale circulation is lower than the mean CWV obtained at equilibrium in the corresponding RCE simulation. A column-mean CWV equivalent to that obtained in the corresponding RCE simulation is not achieved in the coupled-column system unless it is at equilibrium with no large-scale circulation.

The relative humidity profiles in each of the columns are examined to understand why the system-mean CWV at equilibrium with a diagnosed large-scale circulation is lower than the value obtained in the equivalent RCE simulation. In the coupled-column system at equilibrium with a large-scale circulation, the moistening of the ascending column is exceeded by the drying of the subsiding column. An example is the dotted and long dashed curves on the left and right-hand panel of Figure 5.19 which shows the mean relative humidity profiles for columns 1 and 2 in the coupled columns simulations performed with an SST difference of 1 K between the columns. In the subsiding column, the change in relative humidity with respect to the RCE profile (solid curve) is large compared to that in the ascending column. As a result , the system-mean relative humidity is lower than in the corresponding RCE state. A similar result is obtained in the coupled-column system built from coupling two columns of a simple and relatively cheap version of the Single Column Model via the WTG approximation as described in Chapter 2 (result not shown). This result was also obtained in the numerical experiments performed by Bretherton et al. (2005) and Tompkins (2001), in which it was perceived as being a consequence of aggregation of convection within the simulated domain.

5.4 Conclusions

Most of the WTG studies to date have followed a reference-column approach and have focused on the sensitivity of the simulated precipitation in the test column to the difference in surface forcing. A similar set of experiments is performed here with both the reference-column approach and the coupled-column approach. For columns with very different areas, the coupled-column system with large differences in surface forcing behaves very similarly to the analogous configuration using the reference column approach, which for our model has a similar sensitivity to previous studies. Differences in behavior do, however, remain for small changes in surface forcing. For columns of equal area, the coupled-column approach results in much weaker sensitivity to surface forcing than the reference-column approach. This can be understood as a consequence of the strong constraint on the extent of possible sensitivity in the coupled-column approach, due to the prescribed cooling in combination with the closed energy budget of that system. This combination sets the total precipitation in the two columns in the coupled-column approach. No such constraint applies in the reference-column approach, even for conditions of prescribed cooling.

The state of the test column of the reference column approach was compared to the state obtained in the equivalent RCE simulation. In the reference column simulations at equilibrium with no large-scale circulation, the mean column water vapor of the test column was very close to that obtained in the corresponding RCE simulation. However, in the reference column simulations at equilibrium with a large-scale circulation, the mean column water vapor of the test column was smaller compared to the corresponding RCE value.

The system-mean state of the full coupled-column approach was compared to the state obtained in the corresponding RCE simulation. In the coupled-column simulations at equilibrium with no large-scale circulation, the mean-state of the system was similar to that of the corresponding RCE simulation. However, in the coupled-column simulations

at equilibrium with a large-scale circulation, the system-mean state was relatively dry compared to the state obtained in the corresponding RCE simulation. The latter behavior was the consequence of the non-linearity in the change in relative humidity with respect to the large-scale vertical motion within the ascending column. A similar result was obtained by Bretherton et al. (2005) and Tompkins (2001).

The differences in behavior of the coupled-column and reference-column approaches highlight the importance of a careful consideration of the appropriate energy and moisture budgets when interpreting results from studies of this nature. Chapter 6 examines the transient evolution from suppressed to active phase of convection under the coupled-column approach.

Chapter 6:
Transition from suppressed to active convection

6.1 Introduction

The coupled-column configuration permits two-way interactions between convection and the large-scale circulation to be studied within limited area models. The equilibrium responses of the coupled-column configuration to uniform and non-uniform boundary conditions have been examined in Chapters 4 and 5 respectively. Knowing that the variability of tropical convection is associated with large-scale dynamical features such as the Madden Julian Oscillations (MJO) and equatorial waves and that these large-scale features develop in response to moist convection, it is valuable to examine the transient evolution of convection in a system where convection is fully coupled to the evolution of the large-scale dynamics.

The dynamics of the transition from shallow to trade-cumulus-topped boundary layer clouds have been explored with column models and limited area CRM simulation models by Bretherton and Wyant (1997); Wyant et al. (1997). The study has been extended to the transition to deep convection by Sobel and Bretherton (2000); Kuang and Bretherton (2006); Khairoutdinov and Randall (2006); Wu et al. (2009). The aim of this study is to identify the important processes that might influence the transition from suppressed to active convection under the WTG approximation. Here, the concept of transition is justified by assuming that the formation of deep convection arises from the growth of shallow convection. For this study, a typical situation will be to consider that a large-scale

circulation develops over a tropical ocean. The large-scale circulation will be expected to enhance convection within the ascending region and suppress convection within the descending region. The next step will be to consider situations where the large-scale circulation is reduced through a combination of various factors and, a typical objective will be to examine the transient evolution of convection from a suppressed to a more active phase modulated by the large-scale circulation.

In this study, idealized, two-dimensional CRM simulations of a gradually forced transition from a suppressed to a more active phase of convection are performed by adopting the strategy described below.

1. Run the coupled-column model to equilibrium with non-uniform surface conditions.
2. Use the instantaneous states of the columns in their quasi-steady state as a set of initial conditions for the simulations of the transition.
3. Force the column with suppressed convection to undergo the transition to more active phase of convection by changing the surface forcing to uniform values across the columns.
4. Finally, examine the transient response of convection to the change in surface forcing and to the resulting change in the strength of the large-scale circulation that is caused by the change in surface forcing.

The transition to active convection is forced within the column with suppressed convection by changing surface forcing towards uniform values within both columns in three different methods which are:

1- The locally forced transition method which is conducted by increasing surface forcing in the column with suppressed convection.
2- The remotely forced transition method which is conducted by decreasing surface forcing within the column with enhanced convection.
3- The locally and remotely forced transition method which is conducted by increasing surface forcing within the column with suppressed convection while simultaneously decreasing surface forcing within the column with enhanced convection such as to obtain

uniform surface forcing within both columns.
The change in surface forcing is done by either changing the SST or the surface wind speed perpendicular to the simulated domains. However, the results from the two methods are broadly similar. Hence, only the results from changing the SST will be discussed here. An advantage of using a two-dimensional CRM is that it is computationally cheap to run compared to the three-dimensional CRM. Hence, a large number of simulations can be performed in order to obtain an ensemble-averaged behavior or in order to test different mechanisms of the transition and assess sensitivity.

This chapter is organized as follow. It begins in Section 6.2 with the description of the quasi-equilibrium states achieved within each column before the simulations of the transition. It continues in Section 6.3 with the description of the main results of simulations that applied the locally forced transition method. Section 6.4 compares these results to those of the simulations that applied the two other methods to force the transition. The same section presents results of sensitivity studies to tropospheric moisture. The transition from suppressed to active convection is quantified in Section 6.5. The roles of the large-scale circulation and surface forcing are decoupled in Section 6.6, followed by the summaries of the main findings in Section 6.7.

6.2 Mean states of the columns prior to the simulation of the transition

Three simulations are performed under the coupled-column approach with an SST difference of 2 K between the columns. In each of these simulations, column 1 is chosen to be colder than column 2 (see Table 6.1 which shows the values of SST within columns 1 and 2), the WTG coupling time scale τ is 2 h and the columns have equal areas. Each column is initialized with the mean profiles obtained in the radiative-convective equilibrium (RCE) simulation performed with the SST equal to the value within that column. These

three simulations have different mean values of SST. They are classified as C, M and W. The marks C, M and W stand for "cold", "medium" and "warm" respectively. The coupled-column system classified as M is 1 K warmer in its mean SST than the system classified as C. Likewise, the system classified as W is 1 K warmer in its mean SST than the system classified as M and hence, is 2 K warmer in its mean SST than the system classified as C.

Experiment	SST_1	SST_2
C	300.7	302.7
M	301.7	303.7
W	302.7	304.7

Table 6.1 *Values of SST (K) for columns 1 and 2. The simulations are performed with columns of equal areas and with the WTG coupling time scale* τ *of* 2 *h.*

6.2.1 Parameterized large-scale circulation

The coupled-column system is run for 50 days with the WTG calculations active. An average over the last 20 days is used to define the mean state and statistics at equilibrium. Figure 6.1 presents the mean profiles at equilibrium of heating and moistening rates from the large-scale circulation. The profiles are shown for column 1 for each of the simulations listed in Table 6.1. These heating and moistening rate profiles are used to evaluate the strength of the large-scale circulation that develops at each model level of the coupled-column simulations with the column-mean SST classified as C, M and W. As presented in Chapter 5, the absolute difference in SST drives an overturning circulation with its ascending branch being over the warmer region and its descending branch balancing the reduction in precipitation over the cooler region. The large-scale circulation at equilibrium in these three simulations are similar.

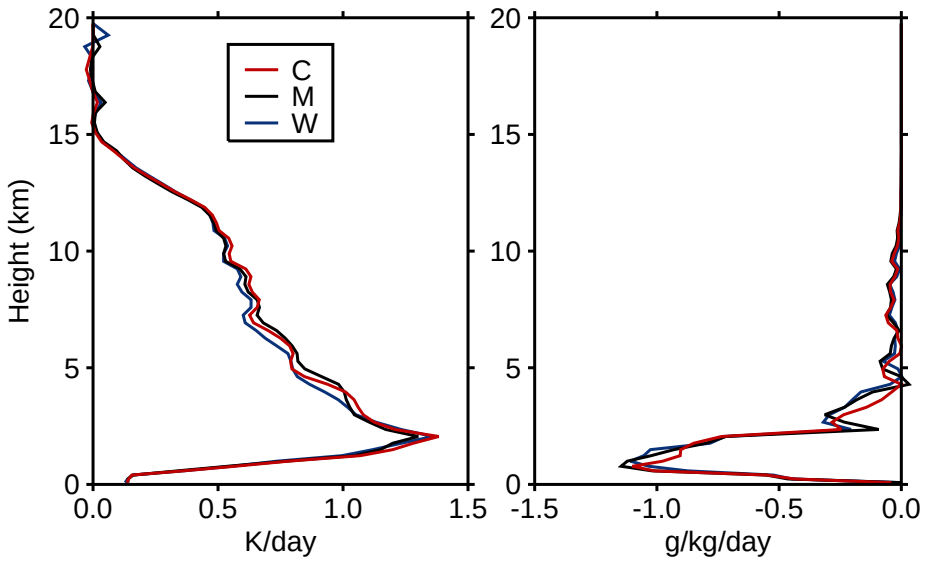

Figure 6.1 *Profiles of heating (left-hand side) and moistening (right-hand side) rates from the WTG-derived large-scale circulation. The profiles are for column 1 in the simulations listed in Table 6.1. They are obtained by averaging over the last 20 days of each simulation. Color definitions are as in Figure 6.1.*

6.2.2 Thermodynamic profiles

Figure 6.2 shows the domain-averaged profiles of heating and moistening rates from microphysics. The drying and warming effects from the descending branch of the large-scale circulation inhibit convection within column 1. By day 10, the system is approaching a quasi-equilibrium state with suppressed convection in column 1. Figure 6.3 shows the domain-averaged relative humidity profiles for columns 1 and 2. The cooling and moistening effects from the ascending branch of the large-scale circulation enhance convection within column 2. As the result, column 1 becomes relatively dry (dominated by shallow convection) while column 2 becomes relatively moist compared to their RCE states.

The quasi-equilibrium states achieved in these three simulations are very similar. In

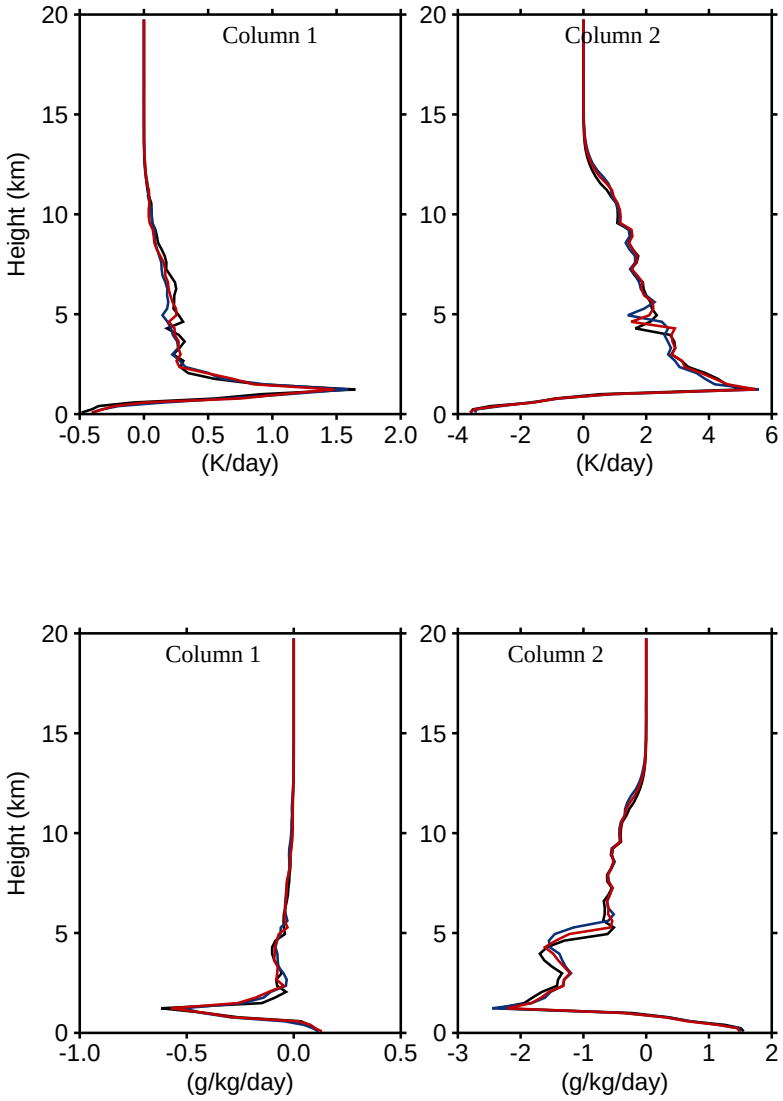

Figure 6.2 *Domain-averaged profiles of heating (top) and moistening (bottom) rates from microphysics. The profiles are for columns 1 (left-hand side) and 2 (right-hand side) in the simulations listed in Table 6.1. They are obtained by averaging the domain-averaged profiles over the last 20 days of each simulation. Color definitions are as in Figure 6.1.*

addition, the mean statistics at equilibrium (for example, the mean rain rates and surface evaporation rates) agree well to within 0.3 mm d^{-1}. The mean rain rate within column 1 has decreased by 79% (now 1 mm d^{-1}) relative to the mean rain rate of about 4.78

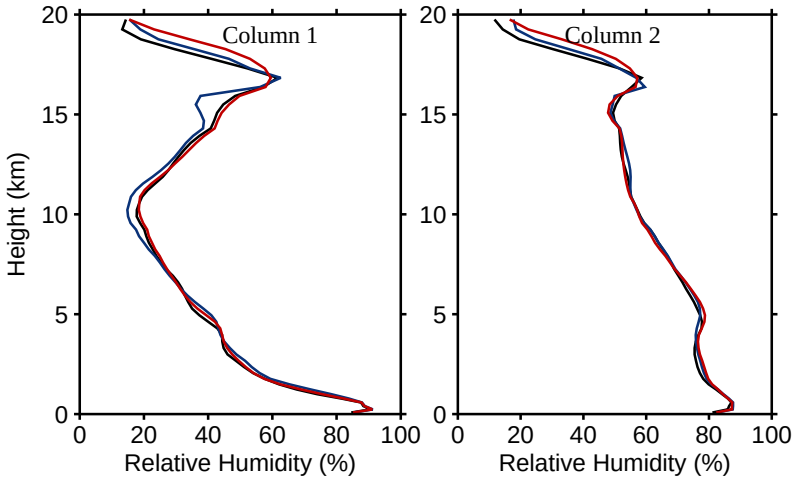

Figure 6.3 *Domain-averaged relative humidity profiles for columns 1 (left-hand side) and 2 (right-hand side) in the simulations listed in Table 6.1. The profiles are obtained by averaging the domain-averaged profiles over the last 20 days of each simulation. Color definitions are as in Figure 6.1.*

mm d^{-1} obtained in the RCE simulations with the SST of 300.7 K, 301.7 K, 302.7 K, 303.7 K and 304.7 K. However, this reduction in precipitation within column 1 must be accompanied by an increase in precipitation within column 2 such as to maintain the energy balance of the whole system. As a result, the mean rate within column 2 is now 8.47mm d^{-1}. The values of surface evaporation are 3.5 and 6 mm d^{-1} for column 1 and 2 respectively.

The simulations listed in Table 6.1 have the same value of SST difference between the columns but the actual SST in each of the columns are different. As presented above, the mean state and statistics at equilibrium in each of the columns and the strength of the large-scale circulation do not depend on the actual SST in each of the columns. Rather, they depend on the SST difference between the two columns.

6.3 Simulations of the transition

In each of the simulations described above, the large-scale circulation that develops in the system suppresses convection within column 1 relative to column 2 and relative to the convective state achieved in the equivalent RCE simulation. In this section, convection within column 1 is locally forced to undergo the transition to more active convection and the evolution of cloud and transport statistics is examined.

The simulation of the transition from suppressed to active convection is conducted with the initial conditions taken from instantaneous profiles at equilibrium of the simulation C. Column 1 is forced to undergo the transition by increasing the SST within column 1 to the value within column 2 over the course of one day. This is an example of the simulation of the transition from suppressed to more active convection which is driven by the change in the underlying SST and then by the induced change in the strength of the large-scale circulation.

The simulation is run for 40 days after the start of the SST transition. The ensemble-mean results are obtained by averaging the results of five realizations, which in this study are differentiated by the time at which the transition is initialized. In this study, there are two days difference in the initial time of each realization and the ensemble averages are made by considering the start of the SST change to be time zero. As presented in Section 5.3.1 of Chapter 5, the time evolution of some fields (for example: precipitation) exhibits high-frequency variability which is partly due to the two dimensional domain used as first noted by Grabowski et al. (1998). Hence, the ensemble-averages are applied to provide a smoother version of features which are also evident in individual realization. This set of ensemble realizations will be henceforth be referred to as experiment 1.

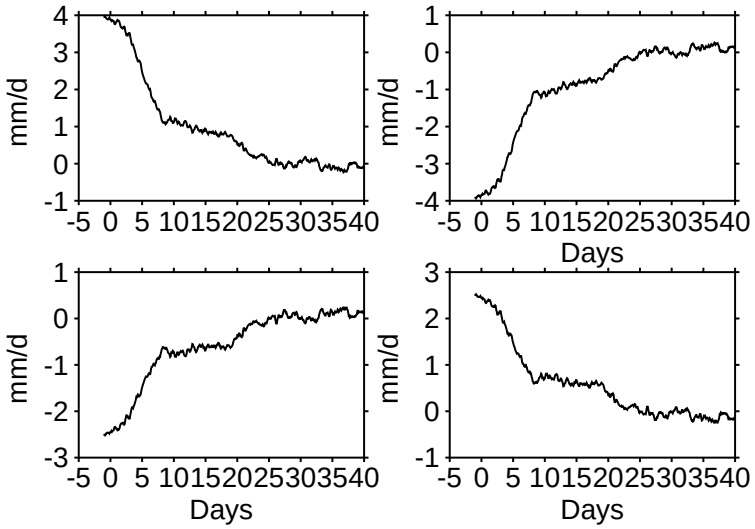

Figure 6.4 *Time evolution of column-integrated heating (top) and moistening (bottom) rates from the large-scale circulation. The results are the five days running mean and ensemble-averaged for columns 1 (left-hand side) and 2 (right-hand side) of experiment 1.*

6.3.1 Time evolution of some column-integrated fields

This section explores how precipitation, surface evaporation and column-integrated transport by the large-scale circulation adjust in response to the change in SST within column 1. Despite the ensemble mean used in this study, the precipitation still contains high frequency variability and unless otherwise stated, the time evolution of all the fields presented here are the five days running mean.

Figures 6.4 and 6.5 present the temporal evolution of column-integrated heating and moistening rates from the large-scale circulation and the temporal evolution of surface evaporation and precipitation rates respectively. The results are the five days running mean for columns 1 and 2. The transition from suppressed to more active phase of convection starts at day 0 (henceforth be referred to as the initial time). Hence, results presented for days before the initial time are those of the simulation C.

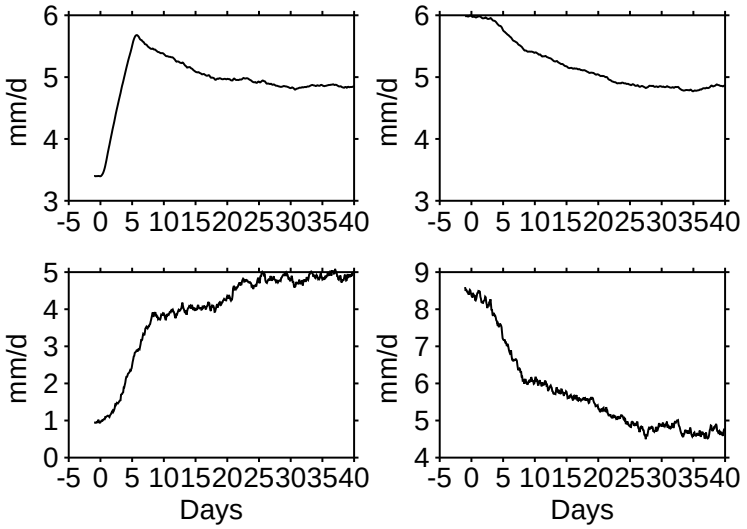

Figure 6.5 *Time evolution of surface evaporation (top) and rain rates (bottom). The results are the five days running mean and ensemble-averaged for columns 1 (left-hand side) and 2 (right-hand side) of experiment 1.*

As already discussed in Section 6.2, surface evaporation and rain rates are reduced within column 1 and enhanced within column 2 in response to the diagnosed large-scale circulation in simulation C that advects moisture from column 1 to column 2. From the initial time, the SST within column 1 is increased at the rate of 2 K d^{-1} until day 1 when it reaches the value within column 2; that is 302.7 K. The change in SST forces change in the strength of the large-scale circulation via the change in the temperature differences between the columns. The large-scale circulation decreases rapidly over the first 8 days, followed by a much slower decrease. Over a long period of integration, the columns adjust towards a final equilibrium state with no time-mean large-scale circulation and with the mean states and statistics very similar to those obtained in the RCE simulation with an SST of 302.7 K (see Chapter 4).

Surface evaporation within column 2 decreases slowly toward the RCE value. However, surface evaporation within column 1 increases abruptly, driven by the increase in the underlying SST, before decreasing slowly toward the RCE value. Over days 0 to 7,

precipitation rate within column 1 presents a rapid increase driven by the weakening in the strength of the large-scale forcing, before evolving slowly and recovers the RCE value by day 25. The effect of an increase in rain rate within column 1 is a reduction in rain rate within column 2. While this effect is present (temporal evolution of precipitation rate within column 2 shown on the bottom panel and right-hand side of Figure 6.5), it also shows a rapid decrease which however, is slightly delayed relative to the rapid increase in precipitation that occurs within column 1.

6.3.2 Time evolution of some vertical fields

Column-integrated values hide information on the vertical structure. Therefore, they cannot be used to evaluate how each model level adjusts. Figure 6.6 presents the time-height cross sections of heating rates from the derived large-scale circulation, domain-averaged relative humidity and domain-averaged heating rates from microphysics. The results presented are for column 1 of experiment 1. As presented in Section 6.2.1, the equilibrium state achieved before the simulation of the transition is an equilibrium state with a large-scale circulation which heats and dries column 1. As a result, convection is suppressed within column 1 and its free troposphere becomes relatively dry.

From the initial time, energy is put into column 1 and hence into the system as a whole. Convective cells become more active. However, they quickly lose buoyancy due to the entrainment of dry environmental air. As a result, the first apparent changes in the vertical structure of convection are delayed until shortly after day 2. After day 1 the SST within column 1 is already equal to the value within column 2. The large-scale circulation is not switched off instantaneously. Rather, its strength reduces and reaches a value very close to zero over a period of about 20 days. Hence, the large-scale circulation delays the transition to deep convection compared to an experiment performed with the WTG calculations off (not shown) from the initial time. As the large-scale circulation is reduced, moisture is recharged into the free troposphere and convective cells deepen

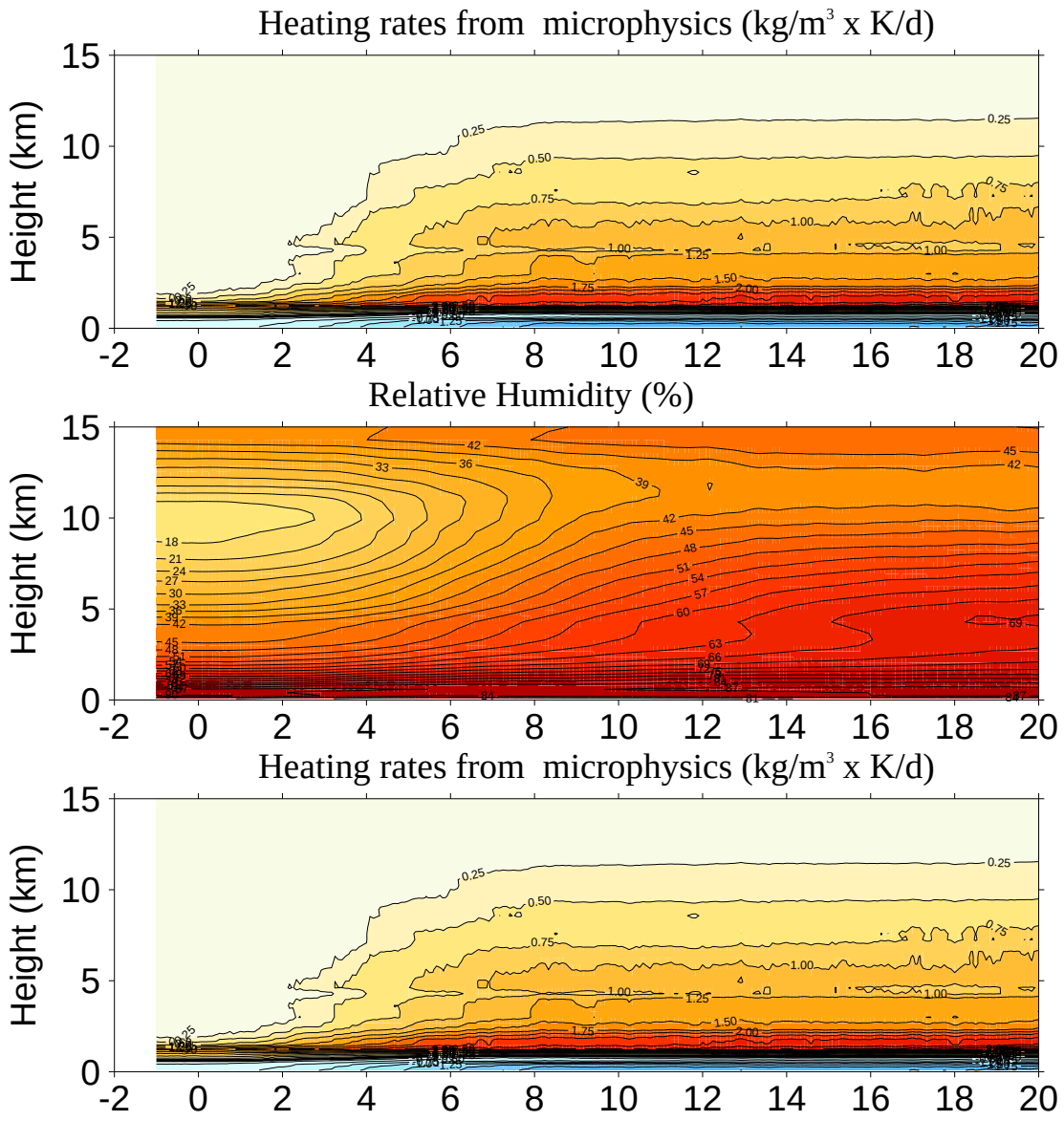

Figure 6.6 *Time-height cross sections of heating rates from the derived large-scale circulation (top panel), domain-averaged relative humidity (middle panel) and domain-averaged heating rates from microphysics (bottom panel). The profiles are the five days running mean and ensemble-averaged for column 1 of experiment 1. The contour intervals are* 0.25 $kg/m^3 \times K\,d^{-1}$ *for the top and bottom panels and* 3% *for the middle panel.*

accordingly. Shortly after day 3, the large-scale circulation is rapidly reduced in the free troposphere and more convective clouds are able to grow past the layer of intermediate

clouds around the freezing level located at about 5 km. After day 8, very little large-scale circulation remains in the whole troposphere. As a result, convective cells are able to emerge with cloud tops as high as the tropopause level. In this experiment, column 1 moves from a state with suppressed convection to a state with more deep convection over a period of about 8 days.

Figure 6.7 compares soundings at four different times during the transition period within column 1. From the initial state to the equilibrium state, there is apparently a little convective inhibition (CIN, see definition in Section 1.1 of Chapter 1). However, the thermodynamic soundings have a considerable amount of convective available potential energy (CAPE, see definition in Section 1.1 of Chapter 1) for an undiluted parcel to rise from the near-surface to the upper troposphere (the dot-dashed lines in Figure 6.7). The CAPE increases from 1323 J kg^{-1} at the initial time to the mean value of 1958 J kg^{-1} obtained by averaging over days 30 to 40. In the initial state, there is an inversion at about 900 hPa, where the boundary layer with temperature tied to the surface temperature of 300.7 K meets the free troposphere with temperature constrained to remain close to the RCE profile at 301.7 K (value of the column-mean SST at the initial time). This inversion caps convection and despite the important amount of CAPE, convective cells which succeed to go beyond the boundary layer entrain the dry air of their surroundings and quickly lose buoyancy due to evaporative cooling (e.g. Derbyshire et al., 2004).

At day 1 the SST within column 1 is already 2 K warmer than its value at the initial time but the large-scale circulation remains for several days. As a result, convective cells which become active are not able to develop or penetrate above 3 km until day 3. Hence, even within an environment characterized by a very low CIN, the availability of positive energy at high levels is not by itself sufficient to prevent the dryness from inhibiting convection. As the large-scale circulation is reduced, the middle tropospheric moisture is increased favoring further development of convection. The increase in moisture in the free troposphere increases convective rainfall (Figure 6.5) but the transition from suppressed to more active convection does not occur until the middle troposphere

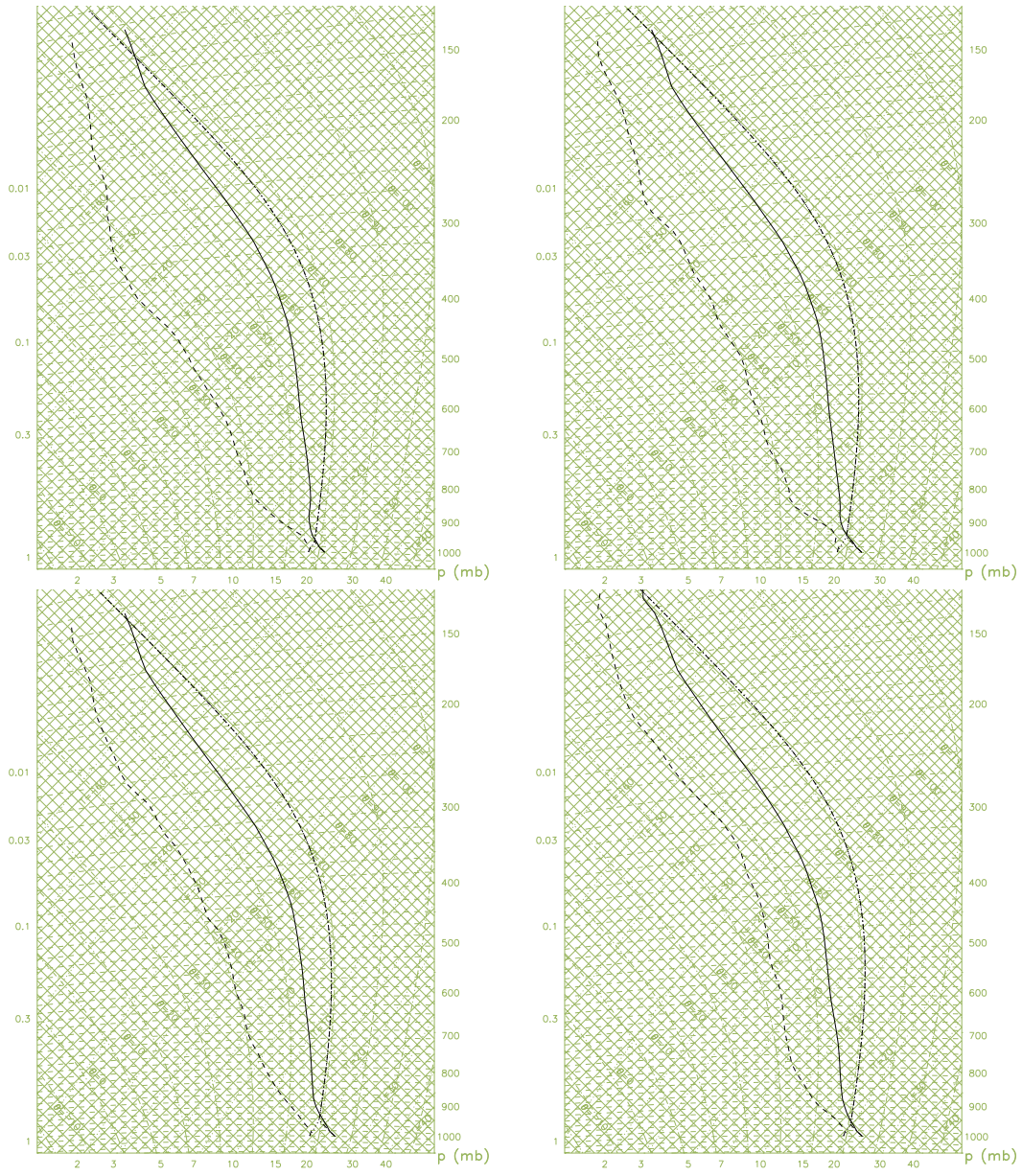

Figure 6.7 *Temperature (solid curves) and specific humidity (dashed curves) profiles for column 1 of experiment 1. The profiles are plotted at the end of days* 0 *(top and left-hand side), 2 (top and right-hand side), 3 (bottom and left-hand side) and 6 (bottom and right-hand side) for column 1 of experiment 1. The dash-dotted curves represent parcel ascent from the surface ignoring entrainment of the environmental air.*

is sufficiently moistened. The inversion located at about 900 hPa at the initial time gets eroded as convection becomes more active and deepens. From day 6, the inversion is no longer apparent. Between days 3 to 6, significant changes occur to the CAPE and

tropospheric moisture. During this period, a transition to deep convection occurs as soon as the middle tropospheric moisture becomes moist enough for the column to be able to sustain convection with properties similar to those obtained in the RCE simulation with an SST of 302.7 K.

From Figures 6.6 and 6.7, it is clear that the structure of convection evolves continuously during the transition period. With this knowledge, it is essential to identify the important processes during the transition from a suppressed to a more active phase of convection which might be useful to evaluate assumptions when developing an unified shallow and deep cumulus parameterization scheme.

6.4 Sensitivity experiments

A transition from a suppressed to a more active phase of convection is simulated in column 1 of experiment 1 described above. However, previous works suggest that the transition mechanism may be sensitive to many factors (e.g. Kuang and Bretherton, 2006; Wu et al., 2009). This study does not consider the sensitivity to parameters that arise in the cloud microphysics and subgrid scale turbulent processes. In contrast, it considers the sensitivity to the method applied to reduce the large-scale circulation in the system and to the tropospheric moisture.

6.4.1 Sensitivity to the method of forcing the transition

In this section, the large-scale circulation that suppresses convection within column 1 is reduced by applying different methods. The different methods applied to eliminate the large-scale circulation from the system are developed using the simulations with column-mean SST classified as W and M so that the final column-mean SST and final state are the same in all the experiments.

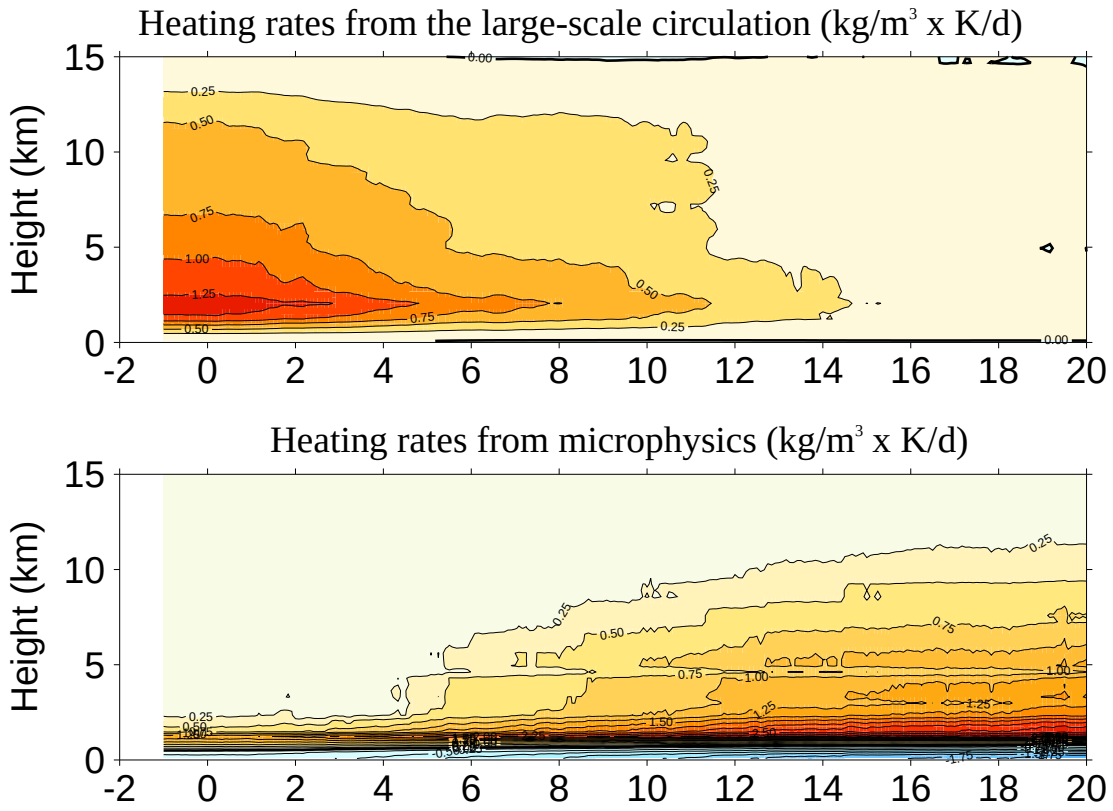

Figure 6.8 *Time-height cross sections of heating rates from the derived large-scale circulation (top) and domain-averaged heating rates from microphysics (bottom). The profiles are the five days running mean and ensemble-averaged for column 1 of experiment 2. The contour interval is* $0.25\ kg/m^3 \times K\ d^{-1}$ *for the top and bottom panels.*

The simulation of the transition is realized five times using the initial conditions taken from five instantaneous states at equilibrium of the simulation W. For each realization, the large-scale circulation is reduced in the system by decreasing the SST within column 2 to the value within column 1 over the course of one day. This is an example of the transition from suppressed to active convection being driven by a change in the large-scale circulation that is caused by the remote change in SST. This ensemble of realizations will be henceforth be referred to as experiment 2.

An experiment has also been performed with five realizations starting from instan-

taneous states at equilibrium of the simulation M. For each realization, the large-scale circulation is reduced in the system by increasing the SST within column 1 while simultaneously decreasing the SST within column 2 such as to obtain the same value of 302.7 K within each of the columns over the course of one day. This is an example of the transition from suppressed to active convection driven by the changes in both the local and remote SSTs and by the resulting change in the large-scale circulation. This ensemble of realizations will be henceforth be referred to as experiment 3.

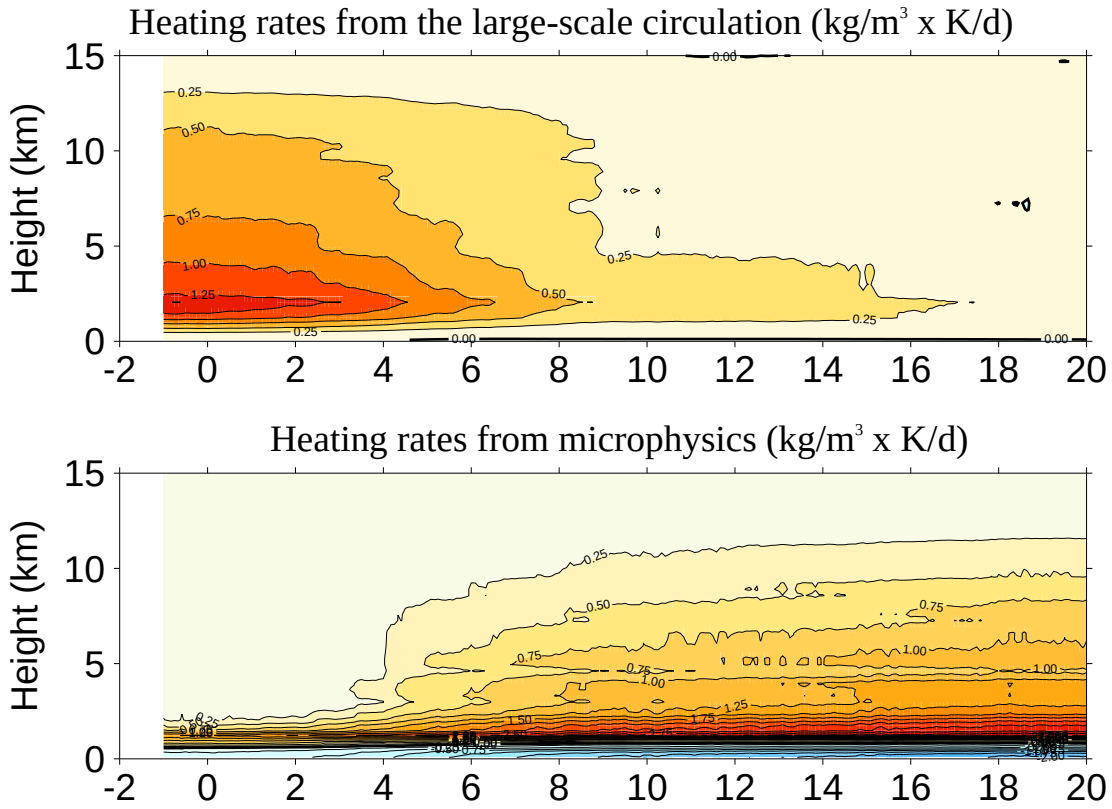

Figure 6.9 *Time-height cross sections of heating rates from the large-scale circulation (top) and domain-averaged heating rates from microphysics (bottom). The profiles are the five days running mean and ensemble-averaged for column 1 of experiment 3. The contour interval is* 0.25 $kg/m^3 \times K\,d^{-1}$ *for the top and bottom panels.*

Figures 6.8 and 6.9 present the time-height cross sections of heating rates from the large-scale circulation and the domain-averaged heating rates from microphysics. These

results are for column 1 of experiment 2 (Figure 6.8) and column 1 of experiment 3 (Figure 6.9). They can be directly compared to the upper and lower panels of Figure 6.6.

By increasing the underlying SST within column 1 of experiment 1, shallow convection becomes more active. The inversion at the top of the boundary layer becomes flat as the boundary layer warms and moistens, suggesting that the column becomes more unstable to convection. Such feedback effects do not occur within column 1 of experiment 2, since its underlying SST is not increased. As a result, convection emerges more quickly within column 1 of experiment 1 relative to column 1 of experiment 2. As expected, the first change in the vertical structure of convection is delayed within column 1 of experiment 2. It appears shortly after day 4. This delay is reflected in all of the diagnostic fields examined. As an example, the large-scale circulation lasts longer in the upper troposphere of experiment 2. As a result, the transition period is extended until day 12 within column 1 of experiment 2 compared to day 8 within column 1 of experiment 1. However, for the 1 K increase in local SST within column 1 of experiment 3 compared to the 2 K increase in local SST within column 1 of experiment 1, such feedback effects do occur within column 1 of experiment 3 but at rates smaller than those occurring within column 1 of experiment 1. Hence, within column 1 of experiment 3 the first change in the vertical structure of convection is delayed relative to experiment 1 but is advanced relative to experiment 2. It appears shortly after day 3 and the transition period is extended until day 9. Nevertheless, the common feature of all these simulations is that as the strength of the large-scale circulation decreases, moisture is recharged into the dry column and convection deepens accordingly.

Experiments 1 to 3 represent different methods of forcing the transition in column 1; the locally forced transition, the remotely forced transition and the locally and remotely forced transition for experiments 1, 2 and 3 respectively. However, the differences in the results do not necessarily indicate a dependency on the methods of forcing the transition. An alternative explanation could be that the differences occur due to different values of the column-mean SST at the initial time. Hence, it is important to investigate separately

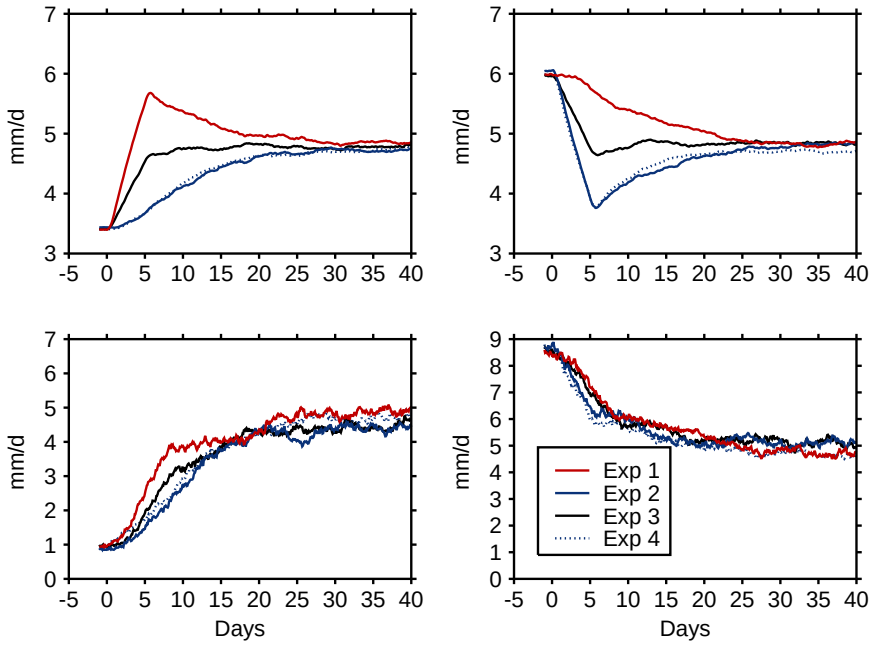

Figure 6.10 *Time evolution of surface evaporation rates (top) and rain rates (bottom). The results are the five days running mean and ensemble-averaged for columns 1 (left-hand side) and 2 (right-hand side) of the experiments 1 to 4.*

the sensitivity to the column-mean SST.

An experiment is performed in which the transition is realized five times using initial conditions taken from five instantaneous states at equilibrium of the simulation C. For each realization, column 1 is forced to undergo the transition from suppressed to active convection by decreasing the SST within column 2 to the value within column 1 over the course of one day. Similarly to experiment 2, this is an example of the transition from suppressed to active convection driven by the change in the large-scale circulation that is caused by a remote change in SST. This ensemble of realizations will be henceforth referred to as experiment 4.

Figure 6.10 compares the temporal evolution of surface evaporation and precipitation rates for columns 1 and 2 in experiments 1 to 4. The results for days before the initial

time are those in the simulations listed in Table 6.1. As already discussed in section 6.2, the strengths of the large-scale circulations that develop in the simulations C, M and W are very close and similarly, the mean states and statistics at equilibrium are also very close. In all these experiments, the changes in SSTs drive changes in the strength of the large-scale circulation and over a long period of integration, there is no time-mean large-scale circulation in the system and the final equilibrium state achieved is very close to the equilibrium state achieved in the equivalent RCE simulation.

The changes in SSTs influence surface evaporation. Surface evaporation within the column that is not forced at the surface adjusts slowly toward the RCE value while surface evaporation within the column that is forced makes an abrupt change, followed by a slow adjustment toward the RCE value. The lower panel of Figure 6.10 shows precipitation. As with evaporation, precipitation increases within column 1 and decreases within column 2 as the large-scale circulation is reduced from the system.

Attention is now turned to the fields obtained within each column of experiments 2 and 4. The results obtained for experiment 2 (solid blue curves) are broadly similar to those obtained for experiment 4 (dotted blue curves). Hence, the transition to active convection is insensitive to the value of the column-mean SST (which is the only difference between the experiments (see Table 6.2)).

6.4.2 Sensitivity to the troposphere moisture

The experiments conducted so far have demonstrated that moisture is continuously recharged into column 1 during the transition period. However, moisture is still advected out of column 1 by the large-scale circulation until approximately 20 days after the transition is initialized (Figure 6.4). As a result, the moisture adjustment back to the RCE state is delayed by the large-scale circulation. With this knowledge, it becomes important to examine the effects of tropospheric moisture on the transition from suppressed to active convection. Using the simulation M, the time scale of moisture adjustment back

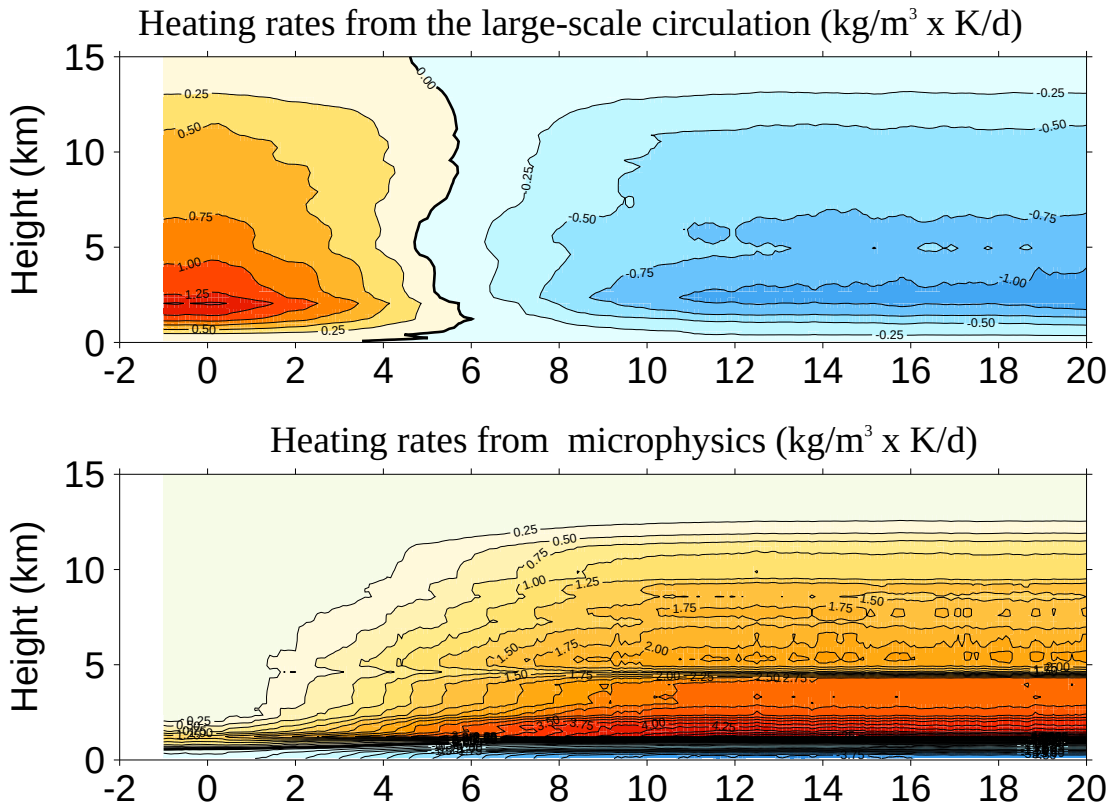

Figure 6.11 *Time-height cross sections of heating rates from the derived large-scale circulation (top) and domain-averaged heating rates from microphysics (bottom). The profiles are the five days running mean and ensemble-averaged for column 1 of experiment 5. The SST reversal starts at day* 0 *and column 1 becomes the new column with higher SST over the course of one day. The contour interval is* 0.25 *kg/m*^{3} $\times$ *K d*$^{-1}$ *for the top and bottom panels.*

to the RCE state is shortened by flipping the SST between the columns such that column 1 becomes the column with the higher SST over the course of one day. This simulation is realized five times and the ensemble realizations will be henceforth referred to as experiment 5.

The heating rates from the large-scale circulation and heating rates from microphysics for column 1 of experiment 5 are presented in Fig. 6.11 . The initial large-scale circulation with descent within column 1 is rapidly reduced over a period of 5 days or so before

a permanent large-scale circulation with ascent within column 1 is established in the system before day 6. In this experiment, the moisture adjustment back to the RCE state is quicker (within 5 days) and the large-scale circulation stars to pump moisture into column 1 shortly after day 5. This time scale is short compared to the time scale obtained in other experiments. As a result, deep convection develops rapidly and the transition period is short compared to the periods obtained in experiments 1 to 4. Hence, similarly to the results of Kuang and Bretherton (2006), the results of experiment 5 confirm the role of mid-troposphere dryness in delaying the development of deep convection.

6.5 The transition time

Experiments	SST_{int_1}	SST_{int_2}	SST_{final_1}	SST_{final_2}
Experiment1	300.7	302.7	302.7	302.7
Experiment2	302.7	304.7	302.7	302.7
Experiment3	301.7	303.7	302.7	302.7
Experiment4	300.7	302.7	300.7	300.7
Experiment5	301.7	303.7	303.7	301.7

Table 6.2 *Values of SST (K) for columns 1 and 2 at the initial time and at the end of experiments 1 to 5.*

Table 6.2 presents the values of SSTs for columns 1 and 2 at the beginning and at the end of experiments 1 to 5. As presented in Section 6.4, the mechanism of transition is not sensitive to the value of column-mean SST at the end of the simulation. Hence, experiment 4 will be omitted in this section. How column 1 evolves from a state with suppressed convection to a state with more active convection is apparently different in experiments 1 to 3. As done by Wu et al. (2009), this study uses the concept of the transition time t^* to study the nature of the transition. Here, t^* is defined based on the rate of increase of the rain rate RR.

The temporal evolution of RR for column 1 in experiments 1, 2, 3 and 5 are presented

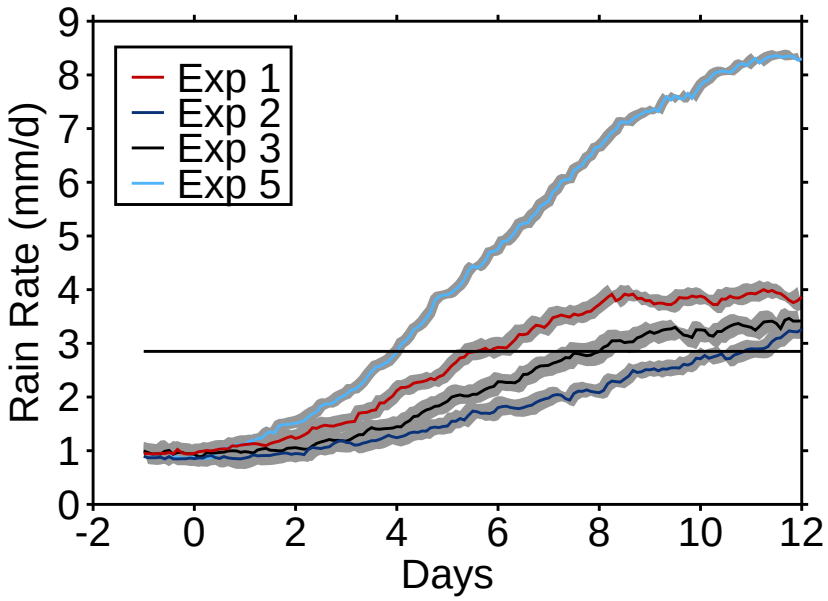

Figure 6.12 *Time evolution of rain rates. The results are the five days running mean and ensemble-averaged (solid curves) for columns 1 of experiments 1, 2, 3 and 5. The shaded areas represent the range of the five ensemble realizations. The horizontal line represents the value of* $\mathrm{RR}^* = 2.85\ mm\ d^{-1}$ *(half way to the RCE control value).*

in Figure 6.12. The range of the five ensemble realizations are also shown. As already presented in Section 6.2, for days before the initial time, precipitation rates produced in all the simulations listed in Table 6.1 are very close. Their values are considerably reduced within column 1 relative to column 2 and relative to the RCE value. From day 0 precipitation rates evolve roughly at the same rate and shortly after, the rate of increase becomes most pronounced within column 1 of experiment 5. This result is in response to the rapid adjustment of moisture compared to the other experiments. From day 2, the rate of increase of rain rate becomes more pronounced in column 1 of experiment 1 and its time evolution remains significantly different from that within column 1 of experiments 2 and 3 until day 12. From day 4, the time evolution of rain rate within column 1 of experiment 3 becomes significantly different from that within column 1 of experiment 2 until day 12.

Since the final equilibrium state achieved in experiments 1 to 3 is known to be the RCE state at 302.7 K, it becomes reasonable to define t^* based on the rain rate deficit $\mathrm{RR_d}$ within column 1. That is calculated as

$$\mathrm{RR_d} = \mathrm{RR_{RCE}} - \mathrm{RR(t<0)} \tag{6.1}$$

where $\mathrm{RR_{RCE}}$ is the rain rate at RCE with an SST of 302.7 K and $\mathrm{RR(t<0)}$ is the mean rain rate obtained by averaging over 10 days before the initial time. t^* is then estimated as the time when the rain rate is halfway to the RCE value. That is:

$$\mathrm{RR(t^*)} = \mathrm{RR^*} \tag{6.2}$$

with

$$\mathrm{RR^*} = \mathrm{RR(t<0)} + \frac{1}{2}\mathrm{RR_d} \tag{6.3}$$

In this study $\mathrm{RR^*} = 2.85$ mm $\mathrm{d^{-1}}$. The values of t^* obtained for column 1 of experiments 1, 2, 3 and 5 are listed in Table 6.3. As expected, the value of t^* for column 1 of experiment 5 is the shortest. For the reasons given in Section 6.4.1, the transition to active convection is expected to be delayed in experiment 2 compared to experiment 1 since the transition mechanism is found to be more effective when the system is forced locally. The value of t^* for column 1 of experiment 2 is the longest. It is about 11 days; a value which is almost twice that obtained for column 1 of experiment 1. Finally, the rates of SST increase and decrease within columns 1 and 2 of experiment 3 are half the rate of SST increase within column 1 of experiment 1 and half the rate of SST decrease within column 2 of experiment 2. As a result, the transition time obtained for column 1 of experiment 3 is in between the values obtained for column 1 of experiments 1 and 2.

Experiments	Experiment 1	Experiment 2	Experiment 3	Experiment 5
transition time, t^*	5.4	10.9	8.0	3.9

Table 6.3 *Transition time (days).*

The present idealized experimental setup allows the transition from suppressed to active convection to occur slowly over the time scale characterizing changes in the strength

of the large-scale circulation that might develop over a warm pool. In this study, the transition time varies between 4 to 11 days. The transition time obtained in the experiment that applied a locally forced transition method is only a day longer than the value of about 4 days obtained by Kuang and Bretherton (2006) in their simulation of the transition that is forced by the local increase in sensible and latent heat fluxes over ocean. However, it is much longer compared to the few hours obtained in the simulation of diurnal evolution of the transition over land (e.g Khairoutdinov and Randall, 2006; Grabowski et al., 2006; Wu et al., 2009) in which the rates of local surface forcing increase are very large compared to the values applied in this study and in the study of Kuang and Bretherton (2006).

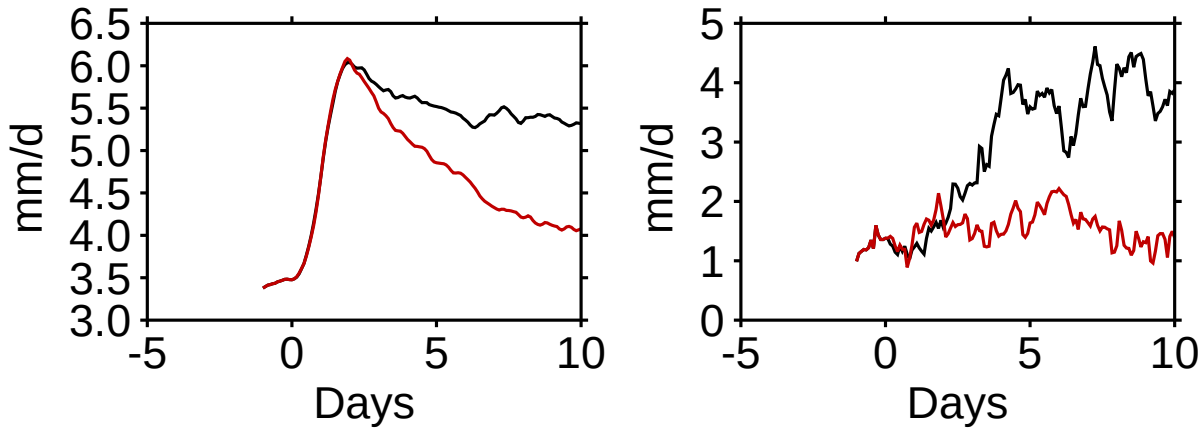

Figure 6.13 *Time evolution of surface evaporation (left-hand side) and precipitation rates (right-hand side). The results presented are daily-averaged and ensemble-averaged for the dry column of experiment 1 (black curves) and for the dry column of an experiment similar to experiment 1 but with fixed profiles of heating and moistening rates from the large-scale circulation (red curves). The forcing profiles are imposed from day* 0 *onwards and are those obtained by averaging over the previous* 10 *days.*

6.6 The roles of surface forcing and large-scale forcing

Within column 1 of experiment 1, the change in convection is a response to the change in underlying SST and to the resulting change in large-scale circulation. However, within column 1 of experiment 2, the change in convection is a response to only a change in large-scale circulation. To isolate the contributions from the change in SST, experiments 1 and 2 are restarted at day 0. On this occasion, the profiles of heating and the moistening rates from the large-scale circulation are fixed to those obtained by averaging over 10 days before the SST change is made.

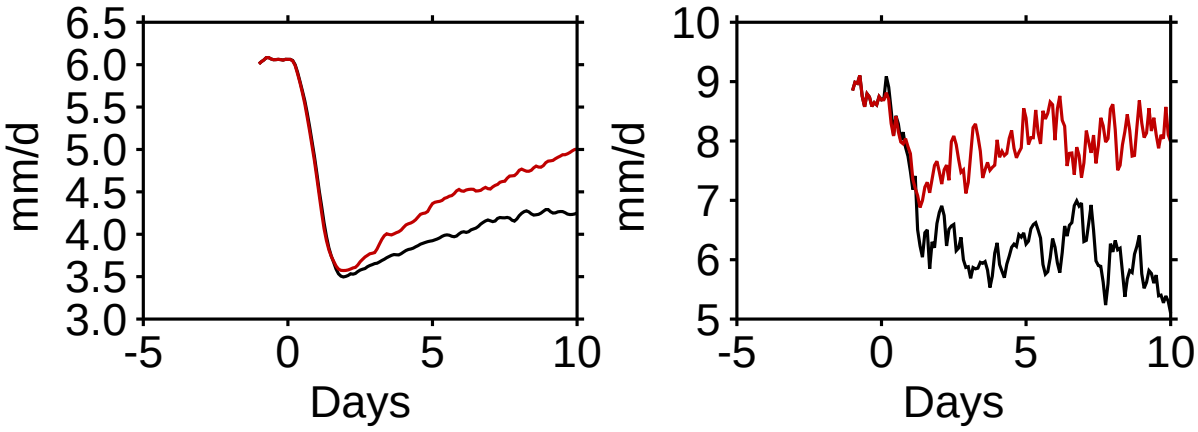

Figure 6.14 *Time evolution of surface evaporation (left-hand side) and precipitation rates (right-hand side). The results presented are daily-averaged and ensemble-averaged for the wet column of experiment 2 (black curves) and for the wet column of an experiment similar to experiment 2 but with fixed profiles of heating and moistening rates from the large-scale circulation (red curves). The forcing profiles are imposed from day* 0 *onwards and are those obtained by averaging over the previous* 10 *days.*

The red curves in Figures 6.13 and 6.14 illustrate the evolution of surface evaporation and precipitation within the dry column (column 1) of the experiment restarted from experiment 1 and within the wet column (column 2) of the experiment restarted from experiment 2 respectively. The apparent fluctuations observed in the time evolution of surface evaporation and precipitation within the dry column of experiment 1 (the black

curves in Figure 6.13) and within the wet column of experiment 2 (the black curves in Figure 6.14) are not all captured in these restarted experiments. From day 0 in the restarted experiments, evaporation rates increase sharply within the dry column and decrease sharply within the wet column. However, as expected from the heat and moisture budgets (result not shown), there is a subsequent adjustment of the columns back towards the mean state they had before day 0. From the time-height cross sections of convective activity, the transition from suppressed to active convection never occurs within the dry column of the experiment restarted from experiment 1, confirming the role of the large-scale circulation in preventing the transition process.

By comparing the red and black curves in Figures 6.13 and 6.14, the change in SST is seen to be very effective over the first two days but, it is the change in large-scale circulation which drives convective responses from day two. The initial response to changing the SST is to instantaneously drive an abrupt change in surface evaporation with the maximum value at day 1 (result not shown). However, with the time running average, evaporation peaks at different time. For instance, it peaks at day 2 and day 5 for the one day and five days running average respectively and for all cases, near linearity is found between the rate of increase (or decrease) of surface evaporation and the rate of increase (or decrease) of the underlying SST. An example is the five days running average shown on the top panels of Figure 6.10). For the rates of SST increase and decrease of 1 K d^{-1} within the dry and wet columns of experiment 3, the corresponding rates of surface evaporation increase and decrease are about 1.2 mm d^{-2} (see the black curves on the top panels of Figure 6.10). This value is nearly half the rate of surface evaporation increase within the dry column of experiment 1 for which the underlying SST was increased by the rate of 2 K d^{-1} (see the red curve on the top left hand side of Figure 6.10) and is nearly half the rate of surface evaporation decrease within the wet column of experiment 2 for which the underlying SST was decreased by the rate of 2 K d^{-1} (see the blue curve on the top right hand side of Figure 6.10).

The change in SST drives surface evaporation which in turns drives the column water

vapor. However, similarly to the results of Raymond (2000), the adjustment time for moisture within a clear and dry column is much longer than the adjustment time for moisture within a column with pre-existing heavy precipitation. Hence, the first response of convection within the dry column is to act more to recharge moisture within the column rather than increasing its precipitation amount. As a result, over the first two days, the change in SST is more effective in reducing precipitation within the wet column than in increasing precipitation within the dry column.

The restarted experiments described above illustrate the key role of the large-scale circulation on the transition mechanism. It should be remembered that in this study the WTG-derived large-scale circulation transports both heat and moisture horizontally between the columns. A useful further step is therefore to uncouple the contributions from the large-scale heat advection and the contributions from the large-scale moisture advection. An additional experiment is conducted in which the contributions from the large-scale heat advection are isolated. This is done by restarting experiment 1 at day 0 with the profile of moistening rates from the large-scale circulation fixed to the profile obtained by averaging over 10 days before the initial time, while the large-scale heating rates remain free to evolve according to the WTG calculations.

Information on the contributions from the heating rates from the large-scale circulation is provided by the red curve in the top panel of Figure 6.15. The figure shows the evolution of column-integrated heating rates from the large-scale circulation, precipitation and surface evaporation for the dry column. The dry column reaches a new quasi-equilibrium state before day 30 and the mean-statistics are obtained by averaging over days 30 to 40. As for the dry column of experiment 1 (see the black curves in Figure 6.15), the change in SST causes a weakening of the heating rates from the large-scale circulation. However, its mean value at equilibrium is about 2 mm d^{-1} (a value which is nearly half the value at the initial state) compared to the value of almost 0 mm d^{-1} obtained at equilibrium of experiment 1. As a result, convection within the dry column of the restarted experiment can not be driven to the same level of activity as within the

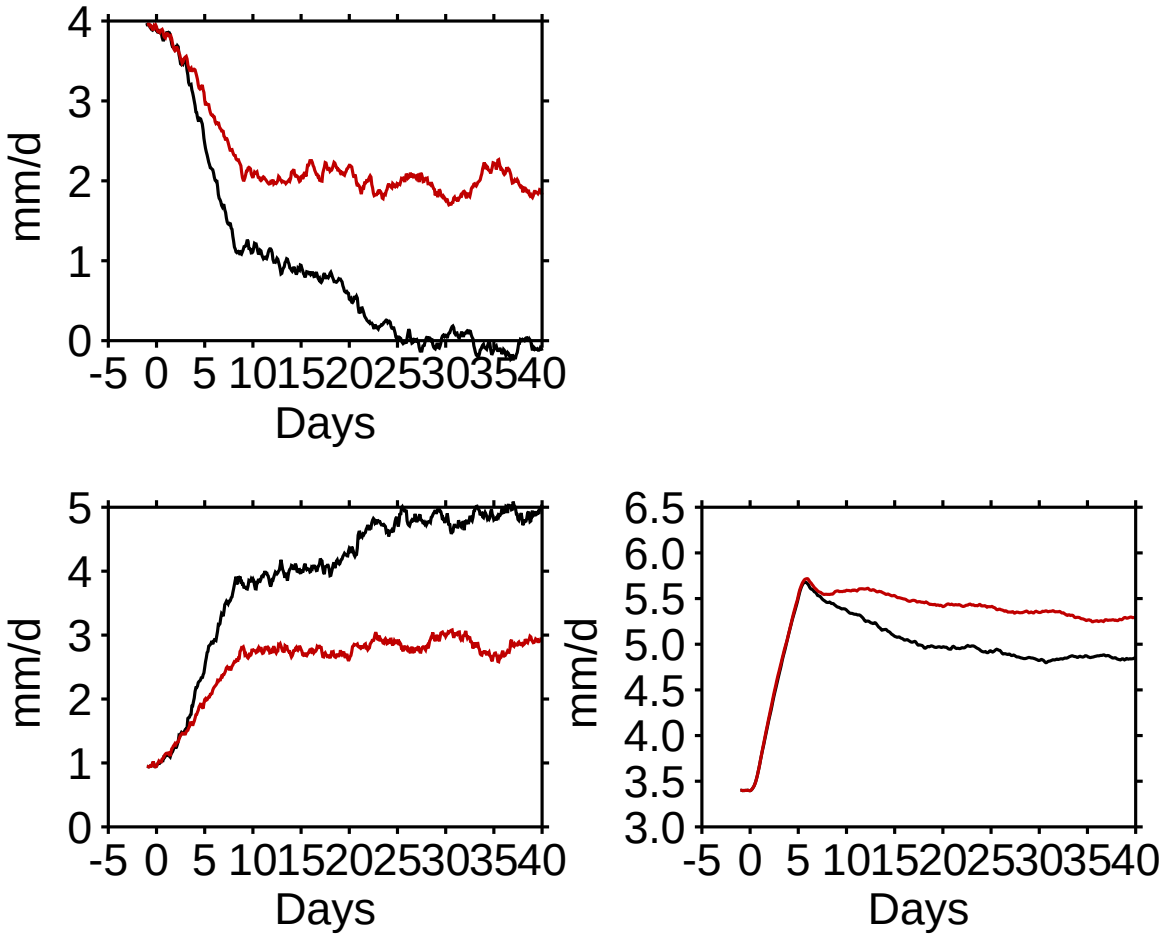

Figure 6.15 *Time evolution of column-integrated heating rates from the large-scale circulation (top), precipitation rates (bottom and left-hand side) and surface evaporation (bottom and right-hand side). The results presented are five days running mean and ensemble-averaged for the dry column of experiment 1 (black curves) and for the dry column of the experiment restarted at day* 0 *of experiment 1 with a fixed profile of moistening rates from the large-scale circulation (red curves). The profile of moistening rates from the large-scale circulation that is imposed from day* 0 *is the profile obtained by averaging over* 10 *days before the initial time.*

dry column of experiment 1. The mean rain rate at equilibrium is only 2.91 mm d^{-1}, an increase of 1.91 mm d^{-1} to the mean rain rate at the initial time. To balance the fixed drying from the large-scale circulation that is prescribed from day 0 onwards, surface evaporation is increased by 1.91 mm d^{-1}, now 5.25 mm d^{-1}. This value of mean rain

rate at equilibrium is almost halfway in between 0.98 and 4.8 mm d^{-1}, which are the values of mean rain rates obtained by averaging over 10 days before the initial time and over days 30 to 40 in the dry column of experiment 1. Hence, the contributions from the large-scale circulation is about equally divided between temperature and moisture effects.

6.7 Conclusions

This chapter presents and discusses the results of idealized two-dimensional cloud-resolving model simulations of the transition from a suppressed to an active phase of convection under the weak-temperature gradient approximation. Simulations of the transition are initialized from instantaneous profiles at equilibrium of the coupled-column simulations over non-uniform surface conditions. The transition to active convection is forced within the column with suppressed convection by increasing the local surface conditions to the value within the remote column, or else, by decreasing the remote surface forcing to the value within the local column or else, by increasing the local surface forcing while simultaneously decreasing the remote surface forcing such as to obtain uniform surface forcing within the two columns.

The evolution of the dynamic state has been studied. In all three experiments, the change in surface forcing drives a subsequent change in the strength of the large-scale circulation. The strength of the large-scale circulation is reduced, but over a period long enough to delay the transition time relative to a simulation performed without the parameterization of the large-scale circulation. An important factor in the delay is that convection first needs to recharge moisture into the dry column until the column becomes moist enough to support deep convection.

In the experiment applying the locally forced transition method, surface evaporation increases abruptly within the dry column, convection becomes more active and the

boundary layer becomes more warm and moist accordingly. However, while the large-scale circulation remains in place and produces descent within the dry column, convective cells stop just above the boundary layer top despite the important amount of CAPE at upper levels. As a result, the first apparent change in the heating rate profile from microphysics is not observed until around day 2. From day 2, convection gradually develops with cloud tops above the freezing level at about day 3. Later, surface evaporation starts to decrease while precipitation continues to increase towards the mean value obtained in the uncoupled control simulation. However, within the wet column, surface evaporation decreases gradually.

The evolution of convection within the dry column has been evaluated by defining the transition time, which is the time when the rain rate is halfway to the value obtained in the uncoupled control run. It is found that the thermodynamic state within the dry column evolves over a period of time characterizing changes in the strength of the large-scale circulation. The results also show that the transition time is insensitive to the value of column-mean SST. However, the free tropospheric dryness delayed the transition to deep convection (similar to the result of Kuang and Bretherton (2006)). On the other hand, the transition time is delayed in the experiment that applied the remotely forced transition method relative to the experiment that applied the locally forced transition method. Finally, the transition time increases as the rate of SST increase within the dry column is decreased.

The roles of surface forcing and large-scale circulation have been highlighted by conducting two additional experiments that isolated the contributions from surface forcing and the contributions from heat advection by the large-scale circulation. By analyzing the time evolution of the thermodynamic state, it is shown that surface forcing is effective during the first two days only and it is the evolution of the large-scale circulation which systematically drives the transition from suppressed to active convection. Finally, the roles of the large-scale circulation are found to be about equally divided between the heating and moistening effects.

Chapter 7:
Conclusions

The interactions between moist convection and the large-scale are the most important processes in the tropical atmosphere. Convection transports large amounts of heat and moisture from the surface to the upper levels where they are redistributed by the large-scale flows. The heat produced by convection constitutes an essential source of energy for the large-scale flows and on the other hand the large-scale flows drive convection.

General circulation models (GCMs) represent the two-way interactions between convection and the large-scale dynamics. However, convection is poorly represented because of its scale, which is often smaller than the model horizontal resolution. GCMs can be run with finer grid spacing to better represent convection. However, such integrations can not be used for sensitivity experiments due to their computational cost. On the other hand, high-resolution and limited area models explicitly resolve convection but they do not represent the large-scale dynamics due to the model domain which is small compared to the scale of the large-scale dynamics. In that case, the large-scale flows which force convection within the simulated domain are often prescribed. However, a downside of such simulations is that the large-scale flows do not evolve in response to the evolution of convection. As a result, the essential two-way interactions between convection and the large-scale flows are not captured by construction. Hence, such simulations can not be useful to understand what factors control the occurrence and intensity of tropical deep convection (Sobel et al., 2004).

To simulate the two-way interactions between convection and the large-scale flows in limited area models there is a need of approaches in which the large-scale flow is parameterized. The simulation of the interactions of convection with a parameterized

large-scale circulation in a cloud resolving model is the focus of this study.

In this study, the widely used weak-temperature gradient approach (WTG) is used to parameterize the large-scale circulation. The underlying physical principle is that gravity waves act to redistribute horizontal density anomalies towards uniformity on isobaric surfaces, with the timescale related to their propagation speed. In that case, the rate of change and the horizontal gradient of potential temperature are assumed to be small. These two assumptions are most nearly satisfied in the deep tropical free troposphere where the action of Coriolis force is almost zero, then the prognostic equation of potential temperature can be approximated to produce the diagnostic equation for the large-scale flow, in which the large-scale vertical motion is proportional to the local buoyancy anomaly.

The standard way to implement the WTG approach is to consider that the simulated convection is isolated within a small domain embedded within a very large reference reservoir domain which remains fixed when the simulated convection interacts with the derived large-scale circulation. The domain-mean potential temperature profile within a small domain is relaxed towards a fixed profile which defines the large reference reservoir domain. Throughout the integration, the diagnosed large-scale forcing is adjusted in response to the simulated convection. In that way, the heat produced by convection affects the large-scale flow via the differences in temperature between the columns. However, heat and moisture which are advected out of the simulated domain do not alter the properties of the surrounding air. Hence, by construction, the energy and moisture budgets of the systems that use the reference column approach are open. This approach was used by Sobel and Bretherton (2000); Raymond and Zeng (2005) and many others although its implementation has varied from one study to the next, particularly in the treatment of the large-scale moisture transport. The main aim of this thesis was to extend the reference column approach to a new framework which allows two columns to vary whilst the simulated convection in each interacts with the derived large-scale circulation. The new framework was built by coupling together two interacting regions of tropical deep

convection, each region simulated by a cloud-resolving model (CRM). The large-scale motion was diagnosed from the requirement that the instantaneous domain-mean potential temperature profiles in the two columns be relaxed towards each other. The relaxation was done over a specified timescale which is thought of as being related to the time for gravity waves to propagate across the system and so is related to the size of the system. Such a system is called the coupled-column system.

The new framework has enabled the option of closing the heat and moisture budgets of the full system. For example, suppose a large-scale descent is diagnosed within one column of the coupled-column system. By mass continuity that is compensated by ascent which cools and moistens the other column. Such compensating feedback effects are omitted within the reference column of the reference column system, since they can be assumed to be weak if distributed over a very large area. With the possibility of investigating systems where the two column have comparable size, the range of situations in which this new approach can be exploited is extended compared to the reference column approach. Theoretically, the reference column approach can viewed as a limit of the coupled-column system, in which one of the columns is much smaller than the other representing the surrounding environment.

Among a number of studies that have simulated the interactions of two regions of the tropical atmosphere (e.g. Nilsson and Emanuel, 1999; Raymond and Zeng, 2000; Shaevitz and Sobel, 2004), the only study that has coupled two regions of tropical deep convection via the WTG approximation is the one conducted by Raymond and Zeng (2000). However, in all of these two column studies, the authors have simulated each region using a single column model (SCM). Hence, this study is the first study that uses the WTG approximation to couple two CRMs. This new framework is proposed as a new tool for investigating a wider range of important problems in tropical meteorology including the influence on local convection of changes in remote convection.

The first part of this study was the implementation of the WTG approximation in a simple SCM. Experiments were performed over uniform and non-uniform surface forcing

and key sensitivities and simulations to be more fully explored using the CRM were identified. The second part of this study was presented in two, parallel directions. In the first direction, the equilibrium response of the reference column system was investigated over uniform and non-uniform surface conditions, with different coupling timescales. The second direction was comparing the results of the simulations performed under the reference column system to the results of the equivalent simulations performed under the coupled-column system in order to assess the fundamental differences between the closed and open systems. The last part of this study investigated the transient evolution of convection from a suppressed to a more active phase under the coupled-column system. The study of the transition was examined for cases triggered by changes in the local and/or remote conditions.

7.1 Summary and discussion

The reference column system, in comparison with the coupled-column system, was used to answer these fundamental questions:

Q1. Can (and if so how, and under what conditions, does) a large-scale circulation driven by convection develop in a homogeneous environment?

This was subject of chapter 4, which discussed the results from the simulations performed under the reference column and coupled-column systems with uniform surface conditions. A quasi-steady state with a large-scale descent develops within the simulated column of the reference column system. This equilibrium state was found to be insensitive to the WTG adjustment rate profile and the initial conditions. It was associated with a net transport of moist static energy into the test column by the WTG-derived large-scale circulation which was partially compensated by a small reduction in the surface evaporation. The incapability of the reference column system to sustain a large-scale ascent was associated with the shape of the large-scale vertical velocity profile. When a large-scale ascent was simulated within the simulated column, the maximal convergence of moisture

was found to occur at upper levels where humidity is relatively small. In that case, the moistening from the large-scale circulation was not enough to balance the cooling from the large-scale circulation and so, moist static energy was extracted from the simulated column. As the integration approached near radiative-convective equilibrium conditions a weak import of moist static energy into the simulated column by the large-scale circulation was observed but this was not sufficient to balance a reduction in the surface fluxes associated with high boundary layer humidity. Thus, the moist static energy of the simulated column was reduced further until a new equilibrium was reached with descent within the simulated column.

The sensitivity of the simulated precipitation and surface evaporation to the WTG coupling timescale, τ, was examined. The values of τ that were used are 2, 6, 12, 24 to 120 h. For gravity waves moving at a speed of 50 m s^{-1}, approximate indications of the associated spatial scales for the large-scale circulation were 360, 1080, 2160, 4320 and 21600 km respectively. It was determined that precipitation increases with τ and a value near to that obtained in the uncoupled control run (see chapter 3) was achieved for the case of very weak coupling; that is the case of simulation performed with a large value of τ, such as $\tau = 120$ h. However, by using a fixed wind speed perpendicular to the simulated domain, the surface flux calculations were relatively insensitive to the reduction in near-surface perturbation winds associated with the reduction in convective activity. Thus, the boundary layer humidity and surface evaporation were relatively unchanged.

The presence of an equilibrium solution with descent and the absence of an equilibrium solution with ascent in the simulated column of the reference column approach was somewhat counter intuitive. Despite the homogeneous forcing that was applied in these simulations, the simulated column and the reference reservoir column were not interchangeable. Moreover, the energy budget of the entire system (reference and test column) was not closed.

A similar dry equilibrium state was obtained in the reference column simulation of Raymond and Zeng (2005). However, other studies that applied the reference column

approach indicate that this result may be model-dependent. For example, Sobel and Bretherton (2000) used a first quasi-equilibrium tropical model (QTCM1) of Neelin and Zeng (2000) in which convection is parameterized and obtained an equilibrium state of the simulated column which was significantly similar to that of the reference column to which it was coupled over uniform surface conditions. In contrast to this study, the simulations of Sobel and Bretherton (2000) did not include the large-scale advection of moisture. However, Sobel et al. (2007) include the large-scale advection of moisture when coupling the GEOS-5 SCM to a reference column but they obtained a stronger precipitation rate in the simulated column.

The role of the fixed reference reservoir column in producing this dry equilibrium state of the simulated column no matter the initial conditions was highlighted by repeating some key experiments in the coupled-column system. It was found that the coupled-column system at equilibrium over uniform surface conditions had no time-mean large-scale circulation and the mean states and statistic of each column were very similar to those obtained in the single uncoupled CRM simulation. This equilibrium state was achieved regardless of the relative areas of the two columns, the magnitude of the initial potential temperature differences between the two columns, and the WTG adjustment timescale and profile. In contrast to this equilibrium response of the coupled-column system over uniform surface conditions, Raymond and Zeng (2000) showed that a large-scale circulation can develop in a system made of two columns of their SCM coupled via the same WTG approximation.

As suggested by the contrasting results of previous studies that used the reference column approach, it may, however, be argued that the presence, or otherwise, of a dry equilibrium state in the reference-column approach may depend on the choice of the cloud models, the representation of the boundary layer mixing, or even on some details in the implementation of the WTG framework. However, the key finding here was that even for large differences in column area the fully-coupled-column approach produces a qualitatively different equilibrium state from the reference-column approach. However,

throughout this study, the reference column and coupled-column systems were compared using the same CRM with the same characteristics. Thus, the investigation was in some sense reduced to comparing the one-way and the two-way couplings via the WTG approximation. Hence, these qualitative differences in behavior highlight the importance of a careful consideration of the appropriate energy and moisture budgets when interpreting results from studies of this nature.

Q2. How does convection develop in response to spatially inhomogeneous boundary conditions (SST variations)?

The sensitivity of precipitation to the surface forcing was studied under the reference column approach and the coupled-column approach. The results were discussed in Chapter 5. It was found that for columns with large differences in areas and large differences in surface forcing, the sensitivity of precipitation to surface forcing in the smaller column of the coupled-column system was very similar to that obtained in the analogous configuration using the reference column approach. This precipitation was also found to have similar sensitivity to previous studies (Raymond and Zeng, 2005). However, the differences in sensitivity do remain for small differences in surface forcing. On the other hand, the coupled-column system with equal areas showed a much weaker sensitivity to surface forcing than the reference-column system. The latter result was understood as a consequence of the strong constraint on the extent of possible sensitivity in the coupled-column system, due to the prescribed cooling in combination with the closed energy budget. This combination sets the total precipitation in the two columns of the coupled-column system. No such constraint applies in the reference-column approach, even for conditions of prescribed cooling.

The column-mean state and statistics obtained at equilibrium in the simulations performed in the coupled-column system with different values of WTG coupling timescale were compared to those obtained at equilibrium in the equivalent simulations performed without the WTG parameterization of the large-scale forcing. It was determined that the column-mean state and statistics of the coupled-column system at equilibrium in which no time-mean large-scale circulation develops were similar to those obtained in the RCE

state corresponding to the mean SST of the two columns. For the case of an equilibrium state in which a large-scale circulation was developed, convection was organized into column with enhanced convection and column with suppressed convection. Similar to the results of Tompkins (2000); Bretherton and Smolarkiewcz (1989), the column with suppressed convection was very dry while the change in the relative humidity within the column with enhanced convection was limited. This leads to a relatively dry atmosphere compared to the RCE state corresponding to the mean SST of the two columns.

The coupled-column system was then used to answer these fundamental questions:
Q3. How does convection evolve in response to time-varying boundary conditions (with prescribed variations)?
Q4. How do two-way interactions between convection and the large-scale influence the transition from a suppressed to more active phase of convection?
Chapter 6 discussed a number of experiments that were conducted under the coupled column system with time-varying boundary conditions. It was found that the responses of the large-scale forcing to the change in surface forcing towards a uniform value between the columns were not instantaneous. Rather, a complete adjustment was delayed by about 20 days.

It was determined that the direct contributions from the change in surface forcing were efficient during the first two days only. An abrupt change in surface evaporation was attributed to the change of the underlying surface forcing. When surface forcing was increased within the dry column, the contributions from early activated convective cells were to increase moisture in the dry column. As a result, the change in surface forcing was less effective in increasing precipitation within the dry column than in reducing precipitation within the wet column. However, the change in surface forcing was not able to drive the transition from suppressed to active convection within the dry column by itself. This result was due to the large-scale forcing which was suppressing convection despite the important amount of convective potential energy that was available at upper levels. From day two, it was the large-scale forcing, with its contributions equally divided be-

tween the heating and moistening effects, which was responsible for modulating the dry column from the state with suppressed convection to a state with more active convection. This result implies that the increase in precipitation rate within the dry column from its initially reduced value to the value obtained in the uncoupled control run was not simply the result of the change in surface forcing. It was mainly the result of the moistening of the dry column that was occurring as the rates of heating and drying produced by the large-scale forcing were reduced.

The transition period, which was defined as the interval between the initial time of the simulation of the transition and the time when convective properties within the dry column become comparable to those obtained in the uncoupled control run, was linked to the timescale of the large-scale response to the change in surface forcing. During this time, cloud top which was initially at the top of the boundary layer was able to develop past the freezing level and ultimately past 10 km although a weak large-scale circulation still remained in the free troposphere. The transition period and the mechanism through which the dry column evolved from a state with suppressed convection to a state with more active convection were sensitive to the free tropospheric moisture, the method applied to force the transition and the rate of surface forcing increase within the dry column.

A rain rate deficit within the dry column, which was defined as the difference between the rain rate in the uncoupled control integration and the rain rate when the simulation of the transition is initialized, provided a useful measure of the transition mechanism. The transition mechanism was quantified using the concept of transition time, t^*, which was identified as the time when the rain rate within the dry column was half-way to the value obtained in the uncoupled control run.

When the transition from suppressed to active convection was triggered in response to an increase in the local surface forcing, the role of early activated convective cells within the dry column was to warm and moisten the boundary layer. These warming and moistening effects were not observed within the dry column in the simulation in which the transition was triggered in response to a decrease in the remote surface forcing. As a

result, the inversion cap within the dry column of the simulation that applied the locally forced transition method was rapidly eroded and the column became quickly unstable to deep convection compared to the simulation that applied the remotely forced transition method.

Warming and moistening effects of the boundary layer were also observed within the dry column of the simulation in which the transition was triggered in response to a combination of an increase in the local surface forcing and a decrease in the remote surface forcing. As the rate of surface forcing increase within the dry column was weak compared to that in the simulation that applied the locally forced transition method, the rate of adjustment of the boundary was also weak. As a result, the transition time that is long relative to the simulation that applied the locally forced transition method but short relative to the simulation that applied the remotely forced transition method.

In the simulation that applied the locally forced transition method, the value of t^* was about 5.4 days. This value is close (just a day longer) to the value of about 4 days obtained in the idealized simulation of the transition over ocean performed by Kuang and Bretherton (2006), in which the rate of local surface forcing increase is comparable to the value used in this study. However, it is much longer than the values obtained in the diurnal simulations of the transition over land performed by Khairoutdinov and Randall (2006), Grabowski et al. (2006) and Wu et al. (2009), in which the rates of local surface forcing increase are much greater than the value used here. It was determined that the transition time was two times longer (about 11 days) when the simulation of the transition was triggered remotely and was almost half-way in between the values obtained in the locally forced simulation of the transition and the remotely forced simulation of the transition. Finally, similar to the result of Kuang and Bretherton (2006), it was found that the free tropospheric dryness delays the transition from suppressed to more active convection.

The simulations of the transition show sensitivity to humidity, with suppressed convection when the free troposphere is dried out by the large-scale forcing and the evolution to more active convection as the strength of the large-scale forcing is weakened. Hence,

the CRMs respond reasonably well to the free tropospheric moisture contains in contrast to the SCMs which show limited adaptation of humidity (Derbyshire et al., 2004). Therefore, similar to the study of Derbyshire et al. (2004), parallel results from the simulations with the SCM may help to improve the cloud parameterization scheme used in SCMs, especially the entrainment into convective plumes.

7.2 Limitations

Although the equilibrium properties of convective ensembles in smaller two dimensional simulations are comparable to those of three dimensional simulations (Tompkins, 2000), the representation of convection could be sensitive to the domain dimension and horizontal resolution.

Key simulations performed under the reference column and coupled column approaches with uniform surface conditions were repeated using; (a) a grid spacing of 2 km, and (b) a 3D CRM with a grid spacing of 2km. For the case of simulations performed using a 3D CRM, the domain size was 50×50 km.

It was found that the WTG simulations performed using a 2D CRM and a coarse horizontal resolution produced the same qualitative results as the analogous simulations with a finer grid spacing. That is: over uniform surface conditions, the reference column system produced a dry equilibrium and the coupled-column system produced an equilibrium state with no time-mean large-scale circulation regardless of the relative sizes of the columns. The coupled-column simulations performed using the 3D CRM and a coarse horizontal resolution also produced an equilibrium state with no time-mean large-scale circulation for the case of columns with equal areas. However, an equilibrium state with a weak large-scale circulation with descent within the smallest column developed in the coupled-column approach with a large difference in column areas.

However, following the results of Bretherton and Smolarkiewcz (1989), Tompkins

(2000) and Petch et al. (2008) it may be recognized that the evolution of convective cells may be sensitive to the geometry of the model. For intense, convective cells do not sufficiently entrain dry air in the 2D domain simulations compared to the 3D domain simulations (Petch et al., 2008). Following the results of Bryan et al. (2003), it may also be recognized that convection may be poorly represented in the simulations that use a grid spacing of 2 km.

7.3 Future work

There are number of areas not investigated in this study. In particular, in collaboration with the Met Office, a useful further direction could be to implement the WTG approximation in the Met Office Unified Model (MetUM). State-of-art GCMs still present biases in the representation of the large-scale tropical dynamics (e.g. Martin et al., 2011) which are partly associated with the poor representation of convection by GCMs. Knowing that the CRM is a powerful tool which explicitly simulate convection, an assessment of how well the key behaviors of the coupled CRM are reproduced by the coupled MetUM could be benefited considerably in providing some recommendations on how to improve the ongoing development work on the parameterization schemes used in the MetUM.

Key simulations performed under the reference column and coupled column approaches could be repeated with an interactive radiation to allow for extra-degree of freedom in the moist static energy budget. For example, Appendix B discusses the preliminary results of the simulations performed under the reference column and coupled-column approaches with configurations similar to those described in Daleu et al. (2012) and an interactive radiation scheme. It was found that the results were sensitive to interactive radiation. For instance, the coupled-column simulations performed over uniform surface conditions with a large difference in column areas and an interactive radiation scheme develops a large-scale circulation with descent within the smallest column. Note that the behavior of the simulations with an interactive radiation may be sensitive to many

aspects of the simulation. For example: the domain size and dimension. In addition, interactive radiation is known to promote spontaneous organization of convection (e.g. Held et al., 1993; Tompkins and Craig, 1998a) which could have very different transport properties from isolated convection.

The work in Chapter 6 that examined the transient evolution of convection has begun to reveal how the large-scale circulation modulates the transition between suppressed and active convection. The CRM under the coupled-column approach and fixed radiative forcing was able to reproduce key behaviors of convective transition over ocean. That includes; timings, final states and the different adjustments of temperature and moisture structure. The differences between transitions that are induced in response to changes in local conditions and transitions that are induced in response to change in remote conditions highlight one of the potential advantages of extending the reference column approach to the coupled-column approach. The ability of the CRM to reproduce key behaviors of convective transition could be assessed under (a) the coupled-column approach with an interactive radiation and, (b) the reference column approach with a fixed radiative forcing or an interactive radiation. Such studies would provide valuable information on the differences in the feedbacks to the large-scale circulation when the system is treated as closed or open.

Note that the experiments conducted so far concern surface conditions that are imposed. However, much of the variability in tropical convection depends upon coupling with the land or ocean surface. Therefore, additional experiments could be performed in which the prescribed surface conditions are replaced by a surface model (e.g. mixed layer or slab ocean) to allow the surface conditions to evolve in response to the convection.

The WTG approximation produces a large-scale vertical velocities that are often too large where the static stability, $\partial\theta/\partial z$, approaches zero, such as in the upper troposphere. The remedy commonly used is to impose a lower bound on $\partial\theta/\partial z$. For instance, a lower band of 10^{-3} K m^{-1} was used by Raymond and Zeng (2005) and Daleu et al. (2012). In addition, the WTG approximation is not valid in the boundary layer. The vertical

velocities there are replaced with the values obtained from the linear interpolation from the diagnosed values at the layer just above the boundary layer to the value of zero at the surface (e.g. Sobel and Bretherton, 2000; Raymond and Zeng, 2005; Daleu et al., 2012). From these two required fixes, the nature of the results may be sensitive to the details of the implementation of the WTG approximation. Note that in the WTG approximation, the vertical velocity is not derived from the governing momentum equation. Rather, it is derived from buoyancy anomalies under the assumption that the large-scale vertical motion consumes buoyancy anomalies over a fixed time-scale. Hence the WTG approximation may not be the appropriate approach to capture the relevant dynamics. An alternative could be to use the weak-pressure gradient (WPG) approach, in which the vertical motion is derived directly from the momentum equations (e.g Kuang, 2008, 2011; Romps, 2012). Thereby supplementing the WTG approach of Daleu et al. (2012). The sensitivity to the parameters within the WPG could be investigated and the strengths and weaknesses of the WPG approach could then be assessed in comparison with the WTG approach. This comparative study could be a guide to identify the range of problems that can be usefully addressed using the WTG, WPG or related approaches.

Throughout the entire work of this thesis and based on the diversity of results obtained in previous study, the feeling was always present that they could be a considerable sensitivity of the results to the choice of the cloud model, the parameters within the cloud model, the choice of the approach used to parameterize the large-scale circulation and the details of the implementation of that approach. An international intercomparison project has recently been initiated that plans to assess the strengths and weaknesses of the different approaches for parameterizing large-scale circulation. Particularly, different details of the implementation of the WTG and WPG frameworks will be applied to a set of models with different representation of convection, different representation of boundary layer mixing, different representation of the cooling due to loss of infrared radiation, different model resolution and different model dimension. This international intercomparison project could guide the international community on the range of processes and/or parameters that the results may be sensitive to. This international intercomparison project has

been given the name of "Weak-temperature gradient project" and it has been accepted as a project of the Global Energy and Water Exchanges (GEWEX) Global Atmospheric System Studies (GASS) panel. Collaboration through GEWEX will enable comprehensive comparison of the results presented in this thesis with those obtained from similar experiments using different models.

Appendix A:
Notation Conventions

LEM	Large-Eddy Model
CRM	Cloud-Resolving Model
SCM	Single Column Model
MetUM	Met Office Unified Model
WTG	Weak-Temperature Gradient
RCE	Radiative-Convective Equilibrium
CAPE	Convective-Available Potential Energy [J kg^{-1}]
T	Atmospheric temperature [K]
SST	Sea-surface temperature [K]
θ	Atmospheric potential temperature [K]
q	Specific humidity of water vapor [kg kg^{-1}]
q^*	Saturation specific humidity [kg kg^{-1}]
CWV	Column-integrated water vapor [kg m^{-2} or mm]
P	Atmospheric pressure [Pa]
P^*	Reference pressure [Pa]
ρ	Density of the air [kg m^{-3}]
L	Latent heat of vaporization [J kg^{-1}]
C_p	Heat capacity at constant pressure [J kg^{-1} K^{-1}]
R	Gas constant [kg s^{-2} K^{-1}]
E and **det**	Entrainment [s^{-1}] and detrainment [s^{-1}]
D_{mix} and D_{final}	Mixed and final detrainment [s^{-1}]
ε and δ	Fractional mass entrainment and detrainment coefficients [Pa^{-1}]
Λ	Rescaling factor of the mass flux at the base of the plume

M_p	Mass flux of an air parcel [Pa s^{-1}]
R_p	Plume radius [km]
Q	Rate of conversion of water vapor to liquid water [kg kg^{-1} s^{-1}]
Δ_ϕ	Increment due to phase change
N	Total number of grid boxes
M_u	Mass flux of strong and buoyant updrafts [kg m^{-2} s^{-1}]
M_d	Mass flux of strong downdrafts [kg m^{-2} s^{-1}]
σ_u	Fractional area covered by strong and buoyant updrafts
σ_d	Fractional area covered by strong downdrafts
Δt and dt_{WTG}	Model time step [s] and WTG coupling time step [min]
τ_{CAPE}	CAPE timescale [h]
τ and τ_{eff}	WTG coupling and effective timescales [h]
t^*	Transition time [day]
ε	Fractional area
H and L	Height and length of the full system [km]
F_S and F_L	Sensible and latent heat fluxes [W m^{-2}]
S_θ	Diabatic source of θ [K s^{-1}]
Q_R and Q_C	Radiative cooling and convective heating rates [K s^{-1}]
$\left(\frac{\partial \chi}{\partial t}\right)_\mu$	Tendency of χ due to microphysics
$\left(\frac{\partial \chi}{\partial t}\right)_{rad}$	Tendency of χ due to radiation
$\left(\frac{\partial \chi}{\partial t}\right)_{WTG}$	Tendency of χ due to the WTG derived large-scale circulation
s and h	Dry and moist static energy [J kg^{-1}]
g	Acceleration due to gravity [m s^{-2}]
B	Buoyancy of an air parcel [m s^{-2}]
λ and λ_0	Mixing length and basic mixing length scales [m]
Δ	Grid spacing [m]
z_0	Roughness length [m]
κ	Von Karman coefficient

Appendix B:
Interactive radiation

B.1 Introduction

The experiments performed so far concern radiative cooling that is prescribed. In that case, the moist static energy budget has less degree of freedom compared to the moist static energy budget in the experiments that use an interactive radiation. In this appendix, key experiments performed in Chapters 3 and 4 are repeated with the fixed radiation profile replaced by an interactive radiation scheme.

The radiation parameterization scheme distributed in the LEM is a flexible two-stream radiation scheme referred to as the Edwards Slingo (here after ES) code. It is described in (Edwards and Slingo, 1996). More detail is given in Ingram et al. (1997) and the details of the features not included in the Unified Model (e.g. the treatment of precipitating hydrometeors) are given in Gray et al. (2001).

B.2 Radiative convective equilibrium simulations

Two RCE simulations are performed with SSTs of 302.7 and 304.7 K. In each case, the model is run for 50 days and an average over days 30 to 50 is used to define the model state and statistics at RCE. In the simulation performed with an SST of 302.7 K, the mean radiative cooling rate at equilibrium is 3.78 mm d^{-1}, nearly 25% lower than the value prescribed in this study. As a result, the mean rain rate at equilibrium is only 3.71 mm d^{-1}. In the simulation performed with an SST of 304.7 K, the mean radiative cooling

rate at equilibrium is 4.22 mm d^{-1} with a mean rain rate at equilibrium of 4.13 mm d^{-1}.

B.3 Reference column approach

Results are shown for a repeat of experiments in which the test column is initialized from the RCE profiles obtained in the uncoupled single CRM with an SST of 304.7 K.

In the reference column approach, the reference column have the profiles previously obtained at RCE of the uncoupled single CRM with an SST of 302.7 K and with interactive radiation. The surface conditions in the test column are the same as in the RCE reference column.

The simulation initially developed a large-scale circulation with ascent in the test column, as was expected from the initial potential temperature difference between the test and the reference columns. Figure B.1 shows the scatter plot of the daily-mean tendency of column-integrated moist static energy due to the large-scale circulation against the difference in the column moist static energy between the test and the reference columns. It also shows the scatter plot of the difference in the daily-mean tendency of column-integrated moist static energy due to surface evaporation and due to radiation. The difference in the column moist static energy is computed as daily-mean value in the test column minus the value for the RCE reference column. The results are shown from day 2 onwards.

The excess of cooling over moistening from the initial large-scale ascent removes energy from the test column. The moist static energy in the test column decreases to a value close to that of the RCE reference column by day 9. From days 9 to 16, the test column is in its first quasi-equilibrium state with small fluctuations of moist static energy around the RCE reference value. From the column-integrated water vapor, the moisture contained in the test column decreases over this period and the radiative cooling rate increases accordingly. However, from day 16, the reduction in surface evaporation associated with

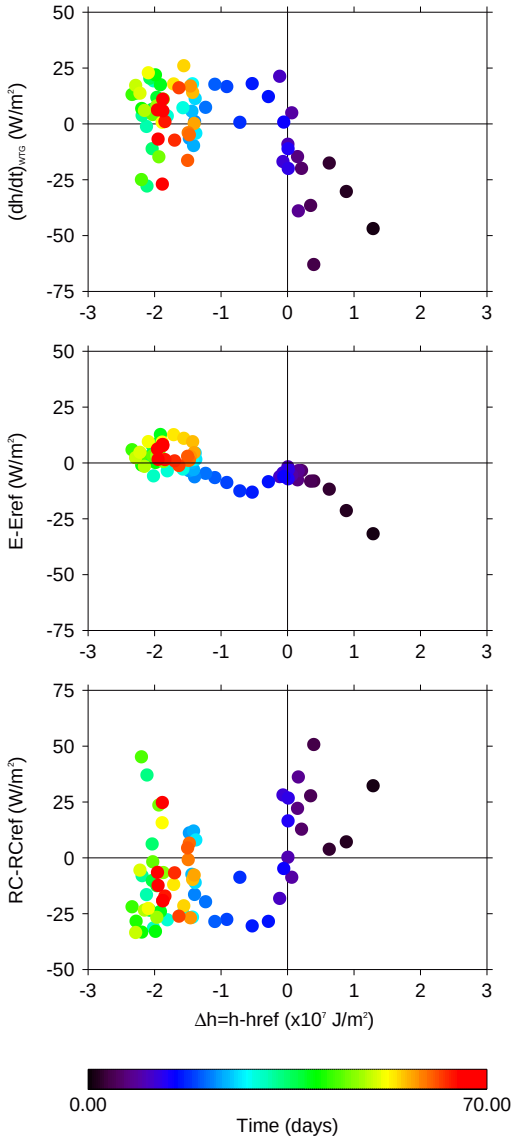

Figure B.1 *As in Figure 4.11 but with an interactive radiation scheme. The y-axis of the first panel shows the column-integrated moist static energy tendency due to the large-scale circulation. The y-axis of the second panel shows the difference in the column-integrated moist static energy tendency due to surface evaporation. The y-axis of the third panel shows the difference in the column-integrated moist static energy due to radiation. The difference is computed as the daily-mean value in the test column minus the value for the RCE reference column. The results are shown from day 2 onwards. The values of* $\Delta h = h - h_{ref}$ *and* $(dh/dt)_{WTG}$ *averaged over day 1 are* 5.2×10^7 *J* m^{-2} *and* -405 *W* m^{-2} *respectively.*

high boundary layer humidity and the increase in radiative cooling associated with the dryness of the simulated column are more than enough to balance the source of moist

static energy produced by the large-scale circulation. Hence, the moist static energy of the test column continues to decrease until a new quasi equilibrium state is established by day 35. This equilibrium state is characterized by an increase in radiative cooling balancing the net transport of moist static energy into the test column by the large-scale circulation and a small increase in surface evaporation.

The mean rain rate at equilibrium was 3.53 mm d^{-1} compared to the surface evaporation of 3.81 mm d^{-1} and the mean cooling rate at equilibrium was 4.11 mm d^{-1} compared to the cooling rate of 3.78 mm d^{-1} obtained in the RCE simulation of the single CRM with an SST of 302.7 K and with interactive radiation. By considering the energy budget in the test column, there was a weak moisture sink from the large-scale circulation compensating for the excess of evaporation over precipitation and there was a weak heat source from the large-scale circulation balancing the deficit of convective heating over radiative cooling. Hence, in this reference column configuration with uniform surface conditions being used for the test and the reference columns, the quasi-steady state established was characterized by non-uniform radiative forcing conditions between the test and the reference columns, a state which was maintained by a weak large-scale circulation with descent in the test column. The presence of this large-scale circulation was insensitive to the WTG adjustment rate profile and the initial conditions.

	$\varepsilon = 1/2$			$\varepsilon = 0.01$		
	Rain	Evaporation	Cooling	Rain	Evaporation	Cooling
Column 1	3.71	3.71	3.75	3.79	3.80	3.85
Column 2	3.75	3.72	3.74	3.54	3.71	4.13

Table B.1 *Mean rain, surface evaporation and radiative cooling rates at equilibrium (mm d^{-1}) for columns 1 and 2. The results are obtained from simulations performed under the coupled-column approach with the ES radiation code and with columns 1 and 2 initialized from the RCE profiles at* 302.7 *K and* 304.7 *K respectively. Results are presented for the case* $\varepsilon = 0.5$ *and* $\varepsilon = 0.01$ *(column 2 is the smaller column) with* $\tau = 2$ *h.*

B.4 Coupled-column approach

The same experiment is now performed under the coupled-column configuration for the case of $\varepsilon = 1/2$ and $\varepsilon = 0.01$ (column 2 is the smaller column). Table B.1 summarizes the values of mean rain rates, surface evaporation rates and radiative cooling rates at equilibrium for columns 1 and 2. For the case of columns of equal area, the mean rain rates, surface evaporation rates and radiative cooling rates at equilibrium are equal in the two columns and are equal to the mean values obtained in the uncoupled RCE simulation to within 0.07 mm d^{-1}. The results are qualitatively insensitive to the initial conditions, to the WTG adjustment time scale and to the choice of the WTG adjustment rate profile. As for the coupled-column simulations performed with uniform surface conditions and a fixed radiative cooling profile, the simulations are always found to adjust to an equilibrium state with no mean large-scale circulation. However, for the case of a large difference in column areas, the equilibrium state established is characterized by a weak large-scale descent in the smaller column balancing the difference in radiative cooling between the two columns. This equilibrium state is very similar to the equilibrium state established in the equivalent reference column simulations and it is insensitive to the initial conditions, to the WTG adjustment time scale and the WTG adjustment rate profile.

B.5 Summary

The reference column system with uniform surface conditions produced an equilibrium state characterized by a large-scale descent in the simulated column. A similar equilibrium state is produced in the analogous simulation with a fixed radiative cooling profile but with a much stronger circulation (see Chapter 4).

The equilibrium state found under the reference column system is associated with net transport of moist static energy into the test column by the WTG circulation. It is accompanied by a small compensating increase in the radiative cooling and surface evap-

oration. For the same reason as given in Chapter 4, the reference-column system cannot sustain a large-scale ascent in the test column because the velocity profile is top heavy and so the test column loses energy due to the excess of large-scale cooling compared to the large-scale moistening. As the simulation approaches the near radiative convective equilibrium conditions a weak import of moist static energy into the column by the large-scale circulation is observed. However this is not sufficient to balance surface fluxes associated with high boundary layer humidity and the increase in the radiative cooling rate associated with the dryness of the simulated column. Thus, the moist static energy of the simulated column is reduced further until a new equilibrium is reached with descent in the test column.

The coupled-column simulations with columns of equal areas adjusts the columns to produce a state with no time mean large-scale circulation and the mean statistics of the uncoupled RCE simulation. This equilibrium was insensitive to the magnitude of the initial temperature difference between the two columns, to the WTG adjustment timescale and profile. However, for a large difference in column areas, the coupled-column simulations recover the behavior of the equivalent reference column simulations.

Appendix C:
Computation of the large-scale vertical motion and the tendency terms

C.1 Introduction

This appendix gives the details on how the WTG approach is implemented in the Large-Eddy Model (LEM) at version 2.4 of the UK Met Office.

C.2 Large-scale vertical velocity

The LEM grid is staggered in the vertical. The large-scale vertical velocity is calculated at half model levels. The algorithm used in the free troposphere of column 1 is the following

$$w_1^{k+\frac{1}{2}} = \frac{0.5[(\theta_1^{k+1}+\theta_1^k)-(\theta_2^{k+1}+\theta_2^k)]}{\tau D^k}$$

where

$$D^k = \begin{cases} MAX\left(\frac{1-\varepsilon}{\varepsilon}\frac{\theta_2^{k+1}-\theta_2^k}{z^{k+1}-z^k}+\frac{\theta_1^{k+1}-\theta_1^k}{z^{k+1}-z^k}, 10^{-3}\right) & \text{if } \frac{1-\varepsilon}{\varepsilon}\frac{\theta_2^{k+1}-\theta_2^k}{z^{k+1}-z^k}+\frac{\theta_1^{k+1}-\theta_1^k}{z^{k+1}-z^k} \geqslant 0 \\ MIN\left(\frac{1-\varepsilon}{\varepsilon}\frac{\theta_2^{k+1}-\theta_2^k}{z^{k+1}-z^k}+\frac{\theta_1^{k+1}-\theta_1^k}{z^{k+1}-z^k}, -10^{-3}\right) & \text{if } \frac{1-\varepsilon}{\varepsilon}\frac{\theta_2^{k+1}-\theta_2^k}{z^{k+1}-z^k}+\frac{\theta_1^{k+1}-\theta_1^k}{z^{k+1}-z^k} < 0 \end{cases}$$

In the boundary layer, the large-scale vertical velocity is calculated by linearly interpolating in height from the value diagnosed at the first model level above the boundary layer, $k_{BL_{top}}$, to the value of zero at the surface. That is:

$$w_1^{k+\frac{1}{2}} = w_1^{k_{BL_{top}}} \frac{z^{k+\frac{1}{2}}}{z k_{BL_{top}}}$$

In column 2, a similar algorithm is used to calculate the large-scale vertical velocity which, following the continuity equation , $(1-\varepsilon)w_1+\varepsilon w_2=0$, compensates for the large-scale motion in column 1.

C.3 Tendency terms due to the WTG-derived large-scale circulation

The diagnosed large-scale vertical velocity is used to advect θ and q. In this section, θ and q are represented by the variable χ. Then, the tendency of χ due to the large-scale motion is represented by $S\chi_{wtg}$. It the sum of $S\chi_v$ and $S\chi_h$, which are the large-scale vertical and horizontal advection terms respectively. The algorithm used to calculate the tendency terms in column 1 is

$$S\chi_1{}^k_{wtg} = S\chi_1{}^k_v + S\chi_1{}^k_h$$

with

$$S\chi_1{}^k_v = \begin{cases} \frac{M_1^{k-\frac{1}{2}}\chi_1^k - M_1^{k+\frac{1}{2}}\chi_1^{k+1}}{Dz^k} & \text{if } M_1^{k+\frac{1}{2}}<0 \quad \text{and } M_1^{k-\frac{1}{2}}<0 \\ \frac{-M_1^{k+\frac{1}{2}}\chi_1^k + M_1^{k-\frac{1}{2}}\chi_1^{k-1}}{Dz^k} & \text{if } M_1^{k+\frac{1}{2}}>0 \quad \text{and } M_1^{k-\frac{1}{2}}>0 \\ \frac{-M_1^{k+\frac{1}{2}}\chi_1^{k+1} + M_1^{k-\frac{1}{2}}\chi_1^{k-1}}{Dz^k} & \text{if } M_1^{k+\frac{1}{2}}<0 \quad \text{and } M_1^{k-\frac{1}{2}}>0 \\ \frac{-M_1^{k+\frac{1}{2}}\chi_1^k + M_1^{k-\frac{1}{2}}\chi_1^k}{Dz^k} & \text{if } M_1^{k+\frac{1}{2}}>0 \quad \text{and } M_1^{k-\frac{1}{2}}<0 \end{cases}$$

and

$$S\chi_1{}^k_h = \frac{(M_1^{k+\frac{1}{2}} - M_1^{k-\frac{1}{2}})\chi_*^k}{Dz^k}$$

where

$$\chi_*^k = \begin{cases} \chi_1^k & \text{if } \frac{M_1^{k+\frac{1}{2}} - M_1^{k-\frac{1}{2}}}{Dz^k}, 0 \\ \chi_2^k & \text{if } \frac{M_1^{k+\frac{1}{2}} - M_1^{k-\frac{1}{2}}}{Dz^k} > 0 \end{cases}$$

$M_1^{k-\frac{1}{2}} = \rho_1^{k-\frac{1}{2}} w_1^{k-\frac{1}{2}}$, $M_1^{k+\frac{1}{2}} = \rho_1^{k+\frac{1}{2}} w_1^{k+\frac{1}{2}}$ and $Dz^k = \rho^k(z^{k+\frac{1}{2}} - z^{k-\frac{1}{2}})$

A similar algorithm is used to calculate the tendency terms in column 2.

Bibliography

Abel, S., and B. Shipway, 2007: A comparison of cloud-resolving model simulations of trade wind cumulus with aircraft observations taken during RICO. *Quart. J. R. Meteorol. Soc.*, **133**, 781–794.

Arakawa, A., and V. Lamb, 1977: Computational design of the basic dynamical processes of the UCLA general circulation model. *General circulation models of the atmosphere.(A 78-10662 01-47) New York, Academic Press, Inc.*, pp. 173–265.

Back, L., and C. Bretherton, 2006: Geographic variability in the export of moist static energy and vertical motion profiles in the tropical pacific. *Geophys. Res. Lett.*, **33**, L17,810.

Bellon, G., and A. Sobel, 2010: Multiple equilibria of the Hadley circulation in an intermediate-complexity axisymmetric model. *J. Climate*, **23**, 1760–1778.

Bretherton, C., and P. Smolarkiewcz, 1989: Gravity waves, compensating subsidence and detrainment around cumulus clouds. *J. Atmos. Sci.*, **46**, 740–759.

Bretherton, C., P. Blossey, and M. Khairoutdinov, 2005: An energy-balance analysis of deep convective self-aggregation above uniform SST. *J. Atmos. Sci.*, **62**, 4273–4292.

Bretherton, C. S., and M. C. Wyant, 1997: Moisture transport, lower-tropospheric stability, and decoupling of cloud-topped boundary layers. *J. Atmos. Sci.*, **54**, 148–167.

Bretherton, C. S., M. E. Peters, and L. E. Back, 2004: Relationships between water vapor path and precipitation over the tropical oceans. *J. Climate*, **17**, 1517–1528.

Brown, A., S. Derbyshire, and P. Mason, 1994: Large-eddy simulation of stable atmospheric boundary layers with a revised stochastic subgrid model. *Quart. J. R. Meteorol. Soc.*, **120**, 1485–1512.

Bryan, G., J. Wyngaard, and J. Fritsch, 2003: Resolution requirements for the simulation of deep moist convection. *Monthly Weather Review*, **131**, 2394–2416.

Bull, J., and S. Derbyshire, 1990: Numerical solutions of the surface layer equations. *Met O (P) Turbulent and Diffusion Note*.

Cohen, B., and G. Craig, 2004: The response time of a convective cloud ensemble to a change in forcing. *Quart. J. R. Meteorol. Soc.*, **130**, 933–944.

Cohen, B., and G. Craig, 2006: Fluctuations in an equilibrium convective ensemble. Part II: Numerical experiments. *J. Atmos. Sci.*, **63**, 2005–2015.

Cullen, M., 1993: The unified forecast/climate model. *Meteorological Magazine*, **122**, 81–94.

Dai, A., 2006: Precipitation characteristics in eighteen coupled climate models. *J. Climate*, **19**, 4605–4630.

Daleu, C., S. Woolnough, and R. Plant, 2012: Cloud-resolving model simulations with one and two-way couplings via the weak-temperature gradient approximation. *J. Atmos. Sci.*, **69**, 3683–3699.

Deardorff, J., 1970a: Convective velocity and temperature scales for the unstable planetary boundary layer and for rayleigh convection. *J. Atmos. Sci.*, **27**, 1211–1213.

Deardorff, J., 1970b: Preliminary results from numerical integrations of the unstable planetary boundary layer(three dimensional numerical model of unstable planetary boundary layer integrated for convecting and turbulent region height, mean lateral shear and Reynolds flux direction). *J. Atmos. Sci.*, **27**, 1209–1211.

Derbyshire, S., A. R. Brown, and A. P. Lock, 1994: The Meteorological Office Large-Eddy Simulation Model. *Met O (APR) Turbulent and Diffusion Note*.

Derbyshire, S., I. Beau, P. Bechtold, J. Grandpeix, J. Piriou, J. Redelsperger, and P. Soares, 2004: Sensitivity of moist convection to environmental humidity. *Quart. J. R. Meteorol. Soc.*, **130**, 3055–3079.

Edwards, J., and A. Slingo, 1996: Studies with a flexible new radiation code. I: Choosing a configuration for a large-scale model. *Quart. J. R. Meteorol. Soc.*, **122**, 689–719.

Emanuel, K., 1994: *Atmospheric convection*. Oxford University Press, USA.

Flatau, P. J., G. J. Tripoli, J. Verlinde, and W. R. Cotton, 1989: The SCU-RAMS cloud microphysics module general theory and code documentation. *Colorado State University*.

Fritsch, J., and R. Maddox, 1981: Convectively Driven Mesoscale Weather Systems Aloft. Part I: Observations. *J. Appl. Meteor.*, **20**, 9–19.

Fulton, S., and W. Schubert, 1985: Vertical normal mode transforms: Theory and application. *Monthly Weather Review*, **113**, 647–658.

Garner, S. T., D. M. W. Frierson, I. M. Held, O. Paulius, and G. K. Vallis, 2007: Resolving convection in a global hypohydrostatic model. *J. Atmos. Sci.*, **64**, 2061–2075.

Grabowski, W., M. Moncrieff, and J. Kiehl, 1996: Long-term behaviour of precipitating tropical cloud systems: A numerical study. *Quart. J. R. Meteorol. Soc.*, **122**, 1019–1042.

Grabowski, W., X. Wu, M. Moncrieff, and W. Hall, 1998: Cloud-resolving modeling of cloud systems during phase III of GATE. Part II: Effects of resolution and the third spatial dimension. *J. Atmos. Sci.*, **55**, 3264–3282.

Grabowski, W., J. Yano, and M. Moncrieff, 2000: Cloud resolving modeling of tropical circulations driven by large-scale SST gradients. *J. Atmos. Sci.*, **57**, 2022–2040.

Grabowski, W., P. Bechtold, A. Cheng, R. Forbes, C. Halliwell, M. Khairoutdinov, et al., 2006: Daytime convective development over land: A model intercomparison based on LBA observations. *Quart. J. R. Meteorol. Soc.*, **132**, 317–344.

Gray, M., J. Petch, S. H. Derbyshire, A. R. Brown, A. P. Lock, H. A. Swann, and P. R. A. Brown, 2001: Version 2.3 of The Met Office Large Eddy Model: Part II: Scientific Documentation. *UK Met Office*.

Gregory, D., and P. Rowntree, 1990: A mass flux convection scheme with representation of cloud ensemble characteristics and stability-dependent closure. *Monthly Weather Review*, **118**, 1483–1506.

Held, I. M., R. S. Hemler, and V. Ramaswamy, 1993: Radiative-convective equilibrium with explicit two-dimensional moist convection. *J. Atmos. Sci.*, **50**, 3909–3927.

Holloway, C., S. Woolnough, and G. Lister, 2012: Precipitation distributions for explicit versus parametrized convection in a large-domain high-resolution tropical case study. *Quart. J. R. Meteorol. Soc.*, **138**, 1692–1708.

Holloway, C. E., and J. D. Neelin, 2009: Moisture vertical structure, column water vapor, and tropical deep convection. *J. Atmos. Sci.*, **66**, 1665–1683.

Holloway, C. E., and J. D. Neelin, 2010: Temporal relations of column water vapor and tropical precipitation. *J. Atmos. Sci.*, **67**, 1091–1105.

Huffman, G. J., R. F. Adler, M. M. Morrissey, D. T. Bolvin, S. Curtis, R. Joyce, B. McGavock, and J. Susskind, 2001: Global precipitation at one-degree daily resolution from multisatellite observations. *J. Hydrometeor.*, **2**, 36–50.

Ingram, W., S. Woodward, and J. Edwards, 1997: Unified model documentation paper No 23.

Islam, S., R. Bras, and K. Emanuel, 1993: Predictability of mesoscale rainfall in the tropics. *J. Atmos. Sci.*, **32**, 297–310.

Johnson, R., T. Rickenbach, S. Rutledge, P. Ciesielski, and W. Schubert, 1999: Trimodal characteristics of tropical convection. *J. Climate*, **12**, 2397–2418.

Jordan, C., 1958: Mean soundings for the West Indies area. *J. Atmos. Sci.*, **15**, 91–97.

Khairoutdinov, M., and D. Randall, 2006: High-resolution simulation of shallow-to-deep convection transition over land. *J. Atmos. Sci.*, **63**, 3421–3436.

Kingsmill, D. E., and R. A. Houze, 1999: Thermodynamic characteristics of air flowing into and out of precipitating convection over the west pacific warm pool. *Quart. J. R. Meteorol. Soc.*, **125**, 1209–1229.

Kuang, Z., 2008: Modeling the interaction between cumulus convection and linear gravity waves using a limited-domain cloud system-resolving model. *J. Atmos. Sci.*, **65**, 576–591.

Kuang, Z., 2011: The wavelength dependence of the gross moist stability and the scale selection in the instability of column-integrated moist static energy. *J. Atmos. Sci.*, **68**, 61–74.

Kuang, Z., and C. Bretherton, 2006: A mass-flux scheme view of a high-resolution simulation of a transition from shallow to deep cumulus convection. *J. Atmos. Sci.*, **63**, 1895–1909.

Kuang, Z., P. Blossey, and C. Bretherton, 2005: A new approach for 3D cloud-resolving simulations of large-scale atmospheric circulation. *Geophys. Res. Lett.*, **32**, L02,809.

LeMone, M., and E. Zipser, 1980: Cumulonimbus vertical velocity events in GATE. Part I: Diameter, intensity and mass flux. *J. Atmos. Sci.*, **37**, 2444–2457.

Leonard, B., M. MacVean, and A. Lock, 1993: Positivity-preserving numerical schemes for multidimensional advection. *NASA STI/Recon Technical Report N*, **93**, 27,091.

Lin, J., K. Weickman, G. Kiladis, B. Mapes, S. Schubert, M. Suarez, J. Bacmeister, and M. Lee, 2008a: Subseasonal variability associated with Asian Summer Monsoon simulated by 14 IPCC AR4 Coupled GCMs. *J. Climate*, **21**, 4541–4567.

Lin, J.-L., G. N. Kiladis, B. E. Mapes, K. M. Weickmann, K. R. Sperber, W. Lin, et al., 2006: Tropical intraseasonal variability in 14 IPCC AR4 climate models. Part I: Convective signals. *J. Climate*, **19**, 2665–2690.

Lin, J.-L., M.-I. Lee, D. Kim, I.-S. Kang, and D. M. Frierson, 2008b: The impacts of convective parameterization and moisture triggering on AGCM-Simulated convectively coupled equatorial waves. *J. Climate*, **21**, 883–909.

Lin, J.-L., B. E. Mapes, K. M. Weickmann, G. N. Kiladis, S. D. Schubert, M. J. Suarez, J. T. Bacmeister, and M.-I. Lee, 2008c: North american monsoon and convectively coupled equatorial waves simulated by IPCC AR4 coupled GCMs. *J. Climate*, **21**, 2919–2937.

Lin, Y., R. Farley, and H. Orville, 1983: Bulk parameterization of the snow field in a cloud model. *J. Appl. Meteor.*, **22**, 1065–1092.

Liu, P., M. Satoh, B. Wang, H. Fudeyasu, T. Nasuno, T. Li, et al., 2009: An MJO simulated by the NICAM at 14-and 7-km resolutions. *Monthly Weather Review*, **137**, 3254–3268.

Liu, W., W. Tang, and P. Niiler, 1991: Humidity profiles over the ocean. *J. Climate*, **4**, 1023–1034.

Mapes, B., 1997: Equilibrium vs. activation control of large-scale variations of tropical deep convection. *The physics and parameterization of moist atmospheric convection*, pp. 321–358.

Mapes, B., 2004: Sensitivities of cumulus-ensemble rainfall in a cloud-resolving model with parameterized large-scale dynamics. *J. Atmos. Sci.*, **61**, 2308–2317.

Mapes, B., and X. Wu, 2001: Notes and correspondence. Convective eddy momentum tendencies in long cloud-resolving model simulations. *J. Atmos. Sci.*, **58**, 517–526.

Martin, G., et al., 2011: The hadgem2 family of met office unified model climate configurations. *Geoscientific Model Development*, **4**, 723–757.

Mason, P., 1989: Large-eddy simulation of the convective atmospheric boundary layer. *J. Atmos. Sci.*, **46**, 1492–1516.

Masunaga, H., 2012: A satellite study of the atmospheric forcing and response to moist convection over tropical and subtropical oceans. *J. Atmos. Sci.*, **69**, 150–167.

Molinari, J., D. M. Romps, D. Vollaro, and L. Nguyen, 2012: CAPE in tropical cyclones. *J. Atmos. Sci.*, **69**, 2452–2463.

Morton, B., G. Taylor, J. Turner, B. Morton, G. Taylor, and J. Turner, 1956: Turbulent gravitational convection from maintained and instantaneous sources. *Proceedings of the Royal Society of London. Series A. Mathematical and Physical Sciences*, **234**, 1–23.

Nakajima, K., and T. Matsuno, 1988: Numerical experiments concerning the origin of cloud clusters in the tropical atmosphere. *J. Meteor. Soc. of Japan*, **66**, 309–329.

Neelin, J., and N. Zeng, 2000: A Quasi-Equilibrium Tropical Circulation Model - Formulation. *J. Atmos. Sci.*, **57**, 1741–1766.

Nilsson, J., and K. Emanuel, 1999: Equilbrium atmospheres of a two-column radiative-convective model. *Quart. J. R. Meteorol. Soc.*, **125**, 2239–2264.

Palmer, T., G. Shutts, and R. Swinbank, 1986: Alleviation of a systematic westerly bias in general circulation and numerical weather prediction models through an orographic gravity wave drag parametrization. *Quart. J. R. Meteorol. Soc.*, **112**, 1001–1039.

Pauluis, O., and I. Held, 2002: Entropy budget of an atmosphere in radiative-convective equilibrium. Part I: Maximum work and frictional dissipation. *J. Atmos. Sci.*, **59**, 125–139.

Petch, J., and M. Gray, 2001: Sensitivity studies using a cloud-resolving model simulation of the tropical west pacific. *Quart. J. R. Meteorol. Soc.*, **127**, 2287–2306.

Petch, J., A. R. Brown, and M. E. B. Gray, 2002: The impact of horizontal resolution on the simulations of convective development over land. *Quart. J. R. Meteorol. Soc.*, **128**, 2031–2044.

Petch, J., P. Blossey, and C. Bretherton, 2008: Differences in the lower troposphere in two-and three-dimensional cloud-resolving model simulations of deep convection. *Quart. J. R. Meteorol. Soc.*, **134**, 1941–1946.

Piacsek, S., and G. Williams, 1970: Conservation properties of convection difference schemes. *J. Atmos. Sci.*, **6**, 392–405.

Pierrehumbert, R., 1995: Thermostats, radiator fins, and the local runaway greenhouse. *J. Atmos. Sci.*, **52**, 1784–1806.

Ramsay, H., and A. Sobel, 2011: Effects of relative and absolute sea surface temperature on tropical cyclone potential intensity using a single-column model. *J. Climate*, **24**, 183–193.

Randall, D., M. Khairoutdinov, A. Arakawa, and W. Grabowski, 2003: Breaking the cloud parameterization deadlock. *Bull. Amer. Meteor. Soc.*, **84**, 1547–1564.

Randall, D. A., R. A. Wood, S. Bony, R. Colman, T. Fichefet, et al., 2007: Climate models and their evaluation. *Climate Change 2007: The physical basis. Contribution of Working Group I to the Fourth Assessment Report of the Intergovernmental Panel on Climate Change*, S. Solomon, D. Qin, M. Manning, Z. Chen, M. Marquis, K. B. Averyt, M. Tignor, and H. L. Miller, Eds., Cambridge University Press, Cambridge, United Kingdom and New York, NY, USA.

Raval, A., A. Oort, and V. Ramaswamy, 1994: Observed dependence of outgoing longwave radiation on sea surface temperature and moisture. *J. Climate*, **7**, 807–821.

Raymond, D., 2000: Thermodynamic control of tropical rainfall. *Quart. J. R. Meteorol. Soc.*, **126**, 889–898.

Raymond, D., and S. Sessions, 2007: Evolution of convection during tropical cyclogenesis. *Geophys. Res. Lett.*, **34**, L06,811.

Raymond, D., and X. Zeng, 2000: Instability and large-scale circulations in a two-column model of the tropical troposphere. *Quart. J. R. Meteorol. Soc.*, **126**, 3117–3135.

Raymond, D., and X. Zeng, 2005: Modelling tropical atmospheric convection in the context of the weak temperature gradient approximation. *Quart. J. R. Meteorol. Soc.*, **131**, 1301–1320.

Raymond, D. J., 2007: Testing a cumulus parametrization with a cumulus ensemble model in weak-temperature-gradient mode. *Quart. J. R. Meteorol. Soc.*, **133**, 1073–1085.

Rennó, N., K. Emanuel, and P. Stone, 1994: Radiative-convective model with an explicit hydrologic cycle. 1. formulation and sensitivity to model parameters. *J. Geophys. Res.*, **99**, 14,429–14,442.

Robe, F., and K. Emanuel, 1996: Moist convective scaling: Some inferences from three-dimensional cloud ensemble simulations. *J. Atmos. Sci.*, **53**, 3265–3275.

Robe, F., and K. Emanuel, 2001: The effect of vertical wind shear on radiative-convective equilibrium states. *J. Atmos. Sci.*, **58**, 1427–1445.

Romps, D., 2012: Weak pressure gradient approximation and its analytics solutions. *J. Atmos. Sci.*, **69**, 2835–2845.

Rotunno, R., J. Klemp, and M. Weisman, 1988: A theory for strong, long-lived squall lines. *J. Atmos. Sci.*, **45**, 463–485.

Rutledge, S., and P. Hobbs, 1984: The mesoscale and microscale structure and organisation of clouds and precipitation in mid-latitude cyclones. *J. Atmos. Sci.*, **10**, 2033–2037.

Sessions, S., S. Sugaya, D. Raymond, and A. Sobel, 2010: Multiple equilibria in a cloud-resolving model using the weak temperature gradient approximation. *J. Geophys. Res.*, **115**, D12,110.

Shaevitz, D., and A. Sobel, 2004: Implementing the weak temperature gradient approximation with a full vertical structure. *Monthly Weather Review*, **132**, 662–669.

Shutts, G., and M. Gray, 1994: A numerical modelling study of the geostrophic adjustment process following deep convection. *Quart. J. R. Meteorol. Soc.*, **120**, 1145–1178.

Shutts, G. J., and T. N. Palmer, 2007: Convective forcing fluctuations in a cloud-resolving model: Relevance to the stochastic parameterization problem. *J. Climate*, **20**, 187–202.

Simpson, J., and V. Wiggert, 1969: Models of precipitating cumulus towers. *Monthly Weather Review*, **97**, 471–489.

Sobel, A., and C. Bretherton, 2000: Modeling tropical precipitation in a single column. *J. Climate*, **13**, 4378–4392.

Sobel, A., and J. Neelin, 2006: The boundary layer contribution to intertropical convergence zones in the quasi-equilibrium tropical circulation model framework. *Theoretical and Computational Fluid Dynamics*, **20**, 323–350.

Sobel, A., G. Bellon, and J. Bacmeister, 2007: Multiple equilibria in a single-column model of the tropical atmosphere. *Geophys. Res. Lett.*, **34**, L22,804.

Sobel, A. H., S. E. Yuter, C. S. Bretherton, and G. N. Kiladis, 2004: Large-scale Meteorology and Deep Convection during TRMM KWAJEX. *Monthly Weather Review*, **132**, 422–444.

Sui, C., and K. Lau, 1992: Multiscale phenomena in the tropical atmosphere over the Western Pacific. *Monthly Weather Review*, **120**, 407–430.

Sui, C., K. Lau, W. Tao, and J. Simpson, 1994: The Tropical Water and Energy Cycles in a Cumulus Ensemble Model. Part I: Equilibrium Climate. *J. Atmos. Sci.*, **51**, 711–728.

Sun, D., and R. Lindzen, 1993: Distribution of tropical tropospheric water vapor. *J. Atmos. Sci.*, **50**, 1643–1660.

Tao, W., J. Simpson, and S. Soong, 1987: Statistical Properties of a Cloud Ensemble: A Numerical Study. *J. Atmos. Sci.*, **44**, 3175–3187.

Tao, W., J. Simpson, C. Sui, C. Shie, B. Zhou, K. Lau, and M. Moncrieff, 1999: Equilibrium states simulated by cloud-resolving models. *J. Atmos. Sci.*, **56**, 3128–3139.

Tompkins, A., 2000: The impact of dimensionality on long-term cloud-resolving model simulations. *Monthly Weather Review*, **128**, 1521–1535.

Tompkins, A., 2001: Organization of tropical convection in low vertical wind shears: The role of water vapor. *J. Atmos. Sci.*, **58**, 529–545.

Tompkins, A., and G. Craig, 1998a: Radiative-convective equilibrium in a three-dimensional cloud-ensemble model. *Quart. J. R. Meteorol. Soc.*, **124**, 2073–2097.

Tompkins, A., and G. Craig, 1998b: Time-scales of adjustment to radiative-convective equilibrium in the tropical atmosphere. *Quart. J. R. Meteorol. Soc.*, **124**, 2693–2713.

Tompkins, A., and K. Emanuel, 2000: The vertical resolution sensitivity of simulated equilibrium temperature and water-vapour profiles. *Quart. J. R. Meteorol. Soc.*, **126**, 1219–1238.

Turner, J., 1963: The motion of buoyant elements in turbulent surroundings. *J. Fluid Mech*, **16**, 1–16.

Vincent, D., 1994: The South Pacific convergence zone (SPCZ): A review. *Monthly Weather Review*, **122**, 1949–1970.

Wang, S., and A. Sobel, 2011: Response of convection to relative sea-surface temperature: Cloud-resolving simulations in two and three dimensions. *J. Geophys. Res.*, **116**, D11,119.

Warner, J., 2010: The water content of cumuliform cloud. *Tellus*, **7**, 449–457.

Webster, P., and R. Lukas, 1992: TOGA COARE: The Coupled Ocean Response Experiment. *Bull. Amer. Meteor. Soc.*, **73**, 1377–1416.

Woolnough, S., P. Blossey, K. Xu, P. Bechtold, J. Chaboureau, et al., 2010: Modelling convective processes during the suppressed phase of a Madden–Julian Oscillation: Comparing single-column models with cloud-resolving models. *Quart. J. R. Meteorol. Soc.*, **136**, 333–353.

Wu, C., B. Stevens, and A. Arakawa, 2009: What controls the transition from shallow to deep convection? *J. Atmos. Sci.*, **66**, 1793–1806.

Wyant, M. C., C. S. Bretherton, H. A. Rand, and D. E. Stevens, 1997: Numerical simulations and a conceptual model of the stratocumulus to trade cumulus transition. *J. Atmos. Sci.*, **54**, 168–192.

Xu, K.-M., R. T. Cederwall, L. J. Donner, W. W. Grabowski, F. Guichard, et al., 2002: An intercomparison of cloud-resolving models with the Atmospheric Radiation Measurement summer 1997 intensive observation period data. *Quart. J. R. Meteorol. Soc.*, **128**, 593–624.

Yanai, M., S. Esbensen, and J. Chu, 1972: *Determination of bulk properties of tropical cloud clusters from large-scale heat and moisture budgets*. Department of Meteorology, University of California.

Yano, J., M. Moncrieff, and J. McWilliams, 1998: Linear stability and single-column analyses of several cumulus parametrization categories in a shallow-water model. *Quart. J. R. Meteorol. Soc.*, **124**, 983–1005.

Zeng, X., W. Tao, M. Zhang, C. Peters-Lidard, S. Lang, et al., 2007: Evaluating clouds in long-term cloud-resolving model simulations with observational data. *J. Atmos. Sci.*, **64**, 4153–4177.

Zipser, E., and M. LeMone, 1980: Cumulonimbus Vertical Velocity Events in GATE. Part II: Synthesis and Model Core Structure. *J. Atmos. Sci.*, **37**, 2458–2469.